ENERGY HARVESTING WITH PIEZOELECTRIC GRASS FOR AUTONOMOUS SELF-SUSTAINING SENSOR NETWORKS

by

Jared Dale Hobeck

A dissertation submitted in partial fulfillment
of the requirements for the degree of
Doctor of Philosophy
(Aerospace Engineering)
in The University of Michigan
2014

Doctoral Committee:

Professor Daniel J. Inman, Chair
Assistant Professor Nakhiah C. Goulbourne
Assistant Professor Jeffrey T. Scruggs
Professor Anthony M. Waas

~~ To my parents ~~

"I can do all things through Christ who strengthens me."

~ Philippians 4:13 ~

ACKNOWLEDGEMENTS

First, I would like to give a sincere thanks to Professor Daniel J. Inman for being such a great advisor, teacher, mentor, and friend. Lessons that I've learned from Dr. Inman have applied to the classroom, to my professional career, and to my personal life, and working with him has truly been a pleasure. Also, thanks to Dr. Nakhiah C. Goulbourne, Dr. Jeffrey T. Scruggs, and Dr. Anthony M. Waas for offering their experience and expertise while serving as members of my Ph.D. committee. Thanks to the many professors responsible for developing my academic foundation by inspiring and challenging me to work hard throughout my undergraduate and graduate studies at Montana Tech, Virginia Tech, and the University of Michigan.

I would like to thank the University of Michigan, College of Engineering for funding the research presented in this dissertation. Also thanks to Science Applications International Corporation (SAIC) for funding portions of this work through the NSF I/UCRC Center for Energy Harvesting Materials and Systems at Virginia Tech.

I would like to thank a few students who I had the pleasure of working with during my final semesters at Michigan. Andrew Gadway – an undergraduate mechanical engineering student from the University of Michigan – performed hundreds of tedious wind tunnel tests. Data collected by Mr. Gadway was critical to the work presented in Chapter 5. Damien Geslain – a visiting graduate student from France – spent many hours with FLUENT and CFX helping to develop the CFD model discussed in Appendix B. Andrew Pocisk – an undergraduate aerospace

engineering student from the University of Michigan – was responsible for performing an experimental study with a piezoelectric grass harvester prototype in water. Results from these water experiments are not discussed in this dissertation.

Thanks to my friends and colleagues at the University of Michigan and at the Center of Intelligent Materials Systems and Structures (CIMSS) at Virginia Tech for always being willing to offer assistance in the lab, discuss ideas, help with homework, or prepare for Ph.D. candidacy exams. Thanks to Dr. Steven R. Anton and Mr. Justin Farmer for all their help in the CIMSS lab. Thanks to Dr. Onur (Baba) Bilgen for teaching me the science and art of wind tunnel design and construction. Thanks to Mr. Daniel J. Inman II for proofreading some of my papers, for numerous trips to Kroger, and for the great friendship. Also, thanks to the guys in the aerospace department tech center and machine shop at the University of Michigan for offering their time, resources, and skills as they assisted with much of my lab work.

Finally, I want to thank my friends and family for their endless support, encouragement, and prayers. I could not have made it this far without them. Thanks to Mrs. Karen West for helping me with high school math, my absolute least favorite subject. To Mr. Rick Bondy for his friendship with me and my family, and for teaching me that, “the more you know about many things, the better you will be at one thing”. Thanks to my big brother, Mr. David L. Hobeck, for always wanting to watch shows such as *NOVA* and *Bill Nye the Science Guy* with me as we grew up. My academic career started when my parents decided to homeschool me some 22 years ago. They taught me the importance of dedication and hard work. My parents have always encouraged me to pursue my passions, and they have guided and supported me every step of the way. Thank you Mr. Kim Hobeck and Mrs. Patsy Hobeck for being such great parents.

TABLE OF CONTENTS

LIST OF FIGURES

LIST OF TABLES

LIST OF APPENDICES

LIST OF SYMBOLS

A	=	Area normal to flow
b	=	Beam width
C_{Dd}	=	Equivalent drag force coefficient
C_{Dv}	=	Viscous drag force coefficient
C_{hp}	=	Specific heat at constant pressure
C_{op}	=	Pressure coherence function
C_p	=	Capacitance of piezoelectric element
c	=	Coefficient of viscous damping for a lumped parameter system
c_a	=	Velocity of sound in air
$\mathbf{c}$	=	Rayleigh-Ritz eigenvectors
c_r	=	Coefficient of strain rate damping
c_v	=	Coefficient of viscous damping
D	=	Electric displacement
d	=	Piezoelectric constant
E	=	Electric field
F_c	=	Fluid coupling force
F_d	=	Drag force

F_f	=	Force of a surrounding fluid on a structure
F_p	=	Flow-induced excitation force
F_v	=	Viscous fluid damping force
f	=	Frequency
f_s	=	Structural vibration frequency
f_v	=	Vortex shedding frequency
$G_{PP}(P,P)$	=	Pressure power spectral density of pressure probe output
$G_{PPc}(P,P)$	=	Compensated pressure power spectral density of pressure probe output
$G_{PP}(HW,HW)$	=	Pressure power spectral density of pressure probe output
g	=	Gravitational acceleration
H	=	Heaviside step function
H	=	Frequency response function
H^*	=	Complex conjugate of a frequency response function
H_c	=	Electromechanical coupling frequency response function
H_P	=	Frequency response function estimate for pressure probe
H_v	=	Electromechanical frequency response function
h	=	Beam height
h_a	=	Location of the bottom of the substrate with respect to the neutral axis of the composite section of the beam
h_b	=	Location of the bottom surface of the piezoelectric material relative to the neutral axis of the composite beam segment
h_c	=	Locations of the top surface of the piezoelectric material relative to the neutral axis of the composite beam segment

h_{pc} = Locations of the centerline of the piezoelectric material relative to the neutral axis of the composite beam segment

I = Area moment of inertia

I_m = Electrical current

J = Acceptance integral value

j = Imaginary number

$\mathbf{K}$ = Rayleigh-Ritz stiffness matrix

$\widetilde{\mathbf{K}}$ = Rayleigh-Ritz stiffness matrix modified to account for added tip mass

$\mathbf{K}_g$ = Geometric stiffness matrix

k_v = Vortex shedding constant for an array of flexible structures

k = Linear stiffness coefficient for a lumped parameter system

L = Beam length

L_c = Characteristic length of a bluff body

ℓ = Pressure probe tube length

M = Bending moment

$\mathbf{M}$ = Rayleigh-Ritz mass matrix

$\widetilde{\mathbf{M}}$ = Rayleigh-Ritz mass matrix modified to account for added tip mass

MSE = Mean squared error

M_t = Tip mass

m = Linear mass density of a beam

$\tilde{m}$ = Mass for a lumped parameter system

m_f = Linear mass density of fluid surrounding a beam

N	=	Number of modes to keep for Rayleigh-Ritz calculations
N_J	=	Number of modes to keep for acceptance value calculations
N_{ae}	=	Number of active elements in a harvester array
N_{pe}	=	Number of passive elements in a harvester array
N_z	=	Axial load
n	=	Number of array elements used in mean squared error calculations
n_t	=	Polytropic expansion factor of fluid inside pressure probe tube
n_v	=	Polytropic expansion factor of fluid inside pressure probe transducer
O_{1-6}	=	Six coefficients used to estimate fluid coupling and damping functions
P	=	Fluctuating pressure
$\overline{P}$	=	Total pressure
P_{ave}	=	Average power output
$\tilde{P}_{ave}$	=	Estimated average power output
Pr	=	Prandtl number
P_s	=	Static pressure
$\tilde{P}_{tot}$	=	Total estimated power output
$\tilde{P}_{\rho}$	=	Area power density of a harvester array
p	=	Pressure time series
p_a	=	Ambient pressure
q	=	Gap distance between two adjacent cantilevers
R	=	Pressure probe tube radius
R_a	=	Universal gas constant for air

R_L = Load resistance

R_{opt} = Optimum load resistance

R_p = Pressure cross-correlation function

S_c = Modal piezoelectric coupling force power spectral density

S_f = Force power spectral density for a single-degree-of-freedom system

S_p = Pressure power spectral density

$S^{p,s}$ = Mechanical strain

St = Strouhal Number

S_u = Displacement power spectral density of a beam

S_v = Strain-induced load voltage power spectral density

S_x = Displacement power spectral density for a single-degree-of-freedom

S_α = Fluid coupling force contribution based on relative displacement

S_γ = Fluid coupling force contribution based on relative velocity

S_η = Modal displacement power spectral density

S_ψ = Modal turbulence-induced force power spectral density

T = Sample time period

T_a = Ambient temperature

TI = Turbulence intensity

$T^{p,s}$ = Mechanical Stress

t = Time

U = Flow velocity

$\bar{U}$ = Mean free-stream flow velocity

$U_{m,n}$ = Orthogonal and orthonormal polynomial shape functions

U_{rms} = Root mean square flow velocity

u = Beam deflection

$\overline{u}$ = Statistically derived beam displacement

$\overline{u}^2$ = Mean square displacement of a beam

V_0 = Steady-state strain-induced load voltage amplitude

$\overline{V}_0$ = Modal mean steady-state strain-induced load voltage amplitude

V_{RMS} = Root mean square voltage

V_t = Pressure probe transducer volume

v = Strain induced voltage across resistive load

x_1 = Initial displacement

$\overline{x}^2$ = Mean square displacement for a single-degree-of-freedom system

Y = Young's modulus

YI = Bending stiffness

z = Lengthwise beam coordinate

Greek Symbols

α = Relative displacement coupling parameter

$\tilde{\alpha}$ = Shear wave number

β = Linearity parameter for flow-induced excitation

Γ_n = Bessel function of the first kind and n^{th} order

γ = Relative velocity coupling parameter

$\tilde{\gamma}$ = Ratio of specific heats

δ = Dirac delta function

Δ = Harvester array element spacing

ε^T = Stress-free dielectric permittivity

ζ = Modal damping ratio

η = Modal displacement

$\overline{\eta}$ = Statistically derived modal displacement

$\overline{\eta}_e$ = Mean modal displacement for a fully elastic beam

θ = Stability threshold parameter for flow-induced excitation

ϑ = Piezoelectric coupling for a unimorph cantilevered beam

λ = Correlation length

λ_t = Thermal conductivity

μ = Modal fluid mass

μ_a = Dynamic viscosity of air

ν = Kinematic viscosity

ξ = Dissipation function for heat transfer due to fluid friction

π = Mathematical constant PI

ρ_a = Mass density of air

ρ_f = Mass density of a fluid

σ = Ratio of transducer volume increase due to diaphragm deflection

$\sigma_{\max}$ = Maximum mechanical stress

τ = Offset or shift in time

τ_c = Time constant for harvester circuit

ϕ = Rayleigh-Ritz mode shapes

φ = Modal constant for a unimorph cantilevered beam

χ = Modal piezoelectric coupling term for a unimorph cantilevered beam

ψ = Modal fluid forcing function

$\overline{\psi}$ = Statistically derived fluid forcing function

ω = Angular frequency

ω_S = Frequency bound of pressure power spectral density

ω_{nyq} = Nyquist frequency

ω_v = Vortex passing frequency for array of flexible structures

Subscripts (unless defined otherwise)

s = Substrate material layer parameter

p = Piezoelectric material layer parameter

c = Composite beam segment parameter

m, n = Integer values that denote a particular mode of vibration

1,3 = Denote z and x axis directions (respectively) for a material parameter

x, y, z = Denote x, y, and z axis directions respectively

Superscripts (unless defined otherwise)

s = Substrate material layer parameter

p = Piezoelectric material layer parameter

ABSTRACT

Energy Harvesting with Piezoelectric Grass for Autonomous Self-Sustaining Sensor Networks

by

Jared Dale Hobeck

Chair: Daniel J. Inman

The primary objective of this research is to develop a deploy-and-forget energy harvesting device for use in low velocity, highly turbulent, and unpredictable fluid flow environments. The work presented in this dissertation focuses on a novel, lightweight, highly robust, energy harvester design referred to as *piezoelectric grass*. This biologically inspired design consists of an array of cantilevers, each constructed with piezoelectric material. When exposed to a wide range of flow conditions, these cantilevers experience vigorous persistent vibration.

Included in this work is an experimentally validated theoretical analysis of the piezoelectric grass harvester generalized for the case of a single cantilever in turbulent cross-flow. Using this distributed parameter model, a brief parameter optimization study is presented. This study demonstrates how the unimorph harvester design could be modified to achieve maximum power output in a given turbulent fluid flow condition.

Two high-sensitivity pressure probes were needed to perform spatiotemporal measurements within various turbulent flows. Measurements with these probes are used to develop a statistically derived turbulent fluid forcing function. This function is then combined with an

analytical structural dynamics model such that not only the modal RMS displacements, but also the modal displacement power spectral density trends are predicted for a given structure. Pressure probe design, turbulence measurement techniques, and both statistical and analytical models are validated with experimental results. These results are produced from several case studies performed with a single cantilever exposed to turbulent cross-flow.

An experimental investigation on the energy harvesting potential of large harvester arrays containing up to 112 flexible piezoelectric structures is presented. Results of several case studies reveal trends in power output as functions of flow velocity and array configuration. These experimental results show that a given array will experience large amplitude, waving, resonant-type vibration over a large range of velocities, and is unaffected by large-scale turbulence upstream of the array. These dynamic characteristics make large arrays of flexible piezoelectric structures ideal for many energy harvesting applications. This work presents the first study found in literature to take advantage of this excitation mechanism for energy harvesting.

Lastly, this dissertation presents the first documented investigation of a flow-induced vibration phenomenon referred to as dual cantilever flutter (DCF). DCF occurs when two similar beams are placed side-by-side in a cross-flow. At a particular combination of flow velocity and distance between the beams, aeroelastic coupling causes the beams to become unstable and undergo limit cycle oscillations. If unaccounted for, DCF vibration has the potential to cause catastrophic structural damage or unwanted acoustic excitation. Experimental results show that DCF can be used as an effective energy harvesting method. An attractive feature of DCF for energy harvesting is that it provides a robust type of flow-induced excitation over a large range of flow velocities similar to the large arrays of piezoelectric grass. An experimentally validated lumped parameter model for DCF is presented along with results of an experimental study on energy harvesting from DCF. Results also include CFD simulations that were setup and executed using ANSYS-CFX.

CHAPTER I

INTRODUCTION AND LITERATURE REVIEW

1.1 Introduction

Research on the topic of energy harvesting has developed into a large, interdisciplinary field over the past two decades. An energy harvester may be defined as a device which can be used to extract ambient or otherwise wasted energy from a natural or man-made source, or from any combination of a vast variety of sources. The most common types of energy sources for existing energy harvesting applications are mechanical vibrations, thermal gradients, flowing fluids, and solar energy. The work presented in the remaining chapters of this dissertation will focus on energy harvesting from a flowing fluid.

Initially, all interest was directed toward applications in water. Due to the convenience of experimenting in air and considering a wind tunnel facility was readily available, proof of concept tests were performed in air rather than in water. Results of these early experiments (presented in Chapter 2) motivated the decision to focus the proposed research on air flow applications. Therefore, the majority of the experimental work and analysis presented in this dissertation is for low velocity (< ~15 m/s), highly turbulent air flow.

1.1.1 Motivation

Existing sensor systems used for environmental monitoring in remote rivers for example, are powered by large, heavy batteries that eventually need recharged or replaced. When considering the one-time cost of a simple flow sensor and data transmission system, compared to the cost of transporting and paying a technician to replace batteries, it is apparent that maintenance costs alone can easily exceed the cost of the entire sensor network. These maintenance costs could be reduced or potentially eliminated if a sustainable energy harvesting system could be designed and implemented as a primary power source. This type of energy harvesting technology would provide clean sustainable energy for any low-power application in or near flowing fluids.

1.1.2 Objectives of the Dissertation

While many fluid flow harvesters in the literature work well in steady and predictable fluid flows, their performance suffers in the presence of turbulence and/or is highly dependent on fluid flow velocity. The primary objective of the research presented in this dissertation is to develop an energy harvesting device where the primary source of ambient energy is low velocity, highly unsteady, turbulent fluid flow.

The harvester should be a self-sustained, lightweight, robust, deploy-and-forget device. It should be capable of withstanding remote, uninhabited, natural or industrial environments for many months or even years without requiring any form of human contact. The power produced should be stored temporarily in small batteries or capacitors which would be charging as long as there is fluid flow. Energy from the device could be available for either constant low-power applications, or even for higher power applications with which a duty cycle type operation would be implemented.

1.1.3 Proposed Harvester Design

There are two major differences between most existing fluid flow energy harvesting methods and the methods presented in this dissertation. First, neither steady conditions nor discrete vortex shedding is assumed to be available in the flow. Secondly, rather than having one harvesting device, the proposed design consists of an array of generating elements in the turbulent wake of a bluff body, or in an entirely turbulent fluid flow environment. Robustness and survivability are major concerns when considering the potential intended environment for the harvester. An attractive feature of this design which directly addresses these concerns is its inherent redundancy. For example: if one element in the array becomes damaged, the device will still produce power. Depending on the size of the array, one damaged element will only contribute to a minor reduction in total power output.

1.1.4 Biological Inspiration

Piezoelectric energy harvesters with biologically inspired designs have been explored by several authors. An artificial kelp design was proposed by Pankonien and Ounaies (2010) for wave or tidal flow [1]. Hobbs and Hu (2011) presented a tree-inspired design for vortex-induced vibration harvesting [2]. A biologically-inspired *flapping-leaf* design was presented by Li *et al* (2009) where a flexible, passive material (the so-called *leaf*) was connected to the tip of a PVDF cantilever [3]. As the leaf fluttered in the wind, it caused the cantilever to vibrate and thus produce power. While [1–3] have an operation concept similar to the harvester presented in this dissertation, the form of excitation used to estimate power output is appropriate for either bulk fluid motion, vortex-induced vibration (VIV), or flutter rather than for turbulence-induced vibration (TIV). Also, the harvesters in [1–3] and in related literature are lacking experimental

and analytical investigations performed on large array dynamics rather than for a single harvester or array of only a few elements.

As the name suggests, the piezoelectric grass harvester design concept was inspired by grass and other similar vegetation that can be observed in nature. When exposed to wind or flowing water, natural vegetation can appear to be in constant and sometimes periodic motion. The piezoelectric grass harvester is able to convert that motion directly into useful amounts of clean energy from a simple, solid-state device.

1.1.5 Potential Harvester Application Areas

Implementation and field testing of the harvesting devices discussed in this work were not considered as main objectives of this dissertation; however, robustness and ability to harvest energy in variable and unpredictable flow conditions were key harvester design objectives. Potential application areas which have these variable and/or turbulent flow characteristics include small rivers, streams, tidal flows, harbors, waterways, ducts, ventilation systems and pipelines. The primary function of the energy harvester is to eliminate the need for batteries and to provide a wireless power source which can be used for autonomous self-sustaining sensor networks. Specific application areas for the piezoelectric grass harvester include powering surveillance and security systems, and sensor networks for structural, environmental, and industrial monitoring. Conceptual application areas of the piezoelectric grass harvester are illustrated in Figure 1.1.

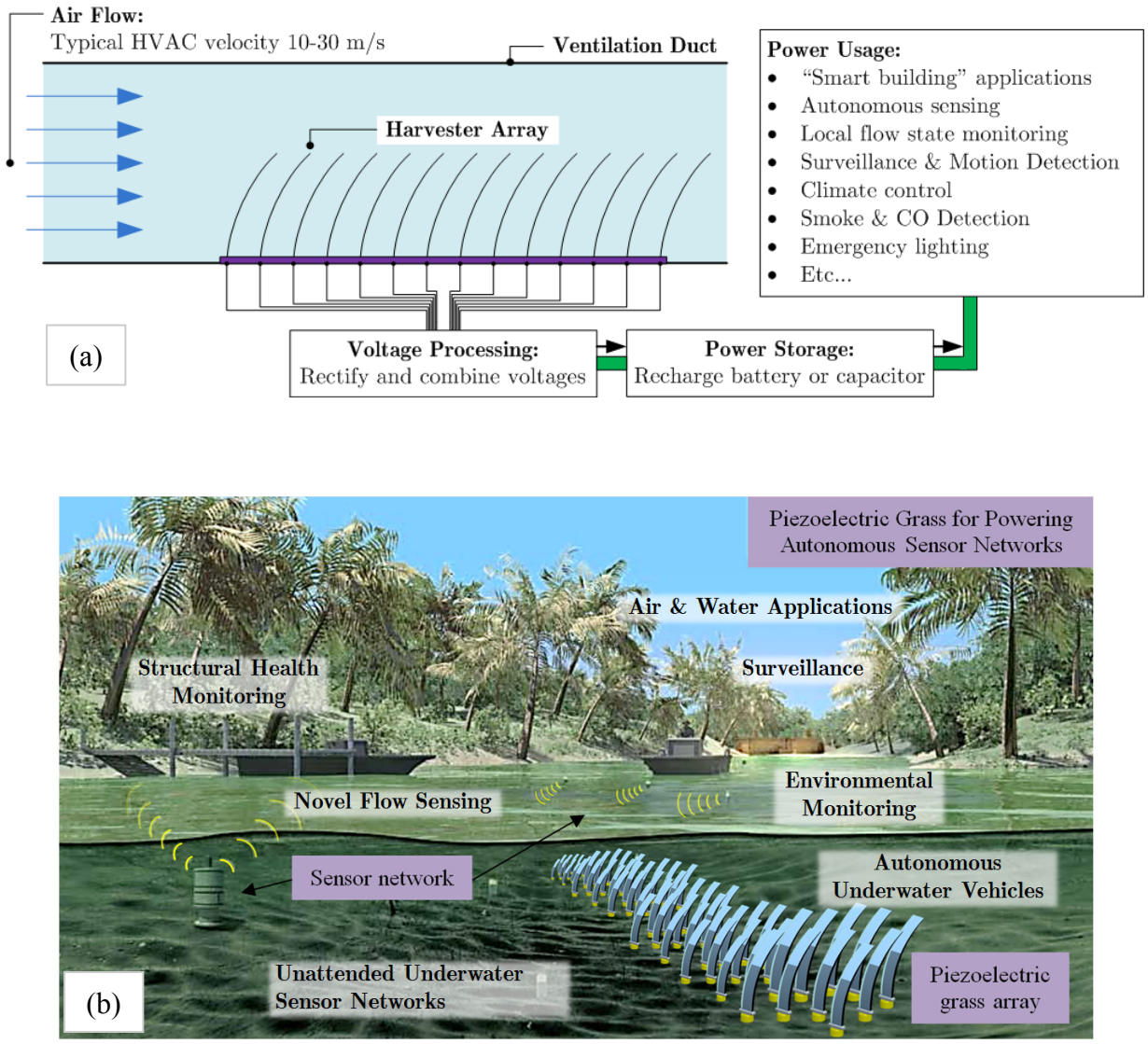

Figure 1.1: Conceptual application areas of the proposed piezoelectric grass harvester array shown in (a) ventilation systems and in (b) natural riverine environments.

1.2 Existing Technologies for Fluid Flow Energy Harvesting

Harnessing the energy of flowing fluid to accomplish useful work is one of the oldest power generation technologies in history. Among the earliest recorded mechanisms for hydropower were used by ancient Greek and Roman civilizations. Some of the earliest known water-mills date back to A.D. 700 [4]. The first documented experimental work on hydroelectricity was performed and published by Armstrong in 1840 [5]. For centuries hydropower has been used for large-scale electric power generation and is currently supplying nearly 19% of the global demand for electricity [6]. In 1887 Professor James Blyth was performing experiments with possibly the world's first electricity generating wind-powered machine [7]. Today, approximately 2.5% of the world's electricity is produced by wind power [8].

Technology for electrical power production from flowing fluids has been developing for centuries; however, these efforts have almost exclusively focused on large-scale power systems producing on the order of thousands to millions of watts. As electronic devices become progressively smaller and more efficient, the power they require to operate decreases. Advances in miniaturizing electronics now make it possible to power entire sensor networks and even small computers using only milliwatts. It was not until recently that powering these miniaturized systems via small-scale energy extraction from fluid flow was investigated.

Among the earliest piezoelectric energy harvesting research found in literature is fluid flow energy harvesting which was presented by Klakken *et al* in 1983 [9] and also by Schmidt *et al* in 1983 [10]. Later, Schmidt (1985) presented a patented flow-induced vibration piezoelectric energy harvesting device [11]. Schmidt then published a more detailed theoretical analysis and experimental results for the harvesters from [9–11] several years later in 1992 [12].

Energy harvesting from fluid flow is a topic that has gained much popularity since the early efforts of Klakken and Schmidt. There now exists an extensive variety of flow energy harvesting methods discussed in the literature. Many authors have explored simple yet effective harvester designs such as miniature windmills and turbines, while others have developed more creative or complex designs. The following sections will introduce several traditional and nontraditional fluid flow harvester types found in the literature. Operating characteristics will be summarized, while various advantages and disadvantages of the harvester design and performance will be highlighted.

Table 1.1 provides a performance summary of various types of selected fluid flow energy harvesting devices from the literature along with results of devices presented in Chapters 2,3,5 and 6. Table 1.1 includes nontraditional harvester types such as TIV, VIV, flutter, and piezoelectric turbines along with traditional electromagnetic (EM) turbine types. Area power density was calculated by dividing the total power output by the harvester area normal to the flow. Volume power density was calculated by dividing the total power output by the harvester volume. Efficiency was calculated by dividing the total power output by the total power available in the flowing fluid. Because electrical and mechanical losses were not considered, all efficiency values in Table 1.1 should be considered as conservative estimates used for comparison only.

Table 1.1: Summary of various types of selected fluid flow energy harvesting devices.

Harvester Type	*Power* (mW)	*Velocity* (m/s)	*Area Den.* (W/m^2)	*Vol. Den.* (W/m^3)	*Efficiency* (%)	*Reference*
TIV	4.00	11.5	1.95	13.0	0.214	Chapter 2
TIV	0.122	8.10	2.65×10^{-2}	0.174	8.31×10^{-3}	Chapter 3
TIV	304	14.3	10.4	12.2	0.598	Chapter 5
TIV	6.00×10^{-5}	11.0	9.38×10^{-5}	6.40×10^{-4}	1.17×10^{-5}	Akaydin *et al* [13]
VIV	4.00×10^{-3}	7.23	8.33×10^{-3}	4.80×10^{-4}	3.67×10^{-3}	Akaydin *et al* [13]
VIV	3.00×10^{-2}	5.00	1.54×10^{-2}	1.95×10^{-3}	2.05×10^{-2}	Gao *et al* [14]
Flutter	0.296	8.00	13.2	165	4.30	Li *et al* [3]
Flutter	3.00	25.0	0.417	-	4.44×10^{-3}	Schmidt [12]
Flutter	0.615	8.00	13.4	167	4.36	Li *et al* [15]
Flutter	2.10	8.00	2.14	6.83	0.698	Bryant *et al* [16]
Flutter	2.50	27.0	0.375	0.770	3.18×10^{-3}	Dunnmon *et al* [17]
Flutter	1.59	13.0	0.123	486	9.37×10^{-3}	Chapter 6
Turbine (PZT)	4.00	10.0	0.286	3.57	4.76×10^{-2}	Karami *et al* [18]
Turbine (PZT)	1.20	5.36	0.134	2.64	0.145	Chen *et al* [19]
Turbine (PZT)	7.50	4.47	0.521	26.0	0.972	Priya [20]
Turbine (EM)	4.32	10.0	5.37	83.9	0.895	Howey *et al* [21]
Turbine (EM)	60.0	9.00	11.9	199	2.73	Flammini *et al* [22]
Turbine (EM)	130	11.8	93.8	1117	9.45	Rancourt *et al* [23]

1.2.1 Traditional Harvesting Methods

Traditional harvester designs include those with turbines or propellers, and their motion typically involves directional rotation of a shaft. The simplest designs produce electric energy via electromagnetism with a classic generator design consisting of permanent magnets, coil windings, a rotor, and a stator [21–30]. Many small-scale windmill designs generate power using piezoelectricity. Most of these energy harvesting windmills typically have piezoelectric cantilevers (i.e., unimorph or bimorph cantilevers) that are excited from a rotating shaft which is being driven by the windmill/turbine blades. Coupling between the rotating shaft and the cantilevers is achieved either by direct contact between the cantilever and a cam [19,20,31–33], or through a non-contact forcing method using magnets [18,34].

Several companies market windmills and water turbines. ABS Alaskan markets so-called *micro-hydropower* turbines and small windmills that have a maximum rated output ranging from 50 W to 5 kW depending on the model [35]. Custom Manufacturing & Engineering Inc. has performed water turbine prototype tests in low velocity (1 m/s) water flow where a venturi housing was used to accelerate the flow as it approached the turbine [36].

All of these traditional designs may perform well in steady fluid flows; however, their performance diminishes significantly when exposed to unsteady flow or high-intensity turbulence. This decrease in performance is primarily caused by a poorly correlated distribution of force across the blades or propellers. Continuously varying flow velocity causes turbines to accelerate rather than operate at a steady speed which results in a further decrease of efficiency. An unattractive characteristic of propellers and turbines is that they have a minimum flow velocity (sometimes referred to as *cut-in* velocity) that is required to overcome forces opposing rotational motion such as friction and cogging torque [37]. If the flow falls below this minimum

velocity, the device will not produce power even though the fluid may still be flowing. Another disadvantage of traditional harvester designs with regard to long-term survival in natural or uncontrolled environments is there susceptibility to damage and fouling. For example, debris may come into contact with the blades or get entangled around a rotating shaft which can damage or jam the device, rendering it useless.

1.2.2 Nontraditional Harvesting Methods

Although less popular than those propeller or turbine type designs discussed in the previous section, many other harvester designs, have certain characteristics that make them a more attractive energy harvesting option depending on the specific application. The following sections discuss numerous energy harvesting techniques that operate on the dynamics of vortex-induced vibration, flutter, or turbulence-induced vibration. Other methods discussed will include microbial fuel cells, electro-magneto-hydrodynamics, and underwater gliders.

1.2.2.1 Vortex-induced Vibration

Flow-induced vibration has proven to be an excellent excitation mechanism for vibration based energy harvesting. One of the most popular techniques used to create these vibrations is from vortex shedding and is called vortex-induced vibration (VIV). Vortex shedding is a fluid dynamic instability that is typically caused when a fluid flows around a bluff body at a Reynolds number (Re) near or above Re = 49 [38]. As vortices shed off of a bluff body, a component of the fluid force acts on the bluff body in a direction perpendicular to the flow. Because vortices shed periodically off each side of the bluff body and rotate in opposite directions, the force acting on the bluff body is also periodically changing direction causing a forced excitation that is approximately sinusoidal. If the bluff body is elastic and its structural dynamics become properly

coupled with the fluid dynamics VIV occurs. For an extensive review of fundamental research focused on VIV, see the work of Williamson and Govardhan (2004) [39].

Many VIV energy harvester designs and modeling techniques have been investigated by numerous authors over the recent years. A device for large scale power generation using VIV was discussed by Bernitsas *et al* in 2008 [40] and later patented in 2009 [41]. Bernitsas *et al* showed that a rigid cylinder supported by springs on both ends while subject to low velocity (0.25 m/s) cross-flow would oscillate perpendicular to the flow at large amplitudes [40]. This motion was converted into electrical energy by connecting the cylinder to electromagnetic generators via a gear-belt system. A smaller, solid-state design developed from 2009 through 2011 by Pobering *et al* consisted of a PZT cantilever mounted to the downstream side of a bluff-body [42–45]. As vortices shed off the bluff body and traveled down the length of the cantilever they produced periodic and opposing pressure fields on the faces of the cantilever causing it to vibrate, thus producing a voltage. Closely related work was also explored by Akaydin *et al* in 2010 [13]. A design introduced by Taylor *et al* (2001) took advantage of an excitation method similar to that of Pobering; however, a flapping sheet of soft PVDF piezoelectric polymer rather than a stiff vibrating cantilever was used to generate power [46]. Another design discussed by Akaydin *et al* (2010) consists of a PZT cantilever held parallel to fluid flow with a cylindrical bluff body attached to its tip [47]. Vortex-induced vibrating motion of the cylinder was then transmitted directly to the cantilever. Similar designs driven by VIV were presented by Hobbs *et al* (2012) [2] and most recently by Gao *et al* (2013) [14]. Vortex shedding methods are quite effective in fairly steady free-stream flow; however, their performance suffers greatly when the upstream flow is spoiled with high levels of turbulence.

1.2.2.2 Flutter

Similar to VIV, flutter or flapping mechanisms operate on the principal of fluidelastic instability. As mentioned near the beginning of section 1.2, Schmidt (1985) was among the first to develop a piezoelectric energy harvesting device from a flow-induced flapping or fluttering type motion [11]. The device proposed by Schmidt generated power via piezoelectricity. Nearly a decade earlier, airfoil-type flutter harvester designs were being investigated by Bade (1975) [48] followed by McKinney *et al* (1981) [49]. Instead of piezoelectricity, these early flutter harvester designs generated power using an electromagnetic generator and gearing system.

Numerous types of energy harvester designs driven by flutter dynamics have been presented in the literature; however, most can be placed in one of only a few categories. Several authors have investigated flutter-type harvester designs that have a piezoelectric cantilever subject to cross-flow [3,15,50,51]. Another popular design type consists of a cantilevered harvester positioned such that fluid flows along the lengthwise (axial) direction of the structure from root to tip [3,15,17,46,52–54]. Most of these axial flow flutter harvesters are made with a piezoelectric material; however, a design proposed by Tang *et al* (2009) converted the fluttering motion into energy via electromagnetism by imbedding conductive coils in an aluminum cantilever and placing it in a magnetic field [54]. Energy harvesting from airfoil flutter dynamics has been investigated by many authors for nearly four decades and is perhaps the oldest flutter-type energy harvester design [16,48,49,55–59].

Bryant and Garcia (2009) were among the first to propose the concept of energy harvesting from vibrations caused by aerodynamic flutter of an airfoil [16,57]. A feasibility study was performed on the concept of energy harvesting from elastic bluff body wake galloping by Jung *et al* (2009) [56]. Pitch and plunge airfoil flutter dynamics were discussed and numerically

simulated by Shimizu *et al* (2008) [55] while an experimentally validated analytical model with application to piezoaeroelastic energy harvesting was presented by De Marqui *et al* (2010) [51].

When introduced to highly turbulent flow, periodic separation and reattachment of flow on the structure becomes sporadic and less coupled to the dynamics of the structure. These conditions may cause intermittent flutter or none at all, thus decreasing or eliminating power output. Another disadvantage of flutter or flapping type energy harvesting mechanisms is that if the flow velocity is less than the flutter speed, the device will not produce power. This minimum operational flow velocity is a concept similar to the *cut-in* velocity for turbine or propeller harvester designs mentioned in Section 1.2.1. Flutter speed is also typically higher than cut-in velocity which means more energy is lost or unable to be harvested if the flow falls below flutter speed. Some flutter devices have both minimum and maximum operating flow velocity which further restricts the harvesting potential in flows having a large range of velocity.

1.2.2.3 Turbulence-induced Vibration

Turbulence-induced vibration (TIV) is generally considered undesirable, and is a phenomenon that if not properly anticipated can lead to catastrophic structural failure. From an energy harvesting perspective however, these types of vibrations have been found to be quite valuable [60]. Unlike vortex-induced vibration, flutter, or acoustic resonance, where vibrations can be minimized or essentially eliminated by design, TIV is inevitable whenever a turbulent flow is in contact with an elastic structure [61]. Analytical investigations of TIV have been performed for decades; however, it was not until very recently that there has been interest shown in developing devices that can generate useful power from these vibrations.

A recent experimental study was performed by Akaydin *et al* (2010) in which a PVDF cantilever beam with dimensions 30mm x 16mm x 0.2mm was placed in fluid flow such that its

length was parallel to turbulent boundary layer flow [13]. Rather than using pure vortex shedding, flutter, or related fluidelastic phenomena; this turbulent boundary layer experiment was the first documented energy harvesting study conducted where turbulent flow was the primary excitation mechanism. The maximum power output was nearly 0.06 μW in a free-stream velocity of approximately 11.0 m/s. This is an extremely low output considering the same harvester was shown to produce more than 4 μW when placed in the vortex street of a cylinder in air with a velocity of only 7.23 m/s [13]. These first TIV energy harvesting experiments showed that the same harvester produced nearly an order of magnitude less power with TIV compared to VIV. This drastic reduction in power output is to be expected given the experimental parameters chosen; however, the power output potential of TIV energy harvesting should not be regarded as insignificant.

1.2.2.4 Other Fluid Flow Energy Harvesting Techniques

Several nontraditional energy harvesting methods found in the literature extract fluid flow energy from physical or chemical phenomena other than VIV, flutter, or TIV. In Section 1.2.1 several turbine and propeller type harvesting devices were discussed. A major disadvantage of these traditional harvesters is that they will not produce any power unless the flow velocity is greater than the cut-in speed. A novel device designed to overcome this challenge of low velocity or "low energy" water flow is referred to as *Deep Green Technology* which was invented by Magnus Landberg and is marketed by Minesto AB [62]. Deep Green Technology consists of a turbine mounted to a winged glider that is attached to an anchored tether and the entire assembly is submerged. The underwater glider maintains a large sweeping figure-eight pattern and travels perpendicular to the flow at a velocity several times greater than the flow itself – the motion is

similar to that of a kite. The turbine is then driven by this amplified flow velocity. A similar method used for air applications is being developed by a company called EnerKite [63].

When a conductive fluid – such as seawater – flows through a magnetic field, an electric field is induced. A novel energy harvesting device which operates on this principle was investigated by Snarski *et al* in 2004, and was called *electro-magneto-hydrodynamic* (EMHD) energy harvesting [64]. Snarski showed that the induced EMHD electric field formed in a flowing conductive fluid could be mapped to a DC voltage across a pair of electrodes placed near a permanent magnet. Very recently Pfenniger *et al* (2013) investigated the possibility of using EMHD energy harvesting from arterial blood flow [65]. Unfortunately this EMHD energy harvesting method only works with conducting fluids and yields a very low output compared other previously discussed harvesting methods.

Another unique approach for energy harvesting is with the use of microbial fuel cells as explored by Habermann *et al* (1991) [66] and more recently by Reimers *et al* (2001) [67]. It was not until 2007 that Zhen *et al* proposed that a rotating cathode driven by natural water current could increase power output by 69% [68]. The primary disadvantages of microbial fuel cells include low power output, and they require marine sediments that are rich in organic matter with a proper amount of oxygen.

St. Clair *et al* (2009, 2010) proposed a novel flow-induced vibration energy harvester that featured self-excited and self-sustained limit cycle oscillations of a piezoelectric cantilever [69,70]. The self-excited dynamic system that inspired St. Clair's design is similar to that which causes a harmonica reed to vibrate. A more through analytical and experimental analysis was performed on St. Clair's harvester by Bibo *et al* (2011) where the proposed equation of motion was based on Van der Pol oscillator dynamics [71].

A few authors have explored fluid flow energy harvesters driven by oscillatory flows such as shallow waves or tidal currents. Two biologically inspired designs for these oscillatory flow environments were artificial sea grass presented by Zurkinden *et al* (2007) [72] and artificial kelp presented by Pankonien *et al* (2010) [1].

1.3 Outline of the Dissertation

This dissertation is divided into seven chapters. Chapters 1 through 6 are intended to be a complete and independent work; however, all chapters are related and occasionally reference other chapters within the dissertation to avoid unnecessary repetition. Not including the introduction, background, and literature review discussed in the first and current chapter, the following is a brief summary of the remaining six chapters.

The work shown in this dissertation began as an open-ended design problem; therefore, Chapter 2 will present several harvester design concepts considered before a final design was chosen. Advantages and disadvantages of these designs will be discussed along with the decisions that led to the piezoelectric grass design concept. Also included in Chapter 2 will be the results of several proof-of-concept wind tunnel experiments performed with various piezoelectric grass harvester prototypes.

Chapter 3 will present a fully coupled electromechanical distributed parameter model for a cantilevered unimorph harvester in highly turbulent cross-flow. Rather than attempting to model an entire array of harvesters, this model was first developed for a single cantilever. This model consists of both analytical and statistical components. The analytical portion of the model predicts structural dynamics and electromechanical coupling, while the turbulence-induced fluid forcing function is derived from the statistical portion.

The statistical model presented in Chapter 3 required the use of two custom pressure probes for measuring highly turbulent air flow. Chapter 4 discusses the design and fabrication details of

these probes along with static and dynamic calibration techniques. Chapter 4 also discusses an analytical model used to successfully predict the acoustic attenuation within the probes. Finally, an experimental validation case study is presented in order to demonstrate how the pressure probes were used for predicting TIV of cantilever beams.

Chapter 5 focuses on large array dynamics of the piezoelectric grass harvester. These large arrays are shown to achieve a resonance condition where aeroelastic coupling between the array elements causes them to experience large amplitude persistent vibrations. The results of many wind tunnel experiments are presented and discussed.

During the experimental work of Chapter 5, a phenomenon referred to here as dual cantilever flutter (DCF) was discovered. Chapter 6 introduces the first known documented study of DCF and also presents a novel DCF energy harvesting device. Analytical and CFD modeling will be discussed, along with experimental model validation case study results.

Lastly, Chapter 7 provides an executive summary of Chapters 2-5 and highlights all major contributions of the work presented in this dissertation. Chapter 7 will also provide a brief discussion on continuing and future work related to topics discussed in the dissertation.

CHAPTER II

EARLY DESIGN CONCEPTS AND INITIAL EXPERIMENTAL ANALYSIS OF THE PIEZOELECTRIC GRASS HARVESTER

Several design concepts were considered before deciding to investigate the piezoelectric grass harvester. The first portion of this chapter will discuss overall design and operational details of these early concepts. The first step taken toward developing the piezoelectric grass harvester was to perform an initial proof-of-concept experimental analysis on several prototypes. The second half of this chapter will focus on the details of these early experiments and present a summary of their results. These results will include plots showing the power output as a function of flow velocity for six different piezoelectric grass array configurations.

2.1 Early Harvester Concepts

This research began as an open-ended design project with few limitations. Five final concept designs were produced and proposed to the project sponsors. These concepts included fluttering mechanisms, miniature turbines with folding blades, and finally a biologically-inspired design named piezoelectric grass. The intended operation and dynamics of each concept will be discussed in this section along with all major design advantages and disadvantages.

2.1.1 Magnetic Flutter

As shown in Figure 2.1 the proposed design will consist of two fins each attached to a main spar. The spar is free to rotate about the A-axis and the fins are free to rotate about the B-axis. To be clear, two rotations are being discussed here: The primary rotation which harvests energy is a sweeping, cyclical, rotation of the fins about the A-axis. The secondary rotation is a "flip-flopping", 90-degree constrained rotation of the fins about the B-axis causing an oscillating moment about the A-axis. Each fin has a fixed 90-degree angular orientation relative to each other such that when one is oriented perpendicular to the flow (broad side facing) the other will be parallel. This will create a moment about axis A causing the spar to rotate toward the perpendicular fin (clockwise in the figure).

A subtle feature that is required for the device to operate well is the placement of each fin's center of pressure axis (C_1 and C_2 axes) relative to their axis of rotation (B-axis). The main spar will only be allowed to rotate the fins 90 degrees relative to the flow about axis B. The dotted lines on each fin show their 90 degree range of motion. The C-axis of each fin will be offset from the B-axis which will cause the following response: First, when one fin is perpendicular to the flow (Fin 1), moment about axis B created by the C_1-axis offset will hold that fin in a stable position against the 90-degree rotation constraint of the spar about axis B. Secondly, as the spar rotates about the A-axis, one of the fin magnets will be forced into the field of an opposing magnet fixed to the support structure. This magnetic interaction will force the fins to rotate about the B-axis out of the current stable position. While parallel, the fin's C and B axes (C_2 and B in the figure) are aligned with the flow direction; thus, there is no net moment about axis B.

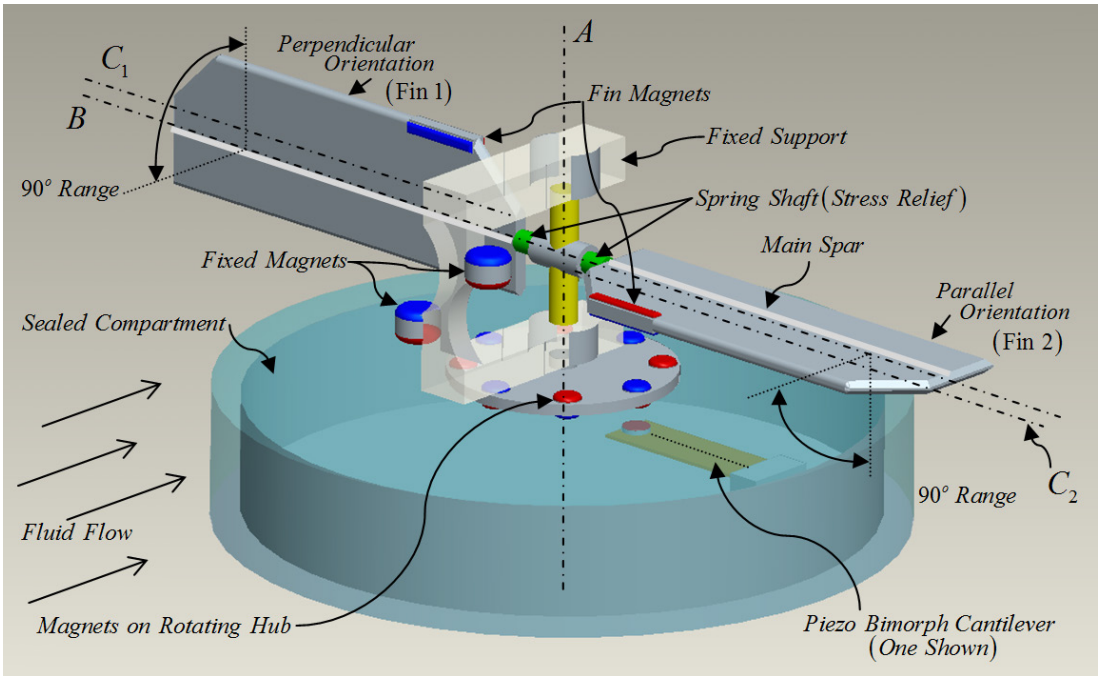

Figure 2.1: A detailed illustration showing the magnetic flutter harvester (concept #1)

As the parallel fin (Fin 2) begins to rotate about axis B due to the force of the opposing magnets toward its perpendicular orientation, the C-axis will be forced above or below (C_2 will be forced below in the figure) the B-axis becoming unstable. This instability is created by an unrestrained net moment about axis-B causing immediate rotation of the fins about the B-axis until they reach their other 90-degree rotational constraint of the spar. After the fins change orientation, moment about the A-axis changes direction and this "flip-flopping" process repeats itself. Placement of the device in continuous flow will cause oscillating rotation of the hub about the A-axis. Energy will be harvested from this motion primarily via a network of piezoelectric cantilevers and possibly an added electromagnetic component (not shown).

Many design considerations for concept #1 have been made that address the issue of durability and robustness. The main spar at the base of each fin will be made with a spring shaft stress relief. This spring will be designed such that it will not deflect in rotation or bending under

normal operating conditions. In the event that an obstruction comes in contact with a fin and causes stress to exceed design limits, the spring will elastically deflect until the obstruction is no longer in contact with the device. Essentially, the spring shaft portion of the spar will be designed to allow each fin to bend 180 degrees at their base while still allowing for a full elastic recovery to their zero position as shown in Figure 2.1. Only a cut-away portion of the support structure is shown; however, the complete structure will be reinforced and streamlined to guard against fouling and to protect the shaft and hub.

To further address the issue of durability, all electrical elements i.e. piezoelectric structures and electromagnetic devices will be coupled to the motion of the main shaft (A-axis) via a magnetic hub. This allows for both zero contact force transmission to eliminate the possibility of exceeding max stresses for the piezoelectric elements, and also for placement of these electronic devices within a sealed, water-tight compartment to eliminate the possibility of short-circuiting electronic components. Figure 2.1 illustrates how the piezoelectric harvesting system will be implemented using piezoelectric bimorph cantilevers with tip magnets. The cantilever magnets periodically align with opposing and attracting magnets fixed on the rotating hub causing the cantilevers to deflect up and down.

A second magnetic flutter design (concept #2) was inspired by concept #1 and was intended to be a significantly smaller device. The overall motion of the fins along with the 90-degree 'flip-flopping' action about axis-B caused by magnets is the same as that previously described for concept #1. The major difference is that rather than a magnetic hub exciting an array of piezoelectric cantilevers, concept #2 only has one piezoelectric beam. This beam is connected directly to the main shaft such that as the fins rotate about axis-A the beam deflects as shown in Figure 2.2.

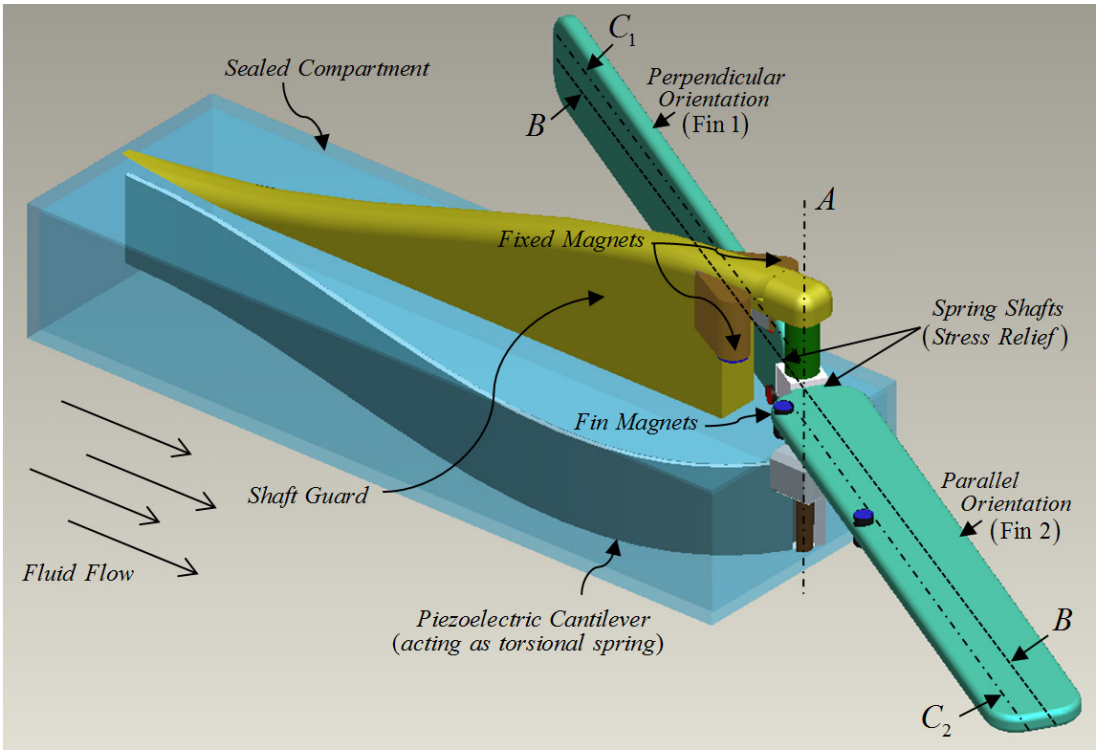

Figure 2.2: A detailed illustration showing the magnetic flutter harvester (concept #2)

The beam will act as a torsional spring by causing a moment about the A-axis that opposes the moment imposed by the force of fluid on the perpendicular fin (Fin 1). Concept #2 also has a streamlined shaft guard. This guard is intended to deflect large debris and to prevent debris from snagging on the device and possibly hindering the motion.

2.1.2 Folding Fin Turbines

Concepts #3 and #4 have a more traditional turbine or propeller type of design. The basic motion of these two designs can be described as follows. Each fin is free to rotate only 90 degrees at its base. This 90 degree range of motion allows each fin to go from completely horizontal (parallel with the flow) to vertical (perpendicular to the flow).

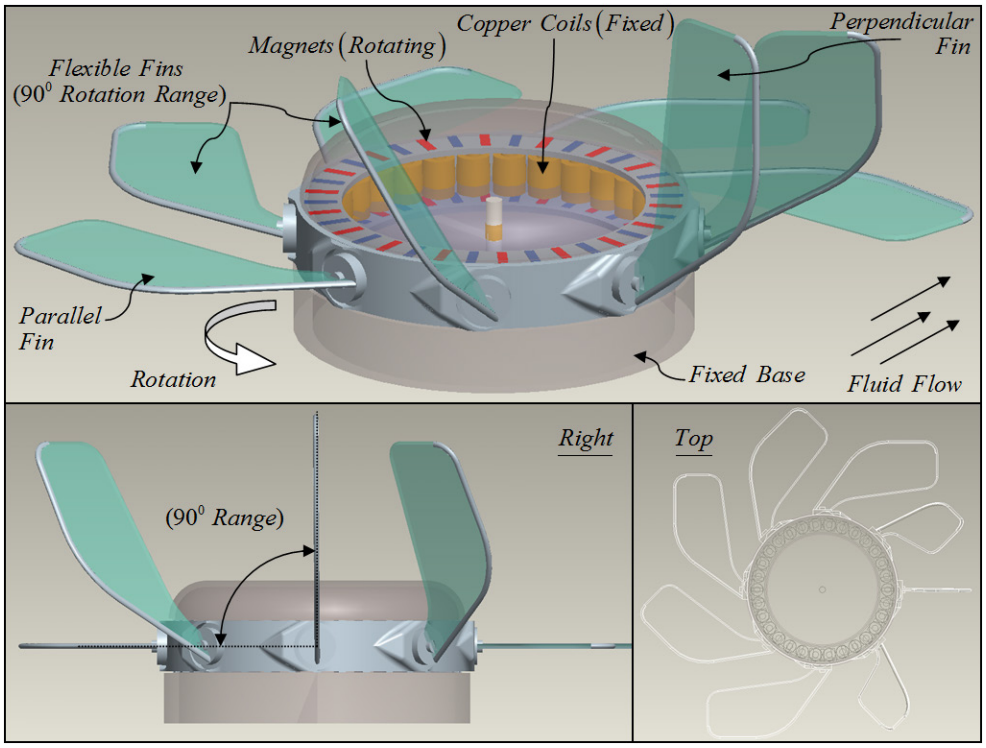

Figure 2.3: A detailed illustration showing the folding side fin harvester (concept #3)

Each fin is flexible enough to completely collapse under excessive loads, yet stiff enough to withstand fluid forces under normal flow conditions. The fins are curved in such a way as to allow the fluid to push them up from a parallel to a perpendicular orientation based on their position relative to the flow. This curvature is not shown for concept #3 in Figure 2.3; however, it is shown for concept #4 in Figure 2.4. In continuous flow conditions the fins and magnet assembly will rotate in one direction. Magnets placed on the rotating part of the assembly will be made to interact with piezoelectric, electromagnetic, or coupled piezo-electromagnetic generating elements fixed on the stationary portion of the assembly.

Concepts #3 and #4 offer several advantages. First, the folding fin design could greatly increase harvesting efficiency compared to traditional propellers or devices with oscillating, non-directional motion such as concepts #1, #2, and #5.

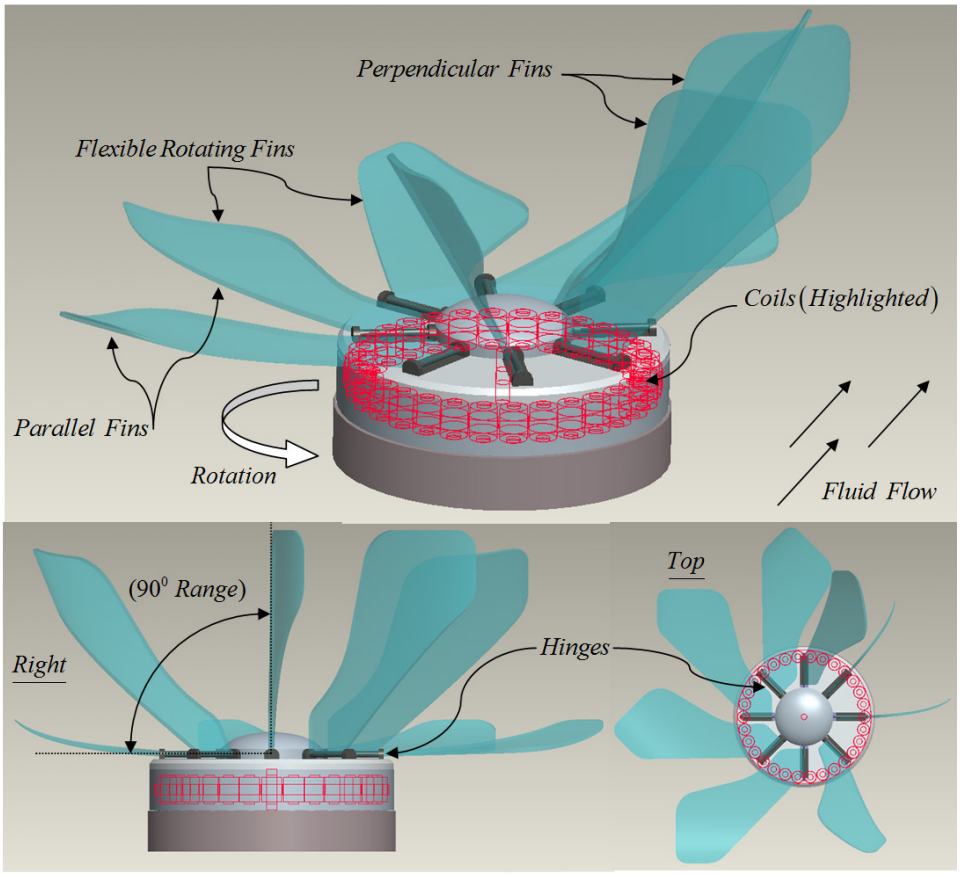

Figure 2.4: A detailed illustration showing the folding top fin harvester (concept #4)

Additionally, all circuits and generating elements would be contained within a dry, sealed chamber and would never come into direct contact with the environment. Another advantage of concepts #3 and #4 is that flow can approach from any direction (provided that it is perpendicular to the axis of rotation) and the harvesters will still operate as expected. The primary disadvantage of concepts #3 and #4 is that continuous rotation of the fins causes these designs to be more susceptible to motion-hindering debris. For example: vegetation could become entangled in the device rendering it useless. Another disadvantage is that there are several moving parts, joints, bearings, etc. that may reduce the life span of the harvester.

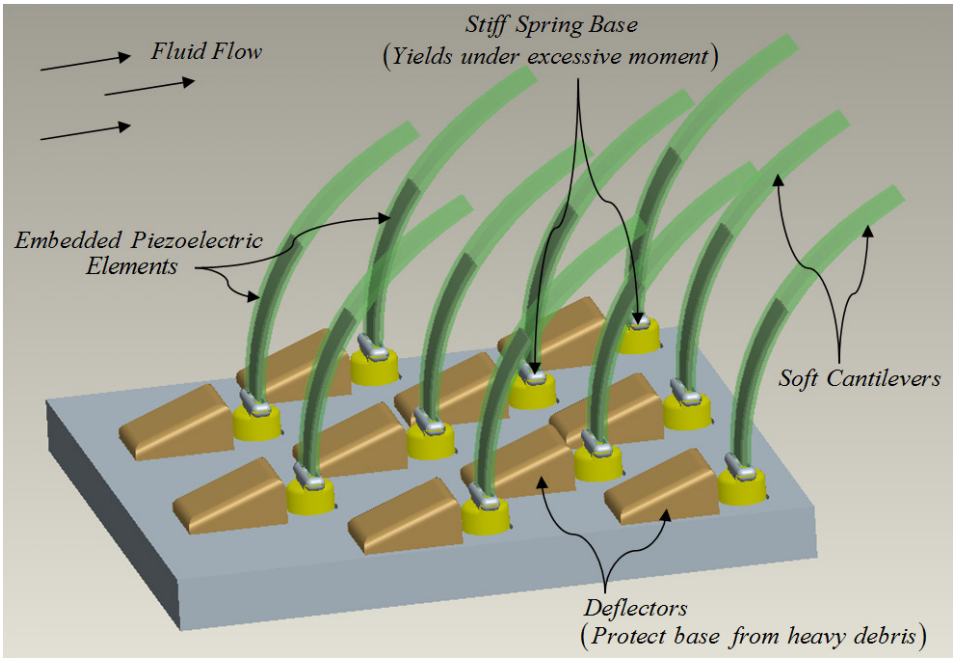

Figure 2.5: A detailed illustration showing the piezoelectric grass harvester (concept #5)

2.1.3 Piezoelectric Grass

The final harvester concept (concept #5) was a biologically-inspired design called piezoelectric grass. Compared to the previous concepts, the piezoelectric grass concept was very simple. Concept #5 consisted of an array of elastic cantilevers that had piezoelectric material bonded to them in either a unimorph or bimorph configuration. Each cantilever could also be embedded within a soft polymer for added durability as shown in Figure 2.5. Each *blade of grass* could be fabricated either straight or with a specified amount of pre-strain. In normal flow conditions the soft, passive portion deflects along with the imbedded piezoelectric element. If a design-specified maximum moment is ever exceeded (due to contact with debris for example), the base of each member could be designed to safely allow the member to bend 90 degrees without damaging the piezoelectric element. Under continuous flow, the forces experienced by each member are chaotic due to the nature of the flow around them. Motions caused from this highly

turbulent flow within the harvester array are converted directly into electricity via the piezoelectric effect.

A major disadvantage of concept #5 is that based on initial observations and literature studies, the analysis and potential design optimization would be limited strictly to extensive experimental work. Any other type of analysis or energy harvesting predictions would require computationally expensive CFD simulations able to model complex fluid structure interactions in a highly turbulent fluid. Another issue may arise from trying to collect the AC voltages generated from hundreds or possibly thousands of chaotic sources. Simply combining all sources could lead to a large amount of voltage cancellation while rectifying each voltage individually may add an impractical amount of design complexity, weight, and expense.

Advantages of the piezoelectric grass concept design are numerous. First, the extremely simple design would allow for a very quick experimental feasibility study. Also, depending on the efficiency, concept #5 could boast the largest potential energy density (per area) compared to the other concepts. This high energy density is possible because there are no passive fins or propellers preventing the generating elements from being placed very close to each other. Perhaps the most attractive advantage of the piezoelectric grass concept is that it is a solid-state device with a highly redundant design. If one element of the harvester array is damaged, the array will still be able to harvest energy from the other elements. These features made the piezoelectric grass concept the most desirable design option.

2.1.4 Summary of the Proposed Concept Designs

Two major differences exist among the proposed concepts. Concepts #1 through #4 convert the motion of a flowing fluid into a more useful rotational motion for harvesting the energy. Concept #5 converts turbulence-induced vibration caused by ambient fluid motion directly into electricity.

Progressing with the development of concepts #1 through #4 would take a more traditional design approach which would include analytical modeling along with intermediate experimental portions used for model validation. After initial analytical and experimental design optimization, a final prototype could be built and tested. A majority of the time and effort spent on concepts #1 through #4 would be focused on the generating system within the harvester.

Development of the piezoelectric grass concept would include a highly experimental feasibility study that could be accomplished quickly and with little cost. The following section discusses the earliest experimental work performed on a piezoelectric grass harvester prototype.

2.2 Experimental Analysis of the Piezoelectric Grass Harvester Concept

The majority of the work remaining in this chapter focuses on the experimental analysis of several piezoelectric grass harvester prototypes.

2.2.1 Wind Tunnel Facility

A two-stage, open-loop, experimental wind tunnel with continuously variable airspeed control was used to perform all flow experiments. Figure 2.6 shows a snapshot of the wind tunnel with key components of the experimental setup labeled. Design and performance details of the wind tunnel are provided by Bilgen (2010) [73]. Existing wind tunnel instrumentation included static pressure ports for free-stream velocity measurements, and an adjustable pitot tube for local steady velocity measurements. A hotwire anemometer, two custom pressure probes, and a Siglab data acquisition system were added to the wind tunnel for the experiments discussed in Chapters 3 and 4. A virtual control panel implemented with LabVIEW software was used to display, control, and record real-time data for the wind tunnel.

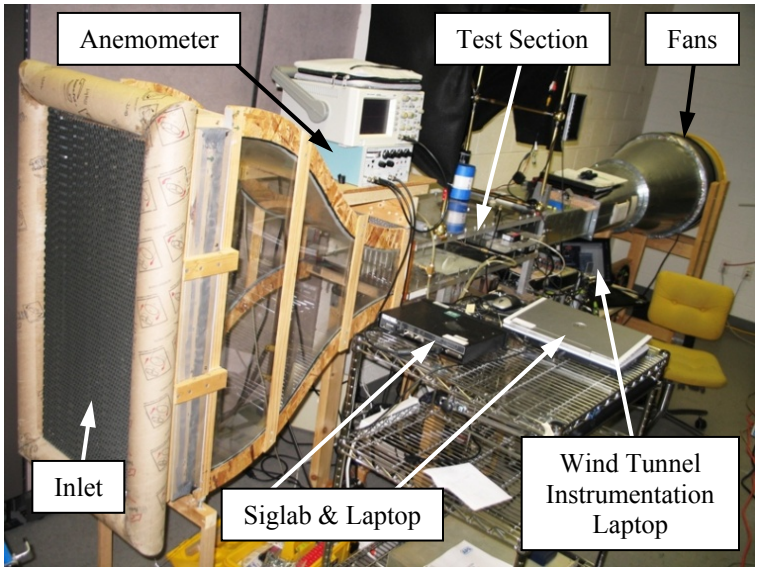

Figure 2.6: Photo of the wind tunnel testing facility.

2.2.2 Harvester Design

Two types of piezoelectric grass harvesters (type-1 and type-2) were designed and built for the initial proof-of-concept experimental study presented in this chapter. The type-1 harvester consisted of six generating elements or *blades of grass*. Each type-1 array element was a PVDF cantilever from Measurement Specialties Inc. (model LDT2-028K/L). The type-2 harvester design consisted of four generating elements. Each was constructed by mounting a PZT wafer QuickPack from Mide Technology Corp. (model QP16n) at the root of a spring steel cantilever. Snapshots of both harvester types are shown in Figure 2.8 and a summary of design parameters for each harvester is given in Table 2.1. Note that there are several more layers than those listed in Table 2.1 for both the PVDF and PZT QuickPack products used in this study. The model presented in Chapter 3 includes more details of the design and construction of the type-2 array elements.

Table 2.1: Summary of design parameters for harvester array elements.

Harvester	*Layer*	*Material*	*Length* (mm)	*Width* (mm)	*Thickness* (μm)
Type-1	Substrate	Mylar	72.60	16.20	178.00
	Piezo	Piezo Film	62.00	12.00	30.00
Type-2	Substrate	Steel	101.60	25.40	101.60
	Piezo	PZT Wafer	45.97	20.57	152.40

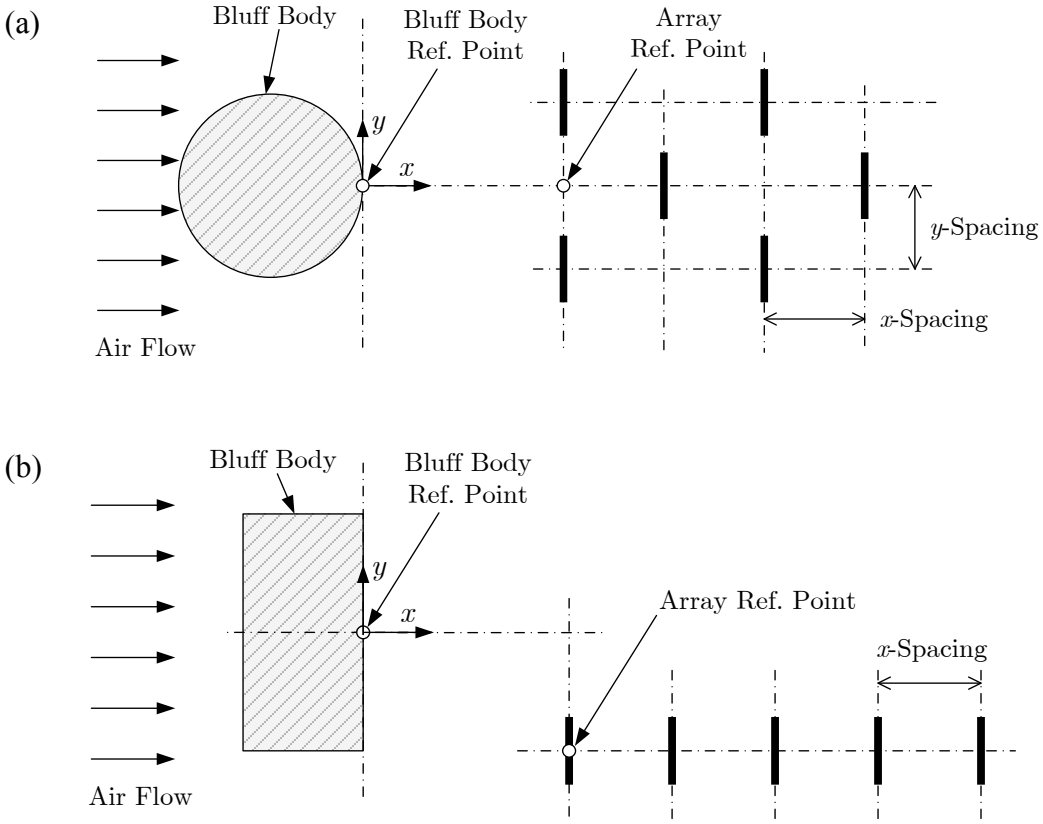

Figure 2.7: Schematic showing a top view of a typical array configuration and bluff body placement for the (a) staggered array type and the (b) inline array type.

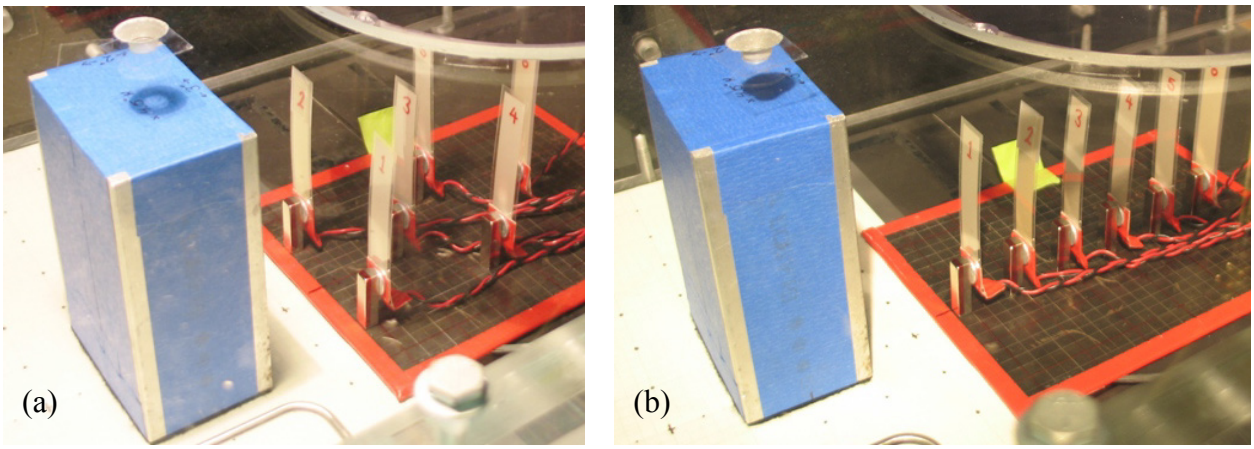

Figure 2.8: Snapshots of the (a) staggered and (b) inline PVDF harvester array configurations, each positioned on a steel grid plate downstream of a rectancular bluff body in the wind tunnel test section.

Individual load resistors were connected across the electrodes of each harvester element such that each element was an independent circuit. The load resistance R_{L} used for each type-1 and type-2 harvester element was 4.70 $\mathrm{M}\Omega$ and 49.2 $\mathrm{k}\Omega$ respectively. These resistor values were chosen using the following relationship for optimum resistance,

$$R_{\mathrm{opt}} = \frac{1}{\omega_1 C_{\mathrm{p}}} \tag{2.1}$$

where ω_1 is the measured, open circuit, first bending mode frequency, and C_{p} is the measured capacitance of the piezoelectric layer [74]. The measured first bending mode frequency for the type-1 and type-2 harvesters was 12.7 Hz and 30 Hz respectively. Note that this method of determining optimum resistance should only be used when backwards coupling effects are small. See Erturk (2009) for methods of determining optimum harvester load resistance when piezoelectric coupling effects are considered [75]. The voltage across each resister was sampled at 2.00 kHz on separate channels with National Instruments data acquisition hardware. In order to allow for convenient rearranging of the individual array elements, magnets were used to secure the cantilevers on a steel grid plate as shown in Figure 2.8.

2.2.3 Harvester Array Experiments

A preliminary experimental study showed that many factors had a significant impact on the harvester array power output. In order to reduce the number of design parameters, it was decided to choose the general design that provided maximum power output as observed in the preliminary study. Figure 2.7 shows the general design which was chosen to be an inline array configuration where the array elements are evenly spaced, aligned in the *x*-direction, and offset from the bluff body in the *y*-direction. Each test consisted of placing a bluff body upstream of the harvester array such that its reference point with respect to the array reference point was known. Free-stream air velocity was then incrementally increased over a range of approximately 1 to 12 m/s where 30 seconds of data was recorded at a rate of 2.00 kHz at each velocity increment. Both the data acquisition and velocity control were automated with LabVIEW. This procedure was repeated while keeping the *y* offset fixed and varying *x* offset.

2.2.4 Results

The results from six sets of tests performed on prototypes of the piezoelectric grass harvester concept are summarized in this section. Plots shown in Figures 2.9 through 2.14 show the average power output per element (per cantilever) as a function of both flow velocity and the streamwise (x-axis) distance between the reference point of the array and the bluff body. Recall Figure 2.7 for detailed schematics showing the inline and staggered array arrangements.

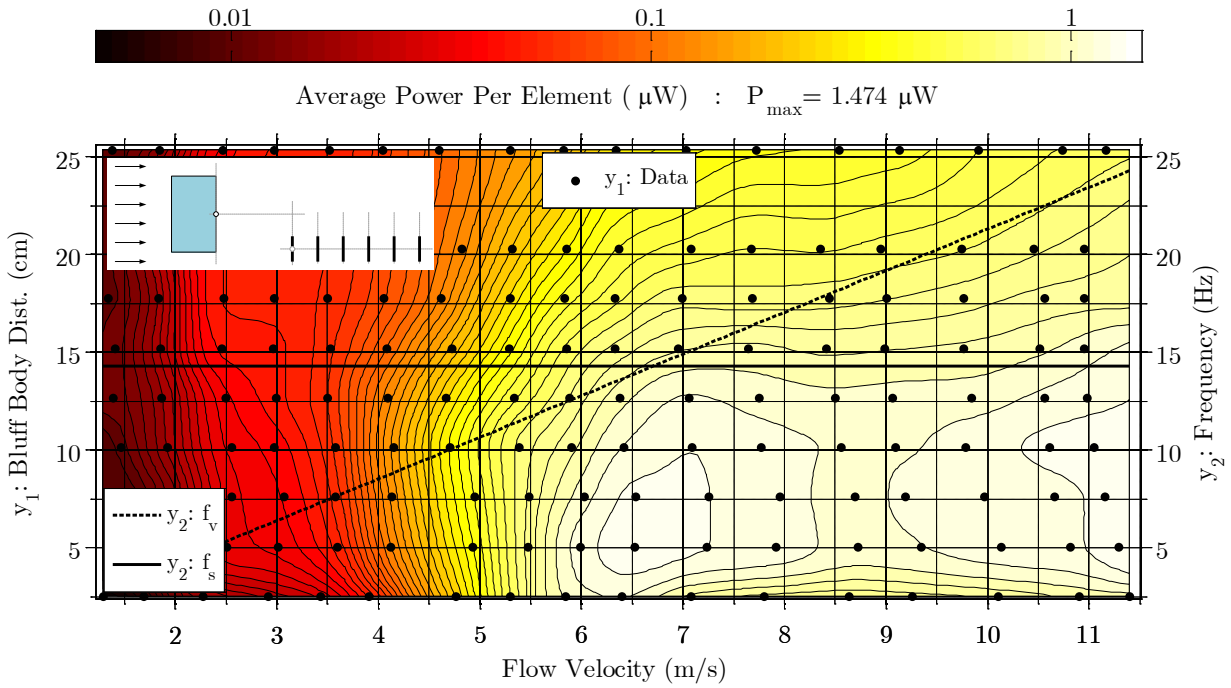

Figure 2.9: The power profile for an inline PVDF array positioned in the turbulent wake of a rectangular bluff body.

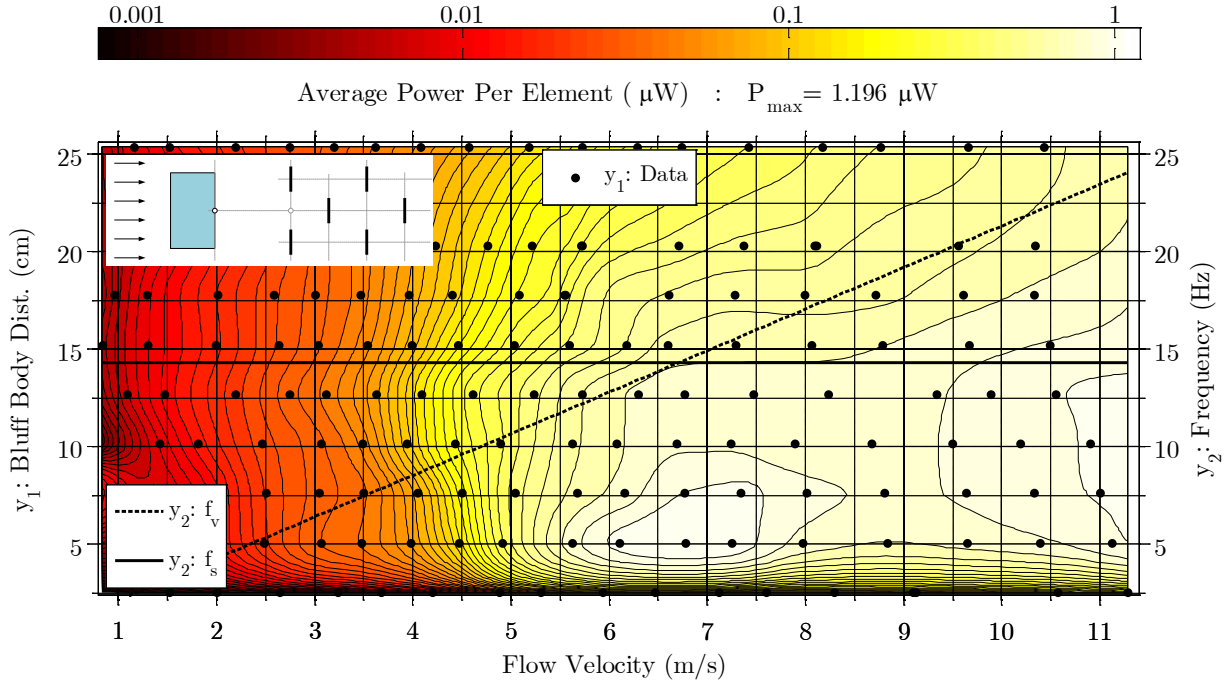

Figure 2.10: The power profile for a staggered PVDF array positioned in the turbulent wake of a rectangular bluff body.

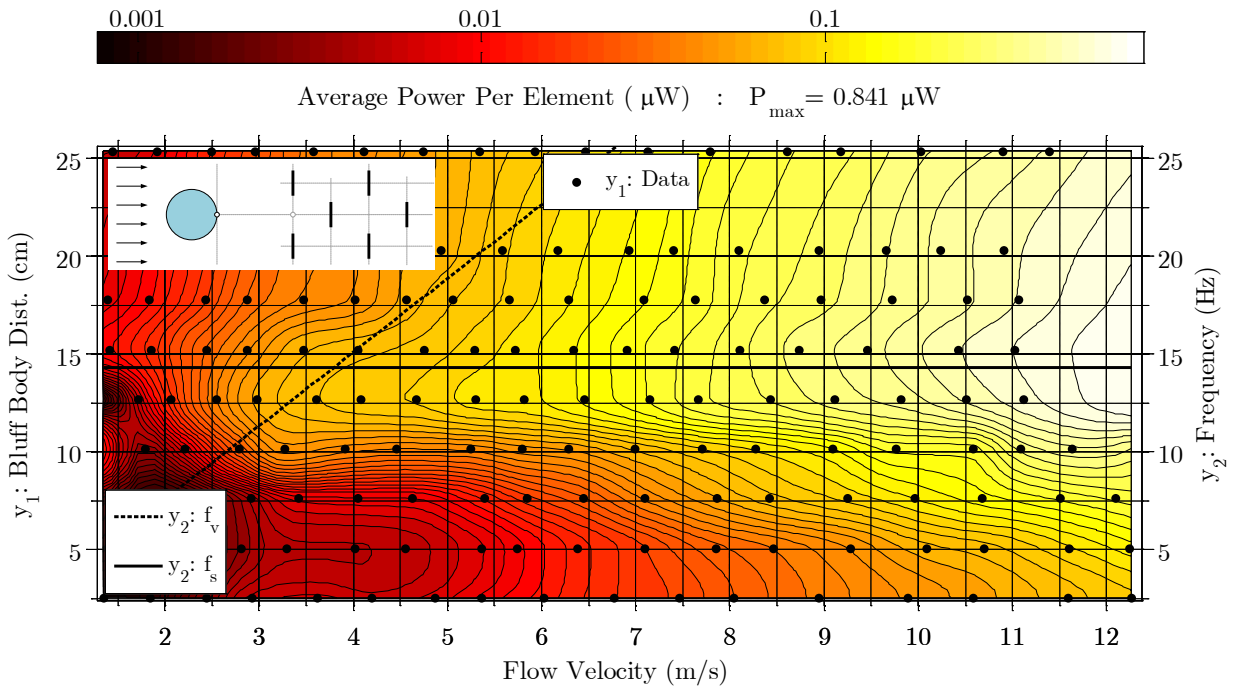

Figure 2.11: The power profile for a staggered PVDF array positioned in the turbulent wake of a small cylindrical bluff body.

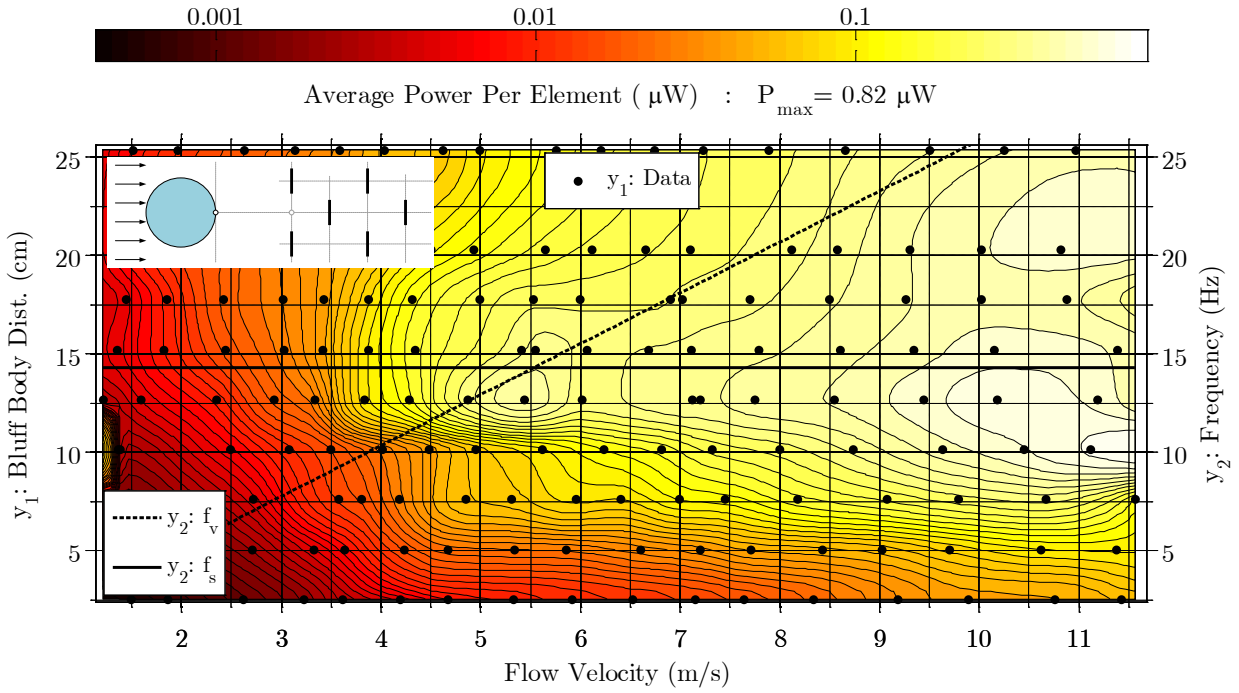

Figure 2.12: The power profile for a staggered PVDF array positioned in the turbulent wake of a large cylindrical bluff body.

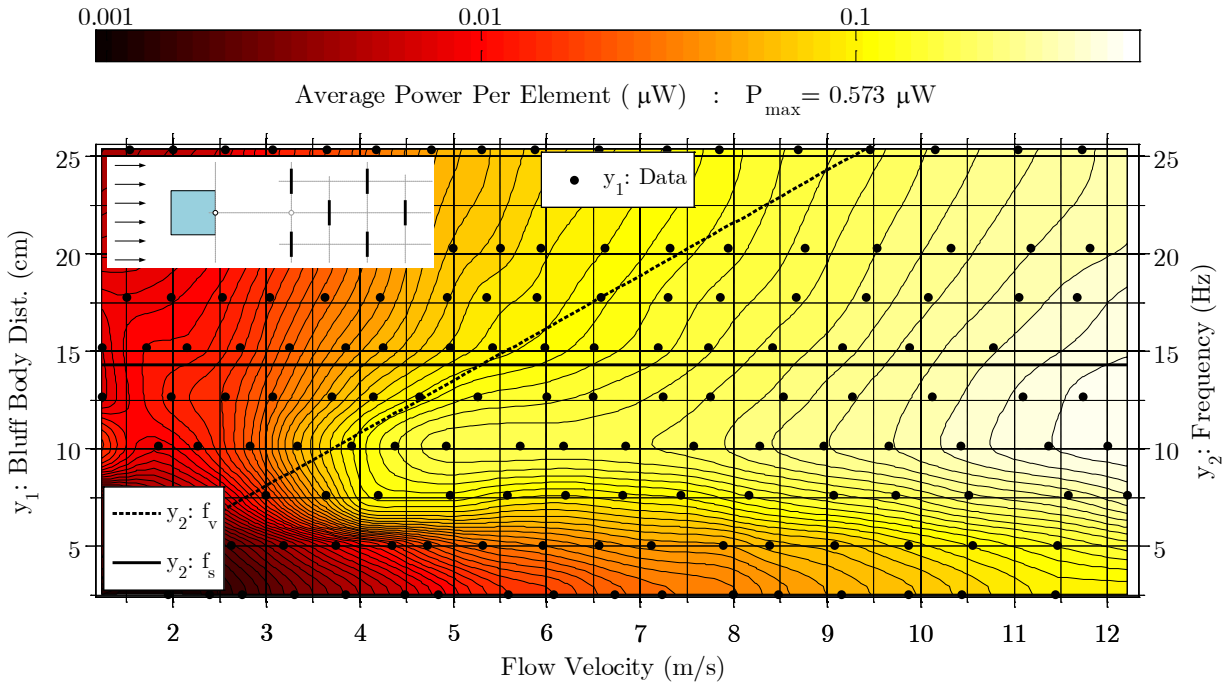

Figure 2.13: The power profile for a staggered PVDF array positioned in the turbulent wake of a square bluff body.

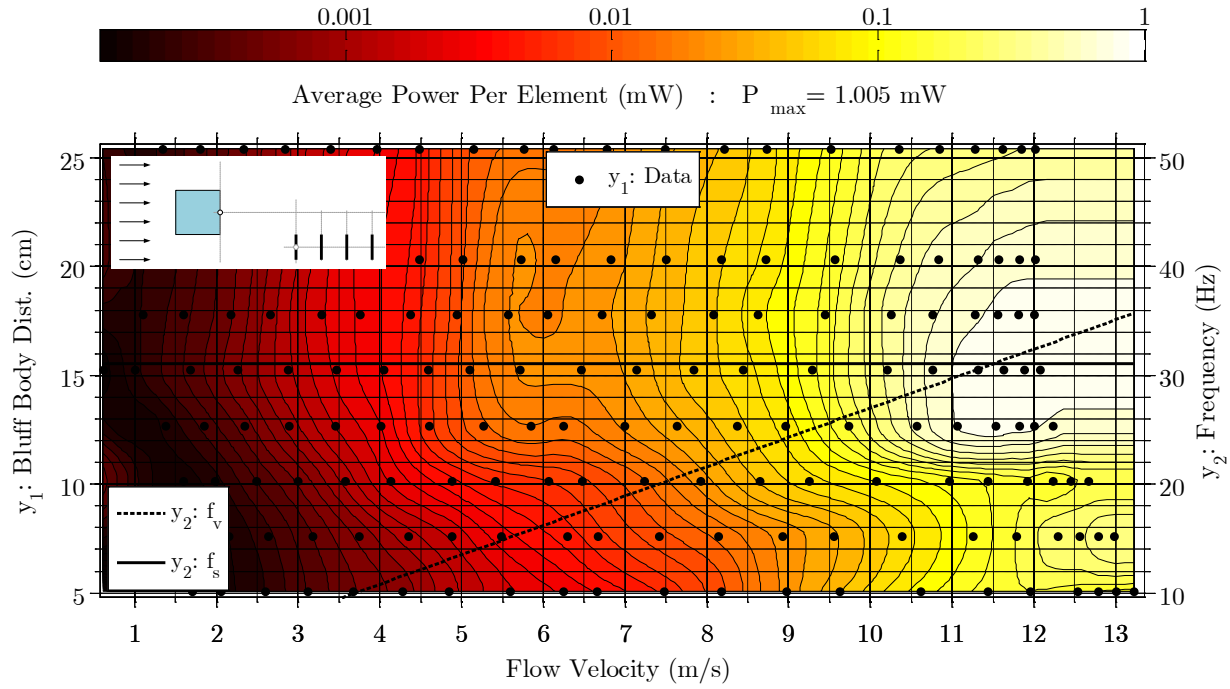

Figure 2.14: The power profile for an inline PZT array positioned in the turbulent wake of a square bluff body.

A solid horizontal line plotted on the secondary y-axis (y_2) of Figures 2.9 through 2.14 corresponds to the first natural frequency of the harvester (f_s). These natural frequencies were measured to be approximately 14.3 Hz and 31.1 Hz for the PVDF and PZT type elements respectively. Also plotted on the secondary y-axis (y_2) is a diagonal dashed line that corresponds to the vortex shedding frequency of the bluff body (f_v). This vortex shedding frequency can be approximated with the Strouhal vortex shedding equation given as,

$$f_v = \frac{StU}{L_c} \tag{2.2}$$

where f_v is the shedding frequency, St is the empirically defined Strouhal number, U is the free-stream flow velocity, and L_c is the characteristic length of the bluff body. The characteristic length used in this study is called the hydraulic diameter which can be given as,

$$L_c = \frac{4A}{P} \tag{2.3}$$

where A and P are the cross sectional area and perimeter of the bluff body respectively. Notice that for bluff bodies with circular and square cross sections, L_c becomes equal to simply the diameter and side length respectively. The Strouhal number for a particular bluff body depends on the shape of the bluff body and the Reynolds number. The Reynolds number (Re) can be expressed as,

$$Re = \frac{UL_c}{\nu} \tag{2.4}$$

where U and L_c are defined for equation (2.2) and ν is the kinematic viscosity of the fluid.

Table 2.2: Summary of parameters and results from the piezoelectric grass proof-of-concept experiments corresponding to the plots in Figures 2.9 through 2.14.

Figure	*Element Type*	*Bluff Body Type*	f_s (Hz)	L_c (cm)	*St*	*U:* $f_v=f_s$ (m/s)	*Re:* $f_v=f_s$ ($\times 10^6$)	P_{max} *(per cantilever)*	
2.9	PVDF	Rectangular	14.3	6.10	0.13	6.71	2.6	1.474	μW
2.10	PVDF	Rectangular	14.3	6.10	0.13	6.71	2.6	1.196	μW
2.11	PVDF	Circular	14.3	6.10	0.23	3.79	1.5	0.841	μW
2.12	PVDF	Circular	14.3	8.89	0.23	5.53	3.1	0.820	μW
2.13	PVDF	Square	14.3	4.45	0.12	5.30	1.5	0.573	μW
2.14	PZT	Square	31.1	4.45	0.12	11.52	3.3	1.005	mW

Table 2.2 summarizes several parameters and results from the six proof-of-concept wind tunnel experiments performed on the piezoelectric grass prototypes. Strouhal numbers used for the rectangular and square bluff body types were chosen to be 0.13 and 0.12 respectively based on results of a study performed by Knisely (1990) [76]. Note that there is a significant amount of variability in circular cylinder Strouhal numbers for Reynolds's numbers within the range $2\times10^5 < \text{Re} < 3.5\times10^6$ which is referred to as the transition range [77]. Because both circular cylinder experiments were performed in the transition range, no clearly defined value for the Strouhal number was found in the literature. Instead, the Strouhal number used for the circular cylinders was chosen to be 0.23 which is the value that causes $f_v \cong f_s$ at a velocity (5.53 m/s) where a local maximum in power output is visible in Figure 2.12.

2.3 Chapter Summary

Five fluid flow energy harvester concept designs were presented. Operational details, advantages, and disadvantages of each design were discussed. A final biologically-inspired concept design called piezoelectric grass was chosen because it addressed and overcame many of the design issues considered for potential application environments.

The results of an extensive experimental study on several piezoelectric grass harvester prototypes were presented. It was shown that the PZT harvester array (Type-2) was able to achieve a power output of 1.0 mW per cantilever with a mean airspeed of 11.5m/s. The similarly sized PVDF harvester array (Type-1) was expected to produce significantly less power due to a lower electromechanical coupling constant, but was still able to achieve an output of 1.47 μW per cantilever at 6.7 m/s. From an application standpoint, note that the PZT harvester produced nearly 1000 times the output for approximately 10 times the cost compared to the PVDF harvester. However, when considering long-term deployment in an uncontrolled environment, the soft, flexible PVDF design is much less susceptible to damage than the brittle PZT design.

Harvester array results show that an optimum turbulence condition for maximum power output exists for all array configurations. It is shown that these ideal harvesting conditions are functions of both flow velocity and harvester location downstream of a bluff body. An estimate of the optimum harvester design can be attained by matching the natural frequency of the harvester to the primary vortex shedding frequency of the bluff body. Plots given in Figures 2.9 through 2.14 show how power trends from PVDF arrays appear as large plateaus which span across a wide range of both flow velocity and bluff body distance. This broadband type of behavior from the PVDF array was very different compared to the sharp peak in power output produced by the PZT array. While the array studies presented here were strictly experimental, these results may provide valuable insight for the future development of mathematical models for large harvester arrays containing many more harvester elements.

CHAPTER III

A FULLY COUPLED ELECTROMECHANICAL DISTRIBUTED PARAMETER MODEL FOR A CANTILEVERED UNIMORPH HARVESTER IN TURBULENT CROSS-FLOW

3.1 Mathematical Modeling

This Chapter presents a model on turbulence-induce vibration (TIV) energy harvesting beginning with time-series pressure measurements made along an array of points in space. This time-series pressure data was then reduced into the frequency-domain by calculating the pressure cross-power spectral density. The data was further reduced into modal fluid forcing functions for a cantilever beam. The modal forcing functions were then combined with the modal equations of the fully-coupled, electromechanical model for a cantilevered unimorph harvester. Finally, the full turbulence-induced vibration energy harvesting model was used to calculate displacement and power output of the harvester.

3.1.1 Spectral Statistics Overview

Velocity measurements of highly turbulent flow in the time domain appear as random noise and do not provide any useful information about the turbulence other than crude estimates of mean velocity and turbulence intensity. This section will discuss how spectral statistics are used to take

time domain pressure measurements and represent them as functions in the frequency domain. A key assumption of this analysis is that the turbulence measurement time-series can be treated as a stationary, random process where the mean, mean square, variance, and standard deviation do not vary with time [78]. In this work, turbulent flow data was attained using an invasive approach where a fast-response pressure probe was placed in the flow and dynamic pressure measurements were made. Further details concerning the turbulence measurement and experimental work can be found in Chapter 4 and in recent work by the author [79,80]. The most useful statistical quantity which is used many times throughout this modeling procedure is called the power spectral density (PSD). The pressure PSD between two points or an array of points is essential in order to provide a measure of spatial dependence of the pressure field. Pressure in the time-domain at a point z_a in space is represented as $p(z_a, t)$ and has units of Pa. The pressure PSD between two points in space is called the pressure cross-power spectral density (CPSD) and can be expressed as,

$$S_p(z_a, z_b, \omega) = \lim_{T\to\infty} \frac{1}{4\pi T} \int_{-\infty}^{\infty} \left\{ \int_{-T}^{T} E\left[p(z_a, t)p(z_b, t+\tau)\right] dt \right\} \mathrm{e}^{-j\omega t} d\tau \tag{3.1}$$

where T is the sample time, τ is a time offset, ω is angular frequency with units of rad/s, and E denotes that an expectation of the two pressure signals must be taken [81]. Units of the pressure CPSD (and PSD) function are Pa^2/rad/s.

3.1.2 Distributed Parameter Electromechanical Model

The first fully coupled distributed parameter energy harvesting model was presented by Erturk and Inman (2008) for cantilever beams with sinusoidal base excitation [82]. The model proposed in this dissertation uses the same approach as in [82]; however, a statistically determined distributed force is applied rather than base excitation.

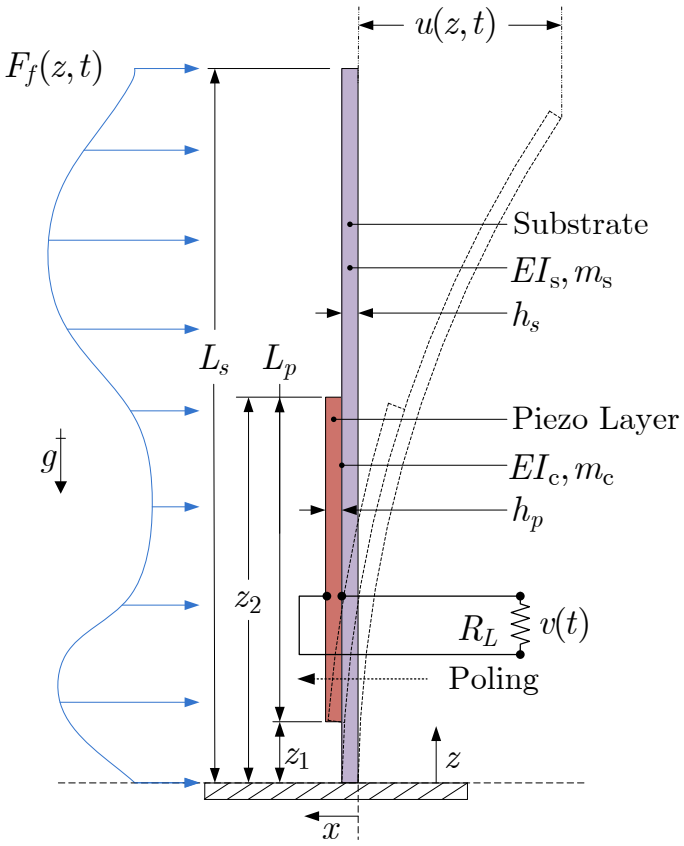

Figure 3.1: Schematic of cantilevered unimorph harvester with distributed fluid force.

The present analysis assumes that the harvester is a long, slender, unimorph cantilever consisting of one piezoelectric layer with continuous electrodes perfectly bonded to an elastic substrate experiencing small transverse deflection. See the work of Priya & Inman (2008) [83] for details concerning both unimorph and bimorph harvester configurations, and Erturk *et al* (2009) [84] for a study on the effects of segmented electrode pairs. The model presented here will apply not only to cases where the piezoelectric layer length L_p is less than that of the substrate L_s, but also for cases where the piezoelectric layer significantly modifies the mass and/or stiffness of the substructure. If the piezoelectric material does not extend the full length of

the substrate, such as shown in Figure 3.1, the mass and stiffness of the beam become discontinuous functions of z. Because of these non-uniform mass and stiffness properties, the Rayleigh-Ritz method is used to provide analytical approximations for natural frequencies, mode shapes, and frequency response functions of the beam. The segment of beam bonded to piezoelectric material will be referred to as the *composite* portion, and may consist of many layers each with their own material properties and dimensions. (See Figure 3.2.)

The governing differential equation of motion for transverse (bending) deflection of a fully coupled, electromechanical, Euler-Bernoulli beam, subject to a distributed force can be expressed as,

$$\frac{\partial^2}{dz^2}\left[YI\,\frac{\partial^2 u(z,t)}{dz^2}\right]+\frac{\partial^2}{dz^2}\left[c_r I\,\frac{\partial^3 u(z,t)}{dz^2 dt}\right]+c_v\,\frac{\partial u(z,t)}{dt}+(m+m_f)\frac{\partial^2 u(z,t)}{dt^2}$$
$$+\vartheta v(t)\frac{d}{dz}\Big[\delta(z-z_1)-\delta(z-z_2)\Big]=F_f(z,t) \tag{3.2}$$

where YI is the bending stiffness, I is the area moment of inertia, c_r and c_v are coefficients of strain rate damping and viscous damping respectively, m is the linear mass density, m_f is added mass of the surrounding fluid, ϑ is the piezoelectric coupling term, v is the strain induced voltage across a load resistor R_L, and F_f is the distributed turbulence-induced force. See Figure 3.1 for a schematic showing a unimorph cantilever in turbulent cross flow. The Dirac delta function δ is used in equation (3.2) to localize electromechanical coupling induced from the piezoelectric material which is bonded to the beam over the distance from z_1 to z_2.

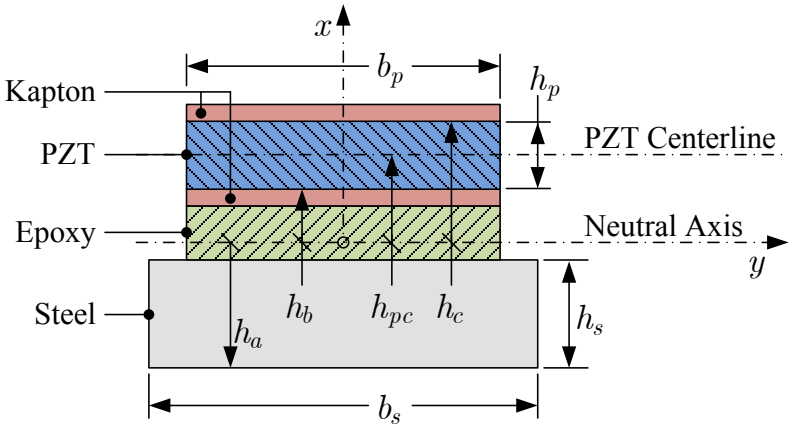

Figure 3.2: Schematic of a typical unimorph beam cross-section showing several dimensional terms used in this analysis.

Constitutive relationships of the piezoelectric material for bending (or *31 mode*) deformation are used to derive the piezoelectric coupling term ϑ. These constitutive relationships are given as [85],

$$\begin{Bmatrix} S_1^p \\ D_1 \end{Bmatrix} = \begin{bmatrix} \frac{1}{Y_1^p} & d_{13} \\ d_{13} & \varepsilon_{33}^T \end{bmatrix} \begin{Bmatrix} T_1^p \\ E_3 \end{Bmatrix} \tag{3.3}$$

and for the fully elastic case where there is no piezoelectric coupling the stress-strain relationship can be shown as,

$$T_1^s = Y_1^s S_1^s \tag{3.4}$$

where – in equations (3.3) – S is strain, D is electric displacement, T is stress, E is electric field, Y is the modulus of elasticity, d is the piezoelectric constant and ε^T is the stress-free dielectric permittivity. The superscripts s and p denote substrate and piezoelectric material respectively. The z and x axis directions within the material layers are denoted with subscripts 1

and 3 respectively. Through derivations of the piezoelectric coupling term ϑ defined in equation (3.5) and the electrical circuit expression given in equation (3.6) for a unimorph cantilevered beam were presented and discussed in [82].

$$\vartheta = -\frac{Y_p d_{31} b_p}{2h_p}\left(h_c^2 - h_b^2\right) \tag{3.5}$$

$$\frac{\varepsilon_{33}^S b_p L_p}{h_p}\frac{dv(t)}{dt} + \frac{v(t)}{R_L} = -\int_{z_1}^{z_2}\left[d_{31} Y_p h_{pc} b_p \frac{\partial^3 u(z,t)}{\partial z^2 \partial t}\right]dz \tag{3.6}$$

In the previous two equations b is width, h is thickness, and subscripts p and s denote piezoelectric material and substrate material respectively. The terms h_b, h_c, and h_{pc} are locations of the bottom surface, top surface, and centerline (respectively) of the piezoelectric material relative to the neutral axis of the composite beam segment. These locations and other dimensional terms used throughout this analysis are illustrated in Figure 3.2.

Composite bending stiffness YI_c and location of the neutral axis of the composite beam segment are calculated using a composite cross-section area transformation technique [86]. This technique can be found in most intermediate mechanics of materials textbooks and will not be discussed here. Material properties of the beam can be defined as functions of z simply by using the Heaviside step function H(f) which is equal to zero if $f < 0$ and equal to unity if $f > 0$. The mass and stiffness material property functions can therefore be represented as,

$$m(z) = m_c\left[\mathrm{H}\left(z - z_1\right) - \mathrm{H}\left(z - z_2\right)\right] + m_s\left[\mathrm{H}\left(z - z_2\right) - \mathrm{H}\left(z - L_s\right)\right] \tag{3.7}$$

$$YI(z) = YI_c\left[\mathrm{H}\left(z - z_1\right) - \mathrm{H}\left(z - z_2\right)\right] + YI_s\left[\mathrm{H}\left(z - z_2\right) - \mathrm{H}\left(z - L_s\right)\right] \tag{3.8}$$

where m_c and m_s are the linear mass densities of the composite and substrate beam segments respectively, while YI_c and YI_s are the bending stiffness values of the composite and substrate segments respectively. The mass and stiffness matrices used for the Rayleigh-Ritz formulation are defined as [87],

$$\mathbf{M} = \int_0^{L_s} m U_m U_n \, dz \tag{3.9}$$

$$\mathbf{K} = \int_0^{L_s} YI \frac{d^2U_n}{dz^2} \frac{d^2U_m}{dz^2} dz + \mathbf{K}_g \tag{3.10}$$

where U are orthogonal and orthonormal polynomial shape functions which were found using the Gram-Schmidt iterative procedure presented by Bhat 1985 [88]. Subscripts m and n are integer values that denote a particular mode of vibration such that $m = 1, 2, 3...N$ and $n = 1, 2, 3...N$ where N is the number of terms used in the Rayleigh-Ritz approximation. The geometric stiffness $\mathbf{K}_g$ was included in equation (3.10) to account for axial loading and is defined as,

$$\mathbf{K}_g = \int_0^{L_s} \left\{ N_z \frac{dU_m(z)}{dz} \frac{dU_n(z)}{dz} \right\} dz \tag{3.11}$$

where N_z is the axial load due to gravity and is given below in equation (3.12).

$$N_z(z) = mg\left(L_s - z\right) \tag{3.12}$$

Note that the acceleration due to gravity is in the negative z direction; therefore, the value for g is a negative quantity *i.e.*, the beam is in compression. Also, note that negative acceleration causes the diagonal terms in the geometric stiffness matrix to become negative.

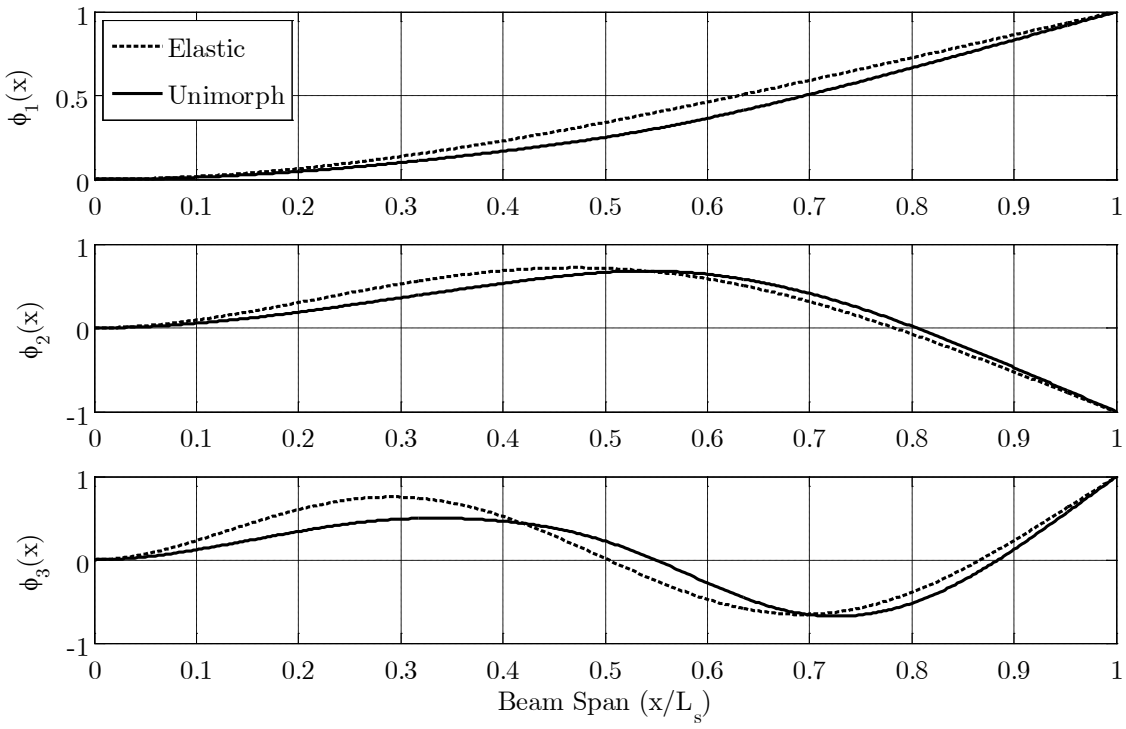

Figure 3.3: Rayleigh-Ritz mode shapes of the unimorph harvester used in the case study from Section 3.2 compared to those of a uniform elastic Euler-Bernoulli beam.

If these negative elements in the geometric stiffness matrix become large enough, the system will go unstable *i.e.*, the beam will buckle. The lowest axial load that causes this instability is called the critical buckling load.

The mass and stiffness matrices of equations (3.9) – (3.11) are used in the following typical eigenvalue problem formulation,

$$\left(\mathbf{K} - \omega_m^2 \mathbf{M}\right)\mathbf{c}_m = 0 \tag{3.13}$$

where $\mathbf{c}$ are the eigenvectors, and ω^2 are the eigenvalues such that the natural angular frequency of the m^{th} mode of vibration is simply ω_m with units of rad/s. The Rayleigh-Ritz mode shapes ϕ

are then found using eigenvectors from the eigenvalue problem solution and are calculated with the following finite summation series.

$$\phi_m(z) = \sum_{m=1}^{N} \mathbf{c}_m U_m \tag{3.14}$$

Figure 3.3 shows the first three normalized Rayleigh-Ritz mode shapes of a cantilevered unimorph harvester calculated from equation (3.14) and how they compare to those of an elastic uniform Euler-Bernoulli beam.

Orthogonality conditions of the Rayleigh-Ritz mode shapes are shown in the following expressions,

$$\int_{z=0}^{L_s} \phi_m \phi_n dz = \delta_{mn} \tag{3.15}$$

$$\int_{0}^{L_s} \left[m(z) + m_f(z) \right] \phi_m^2 \, dz = m_m + \mu_m \tag{3.16}$$

$$\int_{z=0}^{L_s} \phi_m \frac{d}{dz} \left[\delta(z - z_1) - \delta(z - z_2) \right] dz = \left. \frac{d\phi_m}{dz} \right|_{z_1}^{z_2} \tag{3.17}$$

where δ_{mn} is the Dirac delta function which is equal to unity for $m = n$ and zero for $m \neq n$. The modal beam and fluid mass are m_m, and μ_m respectively. Because the Rayleigh-Ritz mode shapes are orthogonal to each other, the equation of motion can be represented as a series of *N* uncoupled, second order, ordinary differential equations which describe the modal dynamics of the beam. Total beam displacement is assumed to have the following form,

$$u(z,t) = \sum_{m=1}^{N} \phi_m(z) \eta_m(t) \tag{3.18}$$

where η is the modal displacement. It is now possible to get the modal equations of motion which can be expressed as,

$$(m_m + \mu_m)\left(\frac{d^2\eta_m(t)}{dt^2} + 2\zeta_m\omega_m\frac{d\eta_m(t)}{dt} + \omega_m^2\eta_m(t)\right) + \vartheta v(t)\frac{d\phi_m(z)}{dz}\Bigg|_{z_1}^{z_2} = \int_0^{L_s}\phi_m(z)F_f(z,t)\,dz \tag{3.19}$$

where ζ is the modal damping ratio. Assuming a sinusoidal response for both voltage and displacement of each mode, the steady-state modal displacements can be solved from the Fourier transform of equation (3.19). The modal displacements can be represented with the following expression,

$$\eta_m(\omega,t) = \frac{\left(\psi_m - \chi_m V_0\right)e^{j\omega_m t}}{\left(m_m + \mu_m\right)\left(\omega_m^2 - \omega^2 + j2\zeta_m\omega_m\omega\right)} \tag{3.20}$$

where V_0 is the steady-state strain-induced voltage across the load resistor R_L. For convenience, the modal fluid forcing term ψ and the modal piezoelectric coupling term χ are defined as follows.

$$\psi_m = \int_{-\infty}^{+\infty}\int_0^{L_s}\phi_m F_f e^{-j\omega t}dzdt \tag{3.21}$$

$$\chi_m = \vartheta\frac{d\phi_m(z)}{dz}\Bigg|_{z_1}^{z_2} \tag{3.22}$$

The numerator terms in parentheses in equation (3.20) are referred to as the forcing terms (or system inputs), while the denominator contains the modal displacement frequency response

function (FRF) terms. The modal displacement FRF of the fully elastic system is defined in equation (3.23) and will be used extensively throughout the remainder of this analysis.[1]

$$H_m(\omega) = \frac{1}{\left(m_m + \mu_m\right)\left(\omega_m^2 - \omega^2 + j2\zeta_m\omega_m\omega\right)} \tag{3.23}$$

Recall the assumed solution form for the mechanical response of the beam given in equation (3.18), substitute it into the electrical circuit expression given in equation (3.6), and perform the integration to get,

$$\frac{dv(t)}{dt} + \frac{h_p}{R_L\varepsilon_{33}^S b_p L_p} v(t) = \sum_{m=1}^{N} -\frac{d\eta_m(t)}{dt}\frac{d_{31}Y_p h_{pc} h_p}{\varepsilon_{33}^S L_p}\frac{d\phi_m}{dz}\Bigg|_{z_1}^{z_2} \tag{3.24}$$

where it is important to recognize that all the terms are now either constants or sinusoidal functions of time only. Therefore, taking the Fourier transform of equation (3.24) yields the following modal representation of the electrical equation,

$$\left(j\omega + \frac{1}{\tau_c}\right)V_0 = \sum_{m=1}^{N} j\omega\varphi_m\eta_m \tag{3.25}$$

where it is convenient to define the time constant τ_c as that of a simple RC circuit [89],

$$\tau_c = RC = R_L\frac{\varepsilon_{33}^S b_p L_p}{h_p} \tag{3.26}$$

[1] Note the difference between the Heaviside step function symbol H used in equations (3.7) and (3.8), and the italicized FRF symbol H.

and the modal constant can be defined as,

$$\varphi_m = -\frac{d_{31} Y_p h_{pc} h_p}{\varepsilon_{33}^S L_p} \frac{d\phi_m}{dz}\bigg|_{z_1}^{z_2} \tag{3.27}$$

Upon substitution of equation (3.20) into equation (3.25), it is possible to show an analytical expression for the fully coupled electromechanical modal response of a piezoelectric unimorph cantilever excited with an arbitrary distributed force along the length of the beam.

$$\left(j\omega + \frac{1}{\tau_c}\right) V_0 = \sum_{m=1}^{N} \frac{j\omega\varphi_m \left(\psi_m - \chi_m V_0\right)}{\left(m_m + \mu_m\right)\left(\omega_m^2 - \omega^2 + j2\zeta_m\omega_m\omega\right)} \tag{3.28}$$

The distributed modal forcing term ψ in equation (3.28) for highly turbulent fluid flow cannot be defined analytically. The following section presents a model for the statistical derivation of this modal fluid forcing term.

3.1.3 Distributed Parameter Turbulence-Induced Vibration

Random vibration theory shows that the mean square displacement $\overline{x}^2$ of a single degree of freedom system is,

$$\overline{x}^2 = \int_{-\infty}^{+\infty} S_x \, d\omega = \int_{-\infty}^{+\infty} \left|H\right|^2 S_f \, d\omega \tag{3.29}$$

where S_x is the displacement PSD, H is the system FRF, and S_f is the force PSD. For distributed parameter turbulence-induced vibration problems, the force PSD is difficult to predict. Powell (1958) developed the acceptance integral approach which is a statistical measure of how well a turbulent pressure field excites particular vibration modes of a structure [90].

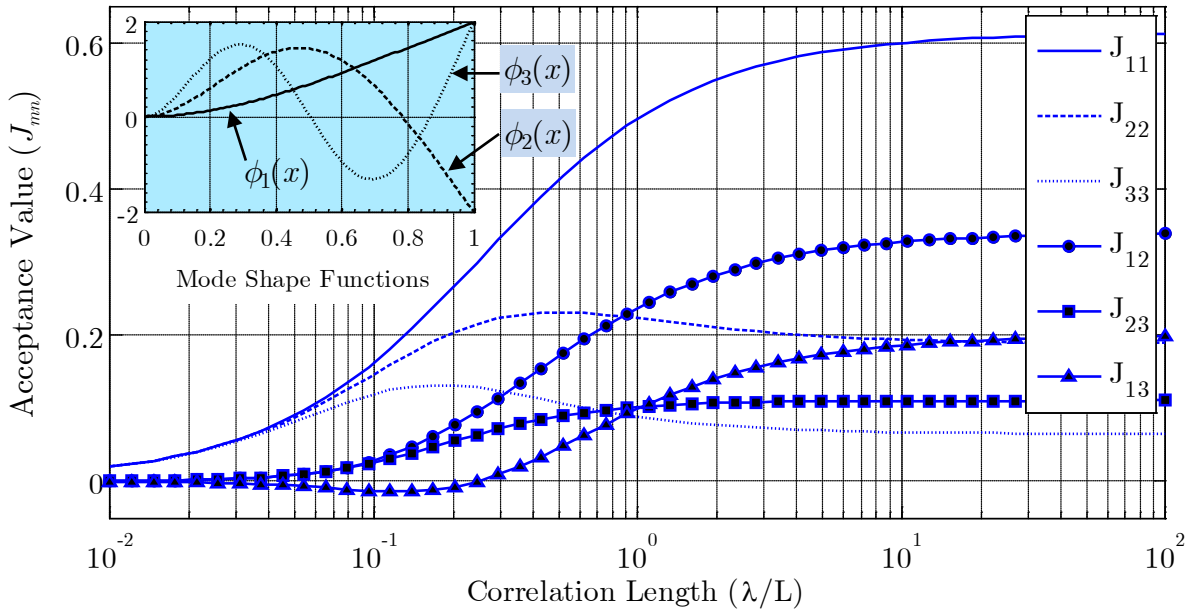

Figure 3.4: Theoretical joint and cross acceptance values with their corresponding mode shapes for the first three modes of a uniform cantilever beam.

One form of the acceptance integral is given as,

$$J_{mn}(\omega) = \int_0^{L_s}\int_0^{L_s} \phi_m(z) S_p(z, z', \omega) \phi_n(z')\, dz dz' \tag{3.30}$$

where J is the acceptance, S_p is the pressure CPSD along the length of the beam, ϕ are the Rayleigh-Ritz mode shapes defined in equation (3.14), and both z and z' are arrays of points along the z-axis [61]. Figure 3.4 shows theoretical acceptance values for the first three modes of a cantilever beam as functions of correlation length λ.

Correlation length can be considered a measure of how the pressure at one point on a surface varies from that of another point over time. A large correlation length in this case means that pressure along the entire beam length varies similarly with time. Notice that as $\lambda \Rightarrow \infty$, the

acceptance trends approach theoretical maximum values. The total beam displacement PSD can be expressed as,

$$S_u(z,\omega) = A\sum_{m=n}^{N_J} \phi_m^2 \left|H_m\right|^2 J_{mn} + 2A\sum_{m\neq n}^{N_J} \phi_m \phi_n H_m^* H_n J_{mn} \tag{3.31}$$

where N_J is the number of modes used to approximate the displacement PSD, A is the area of the cantilever normal to the turbulent flow, and H is the modal displacement FRF for the beam as defined in equation (3.23)[2].

In many cases, the cross acceptance terms (for $m \neq n$) are much smaller than the joint acceptance terms (for $m = n$) and can be neglected with minimal effect on the displacement PSD predictions. Assuming that the cross acceptance terms are negligible, equation (3.31) can be reduced to,

$$S_u(z,\omega) = A\sum_{m=1}^{N_J} \phi_m^2 \left|H_m\right|^2 J_{mm} \tag{3.32}$$

but caution should be taken to validate this assumption. Great inaccuracies may result if conditions such as those discussed by Au-Yang (2000) cannot be met [91]. The example calculations given in Figure 3.5 are from the case study presented in section 3.2. These calculations demonstrate that displacement due to joint acceptance terms are orders of magnitude greater than displacement caused by cross acceptance terms thus validating the use of equation (3.32).

[2] The asterisk (*) in equation (3.31) denotes the complex conjugate of the modal displacement FRF.

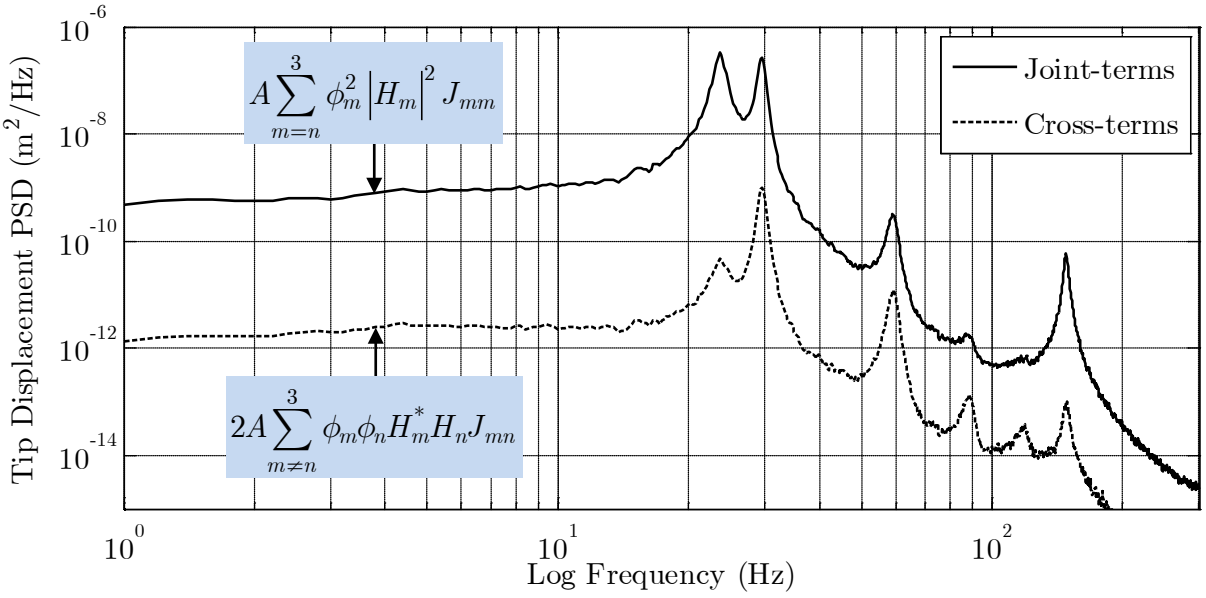

Figure 3.5: Example of tip displacement PSD functions comparing contributions of joint acceptance terms and cross acceptance terms for the first three modes of a long, slender cantilever beam.

Similar to the single degree of freedom expression given in equation (3.29) the total mean square displacement of a cantilever in turbulent cross-flow can be approximated with,

$$\overline{u}_m^2(z) = \int_{-\omega_S}^{\omega_S} \phi_m^2 \left|H_m\right|^2 J_{mm} A\, d\omega \tag{3.33}$$

where ω_S is the frequency bound of the pressure PSD. For practical application purposes ω_s is equal to or less than the Nyquist frequency $(\omega_s \leq \omega_{nyq})$. Realize that equations (3.32) and (3.33) can be expressed in terms of modal displacement rather than physical displacement simply by removing the mode shape terms. It is then possible to define the modal displacement PSD function as,

$$S_{\eta m}(\omega) = \left|H_m\right|^2 J_{mm} A = \left|H_m\right|^2 S_{\psi m} \tag{3.34}$$

where the modal turbulence-induced force PSD $S_{\psi m}$ is simply $J_{mm}A$. Given the previous assumption that the structural response will be sinusoidal, the mean modal amplitude of vibration $\overline{\eta}_e$ can be found by multiplying the modal root-mean-square amplitude by $\sqrt{2}$ such that,

$$\overline{\eta}_{em} = \sqrt{2}\sqrt{\overline{\eta}_{em}^2} = \left[2A\int_{-\omega_S}^{\omega_S} \left|H_m\right|^2 J_{mm}\, d\omega\right]^{\frac{1}{2}} \tag{3.35}$$

where the subscript *e* denotes the fully elastic (uncoupled) system. In other words, equation (3.35) is the mean modal displacement of the cantilever without backwards coupling effects of the piezoelectric material. This result of the elastic system can be combined with the analytical solution for the coupled system to yield the fully coupled electromechanical response as demonstrated in the following section.

3.1.4 Fully Coupled Electromechanical Response

From equations (3.20) and (3.23) it is straightforward to express the mean modal displacement amplitude for the coupled electromechanical system as,

$$\begin{aligned}\overline{\eta}_m(\omega) &= \Big(fully\ elastic\Big) - \Big(electrical\ coupling\Big) \\ &= \left[2A\int_{-\omega_S}^{\omega_S} \left|H_m\right|^2 J_{mm}\, d\omega\right]^{\frac{1}{2}} - H_m\chi_m V_0\end{aligned} \tag{3.36}$$

where the right-hand side of the equation may be thought of as modal displacement of the *fully elastic* structure modified by the *electrical coupling* of the piezoelectric material. The overbar on η serves as a reminder that equation (3.36) has a statistically derived distributed fluid forcing term which can be expressed as,

$$\overline{\psi}_m(t) = H_m^{-1}\left[2A\int_{-\omega_S}^{\omega_S}\left|H_m\right|^2 J_{mm}\, d\omega\right]^{\frac{1}{2}} e^{j\omega t} \tag{3.37}$$

Substituting equation (3.37) into equation (3.28) an expression for the modal mean steady-state load voltage amplitude can be given as,

$$\overline{V}_{0m} = \frac{j\omega_m \varphi_m \overline{\eta}_{em}}{j\omega_m + \frac{1}{\tau_c} + j\omega_m H_m\left(\omega_m\right)\varphi_m \chi_m} \tag{3.38}$$

where the total average power output can then be estimated from,

$$P_{ave} = \frac{V_{RMS}^2}{R_L} = \frac{1}{2R_L}\sum_{m=1}^{N_J}\left|\overline{V}_{0m}\right|^2 \tag{3.39}$$

Upon substitution of equation (3.38) into equation (3.36) and recalling equation (3.18), the total mechanical response of the beam can be given as follows.

$$\overline{u}(z,t) = \sum_{m=1}^{N_J}\left\{\left[2\int_{-\omega_S}^{\omega_S}\left|H_m\right|^2 S_{\psi m} d\omega\right]^{\frac{1}{2}}\left[1 - \left(\frac{j\omega_m \varphi_m H_m\left(\omega_m\right)\chi_m}{j\omega_m + \frac{1}{\tau_c} + j\omega H_m\left(\omega_m\right)\varphi_m \chi_m}\right)\right]\phi_m e^{j\omega_m t}\right\} \tag{3.40}$$

Depending on the desired application of this analysis, it may be necessary to have an expression for the load voltage PSD function. According to equation (3.29), classic random vibration theory shows that the displacement PSD S_x of a single degree of freedom system can be given as,

$$S_x(\omega) = \left|H(\omega)\right|^2 S_f(\omega) \tag{3.41}$$

where an FRF (H) and a forcing function PSD (S_f) are required. In this work the authors present a similar expression for the modal load voltage PSD given in equation (3.43), where H_v is the electromechanical FRF, and S_ψ is the turbulence-induced modal force PSD which was first introduced in equation (3.34). Upon inspection of equation (3.38) an FRF between elastic modal displacement η_e and load voltage V_0 may be defined with the following expression.

$$H_{cm}(\omega) = \frac{j\omega\varphi_m}{j\omega + \frac{1}{\tau_c} + j\omega H_m(\omega)\varphi_m\chi_m} \tag{3.42}$$

Taking the amplitude of the coupling FRF in equation (3.42) and multiplying by the modal displacement PSD S_η yields the following expression for modal load voltage PSD,

$$\begin{aligned} S_{vm}(\omega) &= \left|H_{cm}\right|^2 S_{\eta m} \\ &= \left|H_{cm}\right|^2 \left|H_m\right|^2 S_{\psi m} \\ &= \left|H_{vm}\right|^2 S_{\psi m} \end{aligned} \tag{3.43}$$

where the modal force PSD S_ψ was introduced into the expression upon substitution of equation (3.34). It is then possible to attain the electromechanical FRF H_v from equation (3.43) by multiplying the amplitude of both the coupling FRF H_c and the fully elastic FRF H as show in equation (3.44) below.

$$H_{vm}(\omega) = \frac{j\omega\varphi_m H_m}{j\omega + \frac{1}{\tau_c} + j\omega H_m\varphi_m\chi_m} \tag{3.44}$$

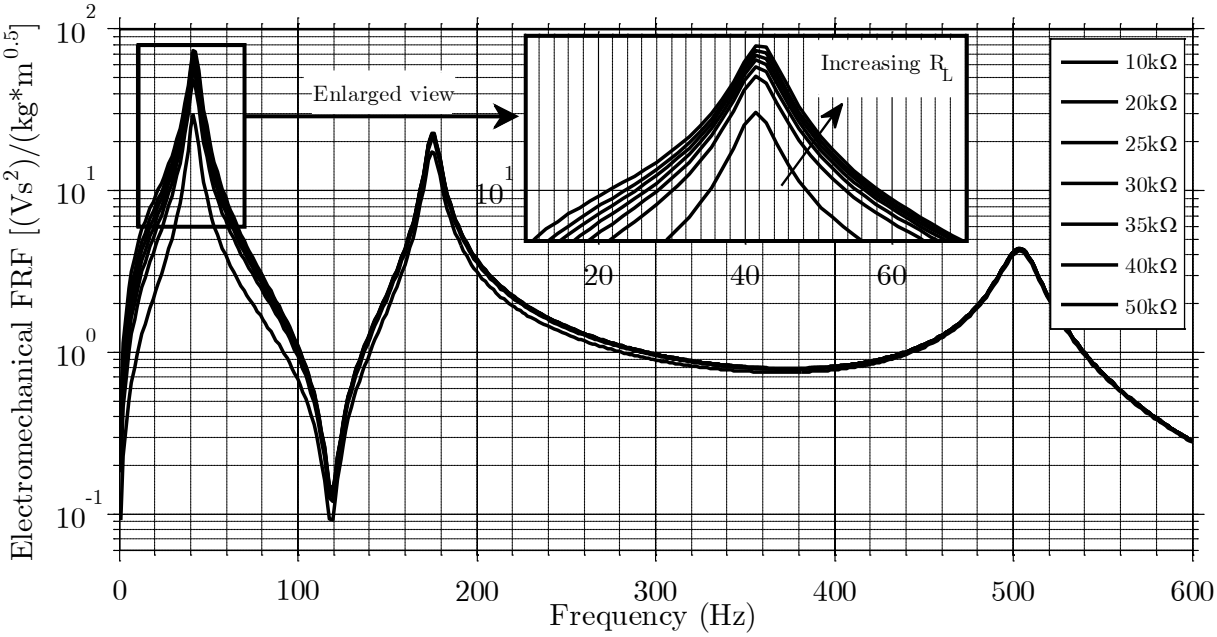

Figure 3.6: Electromechanical FRF as defined in equation (3.44) for various load resistance values.

Figure 3.6 shows the electromechanical FRF defined in equation (3.44) for the cantilevered unimorph harvester used in the case study discussed in section 3.2. One can see in Figure 3.6 that an increase in load resistance causes an increase in amplitude. This increasing trend is clearly shown in the enlarged window surrounding the fundamental mode frequency in Figure 3.6.

Multiplying the modal load voltage PSD given in equation (3.43) by the square of the modal piezoelectric coupling constant, one can obtain the modal piezoelectric coupling force PSD given in equation (3.45) below.

$$S_{cm}(\omega) = \chi_m^2 S_{vm} \tag{3.45}$$

Now that the PSD of both forcing terms is defined in equations (3.34) and (3.45), the fully-coupled displacement PSD can be found by recalling the form of equations (3.32) and (3.36),

$$
\begin{aligned}
S_{um}(z,\omega) &= \Big(fully\ elastic\Big) - \Big(electrical\ coupling\Big) \\
&= \phi_m^2 \left|H_m\right|^2 S_{\psi m} - \phi_m^2 \left|H_m\right|^2 S_{cm} \\
&= \phi_m^2 \left|H_m\right|^2 J_{mm} A\left(1 - \chi_m^2 \left|H_{cm}\right|^2 \left|H_m\right|^2\right)
\end{aligned}
\tag{3.46}
$$

where the squared mode shape terms ϕ_m^2 are included to transform the expression from modal to physical displacement coordinates.

3.2 Experimental Validation

This section provides details about an experimental case study performed for model validation purposes. Results show that the model presented in section 2.1 agrees well with experiment. More details concerning proof of concept experiments and initial modeling strategies can be found in Chapter 2, and in [60] and [80]. See also Chapter 4 and [79] for a more in-depth discussion about predicting turbulence-induced vibration using pressure probe measurements.

3.2.1 Case Study Results

A case study was performed using a single unimorph harvester placed in highly turbulent cross-flow. Material properties and dimensions of the harvester used in this case study are summarized in Table 3.1. The harvester was constructed by bonding a QuickPack™ from Mide Technology Corp. (model QP16n) to a spring steel cantilever with Scotch-Weld™ structural adhesive from 3M (model DP-460). Figure 3.7 illustrates construction details of the unimorph harvester included in the model and shows the relative length and thickness of each material. Neutral axis locations of the bonded and un-bonded portions of the beam are also shown. The ratio of bending stiffness between the composite portion of the harvester and the substrate $(YI_c\ /\ YI_s)$ was 4.58.

Table 3.1: Design parameters for the unimorph harvester used in the case study

Substrate Properties	*Symbol*	*Value*	*Units*
Mass density	ρ_s	7800	kg/m^3
Young's modulus	Y_1^s	205	GPa
Length	L_s	9.53	cm
Width	b_s	2.55	cm
Thickness	h_s	241	μm
PZT Properties	*Symbol*	*Value*	*Units*
Mass density	ρ_p	7700	kg/m3
Young's modulus	Y_1^p	61.0	GPa
Length	L_p	4.28	cm
Width	b_p	2.10	cm
Thickness	h_p	152	μm
Dielectric permittivity	ε_{33}^T	7.35	nF/m
Strain coefficient	d_{31}	-190	pm/V

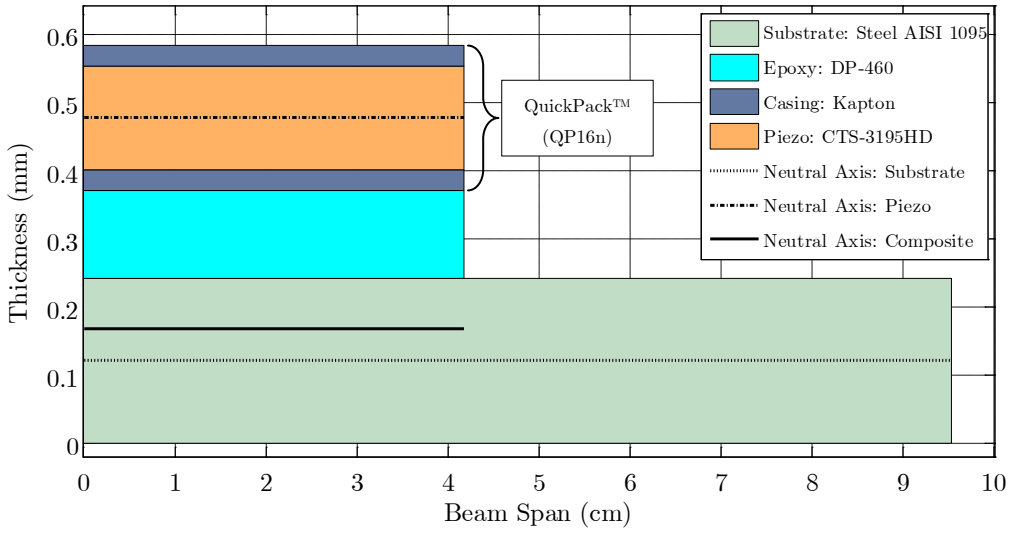

Figure 3.7: A scaled representation of the unimorph used in this case study showing materials and construction details.

Turbulent flow conditions were generated and maintained within a wind tunnel using a vertical cylindrical bluff body. The bluff body had a diameter of 4.83 cm and was positioned 15.24 cm upstream of the cantilever location. Flow velocity was approximately 8.1 m/s. Two custom pressure probes were used to make all turbulence measurements. A laser displacement sensor was used to measure cantilever tip deflection u, while voltage v across the load resistor R_L was measured directly with National Instruments data acquisition hardware. See Figure 3.1 for an illustration that helps define parameters u, v, and R_L.

The general experimental procedure began by first placing the harvester at a known location in turbulent air flow. Tip deflection and load voltage data were recorded for seven load resistor values. Actual load resistance values are listed in table 3.2. While keeping flow conditions approximately constant, the harvester was then removed, and the pressure probes were positioned such that they measured the fluctuating dynamic pressure normal to where the harvester's surface was previously located. Pairs of pressure measurements were made by keeping one probe fixed while the other was positioned at a known separation distance (or known location along the z-axis). Pressure measurements were made at several separation distances along the length of the harvester. These pairs of pressure measurements were then used to calculate the pressure CPSD from equation (3.1) and eventually the distributed fluid forcing function from equation (3.34).

Table 3.2: Actual load resistance values used in the case study

Parameter	*Symbol*	*Values*							*Units*
Resistance No.	n	1	2	3	4	5	6	7	
Load Resistance	R_L	9.88	19.7	24.9	29.5	34.5	39.9	49.6	$\mathrm{k}\Omega$

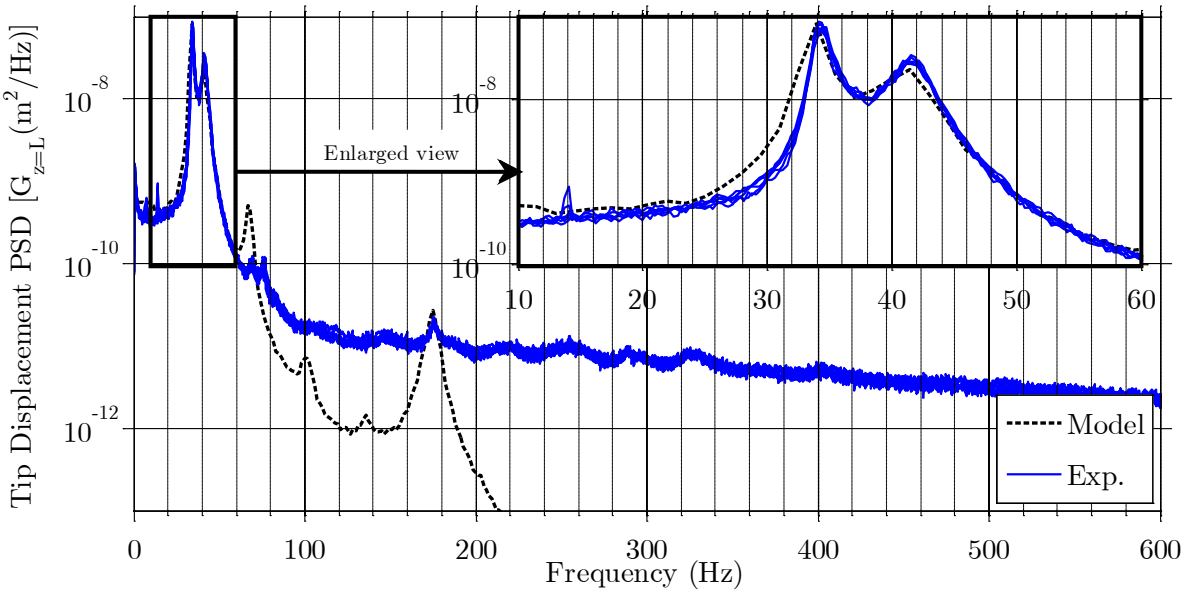

Figure 3.8: Unimorph harvester tip displacement PSD comparing model predictions to experimental measurements.

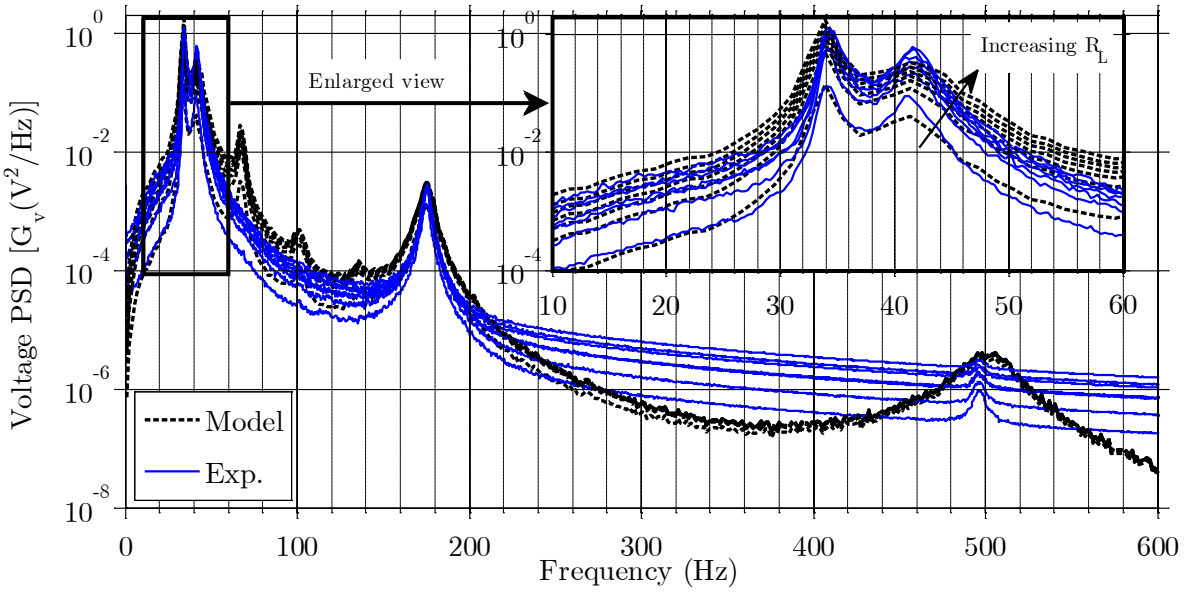

Figure 3.9: Load voltage PSD for various load resistance values comparing model predictions to experimental measurements.

Figure 3.8 and Figure 3.9 clearly demonstrate that the model agrees well with experimental data for both tip displacement and load voltage PSD functions as defined in equations (3.46) and (3.43) respectively. The most prominent peak at in both Figure 3.8 and Figure 3.9 is caused by a dominant frequency contained in the turbulent flow pressure measurements. This dominate frequency of approximately 34.0 Hz corresponds to the primary vortex shedding frequency of the bluff body which can easily be estimated using the Strouhal vortex shedding equation,

$$f_v = \frac{St\bar{U}}{L} \tag{3.47}$$

where f_v is the vortex shedding frequency in Hz, St is the dimensionless Strouhal Number, $\bar{U}$ is the mean flow velocity in m/s, and L is the characteristic length with units of meters. The second highest peak in both Figure 3.8 and Figure 3.9 corresponds to the fundamental bending mode frequency of the harvester. This fundamental bending mode is referred to as f_s and was approximately 41.2 Hz. In this case study f_v was intentionally offset from f_s in order to demonstrate how well the model can predict both the fluid forcing effects and the structural dynamics of the fully coupled distributed parameter system. A majority of the error seen at higher frequencies in the tip displacement PSD and voltage PSD functions can be attributed to electrical noise and bandwidth limitations of the pressure probes as discussed in Chapter 4.

Average power and RMS voltage as defined in equation (3.39) are shown in Figure 3.10 as functions of load resistance. Again, one can see that model predictions agree well with experimental measurements. The optimum resistance was found to be approximately 40 $\mathrm{k}\Omega$ where the maximum power output was 0.122 mW. Recall that the harvester was designed such that the first bending mode frequency f_s was significantly higher than the primary vortex shedding frequency f_v.

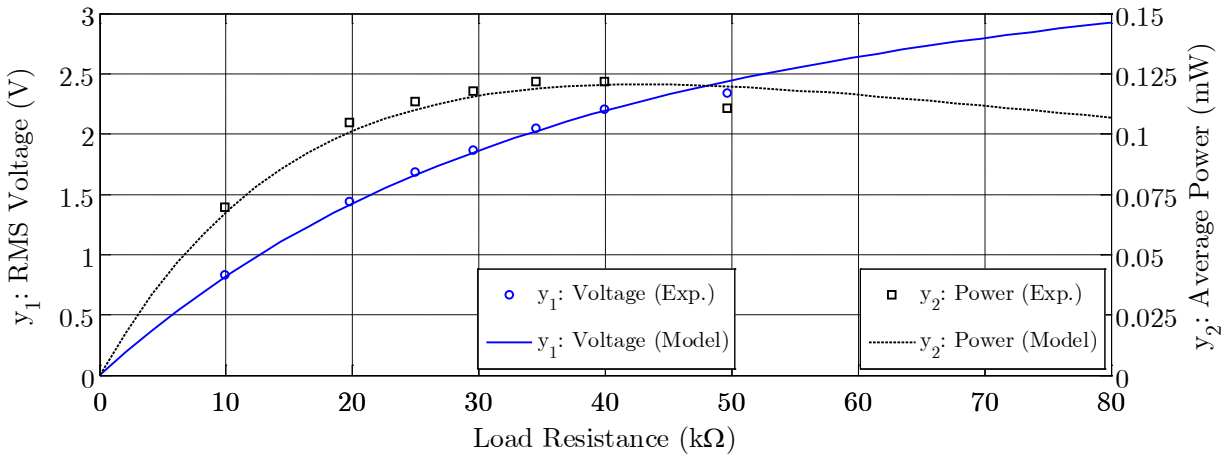

Figure 3.10: Experimental results and model predictions for RMS load voltage and average power output as functions of load resistance.

As these two frequencies coalesce, the harvester experiences a resonance condition where the amplitude of vibration and power output increase drastically. The modal damping ratios were adjusted one time such that the first three structural mode peaks in the displacement PSD predictions matched with those measured in experiment. After this initial damping ratio adjustment, the same damping ratios were used for all results and model predictions presented in this Chapter. The following section demonstrates how the model proposed in Section 2.1 can be used to modify the current harvester design in order to maximize power output.

3.3 Parameter Optimization

A brief analytical study was performed with the model presented in section 3.1. The goal of this study was to demonstrate how the power output of a single harvester could be maximized by modifying the most practical design variables. These variables were chosen to be the length and thickness of the substrate (L_s and h_s) and PZT (L_p and h_p) respectively, the load resistance R_L , and an added tip mass M_t .

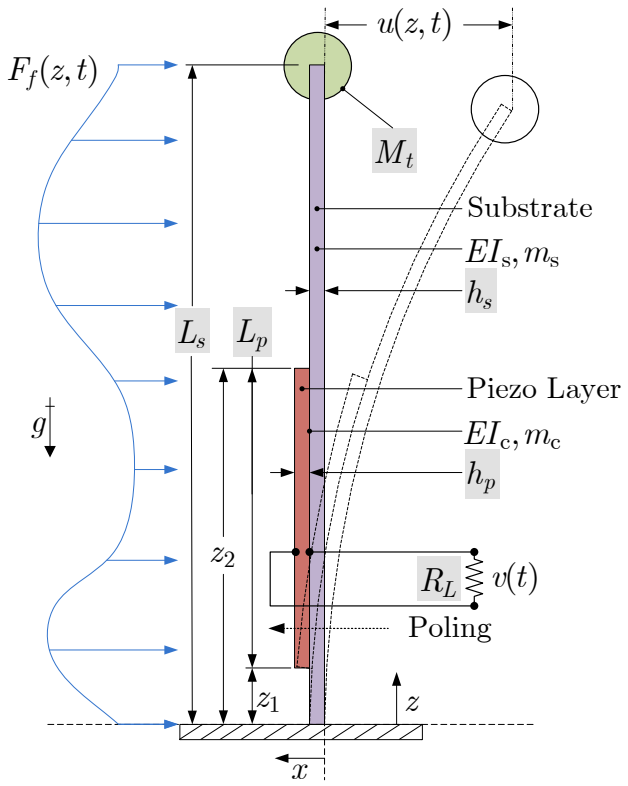

Figure 3.11: Schematic of cantilevered unimorph harvester modeled with a distributed fluid force and added tip mass (all parameters highlighted with a gray box were constrained variables used in the optimization study).

3.3.1 Modified Rayleigh-Ritz Model

Figure 3.11 shows a schematic of the modified unimorph harvester used in this optimization study. For every optimization case the original turbulent flow measurements discussed in section 3.1.3 were used as the fluid forcing function, while only the harvester design was modified. In this section, the harvester design parameters given in Table 3.1 will be referred to as the *initial design*.

The Rayleigh-Ritz model described in section 3.1.2 was modified to account for added tip mass M_t and axial loading from gravitational effects on both the tip mass and distributed beam mass. The modified Rayleigh-Ritz mass $\widetilde{\mathbf{M}}$ and stiffness $\widetilde{\mathbf{K}}$ matrices can be expressed as,

$$\widetilde{\mathbf{M}} = \int_0^{L_s} m U_m U_n \, dz + M_t \, U_m\Big|_{z=L_s} U_n\Big|_{z=L_s} \tag{3.48}$$

$$\widetilde{\mathbf{K}} = \int_0^{L_s} \left\{ YI \frac{d^2U_n}{dz^2} \frac{d^2U_m}{dz^2} + g\Big[\big(L_s - z\big)m + M_t\Big] \frac{dU_m}{dz} \frac{dU_n}{dz} \right\} dz \tag{3.49}$$

where the tip mass M_t contributes to both the total mass and stiffness of the system. Recall from the discussion following equation (3.12) that the acceleration due to gravity is in the negative z direction; therefore, the value for g is a negative quantity.

3.3.2 Effect of Natural Frequency on Power Output

Recall that the natural frequency of the harvester f_s (41.2 Hz) and the primary vortex shedding frequency f_v (34.0 Hz) were intentionally offset in the initial design. It is obvious that the optimum natural frequency of the harvester is where $f_s = f_v$ causing the harvester to be driven at (or near) resonance. A tip mass was incrementally added to the harvester in order to demonstrate the effect that the natural frequency has on the voltage and power output. The results in figures 3.12 and 3.13 show that simply changing the natural frequency with the addition of a tip mass can cause a significant increase in power output.

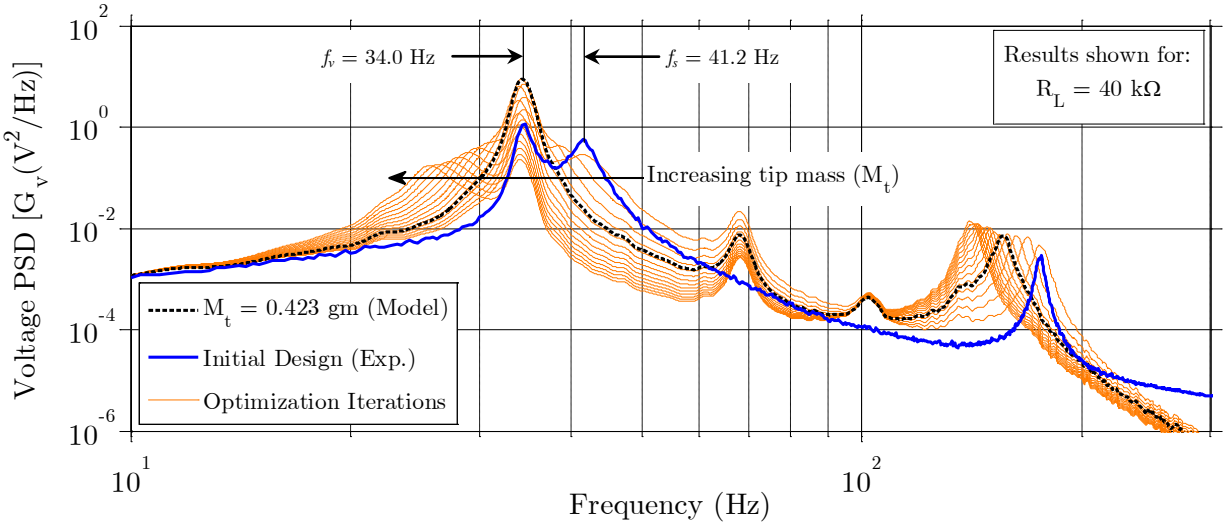

Figure 3.12: Trends in load voltage PSD with increasing tip mass.

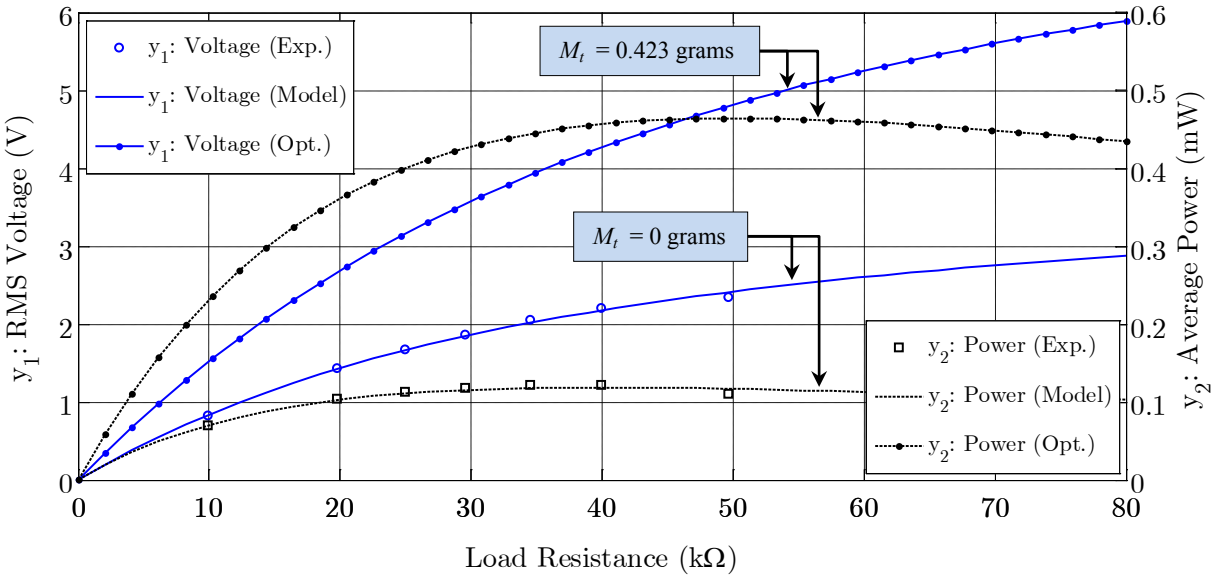

Figure 3.13: Comparison of theoretical maximum power output (with tip mass) and experimental output (without tip mass).

Figure 3.13 shows the experimental results originally shown in Figure 3.10 for no tip mass and an optimum resistance of approximately 40.0 $\mathrm{k}\Omega$ compared to theoretical results given the optimum tip mass of 0.423 grams and an optimum load resistance of ~51.0 $\mathrm{k}\Omega$. The power output at optimum load resistance increased approximately 280% from 0.122 mW for the initial design to 0.464 mW with the added tip mass.

3.3.3 Parametric Sweep Approach

Because every geometric design parameter listed in Table 3.3 affects the natural frequency of the harvester, it was obvious from the results shown in Figures 3.12 and 3.13 that a maximum in power output will occur where $f_s = f_v$. In order to isolate the effect that each of the four primary design parameters (L_s, h_s, L_p, h_p) had on the power output, the natural frequency was held constant by using an added tip mass as a frequency tuning parameter. For example: if the design parameter was chosen to be substrate length, then for every new value of substrate length, a new tip mass was calculated such that the harvester's natural frequency was held approximately constant. This constant frequency was called the *target frequency.*

Calculations for every tip mass were performed iteratively for each new design parameter value using a numerical solver developed with MATLAB software. This iterative tip mass solver (illustrated in Figure 3.14) successfully caused the natural frequency of each design iteration to be within ±0.01 Hz of the target frequency.

Table 3.3: Summary of constrained parameters used in this optimization study.

Parameter	*Type*	*Symbol*	*Constraint Range*	*Units*
Substrate Length	Geometric	L_s	(4.318 - 9.144)	cm
Substrate Thickness	Geometric	h_s	(0.178 - 1.270)	mm
PZT Length	Geometric	L_p	(3.048 - 9.144)	cm
PZT Thickness	Geometric	h_p	(0.127 - 1.270)	mm
Load Resistance	Electrical	R_L	(1.00 - 100)	kΩ
Tip Mass	Mass	M_t	(0.00 - 1.50)	grams

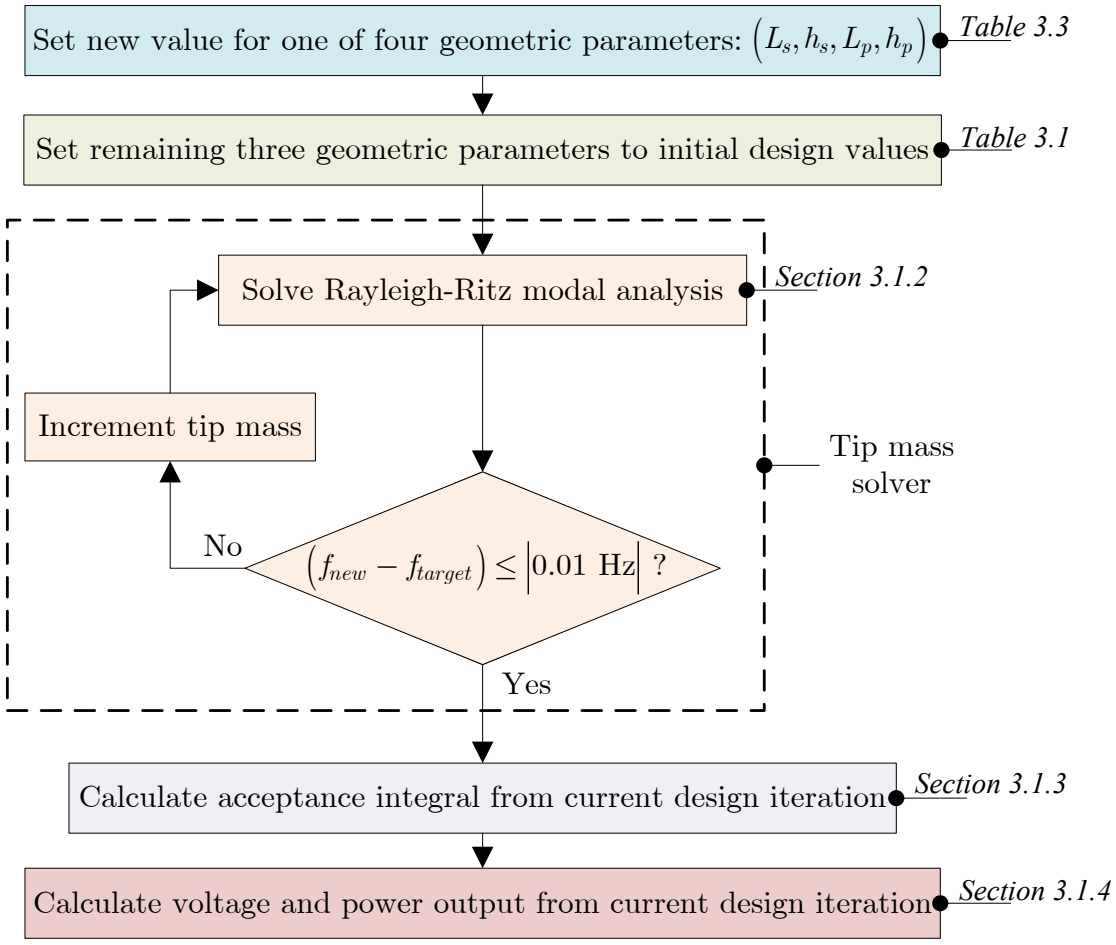

Figure 3.14: Flowchart illustrating the computational procedure followed for each new value assigned to a geometric parameter.

In the present study, the target frequency was set to 34.0 Hz, which is approximately equal to the vortex shedding frequency of the bluff body. Table 3.3 lists each of the six design parameters along with their constraints. The geometric type parameters from Table 3.3 were the primary focus of this optimization study. Parameter constraint ranges listed in Table 3.3 were set using the following practical design considerations:

Substrate Length (L_s)

- **Min:** Cannot be less than initial PZT length.
- **Max:** Cannot cause natural frequency to become less than the target frequency.

Substrate Thickness (h_s)

- **Min:** Cannot cause natural frequency to become less than the target frequency.
- **Max:** Reasonable bound to capture all maximum values and *interesting* trends.

PZT Length (L_p)

- **Min:** Cannot cause natural frequency to become less than the target frequency.
- **Max:** Cannot exceed length of initial substrate length.

PZT Thickness (h_p)

- **Min:** Cannot cause natural frequency to become less than the target frequency.
- **Max:** Reasonable bound to capture all maximum values and *interesting* trends.

Load Resistance (R_L)

- **Max/Min:** Reasonable bound to capture all maximum values and *interesting* trends.

Tip Mass (M_t)

- **Min:** Equal to initial design ($M_t = 0$)
- **Max:** Cannot cause initial design to buckle

The following describes the general computational procedure used to evaluate trends in power and voltage output as functions of all six design parameters listed in Table 3.3. First, a value was assigned to a given geometric parameter of interest from within the constraint range of that parameter. The other three geometric parameters were set to their initial design values given in Table 3.1. Next, a tip mass was added to the new design (if necessary) such that the natural frequency was within 0.01 Hz of the target frequency of 34.0 Hz. The model presented in section 3.1 along with modified equations (3.48) and (3.49) was then used with the new geometric parameter and tip mass to calculate power and voltage output as functions of load resistance. Finally, the value of the geometric parameter of interest was incremented to its next value and the procedure was repeated. See Figure 3.14 for an illustration of this procedure.

3.3.4 Mechanical Stress Considerations

It is important to note that the geometric constraints were set without considering maximum allowable stress limits of the PZT or substrate. It was therefore possible for the maximum stress limits to be exceeded before reaching the geometric constraints. In order to identify which design iterations (if any) caused material stresses to exceed allowable limits, maximum bending stresses were calculated for every combination of geometric parameter, load resistance, and tip mass.

The failure strength for an un-bonded QP10n PZT QuickPack was determined to be 176.5 MPa which was the lowest failure strength observed from three-point bending tests performed on 30 samples during a study conducted by Anton *et al* [92]. Based on Anton's results, the maximum allowable stress for the PZT was set to 170 MPa. Note that this allowable stress may be significantly lower for harvester designs that do not encapsulate the PZT wafer between two layers of kapton as is done with QuickPacks (see Figure 3.7).

It was assumed that the first material failure to occur would be fracturing of the brittle PZT ceramic wafer. The maximum stress in the PZT can be expressed as,

$$\sigma_{\max} = \left. \frac{Mh_c}{I_c} \right|_{z=0} \tag{3.50}$$

where $\sigma_{\max}$ is the maximum stress due to bending, M is the bending moment, h_c is the distance from the neutral axis to the outermost surface of PZT (see Figure 3.2), and I_c is the second moment of area of the composite section. The moment was calculated with the following expression,

$$M(x) = YI \sum_{m=1}^{3} \frac{d^2 u_m}{dz^2} \tag{3.51}$$

where YI is the bending stiffness, and u_m is the beam deflection amplitude as defined in equations (3.8) and (3.40) respectively. Only the first three modes were considered in the deflection and stress calculations because higher modes had negligible contributions to the final results.

3.3.5 Parametric Sweep Results

Figures 3.15 through 3.19 summarize the results from five sets of parametric sweep calculations which were performed following the procedure illustrated in Figure 3.14. Each of the five figures below show how the average power output of a cantilevered unimorph harvester varies with the tip mass, load resistance, and each of the four geometric parameters. Recall Table 3.3 for a list of all design parameters and their constraints.

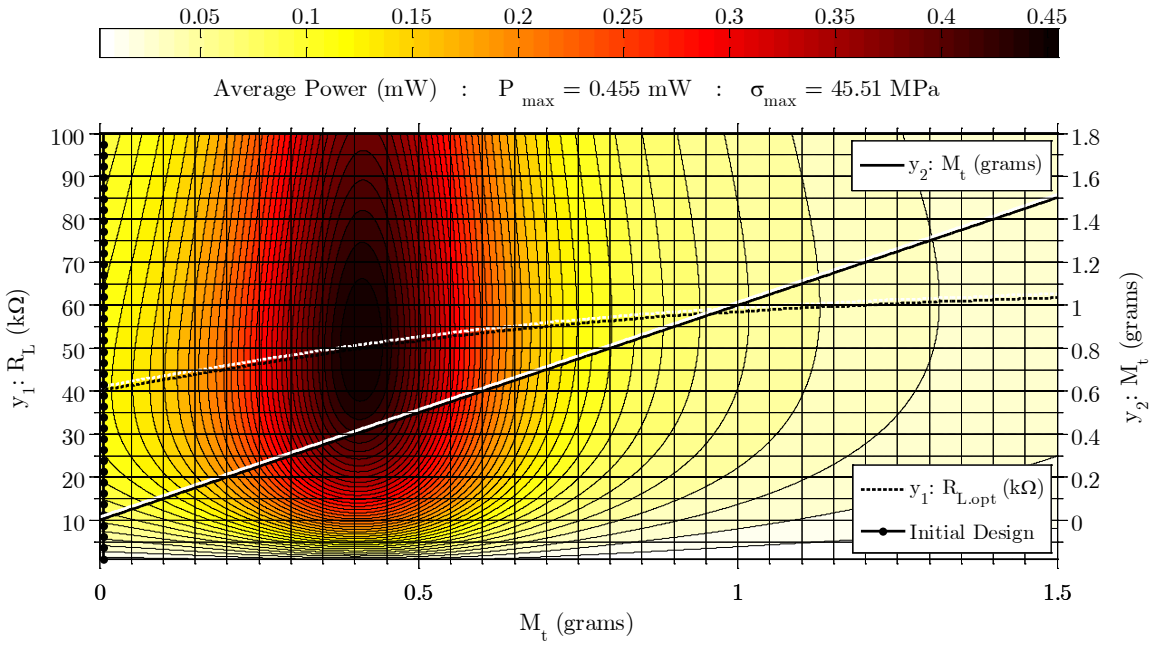

Figure 3.15: Theoretical results showing power output as a function of tip mass and load resistance for a unimorph harvester in turbulent cross-flow. The dashed and solid lines respectively represent optimum resistance and tip mass as functions of the tip mass.

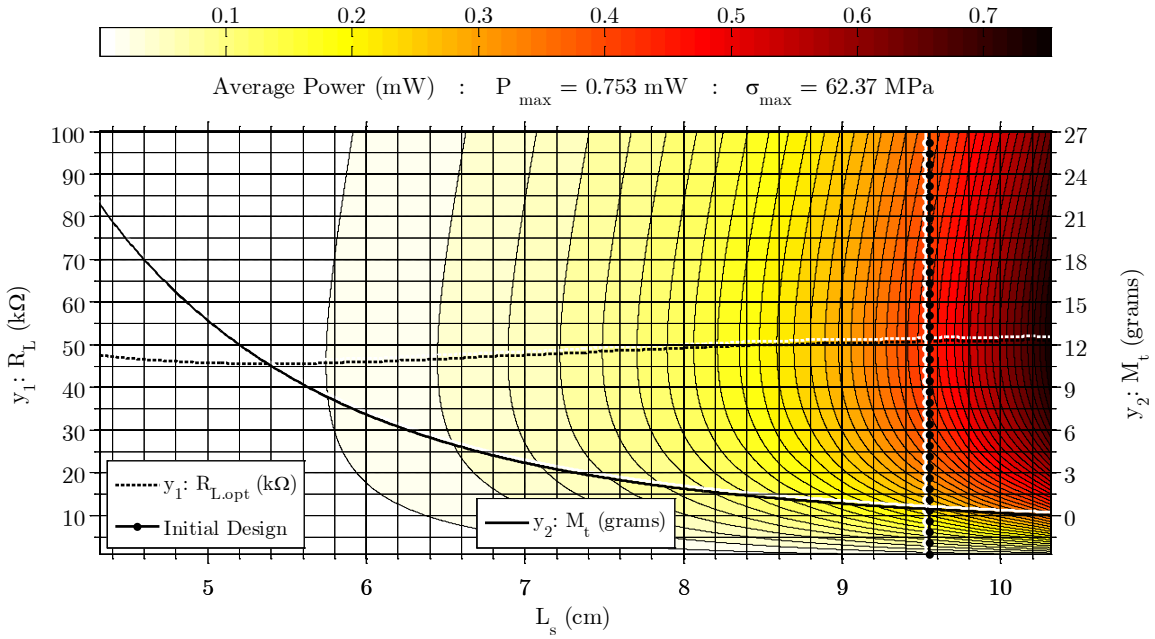

Figure 3.16: Theoretical results showing power output as a function of substrate length and load resistance for a unimorph harvester in turbulent cross-flow with a constant natural frequency of 34.0 Hz. The dashed and solid lines respectively represent optimum resistance and tip mass as functions of the substrate length.

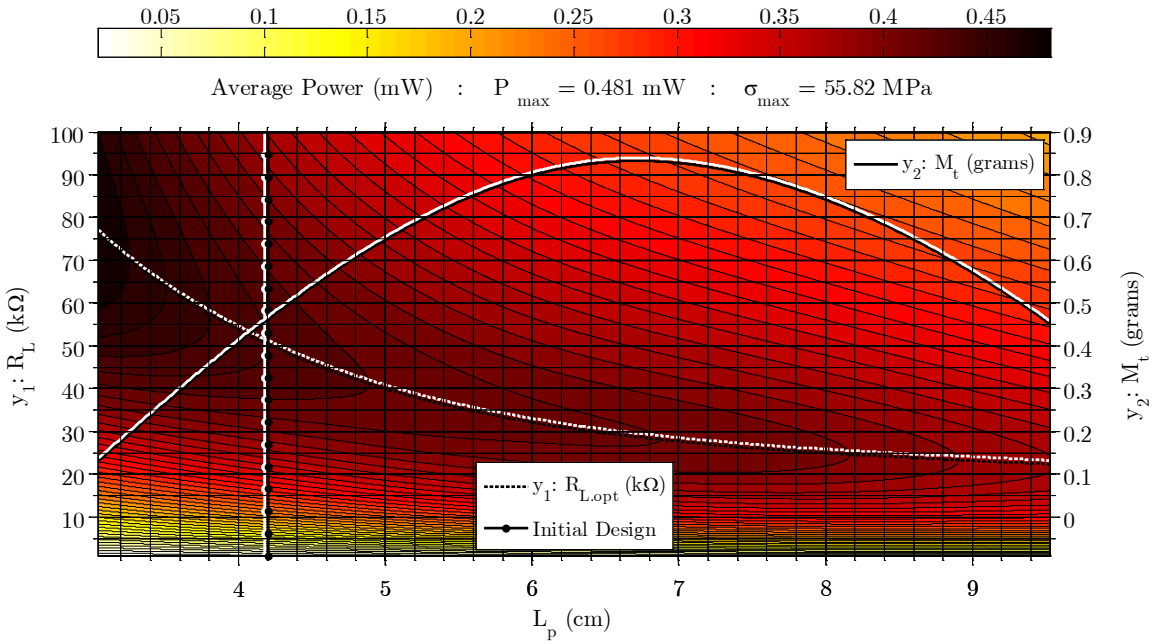

Figure 3.17: Theoretical results showing power output as a function of PZT length and load resistance for a unimorph harvester in turbulent cross-flow with a constant natural frequency of 34.0 Hz. The dashed and solid lines respectively represent optimum resistance and tip mass as functions of the PZT length.

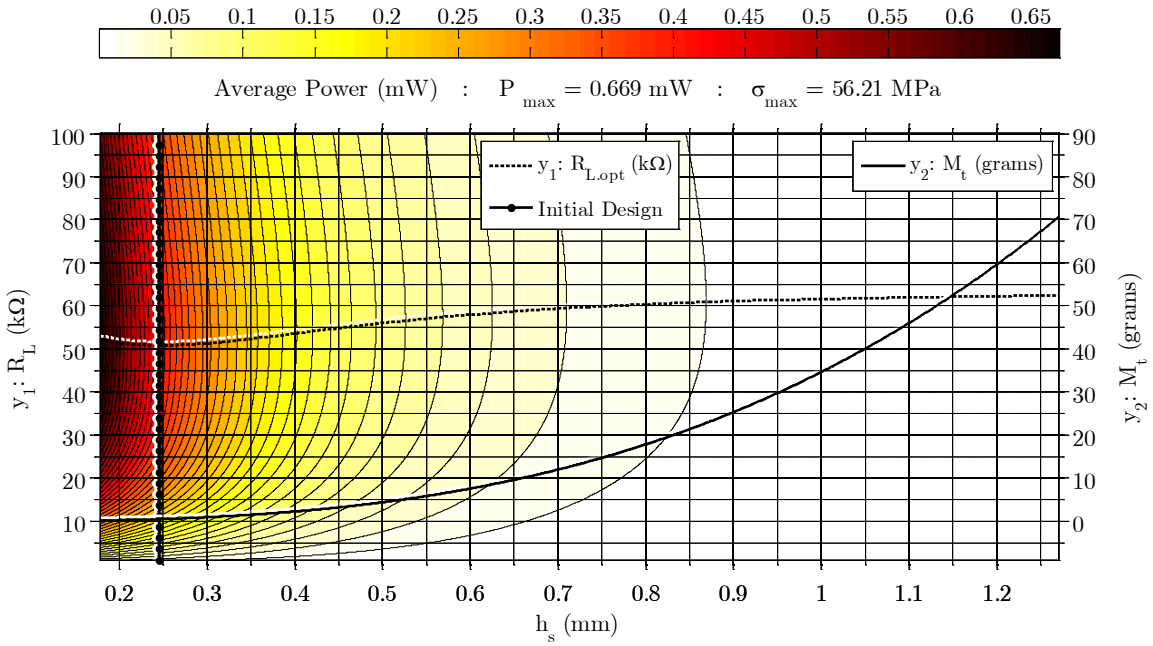

Figure 3.18: Theoretical results showing power output as a function of substrate thickness and load resistance for a unimorph harvester in turbulent cross-flow with a constant natural frequency of 34.0 Hz. The dashed and solid lines respectively represent optimum resistance and tip mass as functions of the substrate thickness.

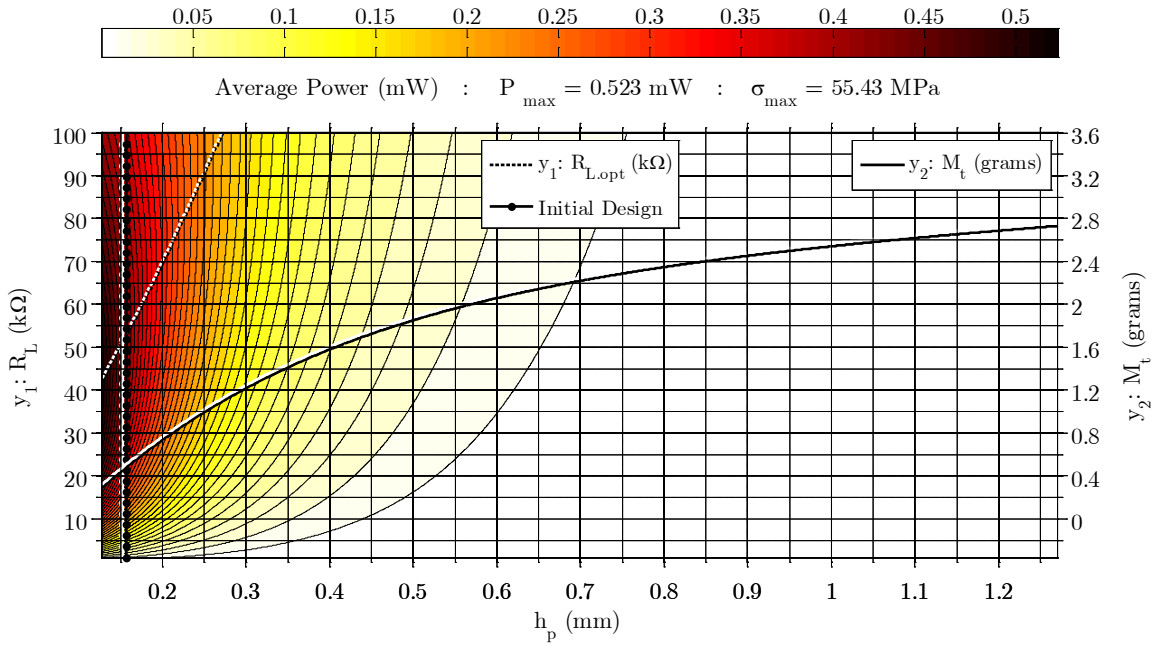

Figure 3.19: Theoretical results showing power output as a function of PZT thickness and load resistance for a unimorph harvester in turbulent cross-flow with a constant natural frequency of 34.0 Hz. The dashed and solid lines respectively represent optimum resistance and tip mass as functions of the PZT thickness.

Figures 3.15 through 3.19 plot the geometric parameter on the x-axis, the load resistance on the primary y-axis (y_1), the average power output on the z-axis, and the tip mass on the secondary y-axis (y_2). The dashed line shows the optimum resistance or maximum power output as a function of geometric parameter. The solid line shows tip mass as a function of geometric parameter. Lastly, the vertical dotted line is located at the initial design value of the geometric parameter only. Recall that the initial design had no tip mass while the results in Figures 3.15 through 3.19 have a varying tip mass.

The results in Figure 3.15 clearly show the optimum tip mass and load resistance of 0.423 grams and 51.0 $k\Omega$ respectively. Note that Figure 3.15 contains the average power output trends first shown in Figure 3.13 for a tip mass of 0 and 0.423 grams. Figure 3.16 shows theoretical average power output as functions of substrate length and load resistance. It is interesting to note

that changing the substrate length modifies the forcing function $S_{\psi m}$ defined in equation (3.34) because the area A and the acceptance integral J are functions of substrate length.

Figure 3.17 shows a clearly defined ridge of optimum resistance values. Here we see that the tip mass initially increases as the PZT length increases then it reaches a maximum and begins to decrease all while keeping the natural frequency constant. This initial increase of tip mass is caused by an increase in beam stiffness. As the length of the PZT increases, it continues to increase the mass of the beam but has a decreasing influence on the stiffness. This added mass increases the axial compressive load in the beam which begins to soften the structure; thus, decreasing the tip mass required to maintain a constant natural frequency.

Figures 3.18 and 3.19 show that by minimizing the substrate and PZT thickness, one can maximum power output. Minimizing PZT thickness influences the power output by causing an increase in capacitance and mechanical stress in the PZT. Minimizing the substrate thickness decreases the piezoelectric coupling and modal constant given in equations (3.22) and (3.27) respectively. Furthermore, minimizing PZT or substrate thickness causes a significant increase in amplitude of vibration which also causes an increase in stress and ultimately power output. The power appears to increase without bound as the PZT or substrate thickness is minimized. For all cases, the maximum bending stress in the PZT never exceeded the allowable limit of 170 MPa.

3.4 Chapter Summary

A fully coupled electromechanical distributed parameter model for energy harvesting from turbulence-induced vibration of a cantilever unimorph harvester was presented and experimentally validated. The model includes a combination of both statistical and analytical components. The distributed turbulence-induced force was derived using a statistical model called the *acceptance integral* technique. Natural frequencies, mode shapes, and frequency

response functions of the harvester were calculated using the Rayleigh-Ritz analytical approximation method. Lastly, the electromechanical coupling terms of the unimorph harvester were derived from constitutive relationships for the 31 bending mode of a piezoelectric material.

Two custom pressure probes were used to take measurements at several locations in the turbulent wake of a bluff body in air. These measurements were used to calculate the pressure CPSD in equation (3.1) and eventually the modal forcing function given in equation (3.34). Figures 3.8-3.10 show good agreement between experimental measurements and model predictions for tip displacement PSD, load voltage PSD, RMS load voltage, and average power output as defined in equations (3.46), (3.43), and (3.39) respectively.

A brief parameter optimization study was performed using the proposed model. It was shown that simply adding a tip mass could increase the power output by 280%. This drastic increase in power was caused when the natural frequency of the harvester approached the primary vortex shedding frequency of the turbulent flow. For each optimization case, a sweep parameter was set, then a tip mass was iteratively solved for such that the harvester's natural frequency remained constant. The four geometric sweep parameters were chosen to be the length and thickness of the substrate and PZT. For every new geometric parameter value and corresponding tip mass, the power was calculated and plotted as a function of the geometric parameter and load resistance. This parametric sweep optimization study demonstrated that minimizing the thickness of the PZT or substrate, or maximizing the substrate length can cause significant increases in power output.

CHAPTER IV

DUAL PRESSURE PROBES FOR PREDICTING TURBULENCE-INDUCED VIBRATION

Measuring highly turbulent fluid flow is challenging, especially in cases where the turbulence intensity exceeds acceptable limits for hot wire anemometry techniques. Using fast response pressure probes is an effective and well documented turbulence measurement method; however, there is little mentioned in the literature about using pressure probes to measure turbulence in low mean velocity air flows (0-12 m/s). Also lacking in the literature is a complete method of using pressure probe measurements to predict turbulence-induced vibration. Pressure probes are commercially available; however, they are intended for high-velocity environments (e.g. jet engine exhaust) and have a bandwidth on the order of 10 kHz. Considering the low-velocity (0-12 m/s), low bandwidth (300 Hz), and high sensitivity needed in the current study, it was decided to design, build, calibrate, and model a custom pair of pressure probes.

In this chapter the design and analysis of two high-sensitivity pressure probes is discussed. It will be shown how measurements with these probes are used to develop a statistically derived turbulent fluid forcing function. This function will then be combined with an analytical structural dynamics model such that not only the modal RMS displacements, but also the modal

displacement power spectral density plots can be predicted for a given structure. The pressure probe design, turbulence measurement techniques, and both the statistical and analytical models will be validated with experimental results. The results shown in Section 4.4.3 of this chapter are for three case studies, each performed with a single cantilever exposed to highly turbulent cross-flow.

4.1 Introduction

Turbulent and highly unsteady fluid flows are abundant in nature and are commonly encountered in real-world engineering applications. When elastic structures are exposed to turbulent flow, turbulence-induced vibration (TIV) is inevitable. In many cases TIV is problematic, and can cause catastrophic structural damage. In other cases, such as energy harvesting applications for example, one may wish to maximize vibration caused by turbulence [13,60,80]. Regardless of the application, the most challenging aspect of understanding and modeling turbulence-induced vibration is that turbulent flows are both unpredictable and difficult to measure. Therefore, the motivation behind the work presented in this chapter is not only to propose an effective method of turbulence measurement, but also to show how these measurements can be used to predict turbulence-induced vibrations. The modeling techniques developed in this work could then be used to modify the design of any structure to allow only desired levels of turbulence-induced vibration.

Motivation for the research presented in this chapter began during a recent investigation of energy harvesting methods in low velocity flows with high-intensity turbulence [60,80]. Many authors have explored energy harvesting techniques for flow-induced vibration; however, most harvester designs and modeling methods found in the literature are focused on either vortex

induced vibration (VIV) or flutter[3]. The first TIV energy harvesting study was performed by Akaydin *et al* (2010) with a piezoelectric cantilever in boundary layer turbulence; however, this was purely an experimental study and no TIV modeling was presented [13]. An experimentally validated model for energy harvesting from TIV remained absent from the literature until Hobeck and Inman (2011-2013) [60,80,93]. Although an energy harvesting study inspired the work presented here, this chapter focuses on the details of modeling TIV which proved to be a necessary and interesting aspect of the energy harvesting research.

4.1.1 Existing Methods for Measuring Turbulent Flow

Extensive efforts have been put toward the development of fast response pressure probes for measuring turbulent flow. Work done by Jezdinsky (1966) is among the earliest discussed in literature on the topic of measuring turbulent flows with pressure probes [94]. The majority of research on this topic has been developed for high velocity turbulent flow environments such as those encountered in turbomachinery [95–98]. The work presented in this chapter, however, is to make measurements and predictions based on low-velocity turbulent flows such as those found in ventilation systems, slow moving vehicles, or natural environments i.e., wind and streams.

The proposed turbulence-induced vibration model is a modification of a model first developed by Powell (1958) [90], used extensively by Au-Yang [99–101], and more recently by Finnveden *et al* in 2005 [102]. This original model was only applied to direct measurement techniques where pressure fluctuations are measured by arrays of transducers fixed on the surface of the structure. Direct measurement techniques could not be implemented in the current

[3] See Chapter 1, for an extensive review of various flow-induced vibration energy harvesting techniques.

study because fixing an array of transducers to the structure surface would greatly modify or hinder the true turbulence-induced vibration response.

Indirect measurement methods have also been explored, and are discussed in the literature. Indirect measurement refers to a process where the free stream turbulence is measured using hot wire anemometry, pressure probes, or other techniques and the dynamic response of a structure placed in that flow can be approximated. Research done by Grover *et al* (1978) shows extensive experimental analysis of tube bank dynamics where hot wire probes were used to measure the turbulence spectra [103]. Later, Axisa *et al* (1990) performed both theoretical and experimental analyses on turbulent excitation of tubes in cross-flow [104].

The technique presented in this chapter along with the work of Hobeck and Inman (2012) [79] combines *indirect* turbulence measurements with the previously discussed *direct* model approach. The primary advantage to the proposed method is that it is easy to implement, yet still provides very accurate predictions compared to existing techniques. Another key advantage is that after the turbulence is measured, predictions can be made for any structure experiencing similar flow conditions. These advantages along with other performance metrics, calibrations, and a detailed model are discussed later.

4.2 Mathematical Model

Due to the unpredictable nature of high-intensity turbulent flow, the most practical approach toward developing a turbulent fluid forcing function is to employ statistical techniques. The full model consists of an analytical structural dynamics portion which will be combined with a statistically derived forcing function. In order to maintain the focus of this modeling approach on the development of a turbulent forcing function, a simple Euler-Bernoulli cantilever beam will be

used in the analytical structural component (see Figure 3.1). It is important to note, however that this model can easily be adapted to accommodate more complex structures.

4.2.1 Preliminaries on Spectral Statistics

For the proposed model, the measured pressure $p(t)$ is assumed to be a stationary random process in which its mean, mean square, variance, and standard deviation do not change with time [78]. Turbulence measurements performed for this work were recorded as time-series pressure data. It is necessary therefore, to perform several statistical operations which reduced the raw data into more useful and meaningful forms. The correlation function is a measure of how similar the pressure varies with time at two points in space (say z_a and z_b). The pressure cross-correlation can be given as,

$$R_p(z_a, z_b, \tau) = \lim_{T\to\infty}\left(\frac{1}{2T}\right)\int_{-T}^{T} E\left[p(z_a,t)p(z_b,t+\tau)\right]dt \tag{4.1}$$

where T is the sample time period, E denotes that an expectation of the two pressure signals must be taken, and τ is a shift in time t between the two pressure signals. Another statistical measure used commonly in this analysis is called the pressure cross power spectral density (CPSD). The pressure CPSD is a measure of energy content within a signal and how it is distributed across the entire frequency spectrum of interest. Simply by taking the Fourier transform of the cross-correlation function one can get the following expression for the CPSD,

$$S_p(z_a, z_b, \omega) = \lim_{T\to\infty}\frac{1}{4\pi T}\int_{-\infty}^{\infty}\left\{\int_{-T}^{T} E\left[p(z_a,t)p(z_b,t+\tau)\right]dt\right\}\mathrm{e}^{-j\omega t}d\tau \tag{4.2}$$

where *j* is the imaginary number and ω is angular frequency in rad/s. It is important to note that throughout this chapter S_p is referred to as the double-sided CPSD function with units Pa^2/rad/s.

See Figure 4.18a a for a plot of equation (4.2) that was calculated with data collected from measurements made using the pressure probes discussed in this chapter.

4.2.2 Analytical Model

This portion of the model defines the structural dynamics equations and how they are coupled with the turbulence-induced forcing function. The simple case presented here is modeled as a cantilever beam subject to a distributed turbulence-induced fluid force along its length and normal to its surface as illustrated in Figure 4.1.

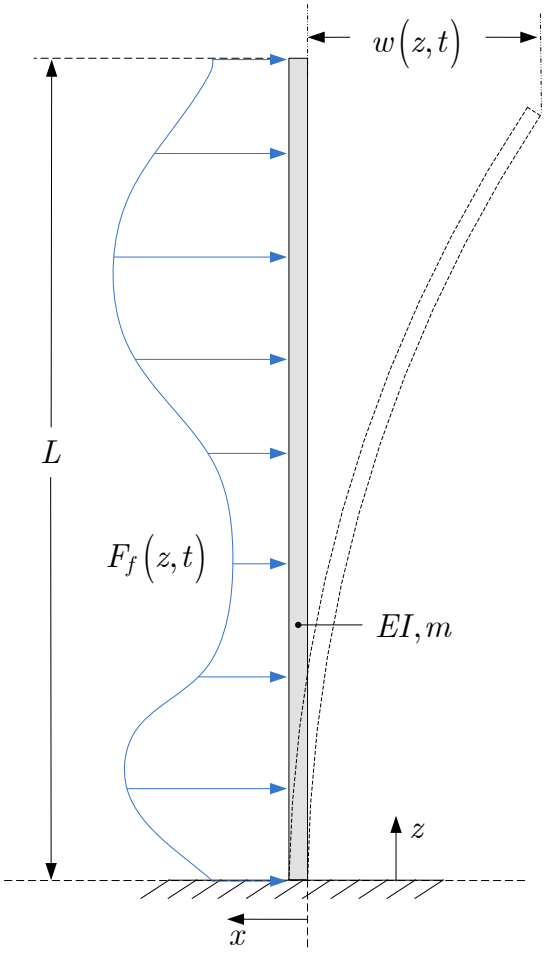

Figure 4.1: Cantilevered Euler-Bernoulli beam subject to a distributed turbulence-induced fluid force

In the following analysis it is assumed that the beam is a long, slender, rectangular, cantilever experiencing small transverse deflections. Provided the previous assumptions hold true, the beam can be modeled using the well-known Euler-Bernoulli beam equations. The governing differential equation of motion for a beam subject to a distributed force can be expressed as

$$YI\frac{\partial^4 u(z,t)}{dz^4} + c_s I\frac{\partial^5 u(z,t)}{dz^4 dt} + m\frac{\partial^2 u(z,t)}{dt^2} + c_a\frac{\partial u(z,t)}{dt} = F_f(z,t) \tag{4.3}$$

where $u(z,t)$ is the transverse beam deflection, Y is the Young's modulus of the beam, c_s is the coefficient of viscoelastic strain rate damping, I is the beam area moment of inertia, m is the linear mass density, c_a is the coefficient of viscous damping, and $F_f(z,t)$ is an arbitrary distributed transverse load along the length of the beam. Assuming that the solution can be expressed as the following infinite and convergent series,

$$u(z,t) = \sum_{m=1}^{\infty} \phi_m(z)\eta_m(t) \tag{4.4}$$

the relationship between steady state modal displacement η_m, and a modal distributed fluid force ψ_m can be expressed as,

$$\eta_m(t) = \frac{\psi_m e^{j\omega t}}{m_m(\omega_m^2 - \omega^2 + j2\zeta_m\omega_m\omega)} = H_m(\omega)\psi_m e^{j\omega t} \tag{4.5}$$

where the subscript m denotes the mode number, ω_m is the natural frequency, ϕ_m is the mode shape and $H(\omega)$ is the complex frequency response function. The damping terms in equation (4.3) can be combined to give a single modal damping ratio ζ_m which can be defined as,

$$\zeta_m = \frac{c_s I\omega_m}{2YI} + \frac{c_a}{2m\omega_m} \tag{4.6}$$

Upon performing the general modal analysis procedure of substituting the assumed solution into equation (4.3), multiplying by the mode shape ϕ_m, integrating over beam length L, and taking the Fourier transform one can attain the following.

$$\psi_m(z,t) = \int_{-\infty}^{\infty} \int_0^L \phi_m(z) F_f(z,t) \mathrm{e}^{-j\omega t} dz dt \tag{4.7}$$

Equation (4.7) is an expression for the modal forcing term due to an arbitrary distributed force. Analytical solutions for predicting the velocity or pressure field within a highly turbulent flow do not exist. Therefore, the time-domain forcing function $F_f(z,t)$ cannot be defined, and either statistical or numeric methods must be used to develop the modal forcing function ψ_m.

4.2.3 Statistical Model

Using classic random vibration theory, one can express the mean-square amplitude of a single degree of freedom oscillator subject to a random forcing function as,

$$\overline{x}^2 = \int_{-\infty}^{\infty} S_x(\omega)\, d\omega = \int_{-\infty}^{\infty} \left|H(\omega)\right|^2 S_f(\omega) d\omega \tag{4.8}$$

where S_x is the displacement power spectral density (PSD) of the system, S_f is the forcing function PSD, and H is the complex frequency response function of the oscillator [78]. A similar approach is taken for the distributed parameter system and is discussed in this section.

The most difficult aspect of predicting turbulence-induced vibrations is estimating the PSD of the distributed forcing function S_f. Powell (1958) developed a technique for estimating turbulence-induced vibration called the acceptance integral method.

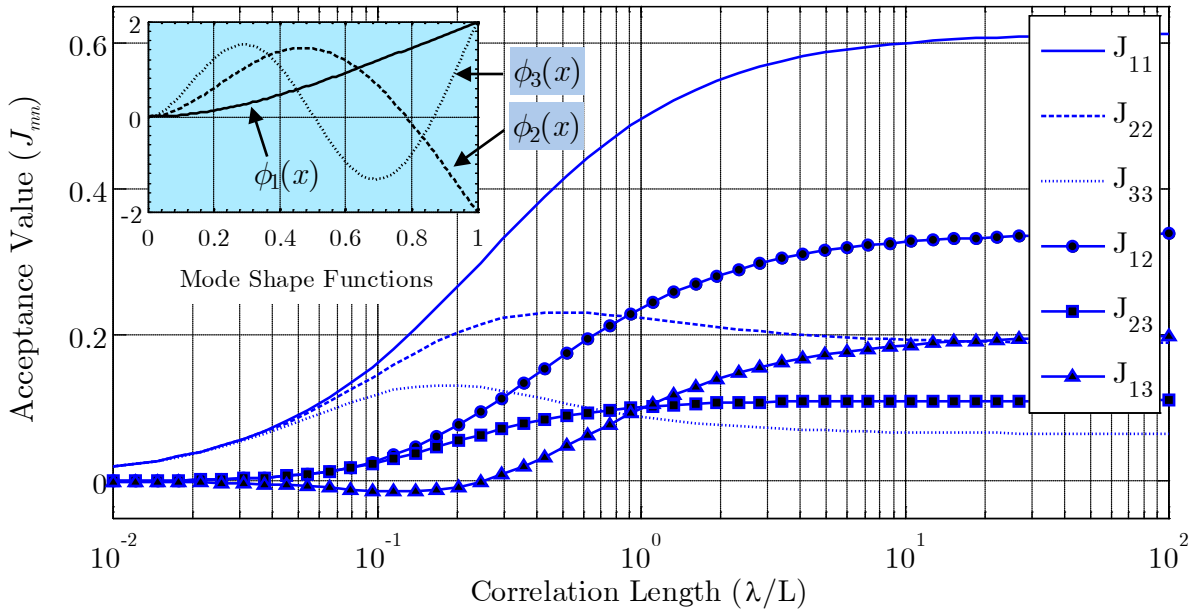

Figure 4.2: Theoretical cross and joint acceptance for first three modes of a cantilever beam.

The acceptance integral is a measure of how effective a turbulent force is at exciting particular dynamic modes of a structure. One form of the acceptance integral can be expressed as,

$$J_{mn}(\omega) = \frac{1}{LS_p(z_0,\omega)} \int_0^L \int_0^L \phi_m(z) S_p(z,z',\omega) \phi_n(z') dz dz' \tag{4.9}$$

where J_{mn} is the acceptance term, L is the beam length, S_p is the pressure CPSD function along the length of the beam, and both z and z' are arrays of points along the z-axis [90].

Figure 4.2 shows theoretical trends of the acceptance for the first three modes of a cantilever beam. An idealized expression for the coherence function as discussed by Au-Yang (2000) was used to evaluate the acceptance integral as a function of *correlation length* λ. The plots in Figure 4.2 can be regarded as upper bounds of the acceptance value where a perfectly correlated turbulent force along the length of the beam causes $\lambda \Rightarrow \infty$ conversely, a poorly correlated force causes $\lambda \Rightarrow 0$.

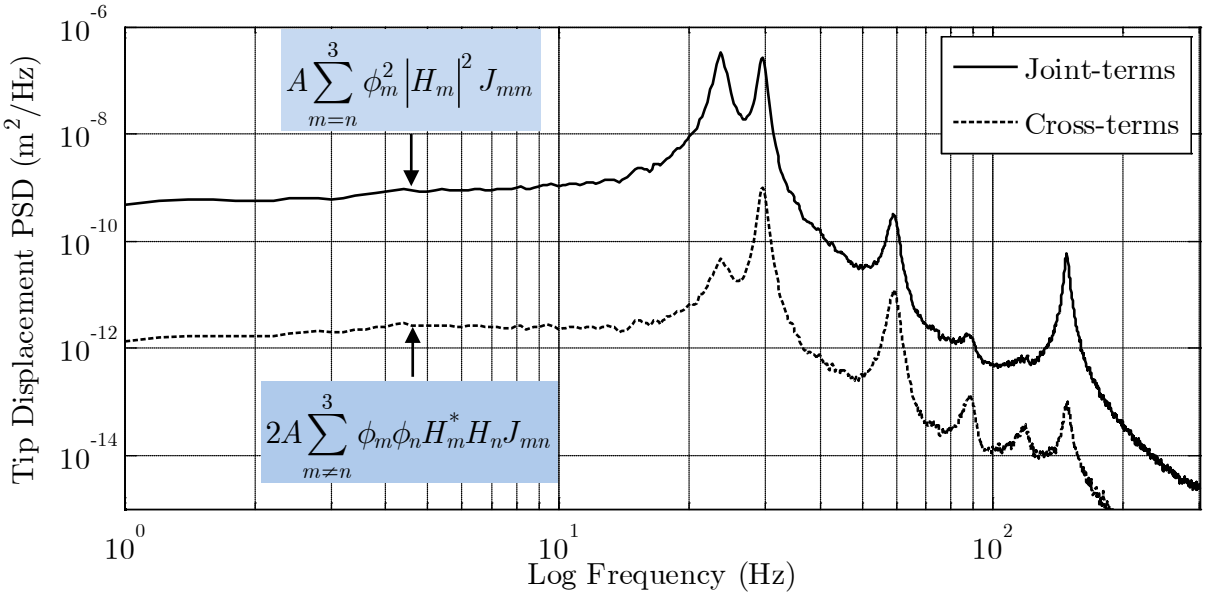

Figure 4.3: Comparison of tip displacement contributions between joint and cross acceptance terms.

Provided that an expression for the acceptance can be attained, the total displacement PSD of a cantilever beam can then be expressed as,

$$S_u(z,\omega) = A\sum_{m=n}^{\infty}\phi_m(z)^2\left|H_m(\omega)\right|^2 J_{mm}(\omega) + 2A\sum_{m\neq n}^{\infty}\phi_m(z)\phi_n(z)H_m(\omega)^* H_n(\omega)J_{mn}(\omega) \tag{4.10}$$

where A is the area of the cantilever normal to the turbulent flow, and H_m is the modal complex frequency response function for the structure as defined in equation (4.5) [100] [4]. In many cases it can be shown that the amplitudes of vibration associated with the cross-terms $(m \neq n)$ in equation (4.10) are significantly less than those for the joint terms $(m = n)$.

[4] The asterisk (*) in equation (4.10) denotes the complex conjugate of the frequency response function.

Assuming that the joint terms are negligible, the total displacement PSD of the cantilever beam becomes,

$$S_u(z,\omega) = A\sum_{m=1}^{\infty} \phi_m(z)^2 \left|H_m(\omega)\right|^2 J_{mm}(\omega) \tag{4.11}$$

For the remainder of this analysis it is assumed that the cross terms are negligible. This assumption is experimentally justified in the case study results from Figure 4.3, where the tip displacement PSD contribution from cross acceptance terms is approximately 2 orders of magnitude less than that of the joint acceptance terms at all frequencies. Because RMS displacement is a function of the integral of the PSD as shown in equation (4.8), one can conclude that the cross term contributions are indeed negligible. Au-Yang states that this assumption to neglect cross-acceptance is only valid if (a) the modal frequencies are well separated or (b) the cross-acceptance terms are small compared with the joint acceptances [100]. Au-Yang also lists and explains several other simplifying assumptions that are typically made while using the acceptance integral approach for TIV.

4.2.4 Combined Turbulence-Induced Vibration Model

Similar to a single degree of freedom system, the mean square displacement of the cantilever is found by integrating the displacement PSD over the frequency range. The modal mean square displacement can then be expressed as,

$$\overline{u}_m^2(z) = A\int_{-\infty}^{\infty} \phi_m(z)^2 \left|H_m(\omega)\right|^2 J_{mm}(\omega)d\omega \tag{4.12}$$

where the overbar on u denotes a time-averaged value. By removing the mode shape terms from equation (4.12) and assuming a sinusoidal response, it can be shown than the mean modal displacement can be attained with the following expression.

$$\eta_m = \left[2A \int_{-\infty}^{\infty} \left| H_m(\omega) \right|^2 J_{mm}(\omega) d\omega \right]^{\frac{1}{2}} \tag{4.13}$$

Upon substituting equation (4.13) into equation (4.4) and recalling the expression for H given in equation (4.5), it is now possible to express the total cantilever displacement as,

$$u(z,t) = \sum_{m=1}^{\infty} \left\{ \left[2A \int_{-\infty}^{\infty} \left| \frac{1}{m_m(\omega_m^2 - \omega^2 + j2\zeta_m\omega_m\omega)} \right|^2 J_{mm}(\omega) d\omega \right]^{\frac{1}{2}} \phi_m(z) \mathrm{e}^{j\omega t} \right\} \tag{4.14}$$

where one can immediately see that an attractive feature of this model is that only the acceptance terms (J_{mn}) are determined statistically. All other parameters of the cantilever (or structure of interest) can be chosen according to desired or allowable levels of vibration.

4.3 Pressure Probes

Two high sensitivity pressure probes were designed and built for the measurement of fluctuating dynamic pressure within highly turbulent, low-velocity flow. Pressure transducers and pitot tubes were preinstalled in the wind tunnel where the experiments were performed; however, they could not be used due to their lack of bandwidth and sensitivity. Because of the extremely high turbulence intensities (>50%), hot wire anemometry could not provide reliable velocity measurements [105].

4.3.1 Probe Design

Each probe consists of a MEMS-based differential pressure sensor enclosed such that one port is exposed directly to turbulent flow while the other is isolated within a breathable chamber. This chamber consists of rigid walls with portions of thick cloth which act as a buffer for the static port to insure fluctuating pressures are measured at the dynamic port only. The pressure sensor in each probe has a differential pressure range of ± 249 Pa with a dynamic response time of $\leq 100\,\mu s$ (All Sensors Corp. Model 1-INCH-D-MV). Overall design details of the probes are listed in Table 4.1, while a schematic and photo of the probes are shown in Figure 4.4.

Table 4.1: Overall design parameters of both pressure probes[5]

Parameter	*Value*	*Unit(s)*
Probe diameter	1.50	mm
Tip length	8.25	cm
Static port length	7.75	cm
Sensor volume	134	mm^3
Pressure range	± 249	Pa
Bandwidth	300	Hz
Output voltage range	± 16	mV
Sensitivity	0.064	mV/Pa

[5] See Table 4.2 and Figure 4.13 for more details concerning pressure probe dimensions.

a)

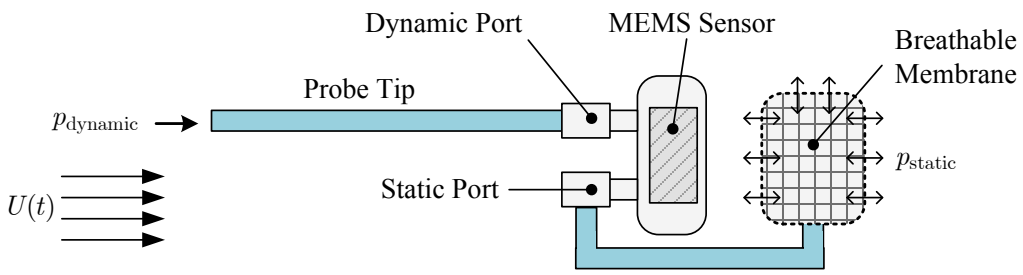

b)

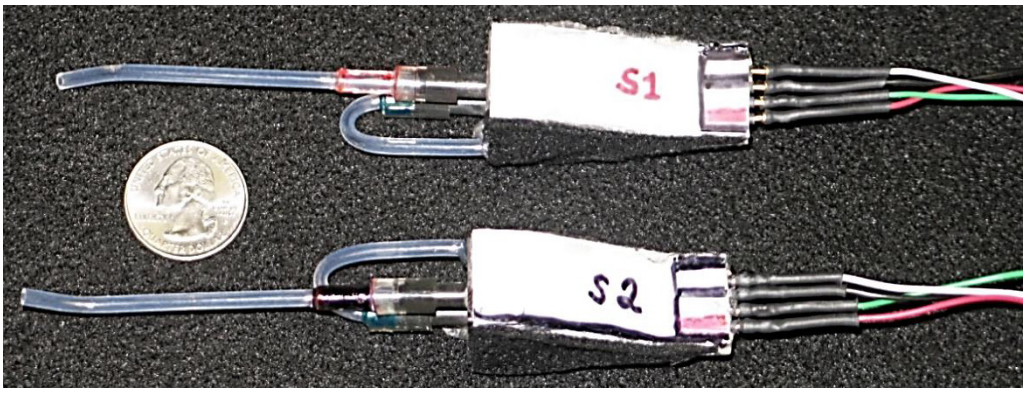

Figure 4.4: (a) Schematic of pressure probe design and (b) a photo showing the two probes used to perform turbulence measurements for the statistical TIV model.

4.3.2 Static Calibration

Static calibration refers to low turbulence intensity (<1%) flow measurement where the average probe sensor voltage output and average flow velocity is recorded at fixed incremental velocities. All calibrations were performed in a small, open loop, single stage wind tunnel with a test section measuring 91.0 cm long with a cross section of 35.6 cm wide and 13.6 cm high. For details on the wind tunnel construction and instrumentation see Bilgen (2010) [73].

Static pressure probe calibration was performed on each probe individually where only the pressure probe and a pitot tube were in a sealed test section during the calibration procedure. Each pressure probe was positioned in the test section such that the probe tip was oriented normal to the mean flow direction and was held in a fixed position throughout the entire calibration procedure. Actual velocity was measured with a pitot tube positioned near the pressure probe. In order to minimize velocity profile effects, the pressure probe tip and pitot tube tip were separated in the widthwise direction yet set at equal height and lengthwise location in the test section. Results of the static calibrations are shown in Figure 4.5.

Wind tunnel velocity and sensor voltage were measured during pressure probe calibration; however, pressure rather than velocity was needed for the model. According to documentation for the pressure sensor, a linear relationship existed between voltage and pressure. A linear function is significantly easier to fit and well behaved over the entire voltage range compared to the non-linear, exponential function shown in Figure 4.5. Because of these practical advantages of establishing a linear relationship between voltage and pressure each probe was calibrated with dynamic pressure instead of velocity.

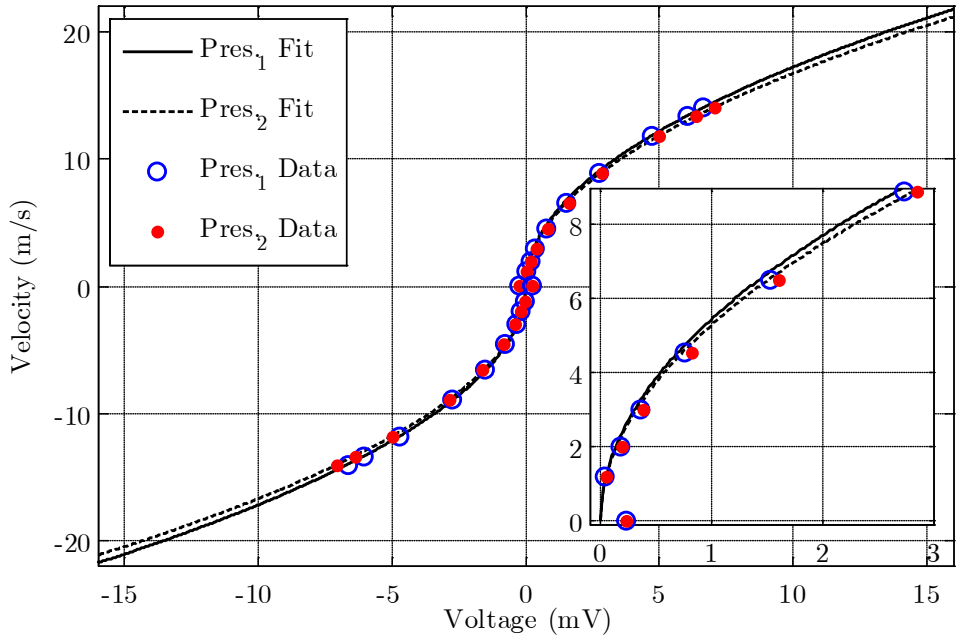

Figure 4.5: Static pressure probe calibration curves for velocity as a non-linear function of voltage output.

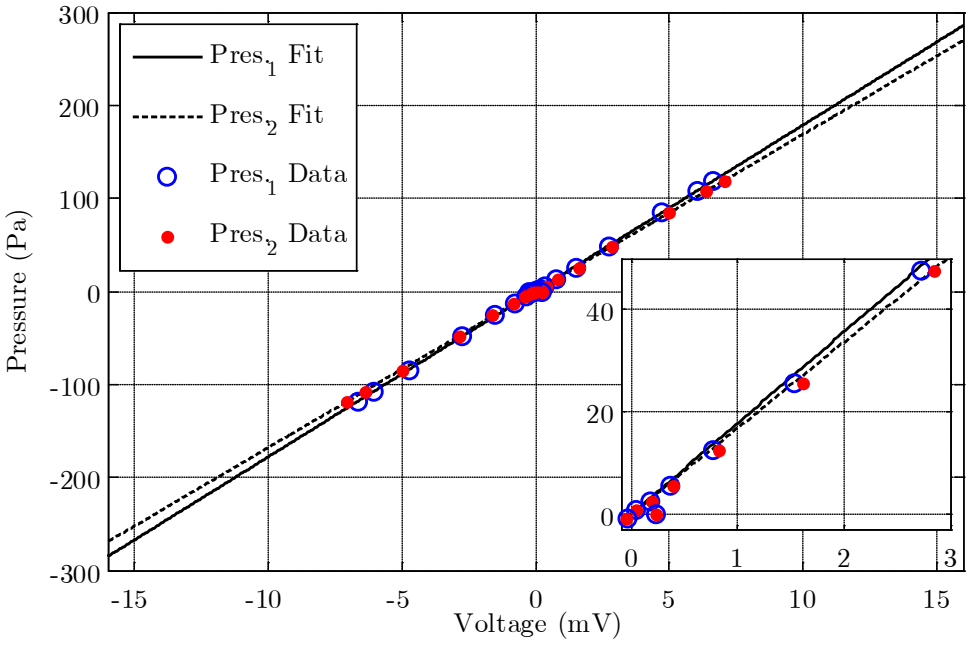

Figure 4.6: Static pressure probe calibration curves for dynamic pressure as a linear function of voltage output.

Dynamic pressure p corresponding to the velocity data was calculated using the following relationship,

$$p = \frac{p_a U^2}{2 R_a T_a} \tag{4.15}$$

where p_a and T_a are ambient pressure and temperature, U is the velocity measured with the pitot tube and R_a is the universal gas constant for air [106]. Table 4.3 lists the actual values used in the calibration calculations for p_a, T_a, and R_a. Both pressure probes were able to demonstrate excellent linearity between voltage and pressure using the data from Figure 4.5 along with equation (4.15). Static calibration results for pressure are shown in Figure 4.6.

A hot wire probe was used to measure the reference velocity for the dynamic calibration procedure in section 4.3.3. Before dynamic velocity measurements could be made, the hot wire probe had to be calibrated statically using the same procedure for the static pressure probe calibrations as discussed previously.

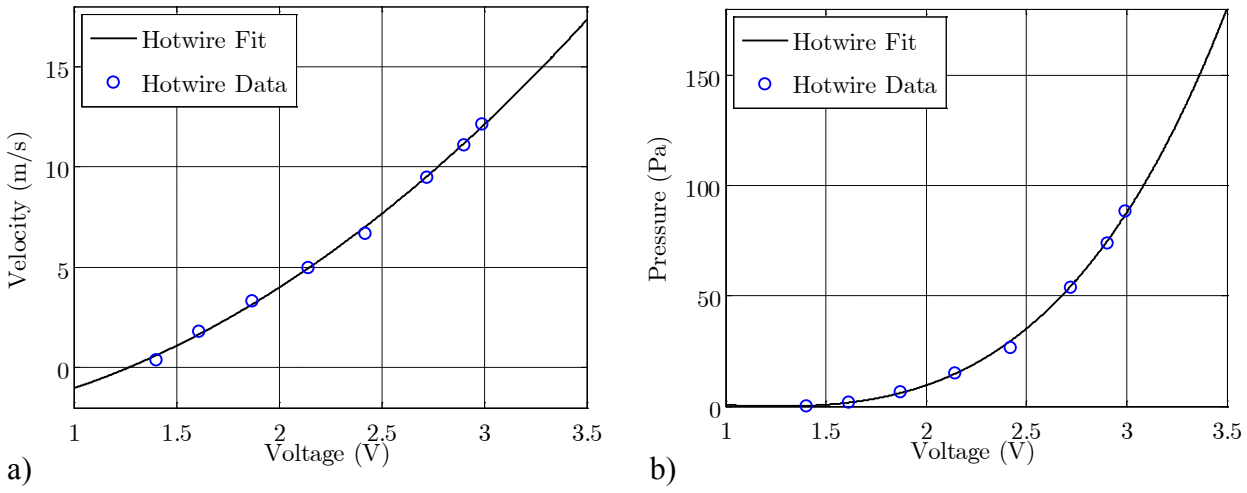

Figure 4.7: Static hot wire probe calibration results for (a) velocity and (b) pressure as non-linear functions of voltage output.

Figure 4.7a presents raw data from the hot wire calibration measurements along with a second order polynomial fitted to the data representing velocity as a continuous function of voltage. Figure 4.7b shows results of using equation (4.15) to calculate dynamic pressure as a function of hot wire voltage output with the data and fitted polynomial function from Figure 4.7a.

4.3.3 Dynamic Calibration

Dynamic calibrations were performed on each pressure probe individually. The dynamic response characteristics of both probes were found using a broadband excitation system identification technique. The general procedure involves measuring the input and output of an unknown dynamic system where the input can be represented as a broadband signal i.e. white or colored noise. The *unknown system* in this case is the pressure probe sensor assembly. This system identification method was used in a similar analysis performed by both Lenherr *et al* (2011) [95] and Ommen *et al* (1999) [107]. Figure 4.8 illustrates the sequence of gathering and processing pressure probe data, and shows where the static and dynamic calibrations were applied. Note that the dynamic calibration calculations were performed after the time domain data was converted to the frequency domain. Performing calibrations on the frequency response was appropriate because the forcing function used in the TIV model (Section 4.2) was applied in the frequency domain. Therefore, it was not necessary to compensate for pressure probe dynamics in the time domain.

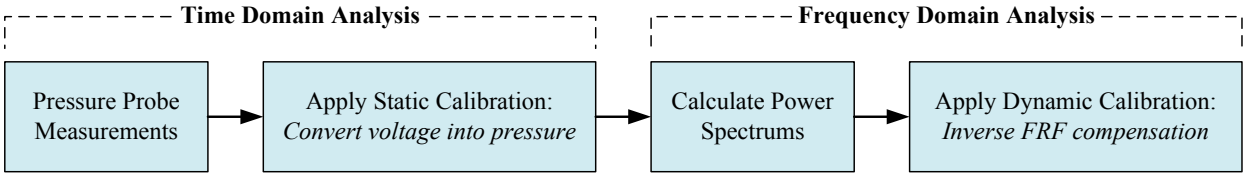

Figure 4.8: Diagram showing the flow of data gathered from the pressure probes.

The input or reference signal was produced by measuring grid turbulence having an intensity of approximately 10%. An intensity of 10% was chosen because it was high enough to excite the pressure probe dynamics, yet low enough to be measured accurately with a single sensor hot wire probe. Grid turbulence refers to a turbulent flow that is assumed to be approximately both homogeneous and isotropic. Turbulence intensity is calculated using the following expression,

$$TI = \frac{U_{rms}}{\bar{U}} \times 100\% \tag{4.16}$$

where U_{rms} is the root mean square velocity, and $\bar{U}$ is the mean flow velocity [105]. Grid turbulence used for the calibrations was produced by placing an array of vertical cylinders at the upstream end of the test section. All cylinders had a diameter of 6.35 mm and were evenly distributed across the test section width spaced at 22.9 mm measured between their centers. Hot wire and pressure probe measurements were made approximately 30.5 cm downstream from the array of cylinders. The mean flow velocity was held constant at approximately 10 m/s for both calibration tests.

The dynamic calibration setup and procedure was similar to that of the static calibration. Two major aspects of the dynamic calibrations that were different from the static calibrations were: first, a hot wire probe rather than a pitot tube was used as the reference velocity; and second, time-series data rather than time-averaged data was measured and recorded.

For a given calibration test, a pressure probe and the hot wire probe were placed in the test section where they measured the grid turbulence simultaneously. Hot wire probe measurements were used as the input to the system, while the corresponding pressure probe measurement was used as the system output. The diagram shown in Figure 4.9 illustrates the components of the dynamic calibration setup.

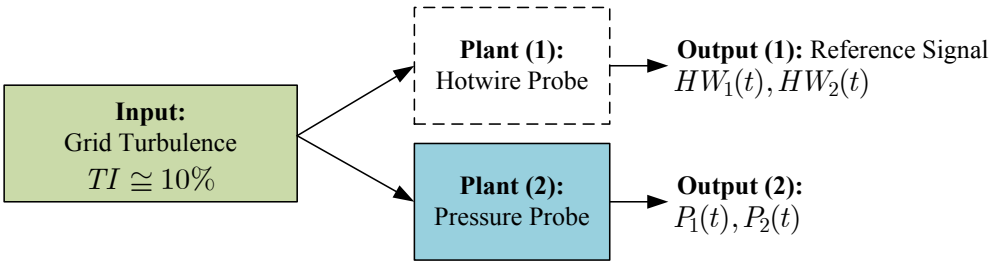

Figure 4.9: Diagram showing the components of the dynamic calibration setup.

Even though the hot wire measurement was an output by definition, it was used as the input or reference signal; thus, hot wire system dynamics were assumed to be negligible compared to those of the pressure probes. This assumption to ignore hot wire sensor dynamics is justified considering that the pressure probes have a bandwidth of 100 Hz (Figure 4.10b) while hot wire probes have a bandwidth on the order of 100 kHz [108].

Siglab software was used to sample and store the time-series voltages of the hotwire and pressure probes at a rate of 5.12 kHz. The output voltage was filtered digitally using lowpass, fourth-order, Butterworth topology with a cutoff frequency of 2.56 kHz. Matlab software was used for all post-processing of the data. The hot wire probe used in these calibrations was a TSI Model 1201 single sensor element. A Dantec 55M01 main unit and a Type 55M10 constant temperature anemometer bridge were used to produce the output voltage of the hot wire probe.

Figure 4.10a shows PSD functions of the hot wire and pressure probe measurements for both pressure probes. Notice that the PSD for both pressure probes clearly shows attenuation due to the first two acoustic resonance modes at approximately 525 Hz and 1580 Hz.

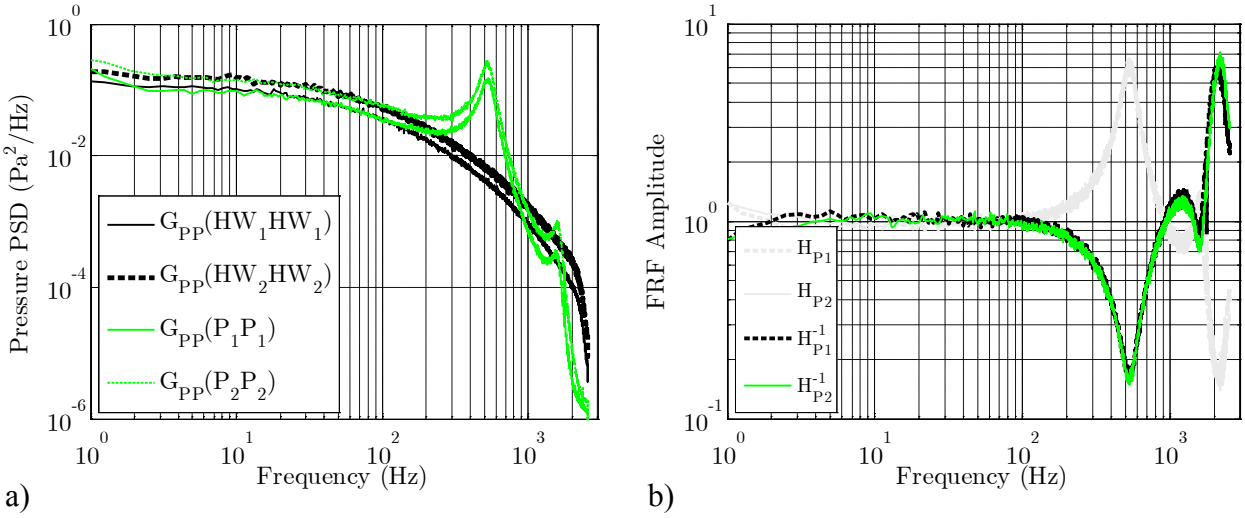

Figure 4.10: Grid turbulence measurements made with hot wire and pressure probes showing (a) pressure PSD functions and (b) FRF estimates.

The DC offset seen between the two sets of data in Figure 4.10a is due to the second calibration test having a slightly higher mean flow velocity. Because the FRF is a function of the ratio between input and output PSD functions, the DC offset seen in Figure 4.10a had no effect on the FRF estimate results shown in Figure 4.10b. Both pressure probes had a similar physical design; therefore, their FRF estimates shown in Figure 4.10b are nearly identical. The following expression was used to calculate the FRF estimates from Figure 4.10b,

$$H_{Pi} = \sqrt{\frac{G_{PP}(P_i, P_i)}{G_{PP}(HW_i, HW_i)}} \qquad for\ i = 1,2 \tag{4.17}$$

where H_P is the FRF, $G_{PP}(P,P)$ is the pressure PSD of the pressure probe output, $G_{PP}(HW,HW)$ is the pressure PSD of the hot wire probe output, and the index i denotes data measured during the first or second pressure probe calibration.

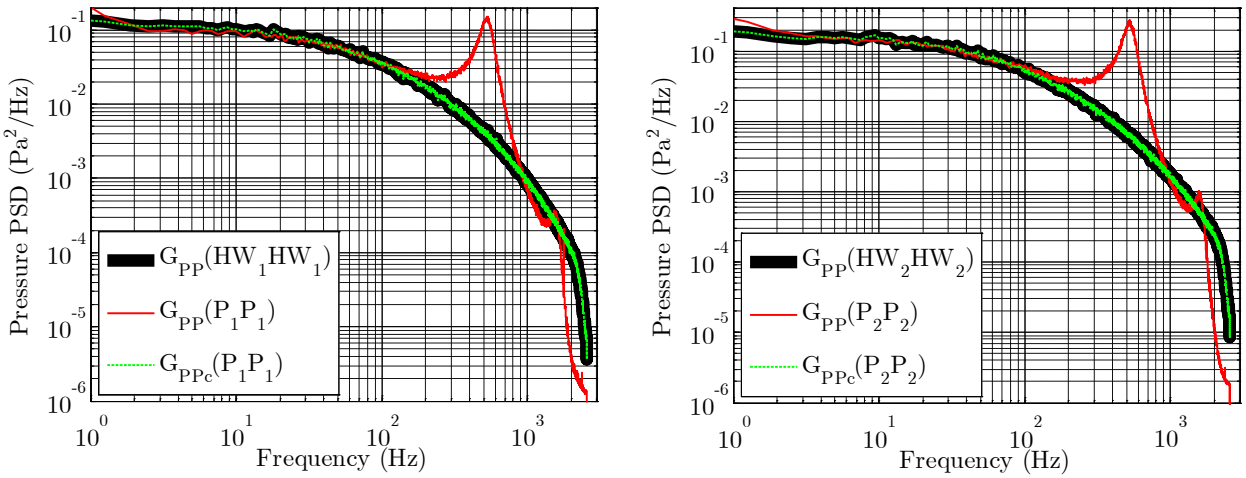

a) b)

Figure 4.11: Results showing how the inverse FRF from figure 4.10b is used to completely eliminate PSD function attenuation caused by acoustic resonance for (a) pressure probe 1 and (b) pressure probe 2.

After determining the FRF for each pressure probe, it is then possible to compensate for the effects of acoustic attenuation in each probe. Compensated PSD and CPSD functions are calculated using the following expression,

$$G_{PPc}(P_i, P_k) = G_{PP}(P_i, P_k) H_{Pi}^{-1} H_{Pk}^{-1} \qquad for \begin{cases} i = 1,2 \\ k = 1,2 \end{cases} \tag{4.18}$$

where G_{PPc} is the compensated PSD for $i = k$, and CPSD for $i \neq k$. Figure 4.11(a,b) demonstrates how the PSD function attenuations are minimized or completely eliminated using equation (4.18). Figure 4.12(a,b) demonstrates how effective the inverse FRF compensation technique is for CPSD calculations with the pressure probe measurements. Both compensated outputs from Figure 4.12(a,b) are calculated using the same set of inverse FRF functions shown in Figure 4.10b. Again, the compensated pressure CPSD appears to be unaffected by the acoustic attenuation.

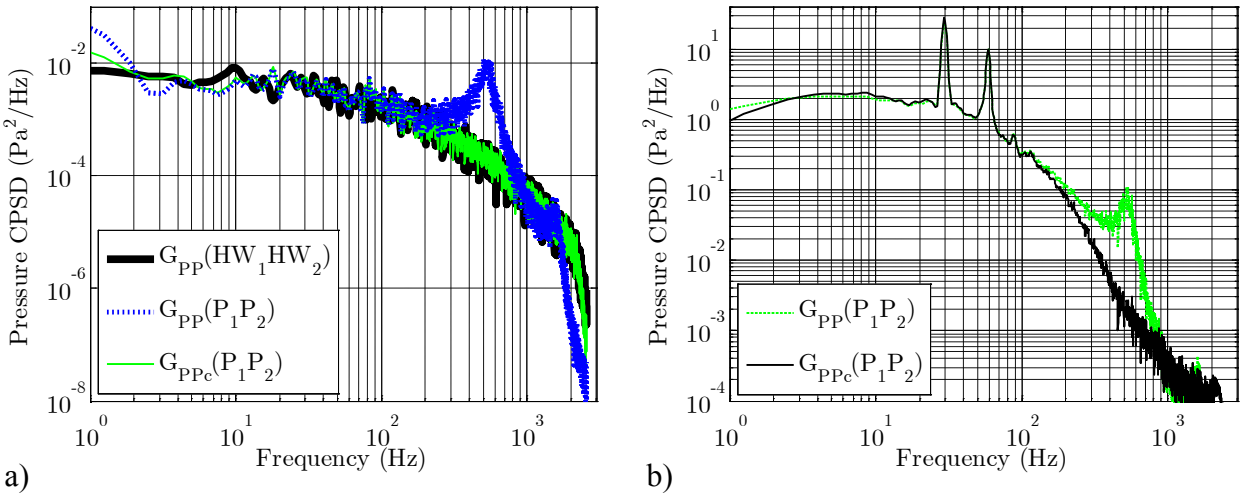

Figure 4.12: Comparisons between uncompensated and compensated CPSD functions calculated from (a) low intensity grid turbulence measurements and (b) from high intensity turbulence measurements made in the near wake of a bluff body.

All of the inverse FRF compensation results previous to (and including) Figure 4.12a have been for low intensity grid turbulence. Because all of the measurements used for the TIV modeling were made in high intensity turbulence, it was necessary to validate the inverse FRF compensation technique with high intensity turbulence measurements. Figure 4.12b shows the pressure CPSD of turbulence measured simultaneously with both pressure probes in the near wake of a bluff body.

Mean flow velocity for this test was measured with the Pitot tube and was set to approximately 10 m/s. The pressure probe tips were spaced approximately 5.72 mm apart and located 15.24 cm downstream of a rectangular bluff body measuring 4.45 cm x 4.45 cm x 10.92 cm. Results in Figure 4.12b show that the inverse FRF compensation proved to be effective even between drastically different turbulence intensities and mean velocities. Figure 4.11(a,b) and Figure 4.12(a,b) demonstrate that the dynamic calibration techniques were able to extend the pressure probe bandwidth by an order of magnitude from 100 Hz to over 1000 Hz.

4.3.4 Modeling Pressure Probe Dynamics

Extensive modeling techniques performed on various pneumatic tube and transducer configurations can be found in the literature [107,109–111]. Among the earliest of these is a model that was presented by Bergh and Tijdeman in 1965 [109]. This early model remains one of the most accurate, and was used to predict the dynamic acoustic response characteristics of both pressure probes discussed in this chapter.

Each pressure probe was treated as a series of tubes and volumes as illustrated in Figure 4.13. For modeling purposes, the probe was split into four sections. Each section was composed of a tube of radius R and length ℓ connected to a cavity having a volume V_t. The two joints where the probe tube is attached to the sensor ports are modeled as a single tube having a discontinuity in its radius; therefore, volumes V_{t1} and V_{t2} are set to zero. The open end of the static port is modeled as having a volume much larger than all other volumes. See Section 4.3.1 for more details concerning the pressure probe design and fabrication.

Table 4.2 lists the final dimensional values of the pressure probes used in the model. The transducer volume V_{t2} was provided by the manufacturer of the differential pressure transducer. Dimensions for the pressure probe ports (ℓ_2, ℓ_3, R_2, and R_3) were fixed to the design specifications of the manufacturer. Dimensions for ℓ_1, ℓ_4, R_1, and R_4 were variable design parameters used to maintain a desired bandwidth while achieving high probe sensitivity.

Bandwidth and sensitivity were two critical design criteria for the pressure probes that were maximized using the following model. It was essential that both pressure probes could accurately measure pressure fluctuations within a frequency range up to approximately 200 Hz. This range contains the first and second natural frequencies of the structures to be tested.

Table 4.2: Dimensional parameters used in the pressure probe model.

Probe Section	*Tube Length* (cm)	*Tube Radius* (mm)	*Transducer Volume* (mm^3)
Sec. #1	$\ell_1 = 6.858$	$R_1 = 0.749$	$V_{t1} = 0$
Sec. #2	$\ell_2 = 1.397$	$R_2 = 0.711$	$V_{t2} = 112$
Sec. #3	$\ell_3 = 1.397$	$R_3 = 0.711$	$V_{t3} = 0$
Sec. #4	$\ell_4 = 6.350$	$R_4 = 0.749$	$V_{t4} \Rightarrow \infty$

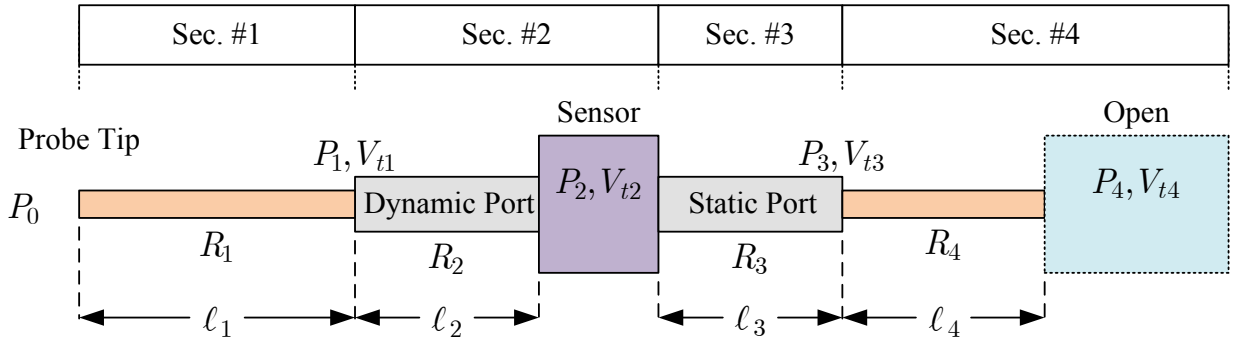

Figure 4.13: Schematic defining terms used for the pressure probe model.

The bandwidth limit was set based on preliminary experimental results that showed no significant structural displacement amplitudes were present from the third mode and higher. With bandwidth requirements determined, design efforts were then focused on maximizing sensitivity. As probe diameter increases, sensitivity increases, and bandwidth decreases. Bandwidth also decreases with increased probe length. Therefore, the probe length was fixed, while the diameter was increased until the uncompensated bandwidth fell to its lowest allowable limit (~200 Hz) thus maximizing sensitivity.

The model developed by Bergh and Tijdeman is a recursion formula that relates the fluctuating pressure in one volume V_{ti} to that of the adjacent volumes $V_{t(i-1)}$ and $V_{t(i+1)}$ [109]. Pressure fluctuations are assumed to be sinusoidal having the following form,

$$\overline{P} = P_s + Pe^{j\omega t} \tag{4.19}$$

where $\overline{P}$ is the total pressure, P_s is the static pressure, P is the fluctuating pressure, ω is angular frequency in rad/sec, and t is time in seconds. The ratio between the amplitude of fluctuating pressure in two adjacent volumes can be given as,

$$\begin{aligned}\frac{P_i}{P_{i-1}} = \Bigg\{ & \cosh(\xi_i \ell_i) + \sinh(\xi_i \ell_i) \frac{n_{ti} \xi_i V_{ti}}{\pi R_i^2} \left(\sigma_i + \frac{1}{n_{vi}} \right) \\ & + \frac{R_{i+1}^2 \xi_{i+1} \Gamma_0(\tilde{\alpha}_i) \Gamma_2(\tilde{\alpha}_{i+1})}{R_i^2 \xi_i \Gamma_0(\tilde{\alpha}_{i+1}) \Gamma_2(\tilde{\alpha}_i)} \frac{\sinh(\xi_i \ell_i)}{\sinh(\xi_{i+1} \ell_{i+1})} \left[\cosh(\xi_{i+1} \ell_{i+1}) - \frac{P_{i+1}}{P_i} \right] \Bigg\}^{-1}\end{aligned} \tag{4.20}$$

where P is the transducer volume pressure, ℓ is the tube segment length, V_t is the transducer volume, R is the tube radius, σ is the ratio of transducer volume increase due to diaphragm deflection, n_v is the polytropic expansion factor of the fluid inside the transducer volume, Γ_0 and Γ_2 are *zeroth* and second order Bessel functions of the first kind respectively, n_t is the polytropic expansion factor of the fluid within the tube, $\tilde{\alpha}$ is the so called shear wave number, and ξ is a dissipation function representing the heat transfer due to fluid friction within the probe. The shear wave number is defined as,

$$\tilde{\alpha}_i = jR_i \sqrt{\frac{j\omega\rho_a}{\mu_a}} \tag{4.21}$$

where j is an imaginary number, ρ_a and μ_a are the mean density and dynamic viscosity (respectively) of the fluid being measured, and ω is angular frequency at which the fluid within the probe oscillates. The dissipation function can be given as,

$$\xi_i = \frac{\omega}{c_a}\sqrt{\frac{\tilde{\gamma}}{n_{ti}}\frac{\Gamma_0(\tilde{\alpha}_i)}{\Gamma_2(\tilde{\alpha}_i)}} \tag{4.22}$$

where c_a and $\tilde{\gamma}$ are the velocity of sound and the ratio of specific heats (respectively) of the fluid being measured. The polytropic expansion factor of the air within each tube segment is defined as,

$$n_{ti} = \left[1 + \frac{\tilde{\gamma}-1}{\tilde{\gamma}}\frac{\Gamma_2(\tilde{\alpha}_i\sqrt{\mathrm{Pr}})}{\Gamma_0(\tilde{\alpha}_i\sqrt{\mathrm{Pr}})}\right]^{-1} \tag{4.23}$$

where Pr is the Prandtl number which is a dimensionless number that represents a ratio of momentum and thermal diffusivity of the fluid being measured by the pressure probe. The Prandtl number can be calculated using the following expression,

$$\mathrm{Pr} = \frac{\mu_a C_{hp}}{\lambda_t} \tag{4.24}$$

where μ_a is the dynamic viscosity, C_{hp} is the specific heat at constant pressure, and λ_t is the thermal conductivity [112]. The fluid properties used in equations (4.21) through (4.24) are provided in Table 4.3.

Table 4.3: Properties of air used in the pressure probe model.

Property	*Symbol*	*Value*	*Unit(s)*
Temperature	T_a	293	K
Atmospheric Pressure	P_a	100.9	kPa
Polytropic constant[3] [106]	n_v	1.4	
Ratio of specific heats[6] [106]	$\tilde{\gamma}$	1.4	
Gas Constant [106]	R_a	287	J kg^{-1} K^{-1}
Specific Heat at Constant Pressure [106]	C_{hp}	1.005	kJ kg^{-1} K^{-1}
Thermal Conductivity [112]	λ_t	25.7	kW m^{-1} K^{-1}
Absolute (Dynamic) Viscosity [113]	μ_a	1.814×10^{-5}	kg m^{-1} s^{-1}
Prandtl Number	Pr	0.7094	
Density	ρ_a	1.2	kg m^{-3}
Speed of Sound	c_a	343.1	m s^{-1}

Figure 4.14 shows all analytical FRFs between adjacent volumes within the pressure probe. Notice that since $V_{t4} \Rightarrow \infty$ the FRF between the static opening P_4 and the static port junction pressure P_3 goes to zero, i.e. $P_4 / P_3 \Rightarrow 0$. The bold solid line in Figure 4.14 is the FRF between the pressure inside the transducer P_2 and the measured dynamic pressure P_0 which was calculated using the following relationship.

$$\frac{P_2}{P_0} = \frac{P_2}{P_1}\frac{P_1}{P_0} \tag{4.25}$$

[6] Note that in this case $k = \gamma$ thus the system is assumed to behave as an isentropic process.

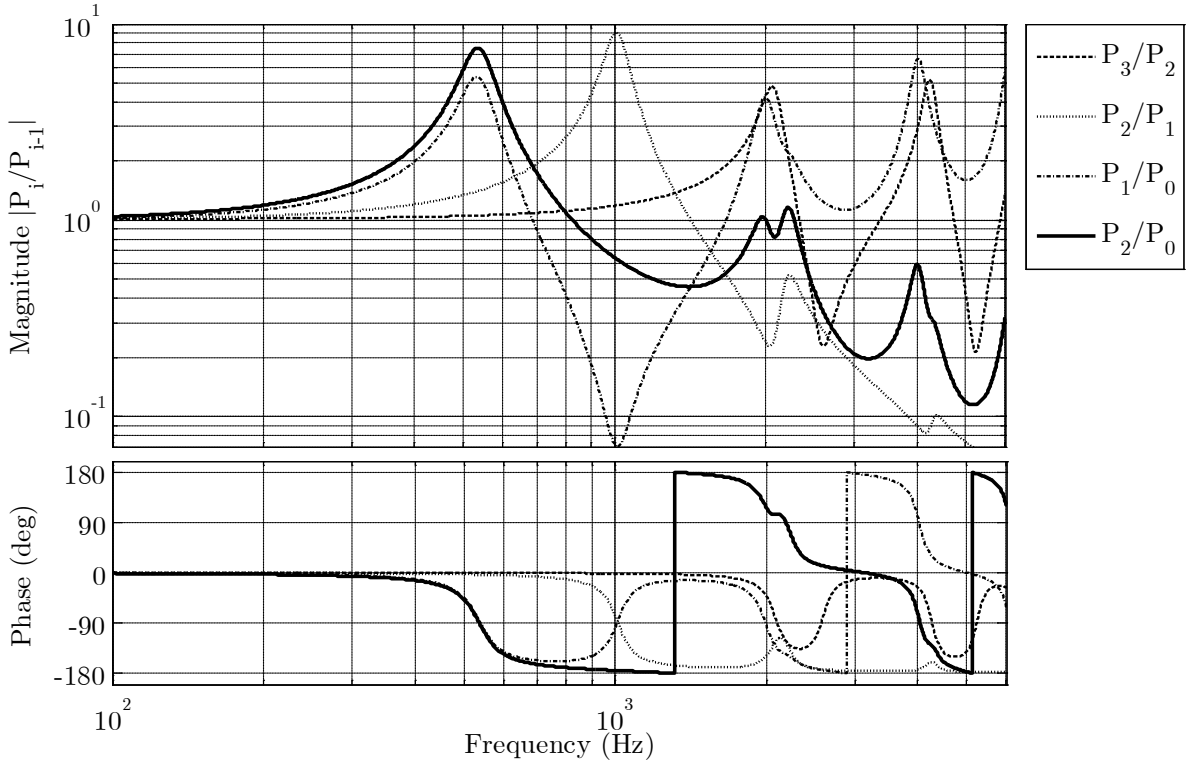

Figure 4.14: Analytical transfer functions between all adjacent tubes and volumes within the pressure probe.

All results in Figure 4.14 are coupled according to equation (4.20) such that P_2/P_1 is a function of P_3/P_2, and P_1/P_0 is a function of P_2/P_1. The FRF in equation (4.25) is of particular interest because it is directly proportional to the FRF between sensor voltage output and the measured dynamic pressure P_0.

Figure 4.15 shows the normalized FRF for P_2/P_0 calculated from the analytical model compared to the measured FRF calculated with equation (4.17) first shown in Figure 4.10b. Results of the model shown in Figure 4.15 demonstrate good agreement between measurement and theory. These results also show that the desired bandwidth of 200 Hz was successfully attained.

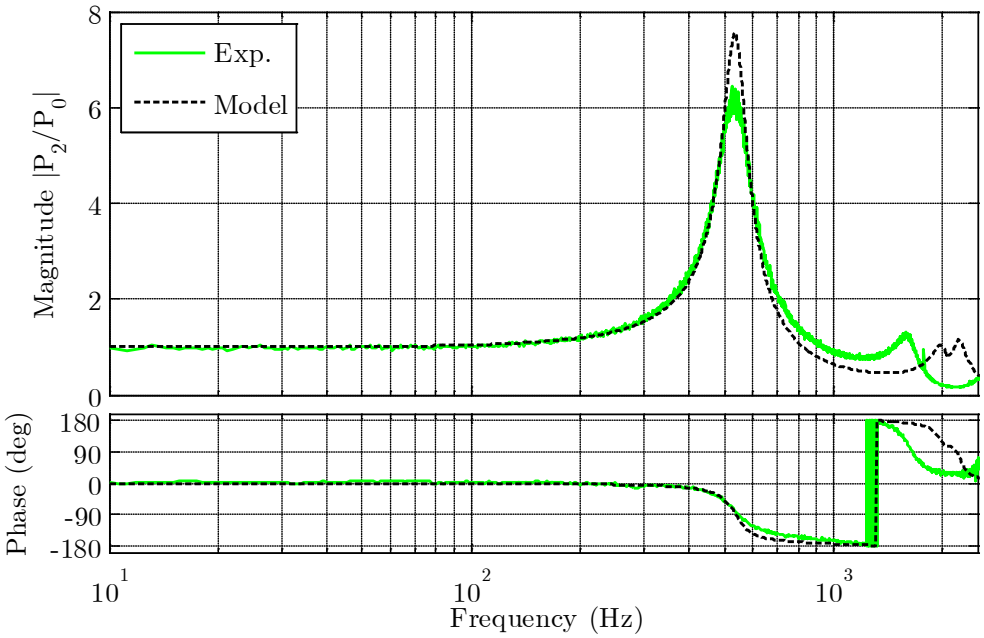

Figure 4.15: Experimental and theoretical results of the dynamic response characteristics for both pressure probes showing acoustic attenuation and phase distortion between measured pressure P_0 and sensor pressure P_2.

The model was able to predict the first acoustic resonance mode very well; however, significant error accumulated as frequency increased. Error between measurement and theory is most likely attributed to the model being unable to account for unknown geometries within the transducer and imperfect junctions between the sensor ports and probe tubes.

4.4 Case Studies & Model Validation

Both the measurement techniques and the turbulence-induced vibration model were experimentally validated by performing three single-cantilever case studies. Procedures and results of these studies are presented in this section.

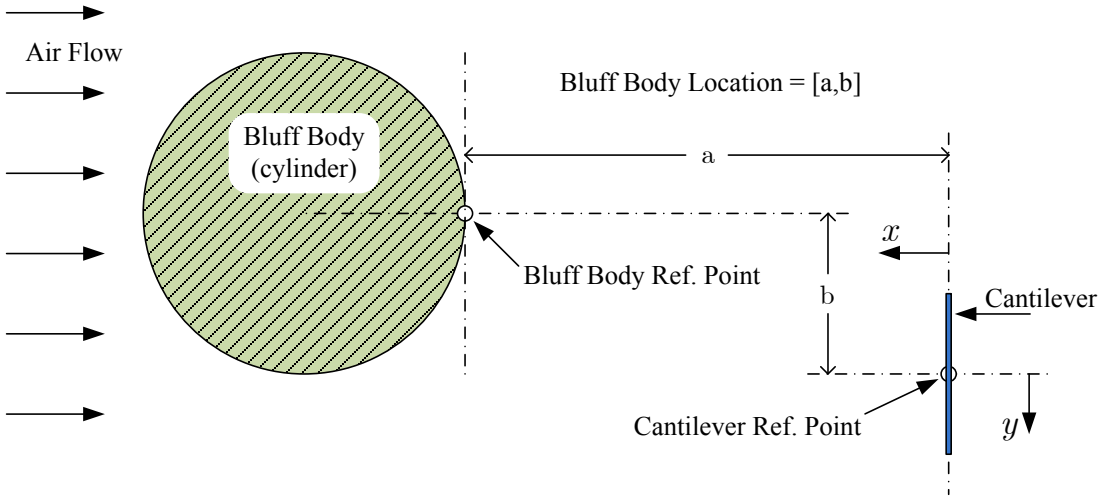

Figure 4.16: Schematic showing the layout, coordinate system, and relevant dimensions of the single cantilever case study experiments (top view).

4.4.1 Experimental Setup

Turbulent flow for all three case studies was generated by placing a bluff body immediately upstream of the cantilever to be analyzed. The bluff body used in the three case studies had a cylindrical cross section with a radius of 4.83 cm and a height of 14.21 cm. The center of the cantilever was both the system origin and cantilever reference point, while the reference point of the bluff body was the edge or face nearest the cantilever. Figure 4.16 illustrates the reference points for both the cantilever and bluff body, and also shows the bluff body location relative to the cantilever.

The layout shown in Figure 4.16 was used for all three case study experiments where dimensions a and b were fixed at 15.24 cm and 2.54 cm respectively. Average flow velocity for all tests was measured with a pitot tube and was fixed at approximately 10 m/s.

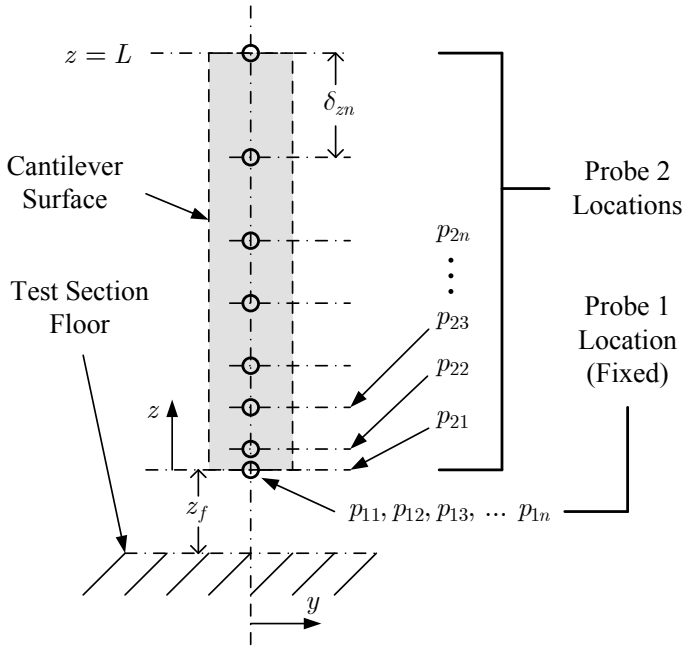

Figure 4.17: Schematic of pressure probe measurement locations relative to the cantilever surface.

4.4.2 Turbulence Measurement Results

Flow near the cantilever contained large vortices that shed off the sides and over the top of the bluff body. Because the turbulence was not homogeneous, both temporal and spatial information had to be measured in order to accurately represent the turbulence spectra over the length of the cantilever. The goal of these pressure probe measurements was to create a statistical profile of the turbulence as a function of both space and frequency. After the turbulence profile was computed, the modal turbulence-induced force exerted on the cantilever could be predicted. The modal forcing function was then applied to the cantilever, and the displacement PSD was calculated using the full model given in equation (4.14).

Without a cantilever in the test section, pairs of pressure probe measurements were made at the origin (i.e. the cantilever reference point in Figure 4.16) spaced vertically along the z-axis in

turbulent flow having a constant mean velocity of 10 m/s. Figure 4.17 illustrates the pressure probe measurement locations relative to where the cantilever would later be positioned.

Each pressure probe was powered with 16 VDC and had an output range of $\pm$16mV providing a pressure sensitivity of 0.064 mV/Pa (Recall Table 4.1). Siglab data acquisition hardware was used to simultaneously power the sensors and measure their output. The time series voltage output from each probe was sampled at 5.12 kHz with a sample size of 2^{21} samples. The duration of each test was approximately seven minutes. At the end of each test, probe-2 was repositioned and the procedure was repeated at a total of 17 locations along the *z*-axis. After the pressure probe measurements were made, the flow conditions were maintained while the probes were removed and a cantilever was placed at the origin. A laser displacement sensor (Micro-Epsilon model ILD 1800-200) was used to measure cantilever tip deflection. The laser sensor had a profile comparable to that of the cantilever and was positioned approximately 25 cm downstream of the test specimen to minimize or eliminate any aerodynamic effects the sensor might have on the beam.

Data from these measurements was processed using the statistical modeling techniques discussed in Section 3.1.1. Pressure probe measurements from these case studies yield the pressure CPSD and coherence functions shown in Figure 4.18 a and b respectively. The pressure coherence function can be considered as a type of normalized CPSD function and is defined as,

$$C_{op}(z, z', \omega) = \frac{S_p(z, z', \omega)}{S_p(z, \omega)} \tag{4.26}$$

which can more simply be considered as the CPSD normalized by the PSD. Probe separation on the y-axis in Figure 4.18(a,b) corresponds directly to the probe locations illustrated in Figure 4.17.

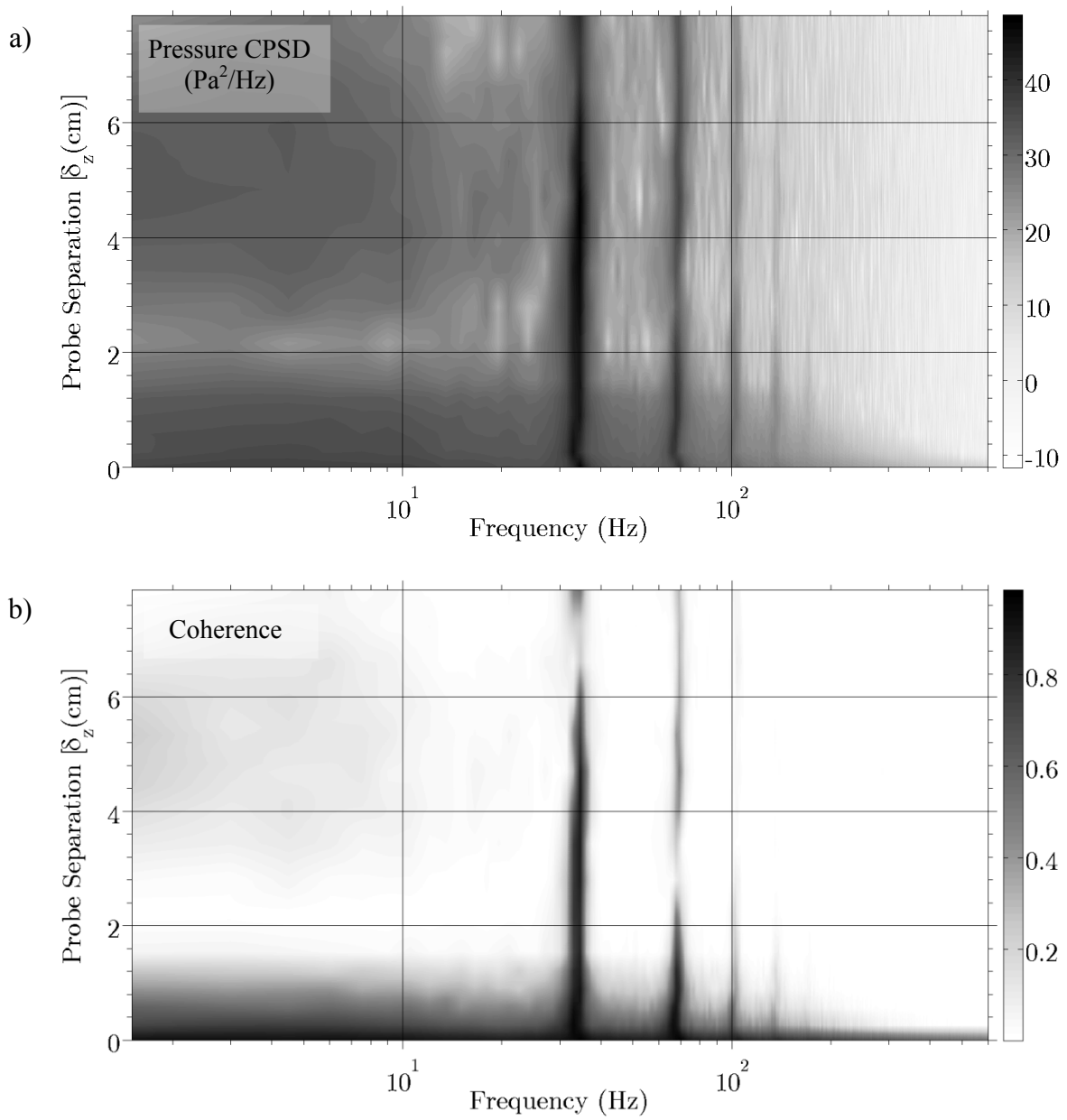

Figure 4.18: Results from pressure probe measurements showing profiles of (a) pressure CPSD and (b) pressure coherence functions.

As expected, the coherence decreases exponentially with increased separation distance. Notice that four prominent frequencies exist in Figure 4.18(a,b). The first and strongest peak occurs at 33.7 Hz and the following three occur at the second, third, and fourth multiples of the first, while steadily decaying in amplitude. All four frequencies appear as dark vertical bands in

both the CPSD and coherence plots of Figure 4.18(a,b). The first dark vertical band is clearly located at the primary (or *first mode*) vortex shedding frequency of the bluff body. This first frequency can easily be estimated with the well-known Strouhal vortex shedding equation given as,

$$f_v = \frac{StU}{L_c} \tag{4.27}$$

where f_v is the vortex shedding frequency in Hz, U is the free-stream velocity past the bluff body, L_c is the characteristic length of the bluff body, and St is known as the Strouhal Number. The higher multiples of the Strouhal frequency are caused when a single vortex shedding off of the bluff body intermittently splits into a pair of vortices. This causes the bluff body wake to contain a combination of single and double vortices. This type of vortex shedding behavior has been well documented by Williamson *et al* [38,39], and is to be expected in high Reynolds number flow such as that in the case studies presented here.

4.4.3 Model Validation

The three case studies discussed in this section were performed to experimentally validate the full turbulence-induced vibration model and the turbulence measurement technique discussed in Section 4.4.2. Three types of beam designs having similar geometries were used for the case study. Table 4.4 summarizes the beam design parameters along with experimental measurements and theoretical predictions of their first two natural frequencies. The elastic beam had uniform material properties while the unimorph and bimorph beams had properties that varied along their length due to QuickPack™ QP10n bonded at the root of each cantilever. Natural frequencies and mode shapes for all three beam types were calculated using a Rayleigh-Ritz model approach.

Table 4.4: Design parameters and modal analysis results of the cantilevers used in the current case studies.

Type	*Dimensions*			*Natural Frequency* (Hz)				*% Error*	
	Length (cm)	Width (cm)	Thick. (mm)	f_1	$f_{1.\exp}$	f_2	$f_{2.\exp}$	f_1	f_2
Elastic	8.814	2.548	0.241	25.6	25.6	161.1	160.0	0.03%	0.69%
Unimorph	9.525	2.548	0.241	41.5	41.9	174.9	175.6	-1.00%	-0.41%
Bimorph	9.525	2.548	0.241	51.3	51.9	198.3	193.8	-1.12%	2.32%

The acceptance integrals were calculated for the first three modes of vibration using the pressure coherence profile shown in Figure 4.18b in conjunction with equation (4.9). Plots of these acceptance integrals are shown in Figure 4.19. As expected, the acceptance associated with the first bending mode of the cantilever (J_{11}) was the largest. Notice that the first mode joint acceptance in Figure 4.19 approaches its maximum theoretical value of 0.6 as shown in Figure 4.2.

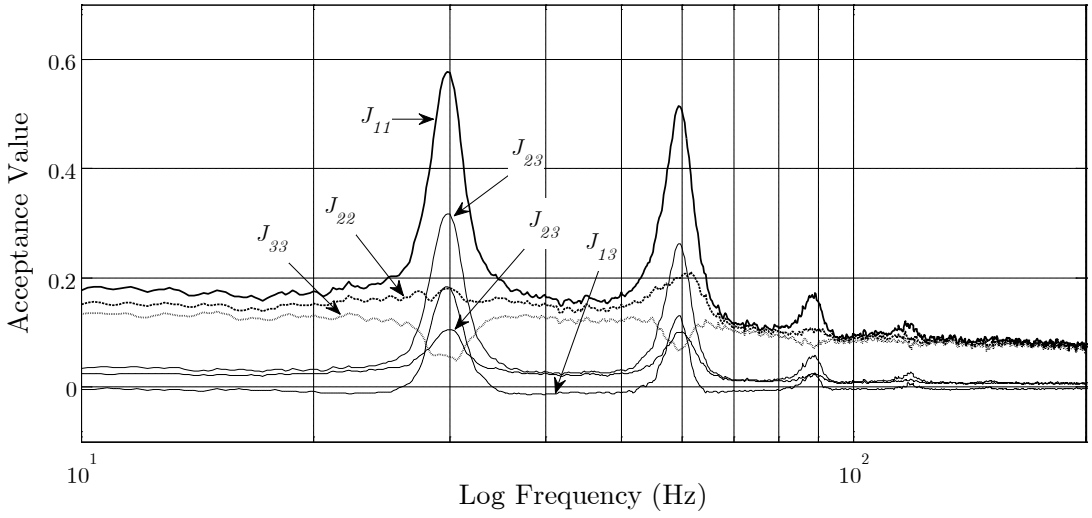

Figure 4.19: Joint and cross-acceptance values calculated from pressure probe data used for formulating a turbulence-induced modal forcing function.

Table 4.5: Experimental measurements compared to model predictions for RMS tip displacement of the beams.

Beam Design	*Load Resistance* (kΩ)	*Capacitance* (nF)	*RMS Tip Deflection* (mm)		*Error* (%)
			Model	Exp.	
Elastic	-	-	1.312	1.313	-0.05%
Unimorph	39.90	123.0	0.570	0.566	0.74%
Bimorph	29.49	251.5	0.338	0.337	0.14%

The three cantilevers were designed such that their fundamental mode frequencies and complex response functions were significantly different from each other and from the primary vortex shedding frequency within the turbulent flow spectrum. By separating these known frequencies of interest, the model's ability to capture both fluid forcing effects and structural dynamics could be demonstrated. Results of the tip displacement PSD shown in Figure 4.20 and RMS tip displacement listed in Table 4.5 show very good agreement between model predictions and experimental measurements.

The unimorph and bimorph tip deflection results listed in Table 4.5 were measured and calculated for a load resistance of $39.90\,\mathrm{k}\Omega$ and $29.49\ \mathrm{k}\Omega$ respectively. The bimorph electrodes were wired in a parallel configuration. The greatest errors were seen for the unimorph and bimorph beams. The majority of these errors can be attributed to uncertainty in material properties and thicknesses. Errors may also be caused by imperfectly bonded layers including un-bonded areas and non-uniform adhesive thickness. More details concerning the construction of the unimorph beam can be found in Chapter 3.

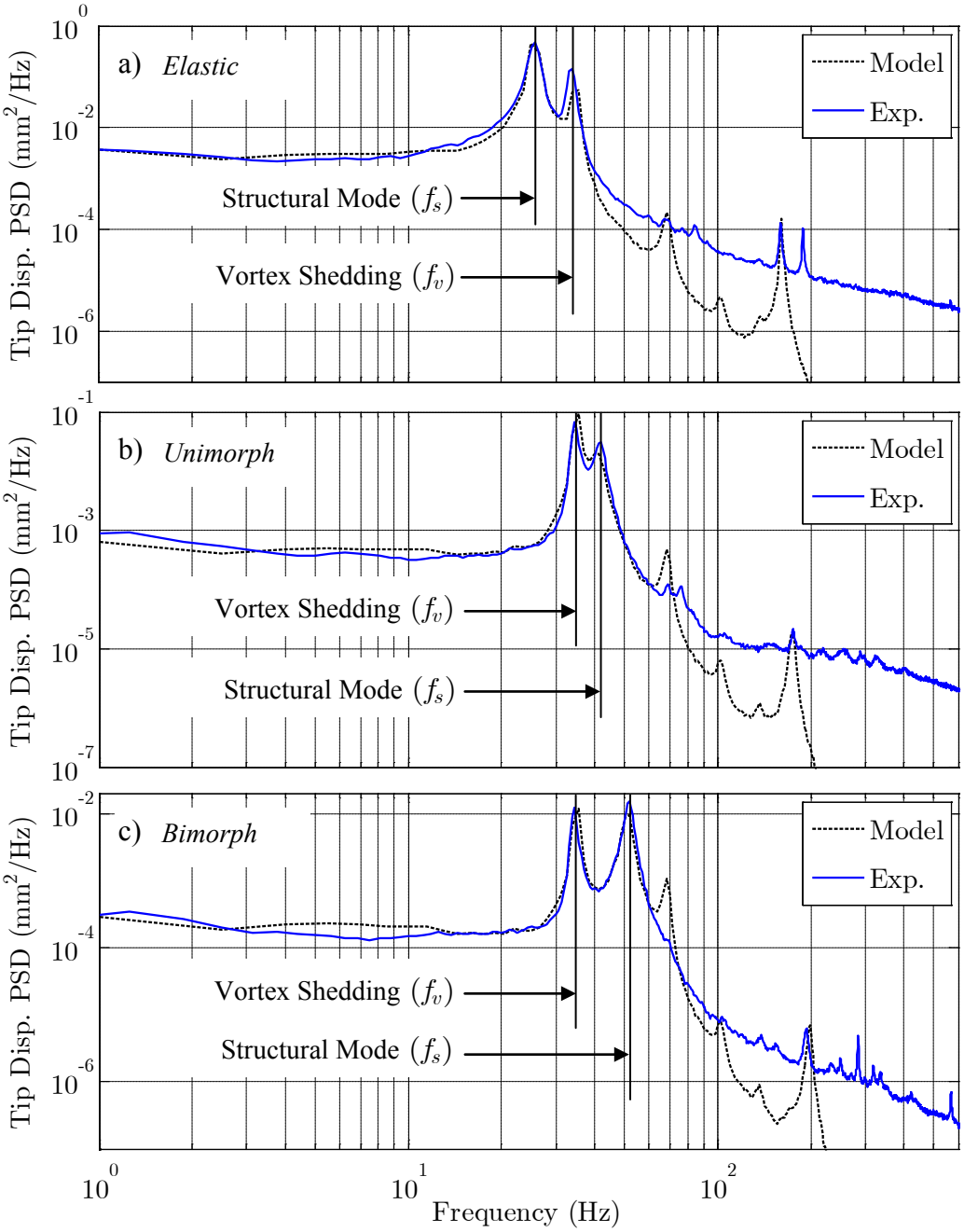

Figure 4.20: Tip displacement PSD functions comparing model results to experimental measurements for the (a) elastic, (b) unimorph, and (c) bimorph beam types.

Pressure coherence and PSD are two forms of the turbulence profile produced from spectral analysis of the pressure probe data (See Figure 4.18.). Applying slightly different forms of the full model, nearly identical displacement PSD results can be achieved by using either the coherence function or the pressure PSD function. The results shown in Figure 4.20 were produced using the pressure coherence function. The first and second peaks of the elastic case are associated with the first mode of the cantilever and the primary vortex shedding frequency respectively. The opposite is true for case-2. The primary vortex shedding frequency is 33.7 Hz.

4.4.4 Error Analysis of Turbulence Measurement Method

Recall that 17 pairs of pressure probe measurements were made in order to calculate the pressure profiles given in Figure 4.18(a,b). These measurements were ultimately used to predict the tip displacement of three types of cantilever beams. The results of these predictions are summarized in Table 4.5. An error analysis was performed to investigate the effect of the quantity and location of pressure probe measurements on the accuracy of beam displacement predictions.

Two error analysis case studies were performed. In each case, the number of total probe measurements was increased from 2 to 18. For each set of probe locations the tip displacement of a cantilever beam was calculated following the steps discussed in section 2.1. Error between the measured displacement and predicted displacement was then calculated and plotted. The results of these two case studies are shown in Figure 4.21 and Figure 4.22. The cantilever beam used in these error analysis case studies was the same elastic cantilever beam discussed in section 4.4.3.

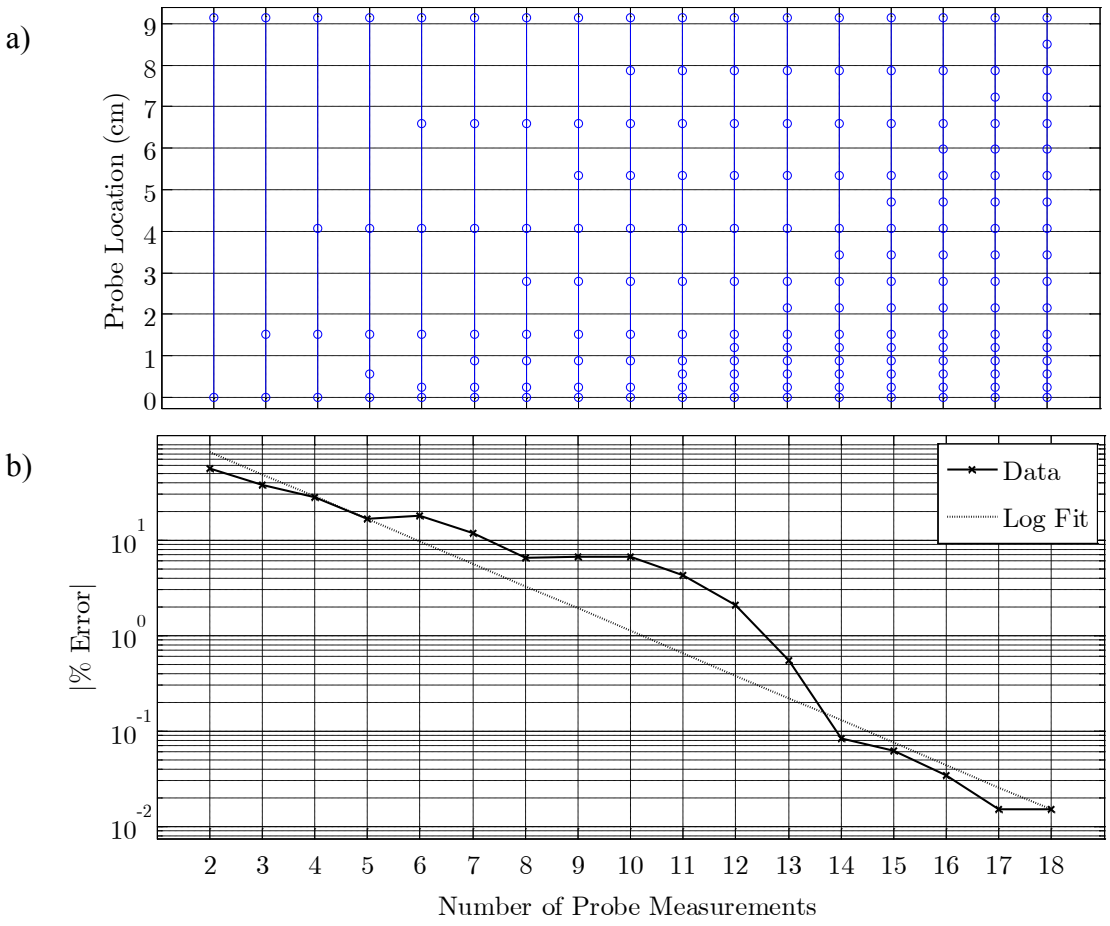

Figure 4.21: Case 1 error analysis results showing (a) pressure probe locations and (b) percent error of tip deflection estimate.

Figure 4.17 and Section 4.4.2 provide a more detailed explanation of how the probe locations are represented in Figure 4.21a and in Figure 4.22a. Note that the probe locations are measured in the positive z direction where 0 cm is located at the clamped base of the cantilever. The probe locations for case 1 (Figure 4.21a) were systematically added such that a more even distribution across the beam length was achieved. In case 2, the probe locations were incrementally added starting at the base of the cantilever and working toward the tip as shown in Figure 4.22b.

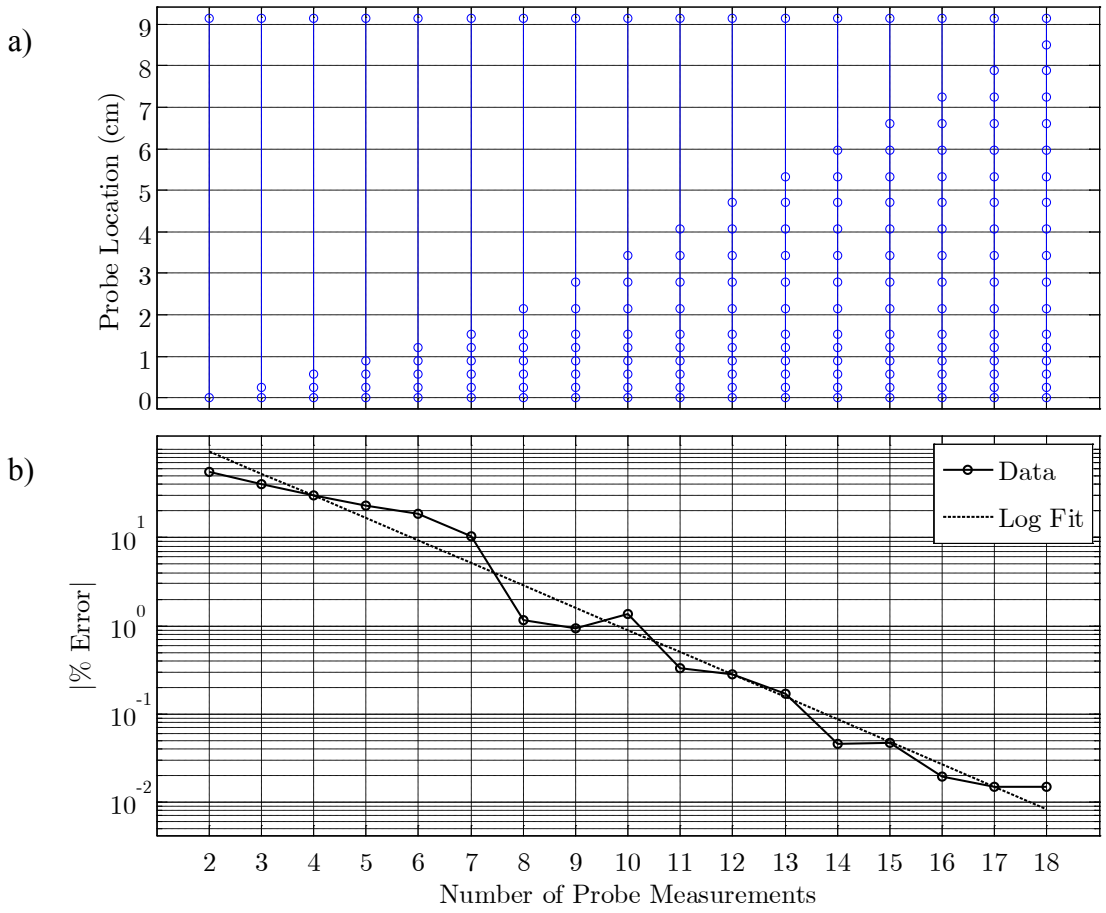

Figure 4.22: Case 2 error analysis results showing (a) pressure probe locations and (b) percent error of tip deflection estimate.

Using the probe locations from case 2 shown in Figure 4.22a one can see from Figure 4.22b that the error was kept below 2% with as few as 8 probe measurements. In Figure 4.21b it can be seen that this same 2% error was not achieved until 12 probe measurements were made. This brief error analysis study shows that a significant amount of time, effort, and computational cost can be saved by taking fewer measurements closer together rather than many measurements spread further apart. If many turbulence profiles are going to be measured, then a more in-depth error analysis should be conducted.

4.5 Chapter Summary

The modeling and turbulence measurement techniques presented in this chapter are shown to be quite effective at predicting turbulence-induced vibration. Pressure probes were designed and constructed such that they were able to measure turbulent air flow with a full pressure range of ± 249 Pa and a sensitivity of 0.064 mV/Pa. The probes had an uncompensated bandwidth of approximately 100 Hz until the first acoustic resonance mode caused significant attenuation. An inverse FRF compensation technique was successfully employed and was shown to extend the probe bandwidth by an order of magnitude from 100 Hz to over 1000 Hz. Successful modeling and calibration methods were applied to the pressure probes to ensure reliable measurements even in highly turbulent air flow with a mean velocity range of only (0-12 m/s). Results of three case studies showed that the turbulence-induced vibration predictions agreed well with those measured in experiments. The largest error associated with predicting RMS tip deflection was found to be 0.74% for the unimorph beam design.

CHAPTER V

ENERGY HARVESTING FROM LARGE ARRAYS OF FLEXIBLE STRUCTURES

The primary driving mechanism for most flow-induced vibration energy harvesting devices can be categorized as either vortex-induced vibration [2,13,40], or aerodynamic flutter [17,51,55]. There are many circumstances where conditions necessary for the onset of vortex-induced vibration or flutter cannot be met; however, turbulence-induced vibration is practically unavoidable in most situations were dynamic fluid is in contact with an elastic structure.

In this chapter the author will discuss the design and experimental analysis of a robust, lightweight, energy harvester to be used in turbulent fluid flow environments such as small rivers, tidal currents, or air ventilation systems. Applications for such a device include powering remote sensor networks for structural health monitoring, environmental monitoring, or surveillance. In recent work the authors showed that properly designed structures made with piezoelectric materials can produce a significant amount of useful power from turbulence-induced vibration [60,114]. Until now, the focus of these previous efforts has been limited to only a single structure or small arrays containing up to 6 elements.

Turbulent flows in crops and natural vegetation is of great interest, particularly to the agricultural and environmental science communities. Models which help explain the fluid-

structure interaction that occurs in vegetated environments have been discussed extensively in the literature. The studies that are most applicable to the work presented in this paper are those dealing with the mechanics of waving wheat or grass. It will be shown that the documented response of waving wheat is very similar to that observed from experiments performed in a wind tunnel on arrays of cantilever beams. It will also be shown that an empirical model proposed by Finnigan in 1979 was able to predict the flow velocity required to cause large amplitude vibrations in the cantilever arrays [115].

5.1 Modeling Strategy

In recent work the authors developed an energy harvesting model for predicting the frequency response and power output of a single unimorph cantilever in turbulent cross-flow [60,114]. One of the most challenging aspects of modeling turbulence-induced vibration energy harvesting is developing the fluid forcing function. For the case of a single cantilever or simple structure, one can use pressure probe measurements to make spatiotemporal turbulence profiles that can be used to very accurately predict the structural response [79]. While the modeling techniques in [60,79,114] provide accurate predictions, they are limited to single structure cases and are not suitable for large array dynamics.

5.1.1 Biological Inspiration

An empirical relationship developed by Finnigan (1979) showed that the periodicity of large-scale coherent structures traveling across the top of waving wheat was approximately 5*L* to 8*L,* where *L* is the wheat height i.e., the array element length [115]. Finnigan also showed that these vortex structures could be as wide as several *L* and travel at a rate of approximately $2\overline{U}$, where $\overline{U}$ is the mean free-stream flow velocity.

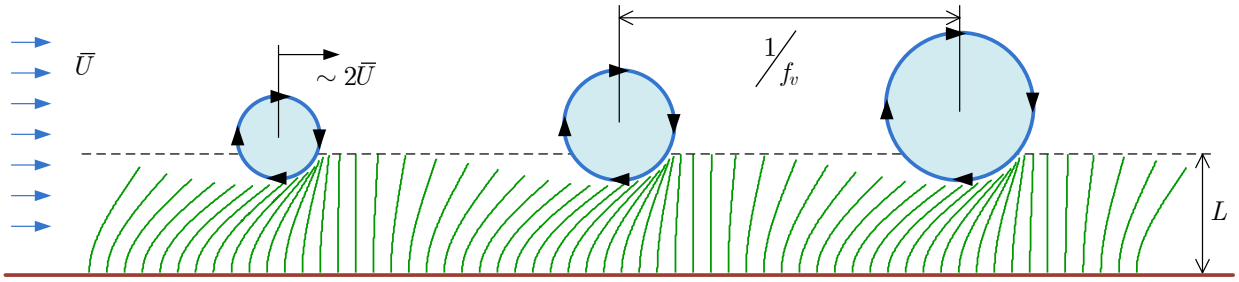

Figure 5.1: Illustration of a cantilever array in fluid flow showing the formation of vortices and how the fluid-structure interaction of the passing vortices causes wave-like motions to form in the array.

Vortices pass over the array at a frequency proportional to flow velocity called the *vortex passing frequency* (f_v) as illustrated in figure 5.1. When these vortices pass over the array at a frequency near the fundamental frequency of the array elements, persistent large amplitude vibrations occur. Because the flow-induced forcing function is traveling across the array at a relatively constant velocity, all array elements are slightly out of phase from their nearest streamwise neighbor. This phase shift gives the array a waving appearance which can be observed in fields of wheat or grass on a windy day. This waving phenomenon (termed 'honami') was first studied and documented by Inoua in 1955 [116].

5.1.2 Proposed Modeling Approach

From the previously mentioned relationships provided by Finnigan and illustrated in Figure 5.1, one can predict the mean flow velocity required to produce large amplitude vibrations of the array elements. Because the current study focuses on the design of an energy harvester, it may be most useful to use the following expression,

$$\omega_v = 2\pi\left(\frac{\bar{U}k_v}{L}\right) \qquad for \qquad k_v = \left(0.25 \;\; to \;\; 0.4\right) \tag{5.1}$$

where ω_v is the vortex passing frequency in rad/s, and k_v represents an experimentally determined coefficient which provides upper and lower bounds of the vortex passing frequency at a given mean flow velocity $\overline{U}$. Because the waving, large amplitude vibrations in the array are a result of array elements being forced into a resonance condition, it is important that all cantilevers in the array have the same fundamental frequency as well as the same length. The energy harvester can therefore be modeled as an array of identical cantilevers all having a length *L* and a fundamental frequency ω_1. For a given application in an environment where the average air velocity is known, a harvester can easily be designed such that its fundamental frequency matches the vortex passing frequency *i.e.*, $\omega_1 = \omega_v$.

Total power output of the harvester array, of course, depends not only on frequency, but also on amplitude of the element vibrations. Predicting the amplitude of vibration for a waving array of cantilevers requires a model that describes the force exerted by the flowing fluid on the cantilevers. Equation (5.1) provides an estimate for frequency but not the magnitude of the fluid forcing function. Details concerning the portion of the model used to estimate this force magnitude will not be presented at this time.

5.2 Initial Experimental Analysis

A brief experimental analysis was performed on a large array harvester prototype for observation and proof of concept design. The harvester array discussed in this paper will serve as a platform for future experimental studies and model validation. This section presents details concerning the harvester array design, and experiments conducted in the current study.

Table 5.1: Array Element Design Parameters

Element Type	*Layer*	*Material*	*Length* (mm)	*Width* (mm)	*Thickness* (μm)	*Fundamental Mode* (Hz)
Passive	Substrate	Steel	304.80	25.40	254	1.95
Active	Substrate	Steel	304.80	25.40	254	2.60
	Active layer	PZT	45.97	20.57	508	

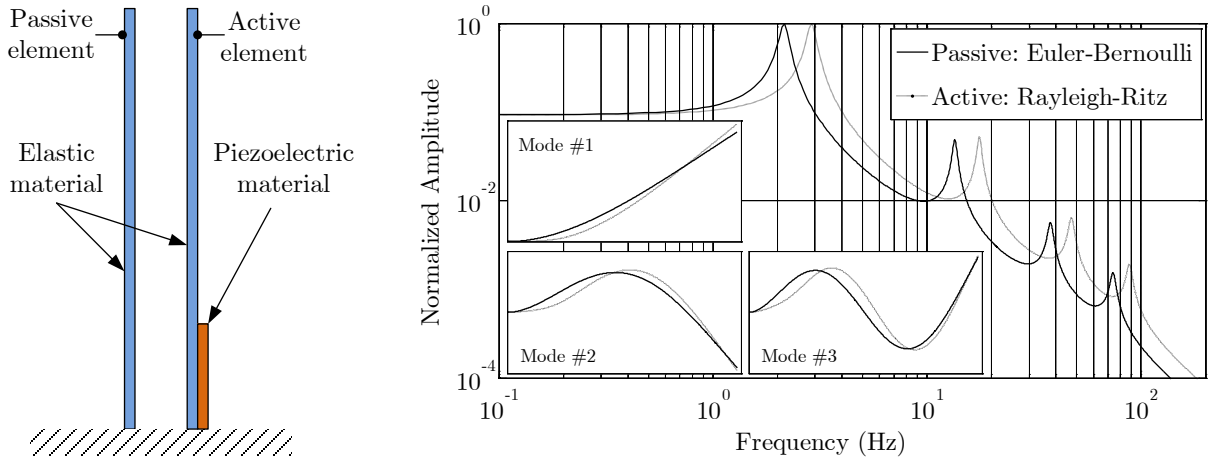

Figure 5.2: Sketch of passive and active array element types used in this study with accompanying plots comparing their frequency response functions and mode shapes.

5.2.1 Array Design

Two types of array elements used in this study are referred to as *passive* and *active*. The passive elements were modeled as uniform cantilevers, and the active elements were modeled as unimorph cantilevers having a patch of piezoelectric material bonded to them as show in the sketch in Figure 5.2. Dynamic response characteristics of both element types were estimated using a distributed parameter, Euler-Bernoulli beam model for passive elements and a Rayleigh-Ritz analytical approximation for active elements.

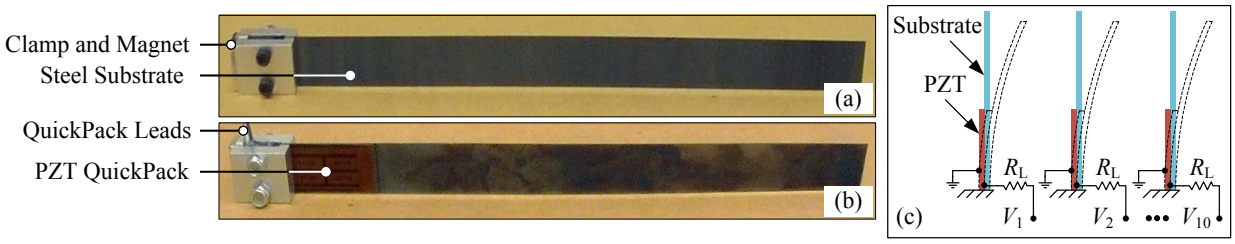

Figure 5.3: Photo of (a) passive and (b) active array elements along with (c) a schematic illustrating electrical circuit connectivity details for the active elements.

The Rayleigh-Ritz approach was necessary because the section of beam bonded to piezoelectric material had significantly greater mass and stiffness than the rest of the beam. A comparison of the frequency response and mode shapes for both element types is shown in Figure 5.2.

The harvester array consisted of up to 112 individual elements. Each element had a grade N42, nickel plated, neodymium magnet from K&J Magnetics (part #BX082) built into its base to provide secure and completely variable element placement. Two types of array elements classified as *passive* and *active* were designed and built for this study. The active elements were piezoelectric unimorph cantilevers constructed by mounting a PZT wafer QuickPack™ from Mide Technology Corp. (model QP10n) to the root of one side of a spring steel cantilever. The passive elements were basic spring steel cantilevers. See Table 5.1 for design parameters of both element types. Photos of the two element types are shown in Figure 5.3(a,b).

In this study, only three array configurations were considered. The first (type-1) had no bluff body and a uniform grid of 14 elements in the x direction with 7.62 cm spacing and 8 elements in the y direction with 5.08 cm spacing. The second (type-2) was the same as type-1 but a bluff body was added 30.48 cm upstream of the array as shown in Figure 5.4a.

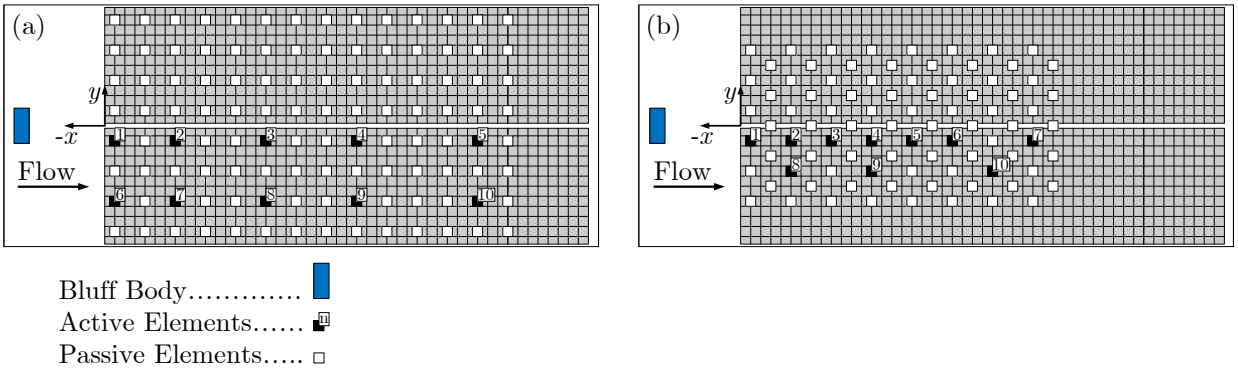

Figure 5.4: Schematics of both the (a) type-2 array and (b) type-3 array drawn to scale showing the bluff body placement and the location of all active elements. The type-1 array had the same element placement as shown in (a) except the bluff body was removed.

Finally, the third configuration (type-3) was a staggered array with 16 elements in the *x* direction, 11 elements in the *y* direction, and a bluff body 30.48 cm upstream as shown in Figure 5.4b. Because this harvester was originally intended for applications in highly turbulent flows, the bluff bodies were added to generate high-intensity turbulence. Performing experiments on arrays with and without upstream bluff bodies allowed for a direct comparison of results which will show how turbulence affects the power output of the harvester. A photo of the type-2 array is shown in Figure 5.5b. Array rows run in the y-direction while columns are in the x-direction. For example: The array in Figure 5.4a has 14 rows and 8 columns.

The schematics in Figure 5.4 are drawn to scale to accurately show the location of each array element and bluff body. The footprint of each array element is represented as 2.54 cm square where active elements are shown as solid black numbered 1-10, and passive elements are shown as white with a black border. The two large rectangular grids in each schematic represent two sheets of steel having dimensions 121.9 cm x 29.21 cm x 2.00 mm that were secured to the aluminum test section floor. Each plate was white with a black 2.54 cm square grid as shown in Figure 5.5b.

5.2.2 Experimental Procedure

Each of the ten active elements had a separate load resister R_L which was connected across the PZT electrode leads such that each element was part of an individual circuit. (See Figure 5.3c.) This was done to avoid out-of-phase voltage cancelation that would occur if the elements were connected in series or parallel. Voltage outputs (V_1, V_2, $\ldots V_{10}$) were sampled at 2.0 kHz on separate channels with National Instruments data acquisition hardware. A laptop with LabVIEW software was used to display both the time and frequency response of the load voltage output for each of the 10 active array elements. For a given test, the air velocity was kept approximately constant and data was recorded for ~270 seconds (approximately 2^{19} samples per channel). The velocity was then adjusted and the procedure repeated for a total of 14 velocity increments.

5.2.3 Wind Tunnel Facility

All experiments were conducted in an open loop, single stage wind tunnel with variable frequency drive (VFD) fan motor control. Inside dimensions of the test section measured 61cm x 61cm x 122cm. The test section sides and top were clear acrylic, and the floor was aluminum. Photos of the wind tunnel showing the experimental setup are provided in Figure 5.5(a,b).

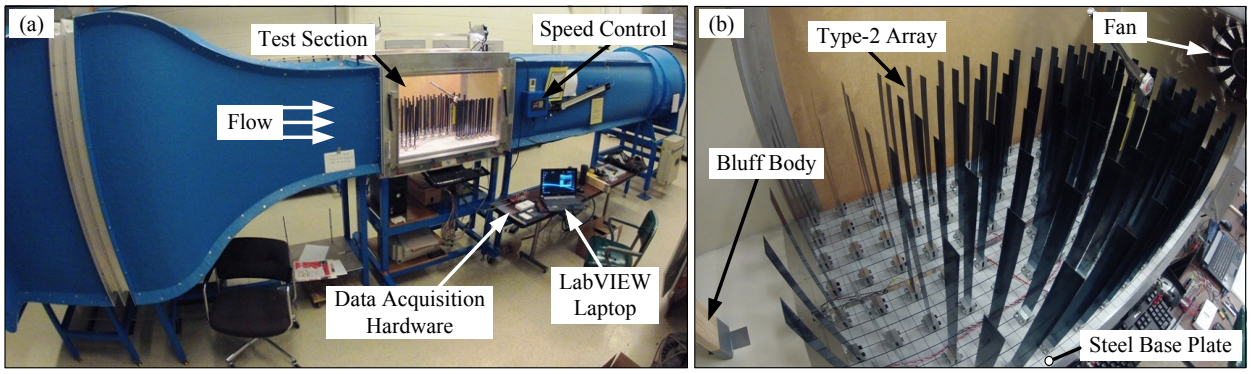

Figure 5.5: Photos showing (a) the 2'x2' wind tunnel and components of the experimental setup, and (b) the type-2 array setup inside the test section.

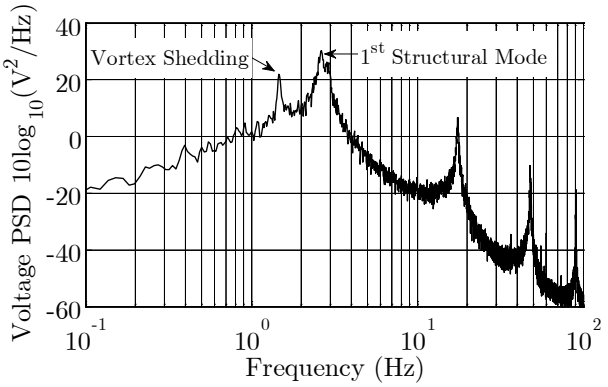

Figure 5.6: Example of voltage PSD measurement used to calculate flow velocity showing a prominent peak corresponding to bluff body vortex shedding.

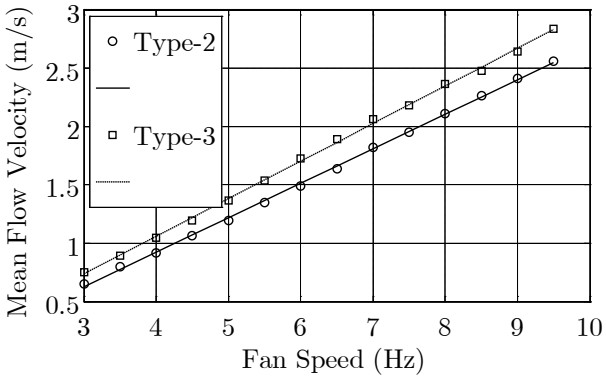

Figure 5.7: Velocities from measured vortex shedding frequencies for type-2 and type-3 array configurations.

Because all experiments were designed for low velocity flow (0-3 m/s), existing wind tunnel instrumentation was unable to provide reliable velocity measurements. Considering the frequency response of the active elements was already being measured and displayed in real-time, the most readily available low velocity measurement technique was bluff body vortex shedding. Frequency measurements were used to estimate the mean flow velocity with the well-known Strouhal vortex shedding equation [117],

$$St = \frac{f_{\mathrm{v}} L_{\mathrm{c}}}{\bar{U}} \tag{5.2}$$

where f_{v} is the vortex shedding frequency, $\bar{U}$ is the mean free-stream velocity, L_{c} is the characteristic length of the bluff body, and St is the Strouhal Number. For this study the bluff body had a rectangular cross section where the thickness (streamwise dimension) was 3.81cm and the width was 8.89cm. The characteristic length was therefore $L_{\mathrm{c}} = 8.89\mathrm{cm}$ and the Strouhal number was $St = 0.2$ [118].

As demonstrated in Figure 5.6, the vortex shedding frequency was well defined and clearly visible on the array voltage output PSD. It was then straightforward to use equation (5.2) to calculate the corresponding mean flow velocity. Because motor speed rather than flow velocity was controlled, the velocity was dependent on the test section blockage ratio. The blockage ratio changed for each array configuration where the maximum and minimum blockage was with the type-2 and type-3 configurations respectively. Velocity trends calculated for the maximum and minimum blockage conditions show a significant increase in velocity when going from the type-2 to the type-3 array. These velocity trends are shown in Figure 5.7. It was assumed that because the blockage ratios for the type-1 and type-2 arrays were very similar, the velocity as a function of fan speed was approximately equal for both arrays.

5.2.4 Results & Discussion

Raw time-series voltage data was saved for the ten active elements at 14 velocity increments for each of the three array types. Post-processing of all 42 test files and 4.7 GB of data was performed using MATLAB software. The following results show trends in average power output and active element voltage power spectral density functions versus flow velocity.

5.2.4.1 Power Trends

Average power output from the ten active elements was calculated using the voltage measured across each load resistor. Trends in the average power output are plotted in Figure 5.8(a-f) as functions of mean flow velocity for each of the three array configurations. For clarity, power trends from the ten active elements were plotted on two graphs for each array configuration.

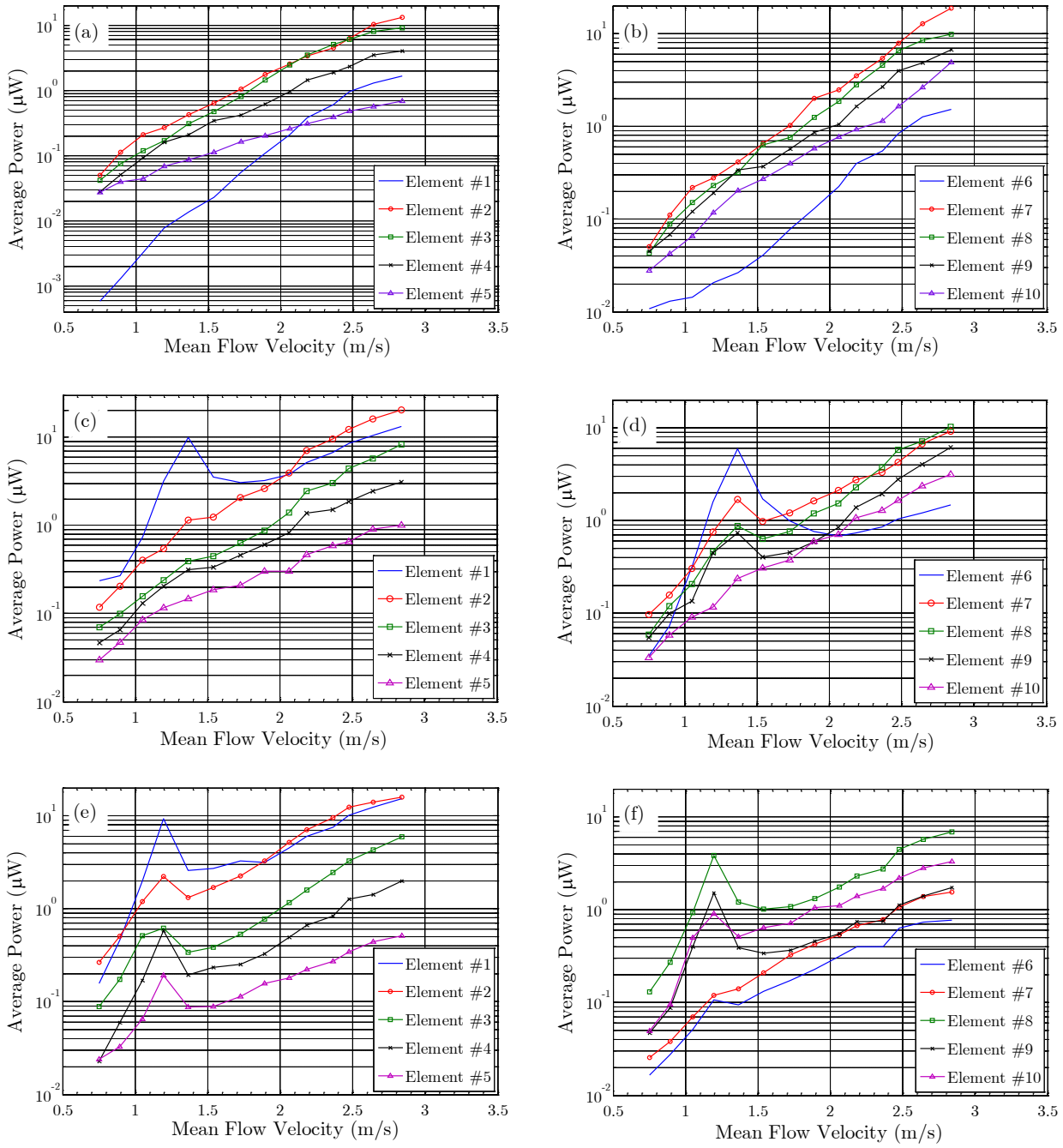

Figure 5.8: Experimental results from (a,b) the type-1 array, (c,d) the type-2 array, and (e,f) the type-3 array all demonstrating the influence of mean flow velocity and element location on average power output per element.

It is important to note that for all cases the waving mode resonance condition of the array (honami) was only allowed to occur for the passive elements. Because the fundamental frequency of the passive elements was less than that of the active elements, the passive elements would experience resonance at a lower flow velocity. Keeping the active elements from reaching resonance was done to avoid over-straining, and potentially damaging the PZT. Flow velocity was therefore increased until the deflection of the active elements reached a maximum allowable limit. Considering the active elements were kept from reaching waving mode resonance the power values presented here represent an output that is significantly less than what could be available in the array. A minor design modification allowed the active elements to safely reach waving mode resonance; however, results from the modified elements will not be presented until Section 5.3.

Figure 5.8(a-d) shows results of an array having the same type 1 and type 2 element arrangements to serve a direct comparison of the power output without a bluff body Figure 5.8(a,b) and with a bluff body Figure 5.8(a-d). Recall Figure 5.4 for the locations of the active array elements. Notice that the presence of a bluff body only has a significant effect on power output from elements on the front row of the array (elements 1 and 6). This is due to the fact that large turbulence structures in bluff body wake are immediately destroyed after contacting the array. The peak in power output seen at a velocity of approximately 1.25 m/s in Figure 5.8(c-f) is the point at which the bluff body vortex shedding frequency matches the natural frequency of the active elements. As velocity increased past 1.25 m/s, output from all active elements increased exponentially.

It is interesting to note that the waving mode resonance condition of the passive elements was not affected by the bluff body. This suggests that the waving mode will occur regardless of

the presence of large-scale upstream turbulence. Another interesting observation was that after the waving mode 'locked-in', large amplitude excitation continued with a velocity increase of over 100%.

5.2.4.2 Frequency Domain Analysis

The power calculations for Figure 5.8 required only average values of the time-series active element load voltages. Analyzing these active element voltages in the frequency domain provided valuable insights to the fluid and structural dynamics of the three array types discussed in Section 5.2.1. The PSD function was calculated for each of the ten load voltages at each velocity increment. For a given element, a PSD profile was created by plotting the voltage PSD as a function of both frequency and flow velocity. A total of ten PSD profiles from each of the three array types were created and analyzed. The following discussion focuses on five of these PSD profiles which are shown in Figures 5.9-5.11.

Plot Description for Figures 5.9-5.11:

a) The primary and secondary y-axes are denoted by 'y_1' and 'y_2' respectively in both of the y-axis labels and in the legend entries for all plots.

b) The vertical dash-dot lines with 'x' (×) markers are plotted at the natural frequencies (*structural modes*) of the active element. As expected, the structural modes are constant for all velocities. Notice that the vertical structural mode lines don't always align exactly on the peaks of the PSD plot. This frequency misalignment is due to the fact that the lines

are plotted at exactly the same frequencies for each figure while the PSD functions are produced from elements #1,#3, and #4 which have slightly different natural frequencies.

c) The vertical dash-dot lines with large dot (•) markers are plotted at the waving mode resonance frequencies (*waving modes*) of the array. The lowest waving mode frequency is equal to the first natural frequency of the passive elements (1.9 Hz). The other three vertical waving mode frequency lines are multiples of the first corresponding to higher vortex shedding modes. These multiples of the first resonant frequency are caused by higher-mode vortex shedding across the top of the array. Higher-mode vortex shedding occurs when a single vortex splits into two or more vortices. Higher-mode vortex shedding is intermittent and occurs more frequently as the Reynolds number increases. See the work of Williamson *et al* for further discussion on this type of vortex shedding behavior [38,39].

d) The curved dash-dot line with square (□) markers is plotted at the vortex shedding frequency of the array (*array vortex*). This array vortex line is calculated from equation (5.1) for a k_v value of 0.4.

e) The curved dash-dot lines with circle (○) markers are located at the vortex shedding frequencies of the bluff body (*bluff body vortex*). These curves were produced from the relationship given in equation (5.2) using a Strouhal number of 0.2 and a characteristic length of 8.89 cm. The lowest frequency bluff body vortex curve corresponds to the primary vortex shedding frequency. The two higher frequency curves are first and second

multiples of the primary frequency. See Plot Description (c) above for an explanation of higher mode vortex shedding.

f) A 2D voltage PSD function is plotted with a solid black line on the secondary y-axis (y_2). This 2D function is the active element voltage PSD calculated at the maximum mean flow velocity. This plot can be made by taking a slice of the 3D PSD profile along its top edge or at the maximum velocity on the primary y-axis.

Figures 5.10a and 5.11a show that the first row of elements in the array is heavily influenced by upstream turbulence. The first and second modes of bluff body vortex shedding frequencies are clearly visible in the 3D PSD profile from first-row elements. Also, no waving modes are visible in elements on the first row which explains why the power output from the first row is extremely low compared to all other elements as seen in Figure 5.8(a,b).

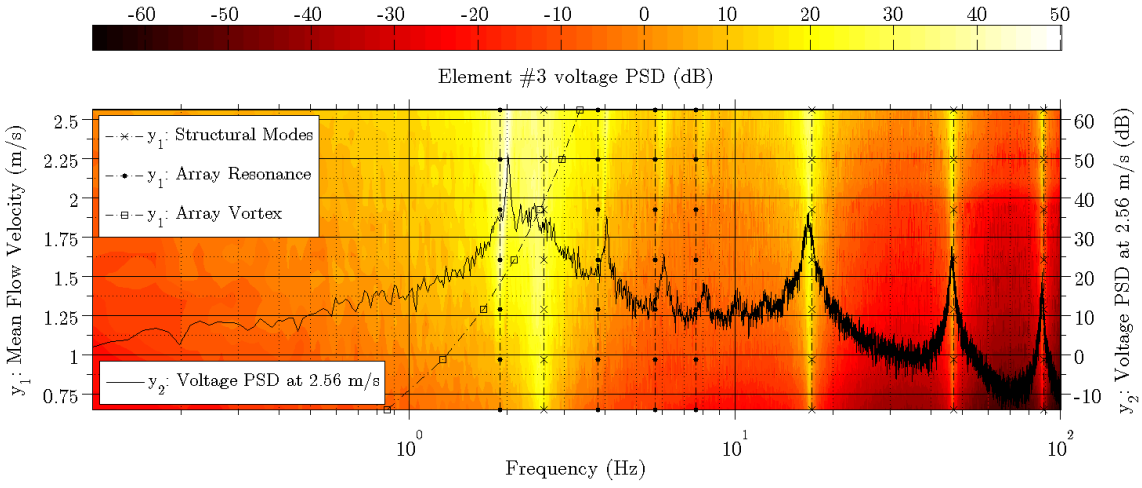

Figure 5.9: Load voltage PSD profile from element #3 of the type-1 array including lines that indicate frequencies for the structural modes, waving modes, and array vortex shedding as functions of flow velocity.

Figures 5.10a and 5.11a also show a large peak in the PSD profile when the primary bluff body vortex shedding frequency equals the natural frequency of the active element. This peak in output can also be seen in the power results shown in Figure 5.8(c-f).

The array vortex frequency is a linear function of velocity as show in equation (5.1). In the PSD profiles of Figures 5.9 and 5.10b one can see that the primary waving mode begins when the array vortex frequency equals the natural frequency of the passive elements. Small amplitude waving mode vibration was first observed and can be seen on the PSD profiles at approximately 1.35 m/s. It was not until 1.45 m/s that persistent large amplitude waving motions were observed. Increasing the velocity beyond 1.45 m/s caused a continued increase in waving mode amplitude while the frequency remained approximately constant.

Initially the vertical waving mode lines appear to be underestimating the actual peak frequencies in Figures 5.9 and 5.10b. A closer look at the trends in waving mode peaks of the PSD profile shows that they increase linearly as a function of mean flow velocity. The waving mode peaks in the PSD profile increase about 8.1% with a 47.3% increase in flow velocity. As velocity increases, higher waving modes become visible in the PSD profile. At maximum velocity the 2D PSD function clearly shows four waving modes in Figure 5.9 and five waving modes in Figure 5.10b.

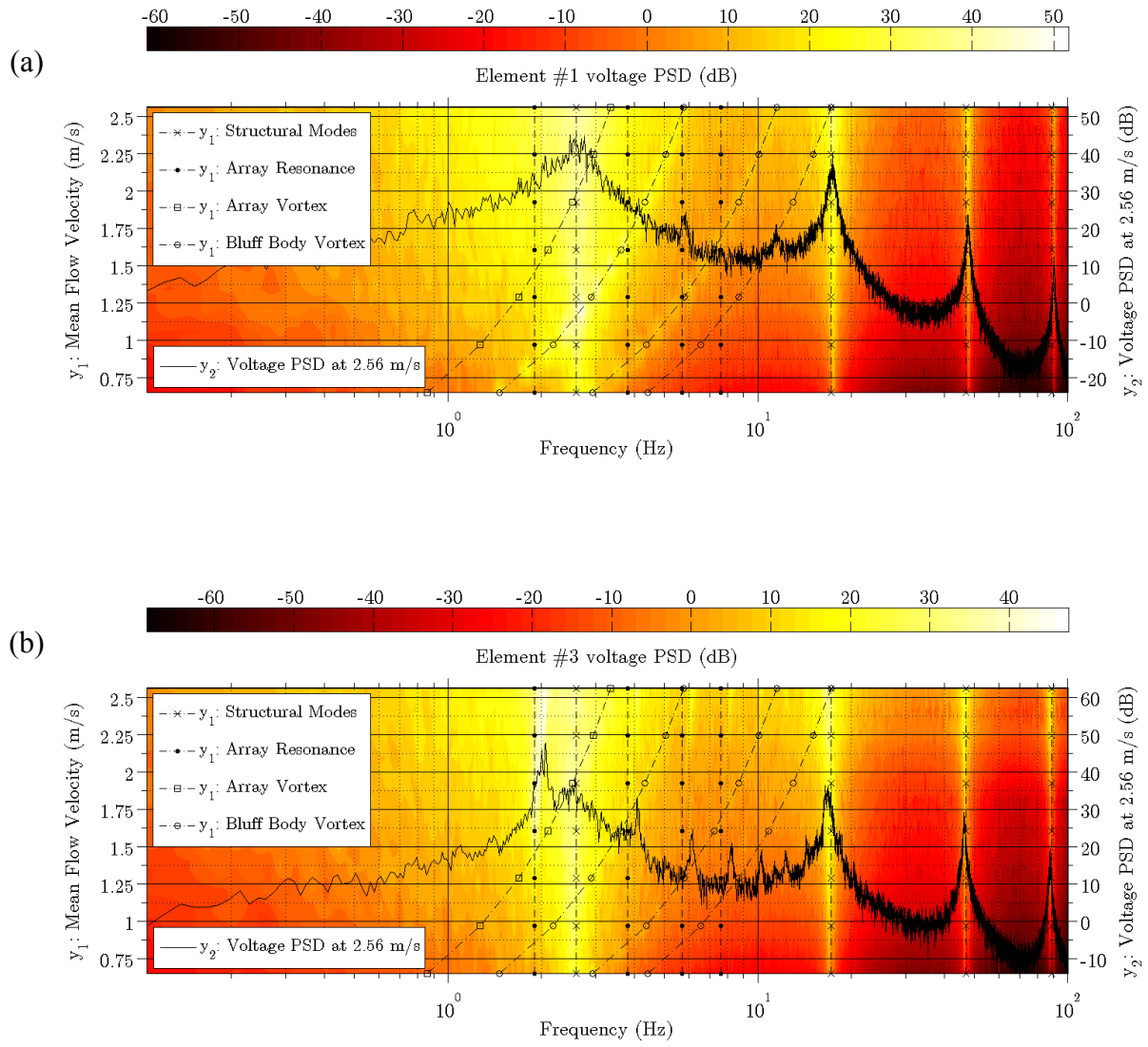

Figure 5.10: Load voltage PSD profile from (a) element #1, and (b) element #3 of the type-2 array including lines that indicate frequencies for the structural modes, waving modes, array vortex shedding, and bluff body vortex shedding as functions of flow velocity.

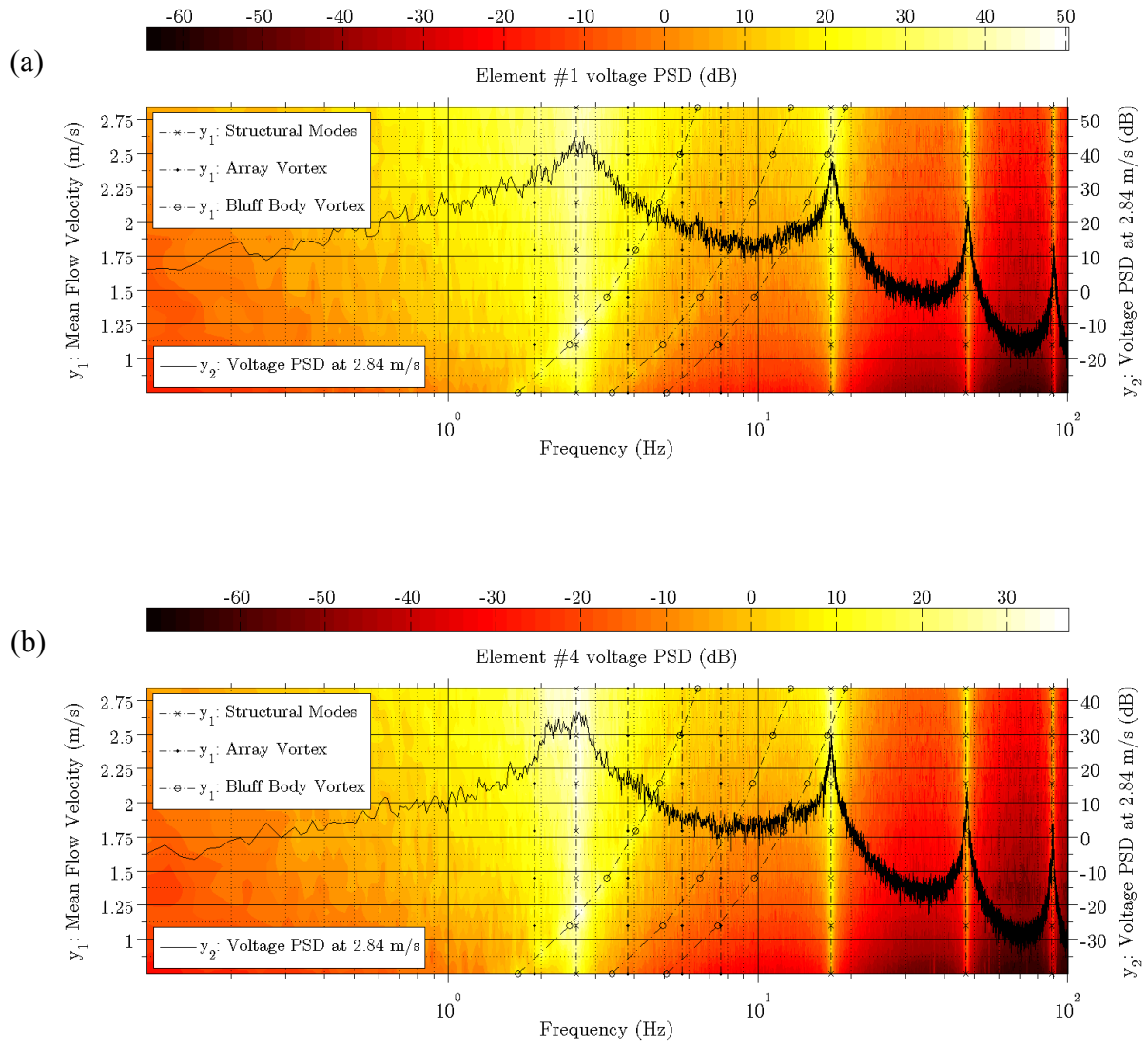

Figure 5.11: Load voltage PSD profile from (a) element #1, and (b) element #4 of the type-3 array including lines that indicate frequencies for the structural modes, waving modes, array vortex shedding, and bluff body vortex shedding as functions of flow velocity.

The following is a list of more subtle observations made both during experiments, and from results of experiments shown in Figures 5.9 and 5.10b.

Subtle observations made during experiments and from Figures 5.9 and 5.10b:

- All elements in columns containing active elements (*e.g.* columns 2 and 4 in Figure 5.4a) were observed to have vibration amplitudes significantly less than those for columns containing all passive elements.
- Results in Figures 5.9 and 5.10b along with experimental observations, showed that waving mode vibrations occurred at (or near) the natural frequency of the passive elements (~1.95 Hz).
- Recall that Figures 5.9 and 5.10b were produced from the load voltage output of an active element which has a natural frequency of 2.6 Hz while the maximum output (*i.e.* highest peak in the PSD function) occurred near 1.95 Hz.

From this list of results and observations, one can conclude that fluid coupling within large arrays causes the array to force all elements to behave similar to the majority of elements in the array. This coupling among multiple dynamic systems is called entrainment or sympathetic excitation. Recall that only 10 active elements are placed among 102 passive elements where their natural frequencies are 2.6 Hz and 1.95 Hz respectively. Therefore, the active elements are being forced at an off-resonance frequency which can explain why columns containing active elements had the lowest vibration amplitudes. This also explains why the maximum output from an active element occurs at the natural frequency of the surrounding passive elements rather than that of the active element.

Lastly, Figure 5.11 shows that waving modes did not occur on the front row nor did they occur within the array. These results along with experimental observations of the type-3 array revealed that staggered array configurations do not work well for energy harvesting. A majority of the power for the type-1&2 arrays was produced from waving mode vibrations; therefore, all future large array tests presented in this chapter are for in-line array configurations (type-1&2) rather than staggered (type-3).

5.3 In-Depth Analysis: Experimental Details

Numerous wind tunnel experiments were performed on the piezoelectric grass harvester to further explore energy harvesting potential. The harvester prototype, wind tunnel, and procedures discussed in this section are significantly different from those of section 5.2. The purpose of these experiments was to identify and quantify trends in power output versus flow velocity for many different array configurations. This section discusses experimental details such as: array materials and design, terminology and coordinate system, data processing, testing facilities, instrumentation, circuitry, and software.

5.3.1 Wind Tunnel Facility

All experiments presented in this section were performed in an open loop, single stage wind tunnel. The test section has a length of 1.22 m, and has a cross-section of 30.5 x 30.5 cm. With exception of the flow straightener and contraction section, the author designed the entire wind tunnel and assembled all of its components. (See Figure 5.12.) Fan speed or flow velocity can be controlled manually or automatically using a 3-phase, 3-hp, variable frequency drive (VFD) controller with build-in PID feedback control (Mitsubishi Electric, Model: FR-E720-110-NA).

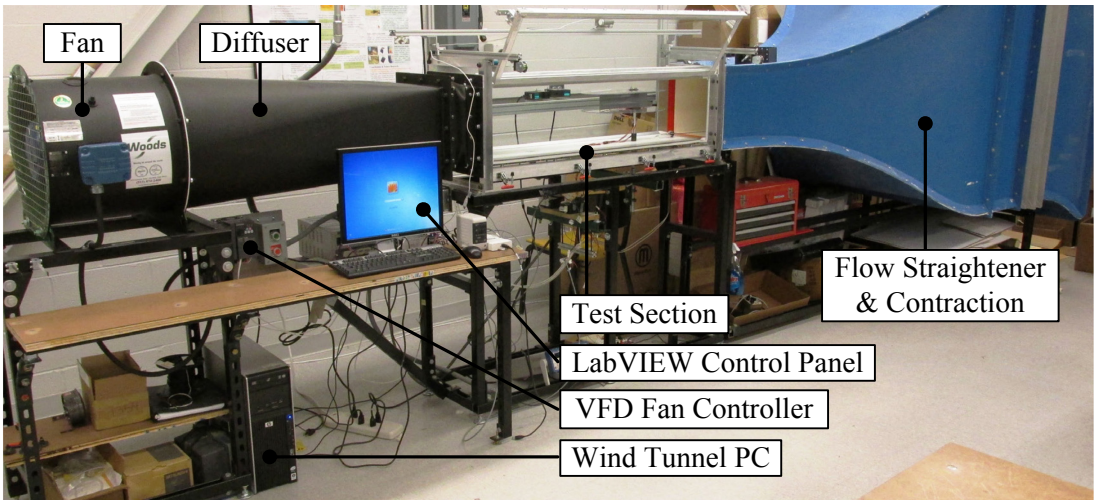

Figure 5.12: Photo of the 1'x1' wind tunnel testing facility

The wind tunnel is able to produce flow velocities ranging from 0 to 35 m/s (approx. 80 mph). Accurate velocity measurements can be made from 35 m/s down to 0.2 m/s using a pitot static tube attached to a differential pressure transducer with a full range of +/-748 Pa (Omega, Model: PX653-03D5V). Air temperature measurements were made with a T-type thermocouple (Omega, Model: 5TC-GG-T-20-36) placed downstream of the test section. LabVIEW development software was used to design a virtual control panel which allows for a PC to interface with National Instruments hardware for data acquisition and control. A 14-bit, multifunction DAQ with 8 analog inputs and 2 analog outputs (National Instruments, Model: USB-6009) was used as the dedicated data acquisition and control hardware. The LabVIEW virtual control panel was used for displaying, controlling, and saving real-time data from the pressure transducer and VFD along with any other external inputs.

Table 5.2: Design parameters for passive and active element types

Type	*Layer*	*Material*	*Length* (cm)	*Width* (cm)	*Thickness* (mm)	*Natural Frequency* (Hz)
Passive	Substrate	Steel	14.610	2.540	0.254	9.3
	Active layer	-	-	-	-	
Active	Substrate	Steel	14.610	2.540	0.254	16.3 (Mt = 0 gm)
	Active layer	PZT	4.295	2.096	0.254	9.3 (Mt = 2.9 gm)

5.3.2 Array Design

Considering factors such as assembly time, material expense, availability of data acquisition hardware, and quantity of data, the authors decided against building an entire array of piezoelectric cantilevers. Rather, only ten cantilevers consisted of a steel substrate with piezoelectric material bonded to them while all other cantilevers in the array were steel with uniform mass and stiffness. The cantilevers with piezoelectric material will be referred to as *active* array elements while all others will be called *passive*. Table 5.2 summarizes the design parameters for both element types.

Figure 5.13 shows schematics of the passive and active array element assemblies. Compared to the passive elements, active elements had increased mass and bending stiffness caused by the bonded piezoelectric material. This increased stiffness caused an increase in natural frequency. Because all elements must have approximately the same natural frequency for waving mode vibration (*honami*) to occur, a tip mass was added to all active elements. Each tip mass was adjusted until the active elements had the same natural frequency as the passive elements. A tip mass of approximately 2.9 grams was found reduced the natural frequency of the active elements from 16.3 Hz to 9.3 Hz.

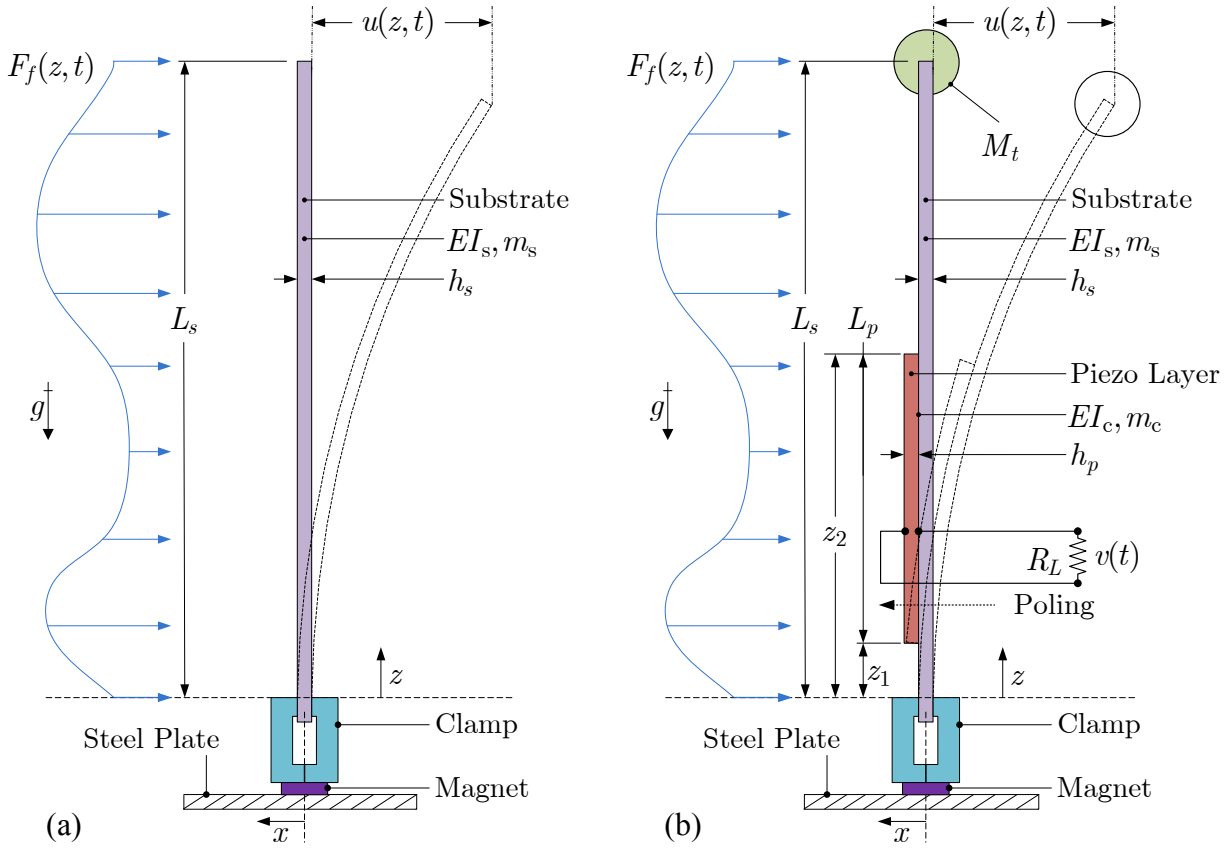

Figure 5.13: Schematic of (a) *passive* and (b) *active* array elements showing details of the magnetic clamp assembly for both element types along with the added tip mass and piezoelectric material for the active element.

All array elements were fixed in individual clamps, and all clamps were attached to a high-grade neodymium magnet. The magnets provided enough attractive force to a steel plate to hold all elements in place during a test, yet allowed for convenient repositioning between tests. The steel plate was centered on and attached to the test section floor and had a 2.54 cm square grid drawn on it for a reference. The grid was used as the x-y plane where the positive x direction was the same as the flow direction. Figure 5.14 shows the coordinate system and defines common terminology used for all large array tests presented in this section.

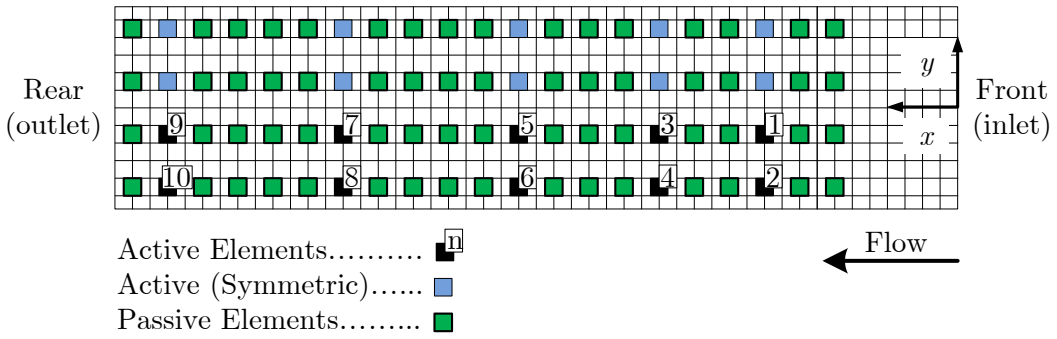

Figure 5.14: Schematic of a top view of the steel plate (drawn to scale) showing the coordinate system, the 2.54 cm square grid, and the locations of all array elements for a given array configuration.

In order to estimate the total power output that could be generated from a given array, active elements were systematically positioned among passive elements. The following is a list of observations made from initial large array experiments. Included below each of these observations is the corresponding conclusion used to determine the placement of active elements for all array configurations in this study.

a) The first row produced a negligible amount of power compared to all other rows:

⇒ No active elements were positioned on the first row.

b) Power output changed rapidly as a function of x-position toward the front of the array:

⇒ More active elements were placed toward the front of the array.

c) The array configuration and power output was symmetric about the y-axis:

⇒ Output from all active elements was assumed to be symmetric about the y-axis.

d) Power output toward the back of the array showed little change as a function of x-position:

⇒ Active element spacing increased as a function of x-position.

Figure 5.14 shows a typical array configuration where one can see how active elements were placed among passive elements in a manner determined by the previous list of conclusions.

5.3.3 Experimental Procedures

All elements were positioned on the steel plate in the wind tunnel test section to a specified x and y spacing. Then, the velocity was increased from 0 to 15 m/s in 15 evenly spaced increments. At each velocity increment, the wind tunnel was allowed come to steady average velocity before data was gathered. All time-series data, including wind tunnel speed settings, velocity, and load voltages from the ten active elements was sampled at 2.0 kHz for 60 seconds and recorded in a LabVIEW measurement file (.lvm). Data recording was then paused while the velocity was adjusted to the next velocity increment. This procedure was automated within LabVIEW. After all 15 velocity increments were completed, the next array configuration was set by adjusting the x or y spacing of the array.

This procedure was repeated for ten different x-spacing values ranging from 3.01 cm to 15.24 cm, and at each x-spacing there were five y-spacing values ranging from 3.49 cm to 6.35 cm. In total, experiments were performed on 50 different array configurations which yielded 750 data sets, and 9.1 GB of data. Table 5.3 gives a test parameter summary for all experiments performed during this study.

Table 5.3: Piezoelectric grass wind tunnel test matrix.

Parameter	*No. of Increments*	*Range*
Velocity	15	(0 - 15) m/s
x-spacing	10	(3.01 – 15.24) cm
y-spacing	5	(3.49 – 6.35) cm

5.3.4 Data Processing

All post-processing of the raw data was performed using MATLAB software. Raw data refers to unfiltered, time-series voltages. These voltages were first digitally filtered, then converted into their respective physical properties via predetermined calibration equations. For each 60 second test, average flow velocity, fan speed, and the active element RMS load voltages were calculated and stored.

In order to ensure that the measured voltage did not exceed limits of the data acquisition hardware, the voltage was split across two resistors in series. The total load resistance was therefore equal to the sum of the two resistors, i.e. $R_L = R_1 + R_2$. The voltage was measured across R_1 therefore the total voltage was calculated using ohms law,

$$v = IR_L = \left(\frac{v_m}{R_1}\right)\left(R_1 + R_2\right) \tag{5.3}$$

where v is the total load voltage, v_m is the measured voltage, I_m is the electrical current, and R_L is the total load resistance as defined earlier. After the total load voltage was calculated, the average power for each element was found using the following expression,

$$P_{ave} = \frac{V_{rms}^2}{R_L} \tag{5.4}$$

where P_{ave} is the average power output and V_{rms} is the root-mean-square voltage.

Recall that symmetry was assumed about the y-axis; therefore, the 10 active elements yielded 20 average power output values for a given array configuration and flow velocity. A smooth 3D surface was fitted to these 20 power values across the array using a *shape-preserving* piecewise cubic interpolation scheme. (See Figures 5.21(a-c) and 5.22(a-c) for results of this interpolation method.) Average power output for all elements could then be estimated as if all passive

elements were replaced with active elements having the same design parameters as those listed in Table 5.2. For example: given the x-y location of a passive element, its average power output could be estimated from the interpolated 3D surface as if that element were replaced with an active element. Finally, the average power values for all elements are combined to yield the total estimated power output for a given array configuration and flow velocity. The total estimated power can be given as,

$$\begin{aligned} \tilde{P}_{tot} &= \sum Active + \sum Passive \\ &= \sum_{n=1}^{N_{ae}} P_{ave} + \sum_{n=1}^{N_{pe}} \tilde{P}_{ave} \end{aligned} \tag{5.5}$$

where N_{ae} and N_{pe} are the number of active and passive elements respectively, $\tilde{P}_{ave}$ is the estimated average power from interpolation at the passive element locations.

The total power output is then normalized by the total area covered by the array to generate plots such as those in figures 5.23 and 5.24. This normalized total power output is called the *area power density* and is calculated using the following expression,

$$\tilde{P}_{\rho} = \frac{\tilde{P}_{tot}}{\Delta_x \left(N_x - 1\right) \Delta_y \left(N_y - 1\right)} \tag{5.6}$$

where $\tilde{P}_{\rho}$ is the area power density, Δ is the element spacing, N is the number of elements, and subscripts x and y respectively denote the x and y directions in which Δ and N are measured.

5.4 In-Depth Analysis: Experimental Results & Discussion

Given the large amount of data recorded in this study, results from all experiments will not be shown. Rather, the results presented in this section will focus first on only 6 (out of 50 total) specific array configurations that have notable differences. Then the results from all 50 array configurations each with 15 velocity increments (750 tests total) will be summarized and discussed.

5.4.1 Test Cases: Single Array Configurations

Average velocity profiles and power output profiles for six different array configurations are presented here. Average velocity profiles were measured at 5 x-locations along the middle of the test section (at y = 0 cm). Each velocity profile was made by taking local average velocity measurements with the pitot-static tube at 10 evenly spaced z-locations. Velocity profiles were made at each x-location for 5 evenly spaced free-stream flow velocities.

5.4.1.1 Velocity profiles

Figures 5.15-5.20 show velocity profiles and their measurement locations throughout the test section. The horizontal bold dotted line in each of the velocity profile plots indicates the array element height while the horizontal bold solid lines indicate the floor and ceiling of the test section. The lower large rectangular plot in Figures 5.15-5.20 show locations of the elements denoted with blue squares while the pitot tube tip locations are shown as red triangles. The bold solid lines in these lower plots indicate the edge of the steel grid plate.

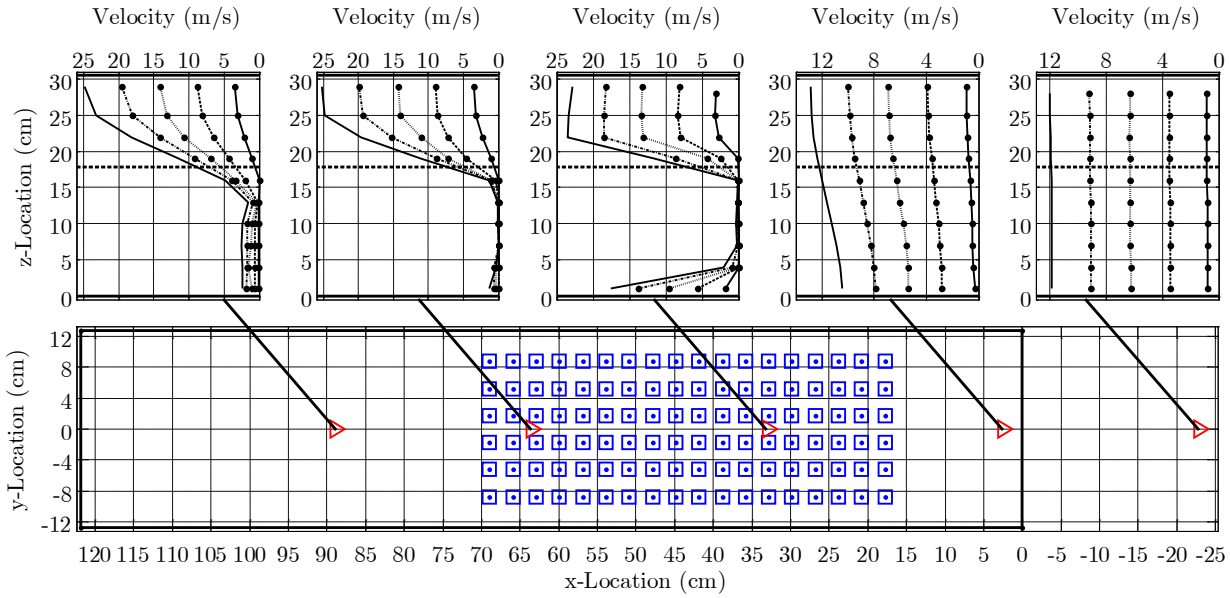

Figure 5.15: Array #1: Velocity profiles as functions of array height shown at five x-locations in the center of a 14x6 element array having an x and y spacing of 3.01 cm and 3.49 cm respectively.

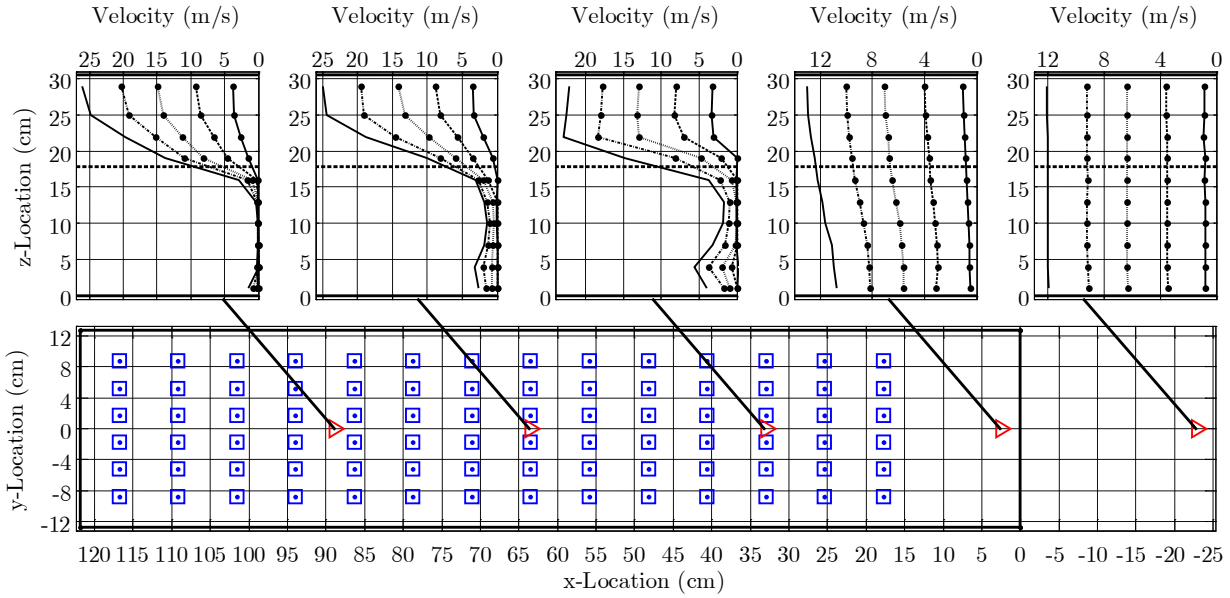

Figure 5.16: Array #2: Velocity profiles as functions of array height shown at five x-locations in the center of a 14x6 element array having an x and y spacing of 7.62 cm and 3.49 cm respectively.

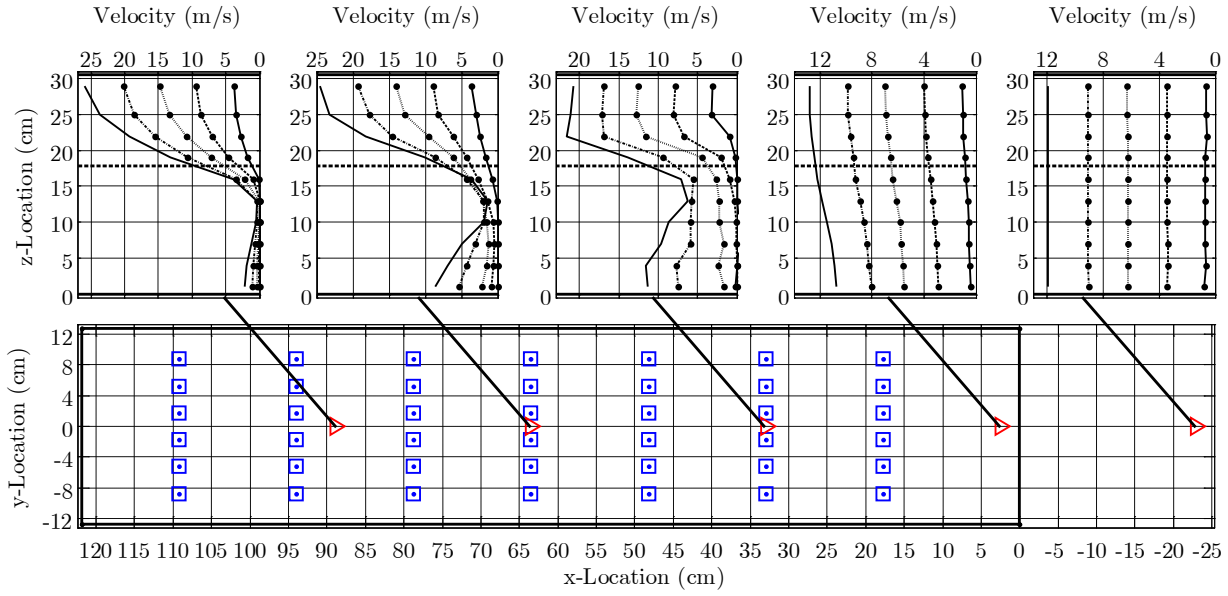

Figure 5.17: Array #3: Velocity profiles as functions of array height shown at five x-locations in the center of a 7x6 element array having an x and y spacing of 15.24 cm and 3.49 cm respectively.

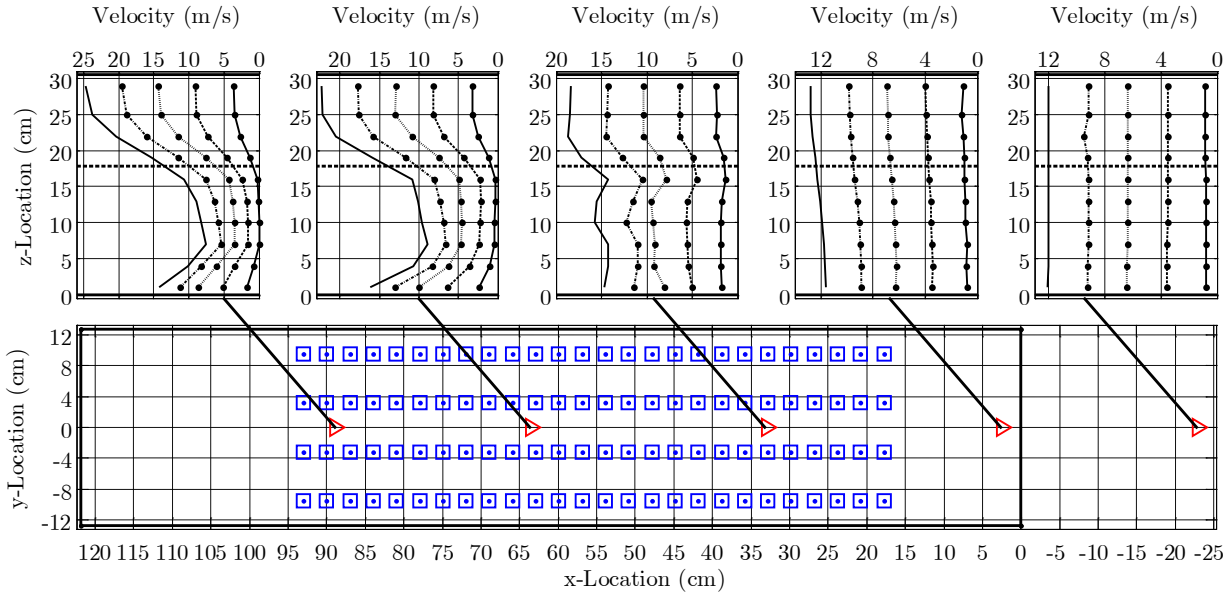

Figure 5.18: Array #4: Velocity profiles as functions of array height shown at five x-locations in the center of a 26x4 element array having an x and y spacing of 3.01 cm and 6.35 cm respectively.

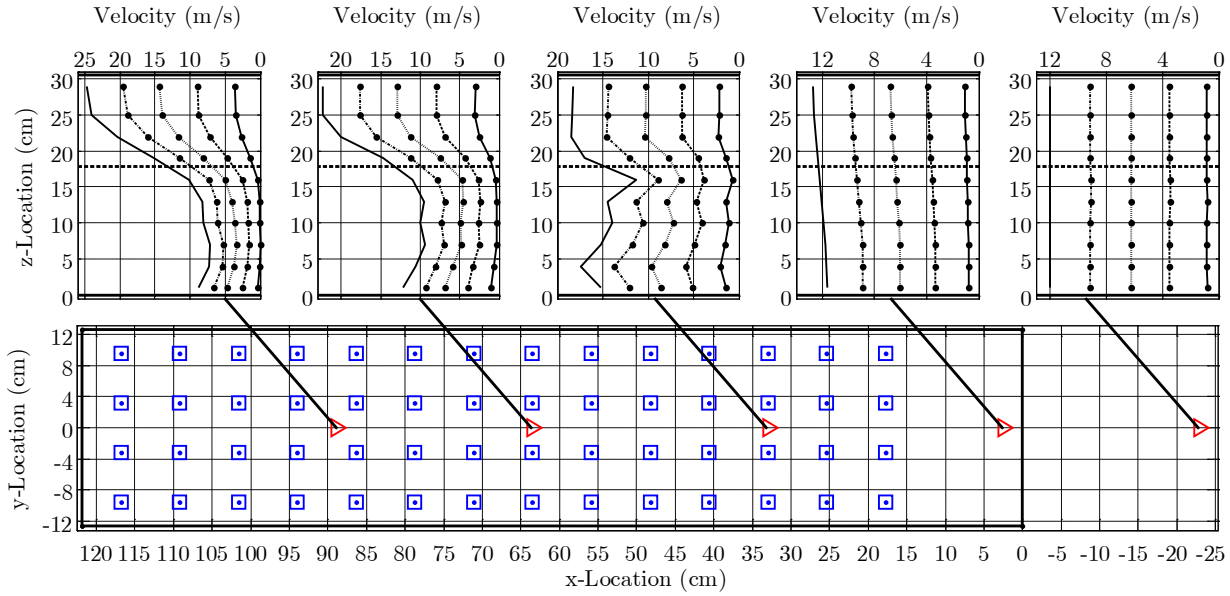

Figure 5.19: Array #5: Velocity profiles as functions of array height shown at five x-locations in the center of a 14x4 element array having an x and y spacing of 7.62 cm and 6.35 cm respectively.

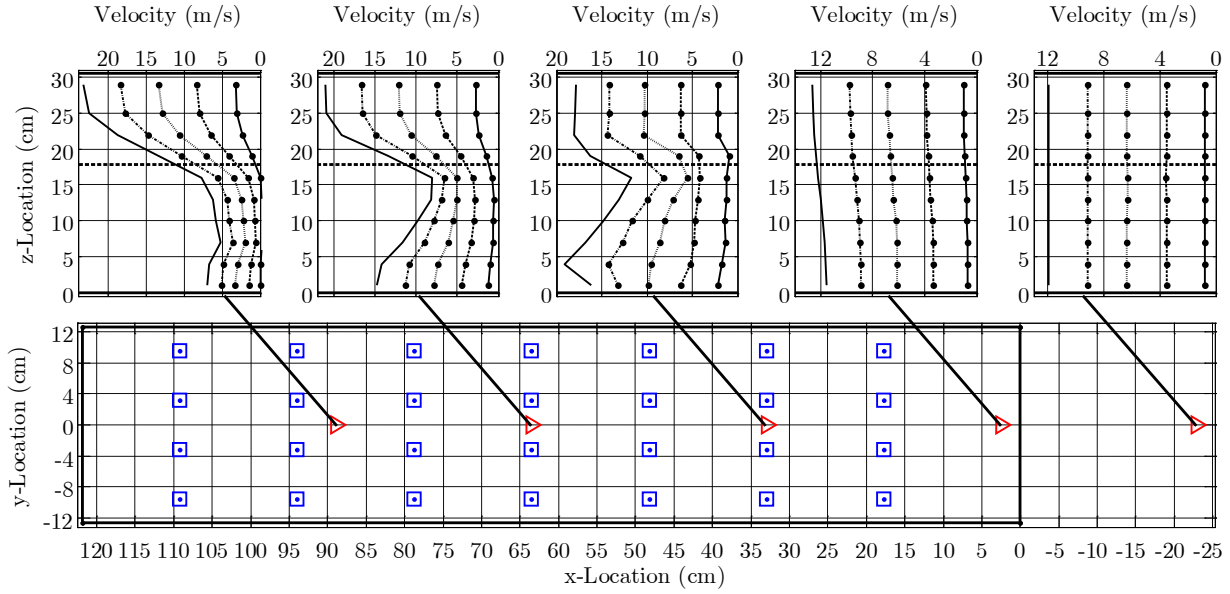

Figure 5.20: Array #6: Velocity profiles as functions of array height shown at five x-locations in the center of a 7x4 element array having an x and y spacing of 15.24 cm and 6.35 cm respectively.

Table 5.4: Single array configurations used for velocity and power profile tests.

Array #	*Rows*	*Cols.*	*x-spacing* (cm)	*y-spacing* (cm)
1	14	6	3.01	3.49
2	14	6	7.62	3.49
3	7	6	15.24	3.49
4	26	4	3.01	6.35
5	14	4	7.62	6.35
6	7	4	15.24	6.35

Three of the six velocity profile tests were performed on array configurations (arrays 1-3) having six columns and a fixed y-spacing of 3.49 cm where only the x-spacing and number of rows were varied. The three remaining velocity profile tests were with array configurations (arrays 4-6) having four columns and a fixed y-spacing of 6.35 cm where only the x-spacing and number of rows varied. See Table 5.4 for a summary of all array configurations used in the velocity profile tests. The following is a list of observations made from the velocity profile results displayed in Figures 5.15-5.20.

Primary observations made from velocity profiles shown in Figures 5.15-5.20:

- As x-spacing increases, the velocity within the array increases.
- Velocity within the array drops drastically as a function of x-location.
- Velocity profiles transition from straight vertical lines at the front of the array to highly skewed functions toward the rear.
- For the measurement location furthest from the front, the velocity within the array drops to nearly zero while the velocity above the array is approximately double that of the free-stream.

Much of the velocity profile trends for arrays 1-3 (Figures 5.15-5.17) are similar to those shown in arrays 4-6 (Figures 5.18-5.20). A more subtle difference between these two sets of velocity profiles is that arrays 4-6 have velocity profiles that are skewed much less than those in arrays 1-3. In other words, the velocity inside the array increases as the y-spacing increases. This increase in velocity is most likely due to the fact that more flow is being allowed to pass through the array rather than being forced above the array. Conversely, one would expect that as y-spacing decreases all flow through the array is forced to go above the array. One would also expect that as y-spacing becomes very large, flow velocity within the array will approach the free-stream velocity.

5.4.1.2 Power profiles

Using the procedure discussed in Section 5.3.4, smooth 3D surfaces were fitted to the average power output of each active element for all 750 data sets. Obviously it would not be practical to show the power profiles for every data set. Therefore, only six profiles from array configurations similar to those mentioned previously in Section 5.4.1.1 will be presented here.

For all plots given in Figures 5.21 and 5.22, active element locations are shown as blue x's while passive element locations are shown as black dots. The steel grid plate is shown as a large rectangle with a bold black-lined border that surrounds the power profile. Flow is in the positive x-direction.

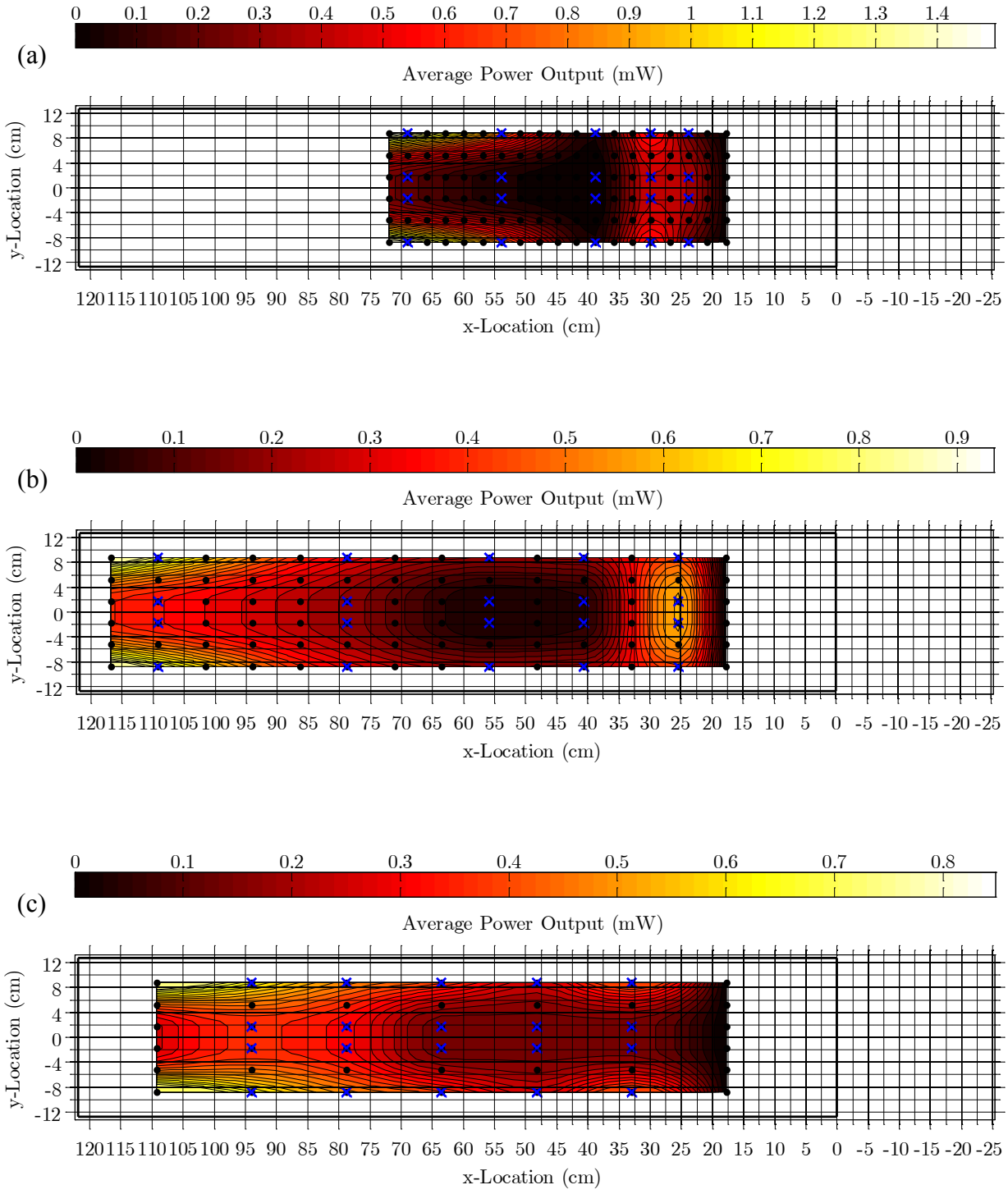

Figure 5.21: Single array power profiles for (a) array 1, (b) array 2, and (c) array 3 showing locations of passive elements (black dots) and active elements (blue x's) relative to the edges of the steel grid plate (bold black lines).

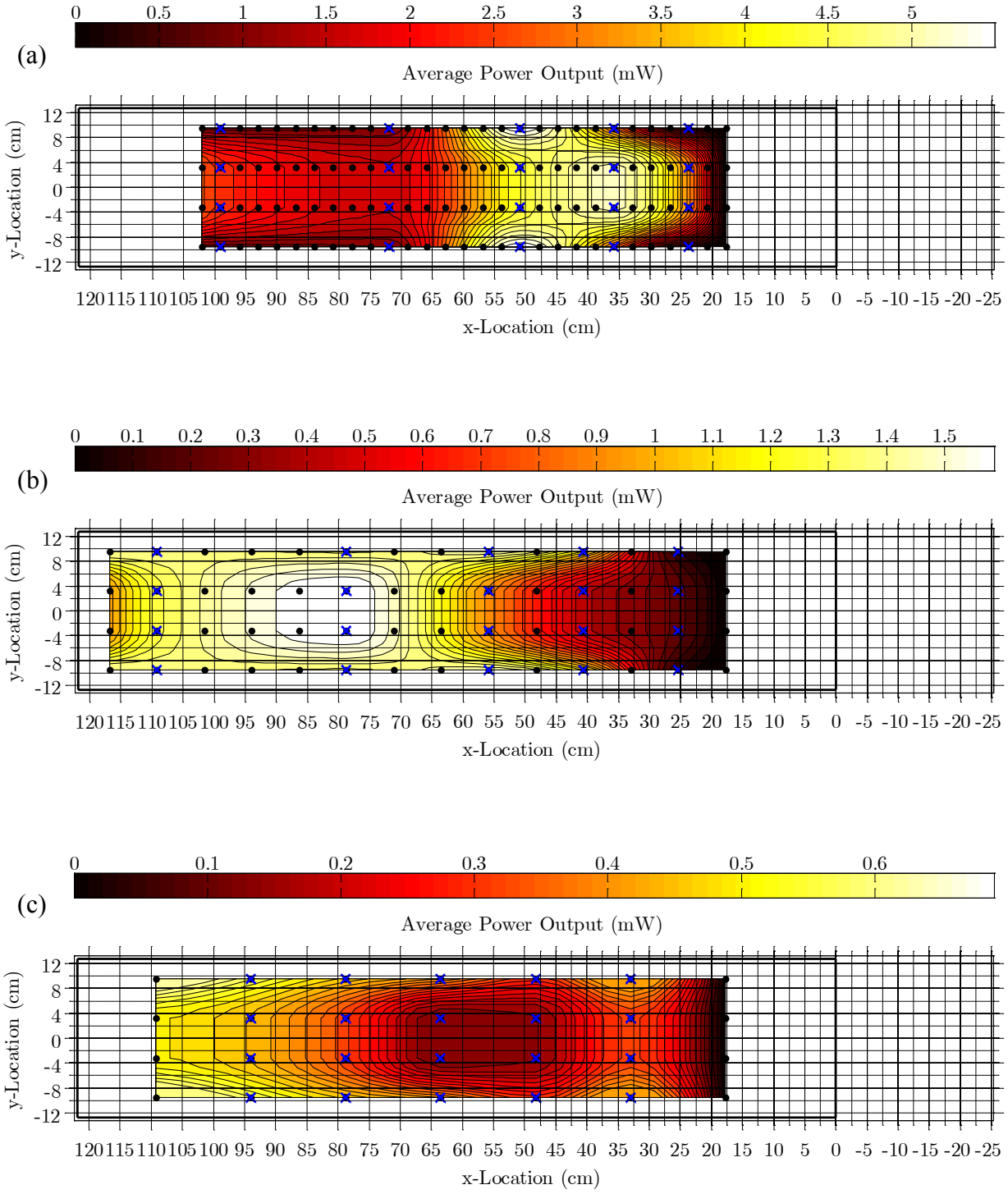

Figure 5.22: Single array power profiles for (a) array 4, (b) array 5, and (c) array 6 showing locations of passive elements (black dots) and active elements (blue x's) relative to the edges of the steel grid plate (bold black lines).

Table 5.5: Summary of results from single array power profiles.

Array #	*Free-Stream Velocity* (m/s)	*Total Estimated Power* (mW)	*Area Power Density* (W/m^2)	*x-spacing* (cm)	*y-spacing* (cm)
1	14.27	42.00	0.44	3.01	3.49
2	14.30	25.53	0.15	7.62	3.49
3	14.27	13.07	0.08	15.24	3.49
4	14.26	303.90	1.89	3.01	6.35
5	14.17	59.77	0.32	7.62	6.35
6	14.16	9.78	0.06	15.24	6.35

All power profiles show that power output as a function of x varied drastically toward the front of the array and became more gradual toward the rear. These results were consistent for numerous tests and agreed with the initial observations listed at the end of Section 5.3.2. The total power output and area power density were calculated for each of the six power profiles using equations (5.5) and (5.6) respectively. The maximum area power density for arrays 1-3 was 0.44 W/m^2 which was achieved at a free-stream flow velocity of 14.27 m/s. The maximum area power density for arrays 3-4 increased significantly to 1.89 W/m^2 at a free-stream flow velocity of 14.26 m/s. All power output results are summarized in Table 5.5.

5.4.2 Test Cases: Multiple Array Configurations

The total average power output of each array configuration at each flow velocity was computed as described in Section 5.3.4. Each power profile was used to estimate total power that could be harvested from all elements in the array. Notice that the area of each power profile (such as those in Figures 5.21 and 5.22) changes along with array element packing density. Packing density refers to the number of elements that are able to populate a square meter for a given configuration. In order to account for the changing area and packing density for each configuration, the total estimated power output was normalized by the area covered by each

power profile. This normalized output is called the *area power density* of the harvester rather than the more conventional volume-based power density performance metric. Equations (5.5) and (5.6) in section 5.3.4 provide formal definitions of the total estimated power output and the area power density respectively.

Plots a, b, and c in Figure 5.23 show the area power density results for arrays with varying x-spacing having a y-spacing of 3.49 cm, 4.45 cm and 6.35 cm respectively. Note that the z-axis (out of the page) is represented in log scale. A single point on each of the power density plots was calculated from arrays with configurations similar to those of the single arrays discussed in Sections 5.4.1.1 and 5.4.1.2. Each power density plot summarizes results from 10 array configurations each at 15 velocity increments.

Results in Figure 5.23 show that decreasing the x-spacing between elements increases the area power density. Notice that the maximum area power density in Figure 5.23 increases as the y-spacing increases and is a maximum of 1.89 W/m^2 in Figure 5.23c for an x and y spacing of 3.01 cm and 6.35 cm respectively. Unfortunately the lowest possible x-spacing was 3.01 cm which is the point at which the clamps (see Figure 5.13) were in contact with each other. Without the clamps, the next limiting factor would be the thickness of the active elements. Considering the trend in Figure 5.23c it is likely that the area power density would continue to increase if it was possible to further decrease x-spacing. It is assumed that should the x-spacing continue to decrease, increasing amounts of contact between cantilevers would cause much of their motion to be suppressed. This excessive contact and suppressed motion would then significantly reduce power output such that the area power density would begin to decrease. These assumptions imply that an optimum x-spacing exists.

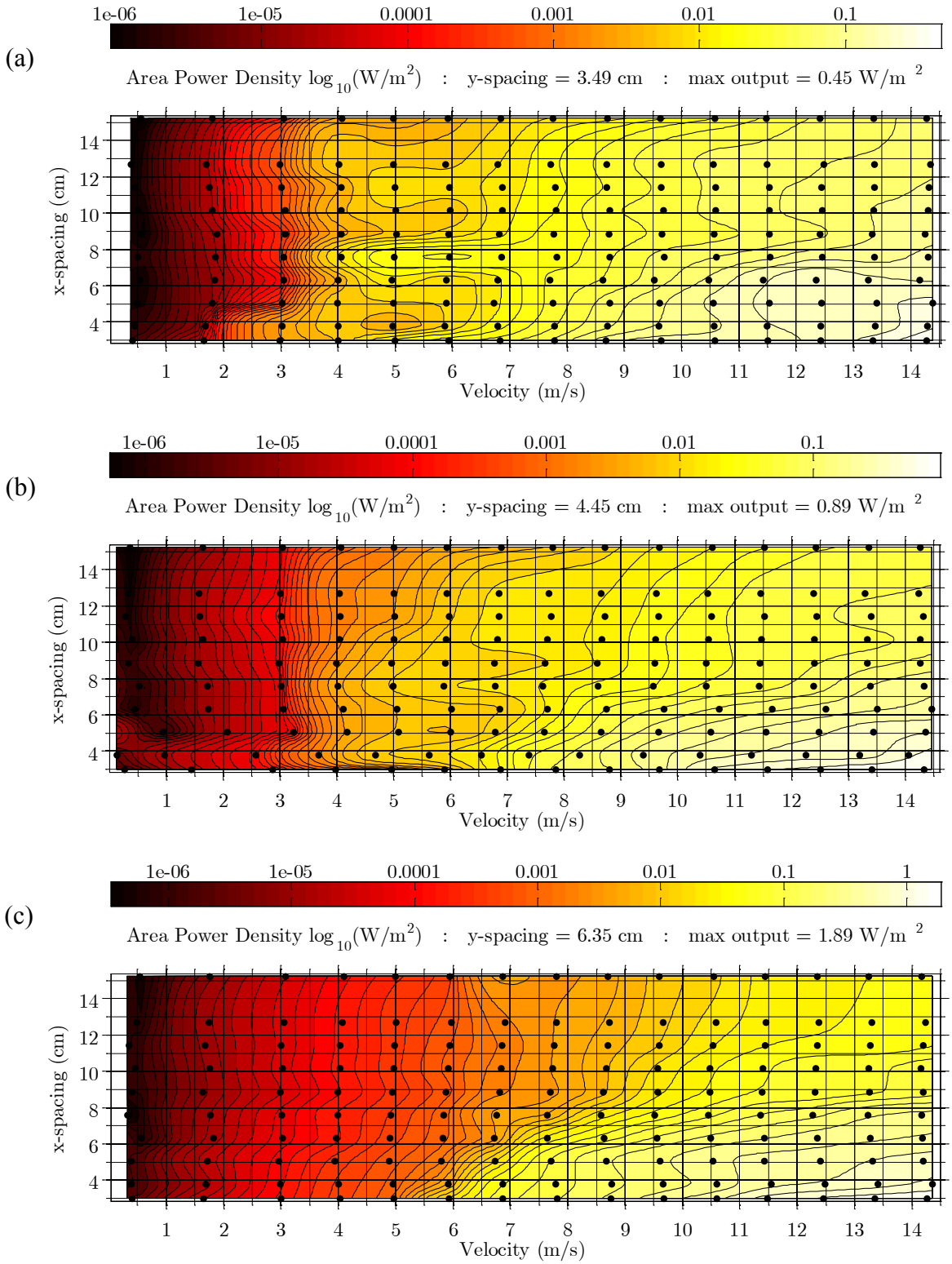

Figure 5.23: Area power density profiles for arrays having a fixed y-spacing of (a) 3.49 cm, (b) 4.45 cm, and (c) 6.35 cm.

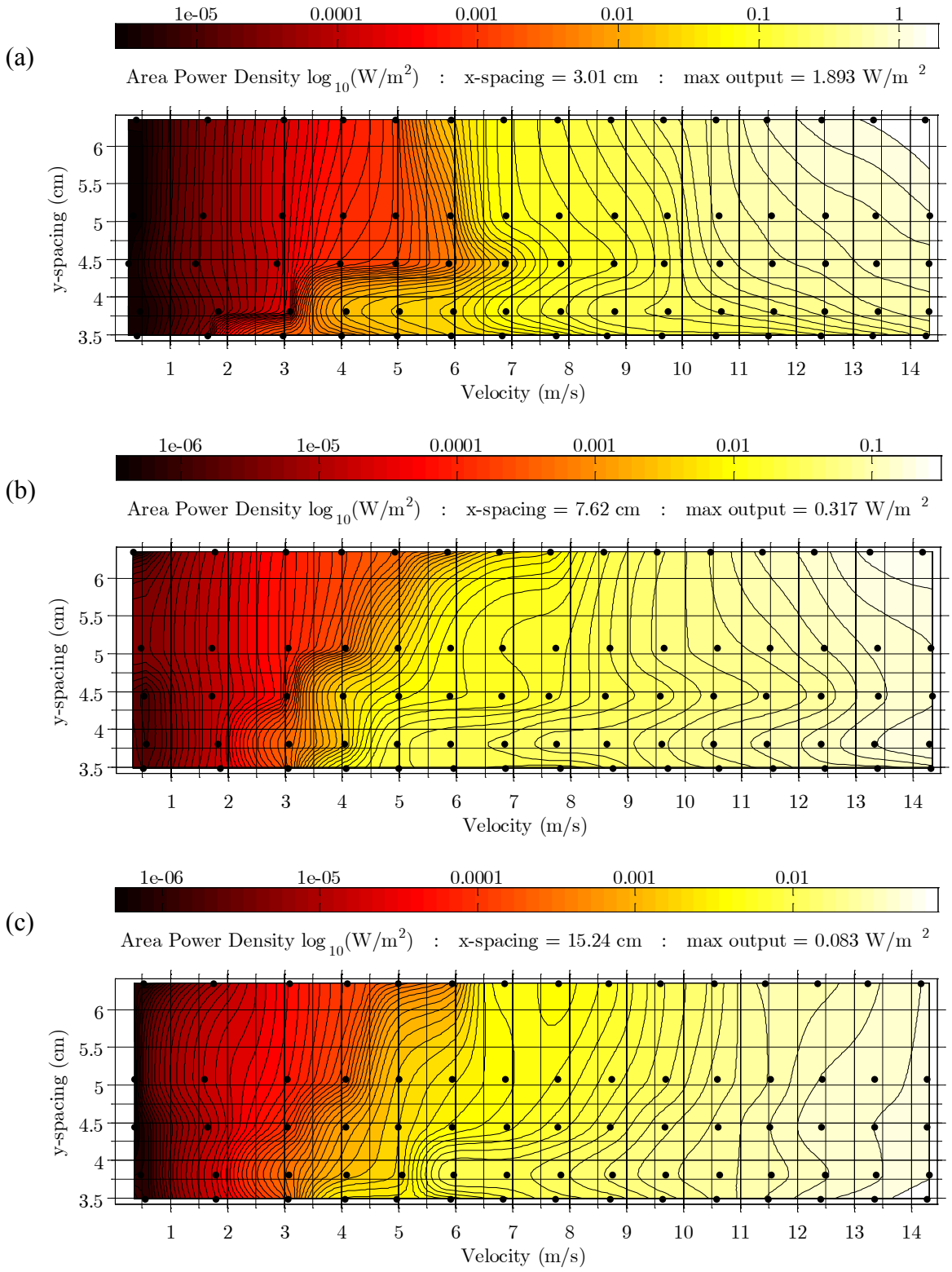

Figure 5.24: Area power density profiles for arrays having a fixed x-spacing of (a) 3.01 cm, (b) 7.62 cm, and (c) 15.24 cm.

Recall that the area power density in Figure 5.23 increased as y-spacing increased for each of the three plots. The plots in Figure 5.24 were created to provide deeper insight to these area power density trends across all y-spacing values rather than x-spacing as displayed in Figure 5.23. Plots a, b, and c in Figure 5.24 show how area power density changes as a function of flow velocity and y-spacing for fixed x-spacing values of 3.01 cm, 7.62 cm, and 15.24 cm respectively. Plots a and b of Figure 5.24 show that power density initially decreases as y-spacing increases. This trend gradually reverses as velocity increases such that power density begins to increase with increased y-spacing. This reversal in power density trends can be understood by considering equations (5.5) and (5.6) along with the following explanation. At low velocities, all elements are driven purely by turbulence such that simply increasing packing density (*i.e.* decreasing y-spacing) increases power density because all cantilevers are producing similar amounts of very low power. As velocity increases, the waving mode vibration begins as discussed in Section 5.2.4.2. The waving mode array dynamics are highly coupled and cause an exponential increase in power output of each element. During this highly coupled waving state of vibration, reducing the packing density (*i.e.* decreasing y-spacing) to improve flow conditions within the array results in a greater increase in output compared to adding more elements to the array.

Plot c of Figure 5.24 shows that power density decreases as y-spacing increases for all velocities. As discussed in the previous paragraph, this decreasing trend suggests that turbulence-induced vibration rather than waving mode vibration is the dominate form of excitation within the array. In this case, increasing packing density also increases power density. Note that Figure 5.24c is for very large x-spacing thus very low power density, and therefore should not be

considered as a general representation of power density trends expected from a well-designed array.

The area power density trend in Figure 5.24a will likely continue to increase as y-spacing increases. It is obvious; however, that eventually an increase in y-spacing will cause a decrease in area power density because the number of power producing elements is decreasing. This suggests that similar to the x-spacing an optimum y-spacing also exists. Further investigation is required to determine this optimum x-y spacing along with scalability and CFD modeling, all of which will be the primary focus of future work.

5.5 Chapter Summary

This Chapter presented results and observations from a thorough experimental investigation of large arrays of piezoelectric grass harvester prototypes. Results demonstrate that large arrays of flexible structures possess dynamic characteristics which make them unique and effective energy harvesting devices. It was shown that unlike earlier studies performed with single cantilevers, the presence of a bluff body does not significantly contribute to the power output of the array. Early large array investigations showed that when the flow velocity reaches a critical point, elements in the array are forced into a resonance condition where they experience large amplitude, persistent vibration. This waving mode resonance state is called *honami* and has been found to be an extremely robust excitation mechanism for flow-induced vibration energy harvesting. Because a harvester of this type could potentially consist of hundreds or thousands of elements, it would continue to produce power even if several of the elements should become damaged. This redundancy of the biologically inspired design makes large array harvesters ideal for applications requiring long term survivability in uncontrolled environments.

The most attractive feature of the excitation mechanism that causes waving mode vibration is that large amplitude vibrations were observed to continue even after the velocity was increased by 100%. From an energy harvesting perspective, this type of broadband performance is extremely valuable. Experiments showed that waving mode vibration of the array elements occurred at nearly the same velocity both with and without a bluff body. Therefore, another advantageous feature of the waving mode excitation is that it appears to be unaffected by the presence of large-scale turbulence upstream of the array.

The model used to predict the minimum velocity at which large amplitude waving mode vibrations are initiated was developed by Finnigan in 1979 [115]. Upon observation of wheat crops waving in the wind, Finnigan was able to relate the wheat height and natural frequency to the flow velocity required for the onset of waving mode vibration. While this relationship given in equation (5.1) estimates the frequency of the fluid force, a model describing the force magnitude or amplitude of vibration is still currently under investigation.

The piezoelectric grass arrays in this study were composed of passive and active elements. Passive elements were spring steel cantilevers with uniform cross section and active elements were made by bonding a piezoelectric material to passive elements. Eventually, a tip mass was added to the active elements in order to tune them to the same natural frequency as the passive elements.

Active elements were strategically positioned throughout the array in order to provide an average power output profile for the entire array. Initial experiments were performed on three array configurations each for 14 velocity increments. Results of this initial study showed that in-line (type-1 and type-2 arrays from Figure 5.4) rather than staggered (type-3) configurations easily achieved waving mode vibration as predicted by equation (5.1). These early experiments

also showed that the waving mode vibration amplitude increased significantly when all elements in the array had approximately the same natural frequency. Considering these observations and results from the early experiments, a more in-depth analysis was performed on in-line arrays where all elements had the same natural frequency.

Power estimates from the in-depth analysis were calculated from 50 different array configurations each for 15 velocity increments. A maximum estimated area power density of 1.89 W/m^2 was achieved. Results from all 792 tests provided trends in power output versus velocity, x-spacing, and y-spacing. It was shown that maximum power density was achieved by minimizing the streamwise gap between elements (x-spacing) and maximizing the y-spacing. These results suggest that an optimum x-y spacing exists which can be attained by minimizing the x-spacing and maximizing the y-spacing. Future work should focus on determining this optimum spacing along with scalability of the array and modeling techniques.

CHAPTER VI

ENERGY HARVESTING FROM THE DUAL CANTILEVER FLUTTER PHENOMENON

6.1 Introduction

Perhaps the oldest and most common form of flow-induced vibration discussed in the literature is vortex-induced vibration (VIV) [38,39,119–124]. Another form of well documented flow-induced vibration popular among those in the aerospace community is flutter [125–128]. This chapter presents a preliminary study on a newly discovered form of flow-induced vibration that occurs with two identical adjacent cantilevers in cross-flow. This flow-induced vibration phenomenon will be referred to here as dual cantilever flutter (DCF).

For the past several decades, many authors have successfully investigated flow-induced vibration energy harvesting techniques that can primarily be categorized as either VIV [2,13,14,40,42,43] or flutter [15,17,49,54,55,57–59]. This chapter will also show the results of an experimental proof-of-concept case study performed with a novel DCF energy harvesting device.

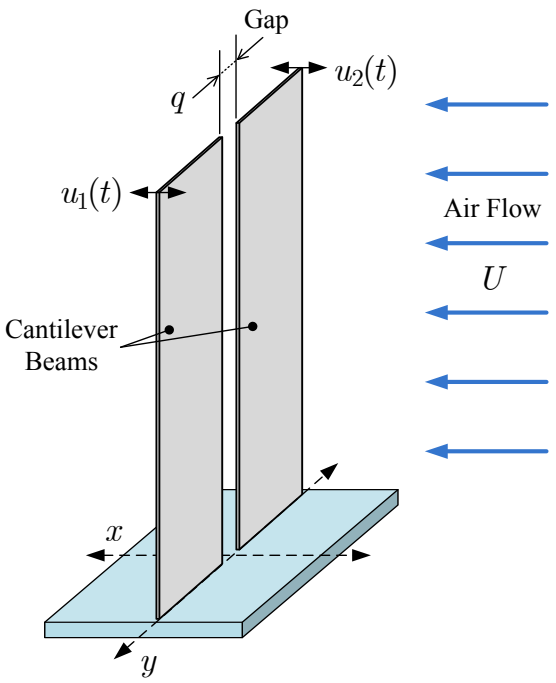

Figure 6.1: A schematic used to illustrate critical components of the dual cantilever flutter mechanism showing identical cantilevered beams positioned side-by-side and oriented perpendicular to air flow.

6.1.1 The Dual Cantilever Flutter Concept

It was demonstrated in Chapter 5 that large arrays of cantilevers experienced large amplitude persistent vibration when exposed to air flow at a certain and predictable velocity [129,130]. While performing wind tunnel experiments on these large arrays of cantilevers, the DCF flow-induced vibration phenomenon was first observed. These early observations of DCF occurred when only two cantilevers were placed side-by-side and positioned such that their faces were perpendicular to low velocity (~6 m/s) air flow. See Figure 6.1 for a schematic of the DCF mechanism. At the appropriate combination of both gap distance (q) between the cantilevers and flow velocity (U), both cantilevers experienced large amplitude persistent vibration at their fundamental bending mode. Cantilever tip displacements are shown in Figure 6.1 as u_1 and u_2 for beam #1 and beam #2 respectively. Visual observations confirmed by laser displacement

measurements showed that during DCF the tip displacements of the two cantilevers are consistently 180 degrees out of phase.

Several series of experiments showed that the cantilevers began to oscillate at relatively small amplitudes where a slight increase of flow velocity initially caused a large increase in the amplitude of vibration. The velocity that caused this large amplitude state of vibration will be referred to as the *lock-in* velocity which is a term adopted from numerous studies on the topic of vortex-induced vibration. During DCF, vibration amplitude and frequency remain nearly constant even after increasing the flow velocity to more than twice the lock-in velocity. Because a large range of flow velocity is able to excite the cantilevers at or near resonance, there may be many cases were DCF-type excitation can cause structural fatigue, unwanted acoustic noise, and even catastrophic structural failure. In energy harvesting applications, this ability to excite the beams at or near resonance for a large velocity range is most desirable. For example: if an energy harvester is to be implemented in an environment with highly unsteady fluid flow, a DCF-type harvester could be designed to operate at resonance for the entire flow velocity range.

6.1.2 Modeling Approach

The analytical model presented in this chapter and the related CFD model discussed in Appendix B are based on a lumped parameter system. First, a single-degree-of-freedom lumped parameter model was developed for both beams without considering fluid damping or coupling effects. Fluid damping was then added to the lumped parameter model. These fluid damping effects were then validated experimentally with results of a single beam in air. The lumped parameter equivalent stiffness and drag coefficient were then experimentally validated the with static deflection measurements of a single beam over a large range of flow velocities. After the single-

degree-of-freedom lumped parameter model was developed and experimentally validated for both single beams, fluid coupling effects between the beams were then considered.

These fluid coupling effects were first implemented and experimentally validated in the lumped parameter model (now a two-degree-of-freedom system) for the case of no flow velocity. This no flow velocity fluid coupling is referred to as *entrainment* or *sympathetic vibration*. The final task of the modeling approach was to add a flow-induced vibration component to the lumped parameter model, thus capturing the full DCF dynamics. See Table 6.2 for a definition of several constants used in this study. Both the entrainment and flutter dynamics of an equivalent 2-D lumped parameter system were also successfully modeled in CFD simulations using ANSYS-CFX. Meshing details and preliminary results of the CFD simulations are discussed in Appendix B.

6.2 Entrainment Modeling

One would expect that as a single beam vibrates, it moves through the surrounding fluid (air in this case) which causes the fluid to move. When two cantilevers are positioned as shown in Figure 6.1, the dynamics of one beam affect the dynamics of the other beam via fluid coupling. The behavior of two or more lightly coupled systems having similar dynamics can become synchronized; *i.e.* their relative dynamics or motion can become similar or predictable. This synchronizing dynamic coupling is called *entrainment* or *sympathetic vibration*.

6.2.1 Observations of Entrainment for a Distributed Parameter System

The effects of entrainment can clearly be seen from the results of a simple experiment using two identical cantilevers positioned as shown in Figure 6.1. A tip mass was used to *fine-tune* the natural frequency of each cantilever to be approximately 9.28 Hz.

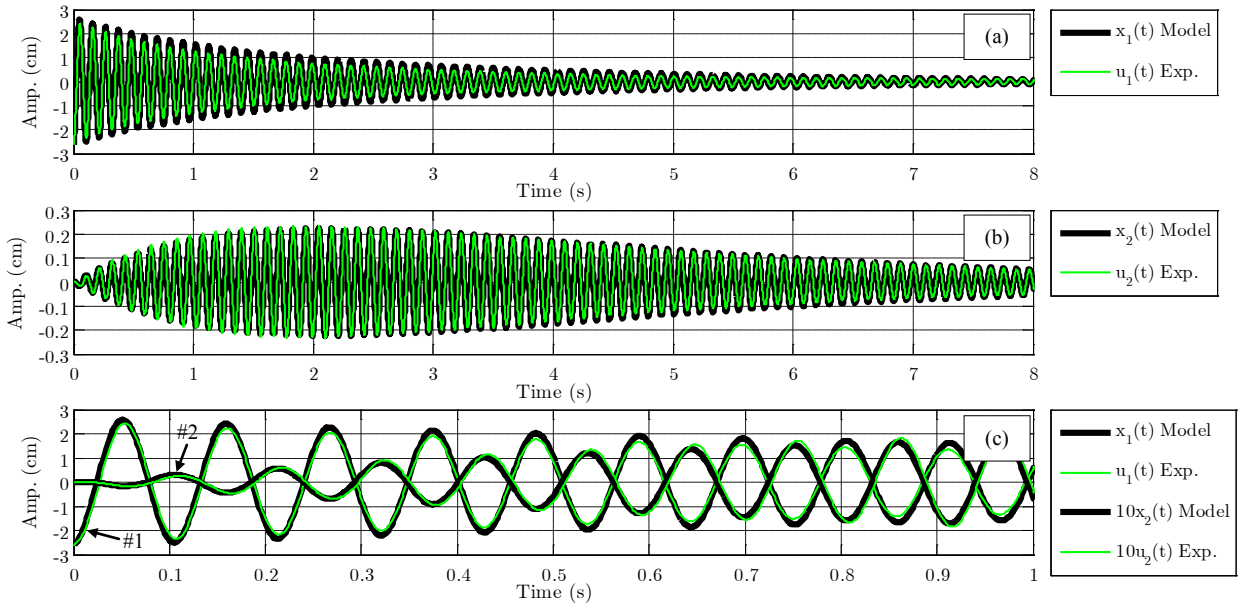

Figure 6.2: Entrainment modeling results showing good agreement between the measured tip displacements of the cantilever beams compared to the displacements of the equivalent lumped masses of the entrainment model for (a) beam and plate #1, (b) beam and plate #2, and (c) both beams and plates.

Then, for the case of no flow velocity ($U = 0$), cantilever #1 began with an initial static tip deflection while cantilever #2 remained at its neutral position (no deflection). After cantilever #1 was released from its initially deflected position, cantilever #2 began to oscillate. The amplitude of cantilever #2 grew gradually before eventually reaching a maximum where the amplitude then began to decay at a rate similar to that of an underdamped oscillator. Even though the motion of cantilever #1 began to excite cantilever #2, the response of cantilever #1 appeared to behave as though there was no coupling between the beams. Results of this experiment are shown in Figure 6.2. Note that the amplitudes of beam and plate #2 in Figure 6.2c are increased by a factor of 10 to show in greater detail their displacements relative to beam and plate #1. It is interesting to note that the displacements of both beams appeared as if they were forced to be 180 degrees out of phase from each other while they oscillated.

A close look at Figure 6.2c shows that the beam initially at rest (beam #2) immediately begins to move toward beam #1 as beam #1 approaches it. This response suggests that the fluid coupling causes the beams to become attracted to each other. If beam #1 was forced to move very slowly past beam #2 at a frequency much lower than the natural frequency of beam #2, it is assumed that fluid coupling would have little or no effect on beam #2. Similarly, it is assumed that if the gap between the two beams becomes very large, the fluid coupling effects would become negligible. These assumptions along with results shown in Figure 6.2 allow one to make the following two statements regarding the fluid coupling between the two beams. First, the attraction between the beams is proportional to their relative velocity and displacement in the x-direction. Second, the coupling between the beams is proportional to the gap or separation distance in the y-direction.

6.2.2 Lumped Parameter Entrainment Model

Beginning with a simple lumped parameter model, it is possible to approximate the dynamics of two beams as two single-degree-of-freedom rigid plates. Each plate has mass ($\tilde{m}$), viscous damping (c), and stiffness (k) as illustrated in Figure 6.3. The uncoupled system without fluid damping has the following governing equations of motion,

$$\tilde{m}_1\ddot{x}_1 + c_1\dot{x}_1 + k_1x_1 = 0 \tag{6.1}$$

$$\tilde{m}_2\ddot{x}_2 + c_2\dot{x}_2 + k_2x_2 = 0 \tag{6.2}$$

where $\tilde{m}$, c, and k are the equivalent mass, damping, and stiffness of the lumped parameter system, x is the displacement, over-dots denote time derivatives such that $\dot{x}$ and $\ddot{x}$ are the velocity and acceleration respectively. Subscripts 1 and 2 will be used throughout this section to denote plate #1 and plate #2 respectively.

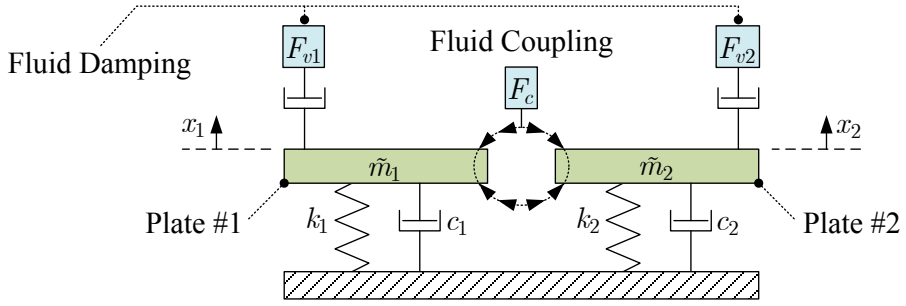

Figure 6.3: A schematic of the lumped parameter system used for the dual cantilever entrainment model.

Fluid damping is estimated by using the drag force equation where the total velocity of the surrounding fluid is estimated to equal the velocity of the plate. Note that the free-stream flow velocity of the surrounding fluid is zero for the entrainment model. The viscous fluid damping force for each plate can therefore be expressed as,

$$F_{v1} = \frac{1}{2}\rho_f A_1 C_{Dv1} \dot{x}_1 \left|\dot{x}_1\right| \tag{6.3}$$

$$F_{v2} = \frac{1}{2}\rho_f A_2 C_{Dv2} \dot{x}_2 \left|\dot{x}_2\right| \tag{6.4}$$

where ρ_f is the density of the surrounding fluid, A is the equivalent area of the plate which is moving normal to the surrounding fluid, and C_{Dv} is the viscous drag coefficient of the plate. The absolute value on the last terms of Equations (6.3) and (6.4) is necessary in order to preserve the correct sign (direction) of the force acting on the plate.

Recall from the assumptions and experimental observations of Figure 6.2 discussed earlier that the fluid coupling force between the beams is proportional to both relative displacement and relative velocity.

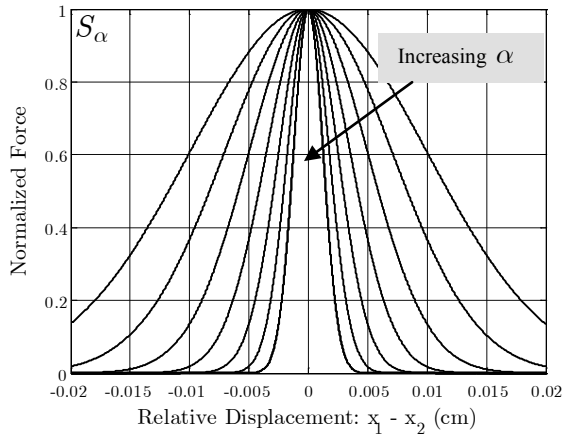

Figure 6.4: Plot of estimated force contribution on plate #1 as a function of both relative displacement between the plates and the displacement coupling parameter (α).

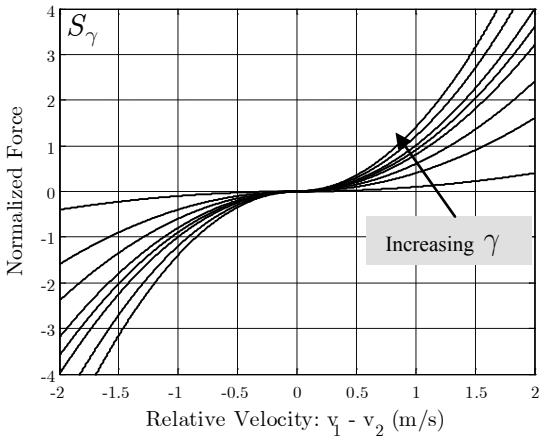

Figure 6.5: Plot of estimated force contribution on plate #1 as a function of both relative velocity between the plates and the velocity coupling parameter (γ).

The coupling force estimate associated with relative displacement of the two plates can be expressed as,

$$S_\alpha = \frac{1}{\left[1 + \left(x_1 - x_2\right)^2\right]^\alpha} \tag{6.5}$$

where α is the displacement coupling parameter. Equation (6.5) is a smooth unit impulse function that equals unity when the plate displacements are equal ($x_1 = x_2$) and approaches zero when the plate displacements become far apart. Increasing α increases the rate at which Equation (6.5) approaches zero. Figure 6.4 displays trends of the displacement coupling force as functions of both relative plate displacement and coupling parameter α. The coupling force estimate associated with relative velocity of the two plates can be given as,

$$S_{\gamma 1} = \gamma\left(\dot{x}_1 - \dot{x}_2\right)\left|\dot{x}_1 - \dot{x}_2\right| \tag{6.6}$$

$$S_{\gamma 2} = \gamma\left(\dot{x}_2 - \dot{x}_1\right)\left|\dot{x}_1 - \dot{x}_2\right| \tag{6.7}$$

where γ is the velocity coupling parameter. Notice that Equations (6.6) and (6.7) have a form similar to that of the previously defined fluid damping terms given in Equations (6.3) and (6.4). Again, the absolute value on the last two terms of Equation (6.6) is used to preserve the sign of the relative velocity of the two plates. This absolute value makes Equation (6.6) unsymmetrical unlike Equation (6.5). Figure 6.5 shows trends of Equation (6.6) as functions of relative velocity of the two plates and coupling parameter γ. Equations (6.5) and (6.6) can then be multiplied together to form the total fluid coupling force estimate which can be defined with the following expressions.

$$F_{c1} = \frac{\gamma\left(\dot{x}_1 - \dot{x}_2\right)\left|\dot{x}_1 - \dot{x}_2\right|}{\left[1 + \left(x_1 - x_2\right)^2\right]^{\alpha}} \tag{6.8}$$

$$F_{c2} = \frac{\gamma\left(\dot{x}_2 - \dot{x}_1\right)\left|\dot{x}_1 - \dot{x}_2\right|}{\left[1 + \left(x_1 - x_2\right)^2\right]^{\alpha}} \tag{6.9}$$

Now Equations (6.8) and (6.9) can be combined with Equations (6.1) through (6.4) to form Equations (6.10) and (6.11) which are the equations of motion for the two-degree-of-freedom, lumped parameter system with fluid damping and fluid coupling.

$$\tilde{m}_1\ddot{x}_1 + c_1\dot{x}_1 + k_1x = \frac{\gamma\left(\dot{x}_1 - \dot{x}_2\right)\left|\dot{x}_1 - \dot{x}_2\right|}{\left[1 + \left(x_1 - x_2\right)^2\right]^{\alpha}} - \frac{1}{2}\rho_f A_1 C_{Dv1}\dot{x}_1\left|\dot{x}_1\right| \tag{6.10}$$

$$\tilde{m}_2\ddot{x}_2 + c_2\dot{x}_2 + k_2x_2 = \frac{\gamma\left(\dot{x}_2 - \dot{x}_1\right)\left|\dot{x}_1 - \dot{x}_2\right|}{\left[1 + \left(x_1 - x_2\right)^2\right]^{\alpha}} - \frac{1}{2}\rho_f A_2 C_{Dv2}\dot{x}_2\left|\dot{x}_2\right| \tag{6.11}$$

This coupled, two-degree-of-freedom lumped parameter model was solved numerically using a standard ordinary differential equation solver (ODE45) with MATLAB programming software. Initial velocity and displacement for plate #2 were set to zero, while plate #1 had zero initial velocity and a non-zero initial displacement. All initial conditions can be summarized as,

$$\text{Initial Conditions} \begin{cases} x_1(0) = x_{1i} \\ \dot{x}_1(0) = 0 \\ x_2(0) = 0 \\ \dot{x}_2(0) = 0 \end{cases} \tag{6.12}$$

where x_{1i} is the initial displacement of plate #1. This initial displacement was set equal to the measured value of initial displacement used in the dual cantilever entrainment model validation experiments.

6.2.3 Parameter Estimation & Results

Results of the numerical simulations using Equations (6.10) through (6.12) agree quite well with experimental measurements as shown in Figure 6.2; however, these results are for only one gap distance and only one initial deflection. An entrainment parameter estimation study was performed for eleven gap distances ranging from 0.66 cm to 2.49 cm. Three different initial displacements ranging from 0.5 cm to 2.54 cm were used at each of the eleven gap distances. The simulated displacement response of both beams for all 33 entrainment cases was matched to the experiments by adjusting the two coupling parameters γ and α along with the viscous drag coefficient C_{Dv}. The goal of this parameter estimation study was to help identify trends in the three parameters as a function of gap distance. See Table 6.2 for a definition of several constants used in this study.

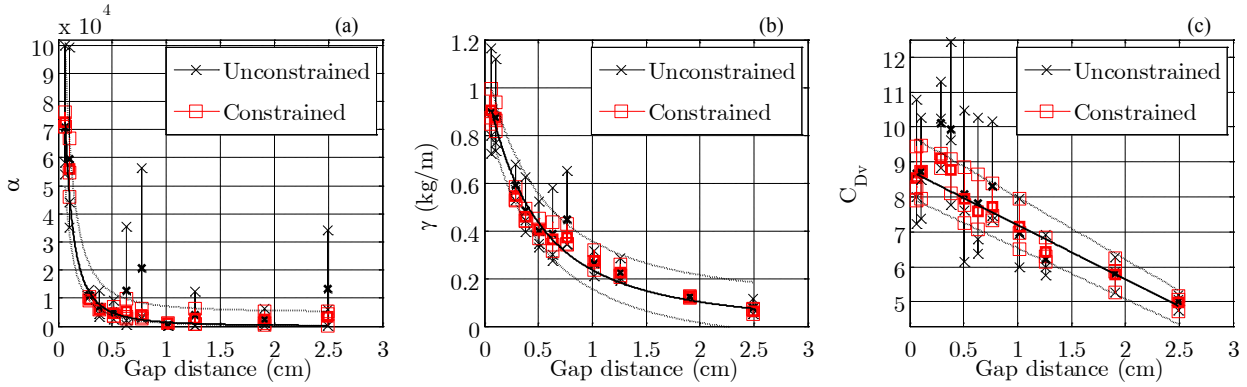

Figure 6.6: Summary of parameter estimation results for the dual cantilever lumped-mass entrainment model showing the (a) displacement coupling parameter α, (b) velocity coupling parameter γ, and (c) viscous drag coefficient C_{Dv}.

Initially, an unconstrained parameter estimation study was performed and the average trend as a function of gap distance was identified for each of the three parameters. Results of the parameter estimation simulations are summarized in Figure 6.6 where the bold x's (×) and bold squares (□) represent the average parameter value found for the three different initial conditions. Using average trends of the unconstrained parameter values, constraint boundaries (shown as dotted lines in Figure 6.6) could then be defined for each of the three parameters. A second parameter estimation study was then performed for all 33 entrainment cases where the parameters were constrained within the boundaries.

Average trends (shown as solid black lines in Figure 6.6) were then fitted to the constrained parameter estimation results. Results of the two coupling parameters (α and γ) were fitted to inverse-square functions which can be defined as,

$$\alpha(q) = \frac{O_1}{\left(q + O_2\right)^2} \tag{6.13}$$

$$\gamma(q) = \frac{O_3}{\left(q + O_4\right)^2} \tag{6.14}$$

Table 6.1: Summary of coefficients used to define the parameter functions fitted to the constrained parameter estimation results for the lumped mass entrainment model.

Parameter function	*Equation*	*Coefficient*	*Value*	*Units*
$\alpha(q)$	(6.13)	O_1	0.1710	m^2
		O_2	8.728×10^{-4}	m
$\gamma(q)$	(6.14)	O_3	8.374×10^{-8}	kg*m
		O_4	9.119×10^{-3}	m
$C_{Dv}(q)$	(6.15)	O_5	-55.38	[ ]
		O_6	3.125	[ ]

and the viscous drag coefficient was fitted to a linear function given as,

$$C_{Dv}(q) = O_5\, q + O_6 \tag{6.15}$$

where q is the gap distance (in meters) and coefficients O_1 through O_6 are constants defined in Table 6.1.

6.2.4 Error Analysis

An error analysis was performed between experimental results of the 33 entrainment tests and a final set of simulations. These final simulation were performed using the analytical model as defined in equations (6.10) through (6.15) with the fitted parameter functions for γ, α, and C_{Dv}. The mean squared error (MSE) for each entrainment case was calculated using the following expression,

$$MSE = \frac{1}{n}\sum_{i=1}^{n}\left(x_i - u_i\right)^2 \tag{6.16}$$

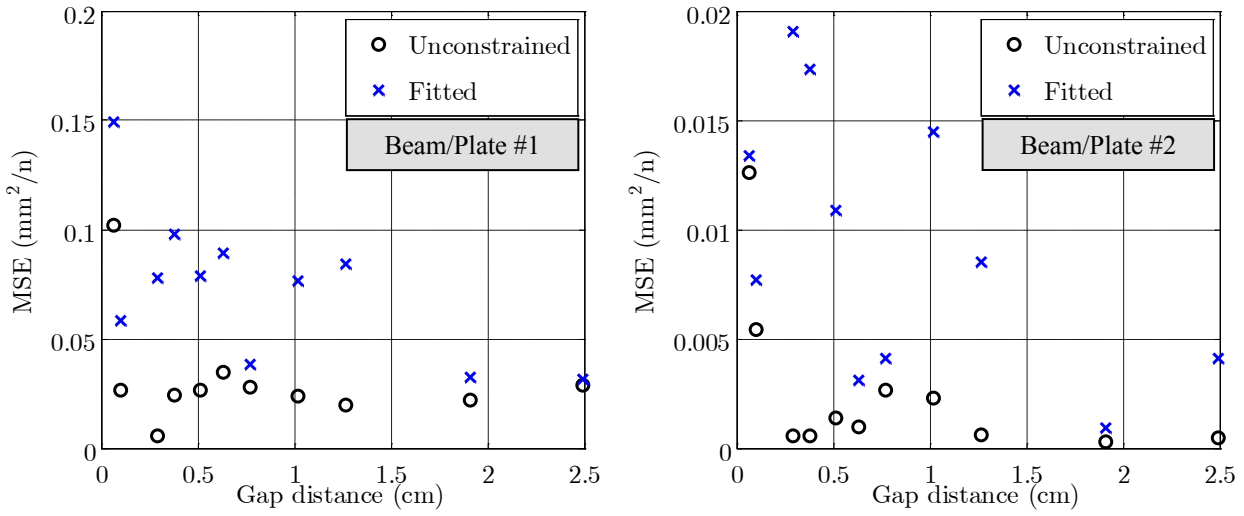

Figure 6.7: Summary of entrainment modeling results showing the mean squared error between model and experiment at various gap distances calculated for the unconstrained parameter estimation results and the fitted parameter functions.

where x is the simulated displacement array, u is the measured displacement array, and n is the number of elements in x and u. Recall that three different initial conditions were used at each of the eleven gap distances; therefore, three MSE values were calculated for each gap distance. The average of these three MSE values is plotted in Figure 6.7 (shown as blue x's) at each gap distance for both masses. Also plotted in Figure 6.7 are the average MSE values calculated using parameters from the unconstrained parameter estimation results (shown as black circles '**o**'). As expected, the error increased when using the fitted parameter functions; however, the maximum average magnitude of error was approximately 0.39 mm or only 2.2% of the average initial deflection.

6.3 Dual Cantilever Flutter Modeling

Previous steps of the modeling procedure presented and experimentally validated the lumped parameter structural dynamics, fluid damping, and fluid coupling between two adjacent beams

vibrating in a quiescent fluid. The final goal of the DCF model was to predict not only the entrainment dynamics, but also the flow-induced excitation at multiple flow velocities and gap distances. This section will discuss two additional components of the lumped parameter model which will predict mean deflection and flutter amplitude of the cantilevers as a function of flow velocity.

6.3.1 Lumped Parameter Model

The flow-induced drag force on both beams can be estimated with the well-known drag force equation which can be expressed as,

$$F_{d1} = \frac{1}{2}\rho_f A_1 C_{Dd1} U^2 \tag{6.17}$$

$$F_{d2} = \frac{1}{2}\rho_f A_2 C_{Dd2} U^2 \tag{6.18}$$

where ρ_f and A are defined for equations (6.3) and (6.4), C_{Dd} is the equivalent drag coefficient, and U is the free-stream flow velocity. As in the previous section, subscripts 1 and 2 denote plate #1 and plate #2 respectively. Notice that these drag force expressions are independent of position, velocity, or acceleration of the beams and therefore create a mean deflection which is proportional to the square of the flow velocity.

As was observed in many experiments, the two cantilevers were stable as long as the total displacement amplitude remained below a certain threshold. Prior to flutter, the beams experienced static deflection due to the drag force defined by equations (6.17) and (6.18). At a certain flow velocity, this static deflection exceeds the stable threshold causing the system to go unstable, thus producing limit-cycle oscillations. These flow-induced vibration characteristics are similar to those of a Van der Pol oscillator. The Van der Pol equation is similar to the differential

equation of motion for a single-degree-of-freedom, spring, mass oscillator with a non-linear, position-dependent damping term. This term causes the system to have a so-called *isolated* and unstable periodic solution called a limit-cycle [131]. A Van der Pol model has been used in previous work to predict flow-induced vibration caused by reed flutter [70].

The key component of a Van der Pol oscillator equation that dictates the stability of the system can be expressed as,

$$F_{p1} = \beta\left(\theta^2 - x_1^2\right)\dot{x}_1 \tag{6.19}$$

$$F_{p2} = \beta\left(\theta^2 - x_2^2\right)\dot{x}_2 \tag{6.20}$$

where β is the linearity parameter, and θ is the stability threshold parameter. The linearity parameter is always positive and determines how linear the system behaves such that a smaller β value produces a more linear (sinusoidal) response. Note that the terms in the parentheses in equations (6.19) and (6.20) can change sign depending on the deflection (x) and the stability threshold parameter (θ).

When equations (6.17) through (6.20) are inserted into the right-hand side of equations (6.10) and (6.11), the full DCF flutter model can be expressed as,

$$\tilde{m}_1\ddot{x}_1 + c_1\dot{x}_1 + k_1x_1 = F_{c1} - F_{v1} + F_{d1} + F_{p1} \tag{6.21}$$

$$\tilde{m}_2\ddot{x}_2 + c_2\dot{x}_2 + k_2x_2 = F_{c2} - F_{v2} + F_{d2} + F_{p2} \tag{6.22}$$

where the four terms on the right-hand side of both equations can be referred to as fluid coupling force (F_c), viscous damping force (F_v), drag force (F_d), and flutter force (F_p). Recall the flutter force defined in equations (6.19) and (6.20), and notice that the terms in parentheses and

β are multiplied by velocity ($\dot{x}$) and therefore create a position-dependent damping expression. If x exceeds a given value of θ, this damping expression becomes negative. Because there are other forms of damping in the full DCF model, it is not until this negative damping expression exceeds a certain limit that the system becomes unstable and flutter occurs.

6.3.2 Parameter Estimation & Results

A parameter estimation study was performed using the full model given in equations (6.21) and (6.22) with the fitted parameter functions given in equations (6.13) through (6.15). The primary goal of this study was to validate the final form of the proposed model and to identify trends in the three remaining unknown parameters C_{Dd}, β, and θ as functions of gap distance (q) and flow velocity (U). For simplicity, it was initially assumed that the linearity parameter (β) could remain constant for a range of gap distances and velocities. This assumption was later validated with results of the parameter estimation study.

For a given gap distance and flow velocity parameters C_{Dd} and θ were varied until the mean displacement and vibration amplitude of the model converged to those from experimental measurements. After the model converged, parameters C_{Dd} and θ were recorded and the velocity or gap distance was incremented. A new set of parameters was recorded for each new set of velocity and gap distance. This procedure was performed for five gap distances ranging from 0.9 mm to 5.3 mm and each gap distance had 20 velocity increments ranging from 0.10 to 15.0 m/s.

For every combination of desired velocity and gap distance, the model was able to very accurately match experimental measurements for both mean displacement and flutter amplitude.

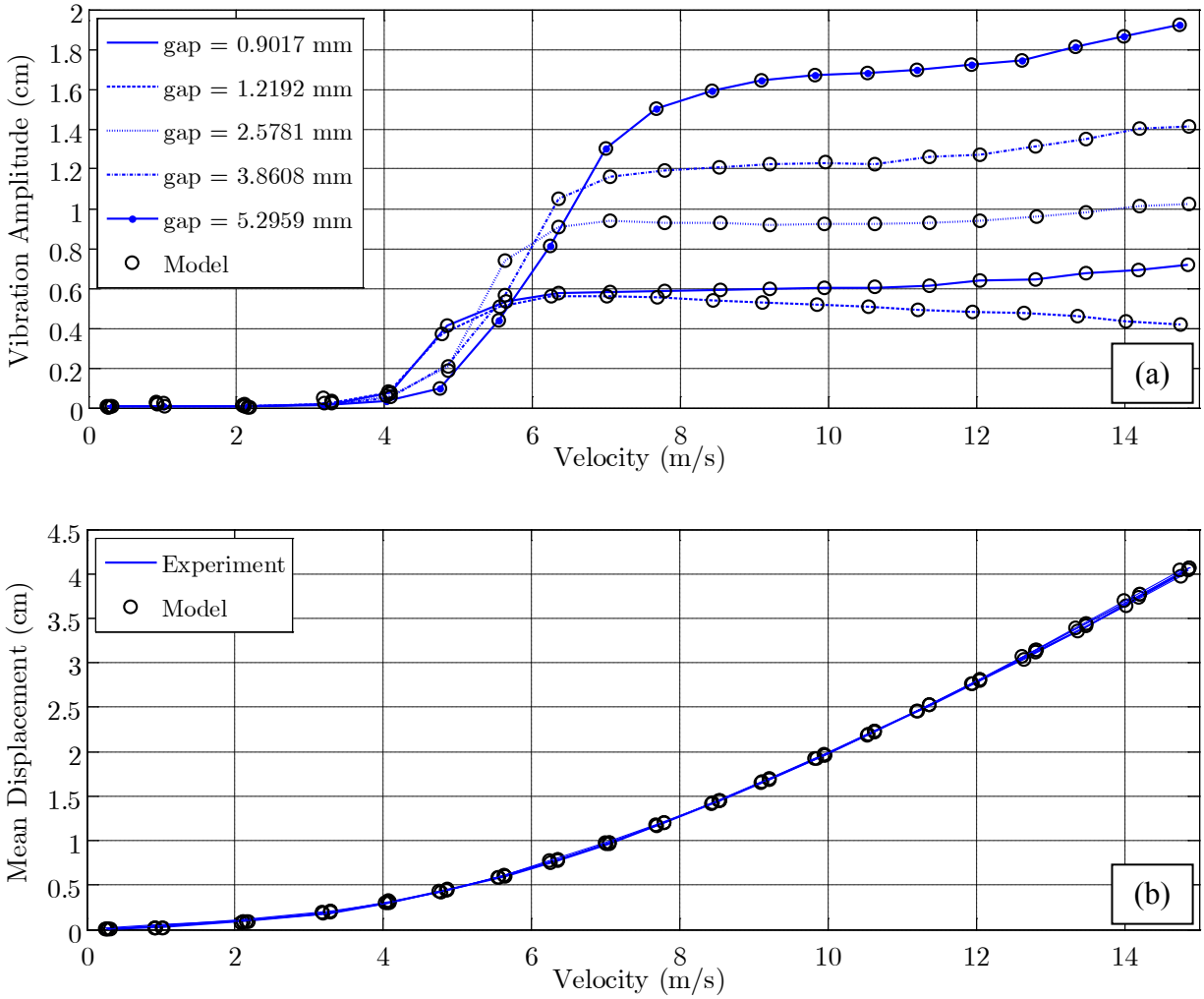

Figure 6.8: Comparison of experimental measurements compared to results of the final DCF model showing (a) average vibration amplitude and (b) mean displacement of both beams as a function of flow velocity and gap distance.

A summary of results from the parameter estimation study is shown in Figure 6.8 where the amplitude of vibration and mean deflection of both beams is given as a function of both flow velocity and gap distance. The blue lines in Figure 6.8 are experimental measurements and the black empty circles (**o**) are solutions of the lumped parameter DCF model from equations (6.21) and (6.22). The mean displacement results shown in Figure 6.8b are plotted for every velocity of all five gap distances. Notice that these mean displacement trends are nearly equal for every gap distance; therefore, it is clear that the drag coefficient is not a function of gap distance.

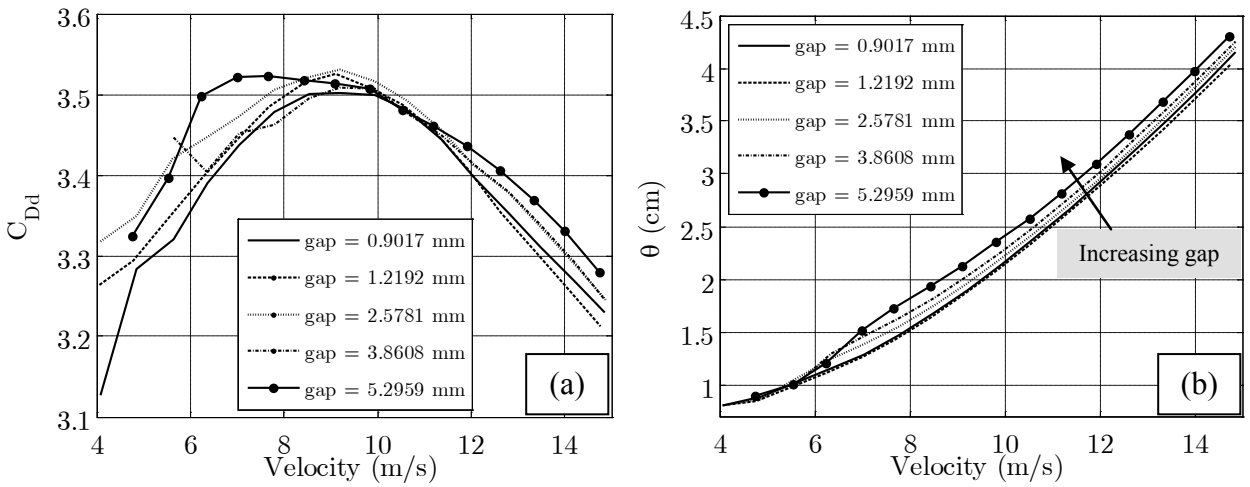

Figure 6.9: Parameter estimation results showing trends in (a) drag coefficient and (b) stability threshold as functions of gap distance and flow velocity.

Figure 6.9 summarizes results of the parameter estimation study where trends in both drag coefficient (C_{Dd}) and stability threshold (θ) are shown as functions of flow velocity and gap distance. Obvious trends are visible for both parameters as functions of flow velocity. The drag coefficient increases as velocity increases until reaching a maximum at approximately 9.0 m/s then gradually decreases as flow velocity increases (see Figure 6.9a). There was no obvious trend in drag coefficient as a function of gap distance. The stability threshold increased exponentially as a function of velocity (see Figure 6.9b). With exception of the two smallest gap distances, it is clear that the stability threshold also increases with increasing gap distance.

Notice that the results in Figure 6.9 are only shown for a velocity range of approximately 4.0 to 15.0 m/s. This limited velocity range is due to the fact that the parameter estimation code (written in MATLAB) was unable to converge on results for C_{Dd} and θ when flutter did not occur. It was also observed that the model was not as sensitive to the stability threshold parameter (θ) when flutter did not occur which was in the lower velocity range (< 4.0 m/s). In fact, θ could be any value ranging from 0 to the minimum value shown in Figure 6.9b

(approximately 0.8 cm) without causing flutter or affecting the mean displacement results. If θ were to exceed this minimum value, then the model would begin to flutter. This lack of convergence and reduced sensitivity to θ is explained by considering how the full model as defined in equations (6.21) and (6.22) can be simplified for the case of no flutter and only static deflection due to drag. For this case, all velocity and acceleration terms go to zero and a single uncoupled solution remains. The full steady-state model for the case of no flutter in a flowing fluid reduces to simply,

$$k_1 x_1 = \frac{1}{2}\rho_f A_1 C_{Dd1} U^2 \tag{6.23}$$

$$k_2 x_2 = \frac{1}{2}\rho_f A_2 C_{Dd2} U^2 \tag{6.24}$$

where the force due to displacement must equal the average drag force of the fluid.

The model results shown in Figure 6.8 for velocities less than 4.0 m/s were produced using the full model from equations (6.21) and (6.22). Values for C_{Dd} and θ were found by extrapolating the trends shown in Figure 6.9. It was understood that because no flutter occurred in this velocity range, the values used for θ had no effect on the results which obeyed the simplified relationship given in equations (6.23) and (6.24).

Table 6.2 defines all constants used in the lumped parameter modeling discussed in Sections 6.2 and 6.3. Because both beams were nearly identical, their properties were assumed to be identical. The effective area (A) equals the beam width (b) multiplied by an effective beam length of 12.0 mm. This beam length was chosen because the unit depth of the 2-D CFD simulations discussed in Appendix B was also 12.0 mm.

Table 6.2: List of constants used in the lumped parameter entrainment and dual cantilever flutter modeling presented in Sections 6.2 and 6.3.

Property	*Symbol*	*Value*	*Units*
Beam length	L	14.69	cm
Beam width	b	2.540	cm
Beam thickness	h	238.8	μm
Effective mass	$\tilde{m}$	9.669×10^{-4}	kg
Effective stiffness	k	3.287	N/m
Viscous damping	c	6.000×10^{-4}	Ns/m
Effective area	A	3.048×10^{-4}	m^2
Fluid density	ρ_f	1.225	kg/m^3
Linearity parameter	β	$m\times10^4$	kg/m^2s

Making the analytical model area (A) equal to the CFD model area was important when comparing equivalent damping parameters and drag coefficients between the models.

6.4 Experimental Details

Many experiments were performed for two primary reasons. First, results of these experiments were (and will be) used for current (and future) model validation. These models include both analytical and CFD models for both entrainment and flutter dynamics of two adjacent cantilevers in a fluid. The second reason for performing these experiments was to produce proof-of-concept results of a novel DCF energy harvesting device.

6.4.1 Experimental Setup

Both the entrainment and flutter experiments had a similar setup where two identical cantilevers were placed side-by-side as shown in Figure 6.11. Entrainment experiments were performed in stagnant (not flowing) air at a temperature of approximately 25^{o}C. Flutter experiments were performed in a wind tunnel at various steady flow velocities.

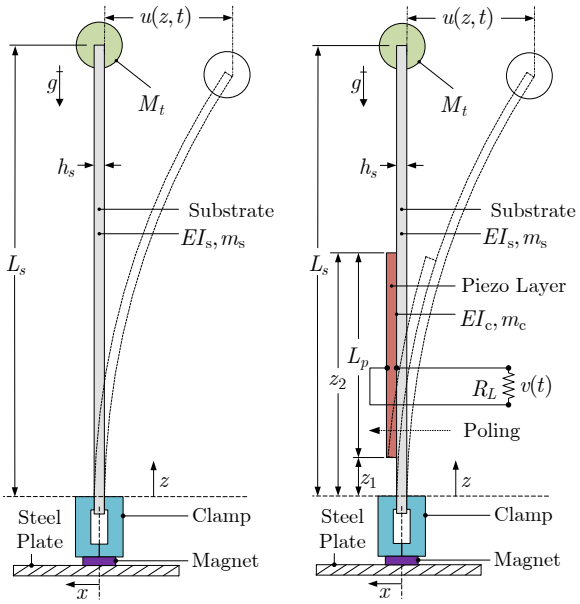

Figure 6.10: Schematics showing details of the (a) passive and (b) active cantilever designs used in the experiments.

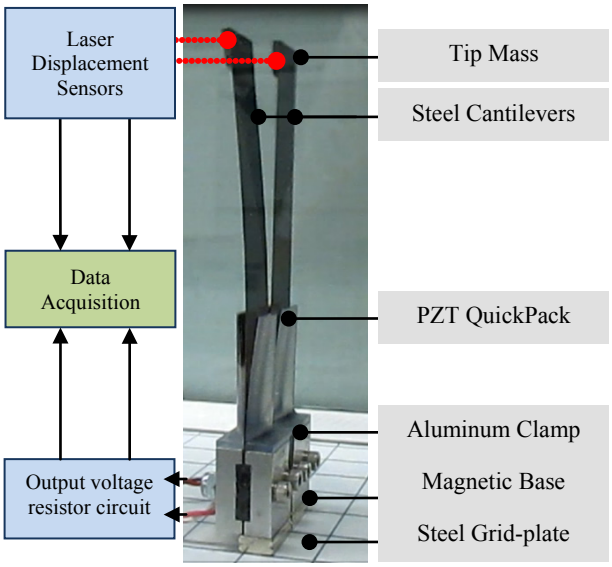

Figure 6.11: A snapshot of the general experimental setup used for both dual cantilever flutter (shown) and entrainment tests.

The tip deflection of each beam was measured simultaneously using a pair of Keyence Corporation laser displacement sensors (Model: LK-G402). Two types of cantilevers referred to here as *passive* and *active* were used in the experiments. Both types of cantilevers had identical lengths, widths, and thicknesses of 14.7 cm, 2.54 cm, and 0.239 mm respectively. (See Table 6.2.) Passive cantilevers had a basic uniform design and were made with spring steel. Active cantilevers were constructed by bonding a QP10n PZT QuickPack (from Mide Technology Corporation) to the base of a spring steel cantilever identical to those used for the passive cantilevers. Tip masses were added to both passive and active cantilevers in order to *fine-tune* their natural frequencies. The natural frequency of each pair of cantilevers was made nearly identical prior to each test. A schematic of the passive and active cantilevers is shown in Figure 6.10. All experiments and results presented in this chapter are for the case of two identical cantilevers, i.e. a pair of passive elements, or a pair of active elements.

6.4.2 Entrainment Tests

Only passive pairs of cantilevers were used in the entrainment experiments because the primary focus of these tests was on fluid coupling effects rather than electromechanical coupling. Two beams were placed next to each other as shown in Figure 6.11 with a known measured gap distance. While measuring and recording tip displacement data for both beams, a single beam was released from an initially deflected state. Displacement data from each sensor was recorded at a sampling rate of 1.0 kHz. After 30 seconds, the vibration amplitude of both cantilevers decayed to nearly negligible values and no further data was collected. This tip deflection data was recorded three times for a given gap distance in order to ensure the quality of measurement. This entire procedure was repeated for a total of 13 gap distances ranging from 0.66 mm to 7.34 cm. Results from one of these experiments is shown in Figure 6.2.

6.4.3 Dual Cantilever Flutter Tests

Both passive and active element pairs were used for the DCF experiments. Both cantilevers were placed in a wind tunnel at a known gap distance, and the velocity in the wind tunnel was adjusted to a desired value. When the velocity became steady, tip displacement and air velocity data were recorded at a sampling rate of 1.0 kHz per-channel for a total of 60 seconds. Active cantilevers were used for the energy harvesting tests where the PZT electrodes of each active element were connected to separate load resistors (R_L) such that they acted as independent circuits (see Figure 6.10b). The load voltage (v) for each active element was then measured and recorded along with velocity data. After 60 seconds of data was gathered at a constant velocity, the velocity was then adjusted and the procedure repeated. Passive element DCF tests were performed at 20 velocity increments and 15 gap distance increments for a total of 300 datasets. Active element tests were performed at 15 velocity increments and 5 gap distance increments for a total of 75 datasets.

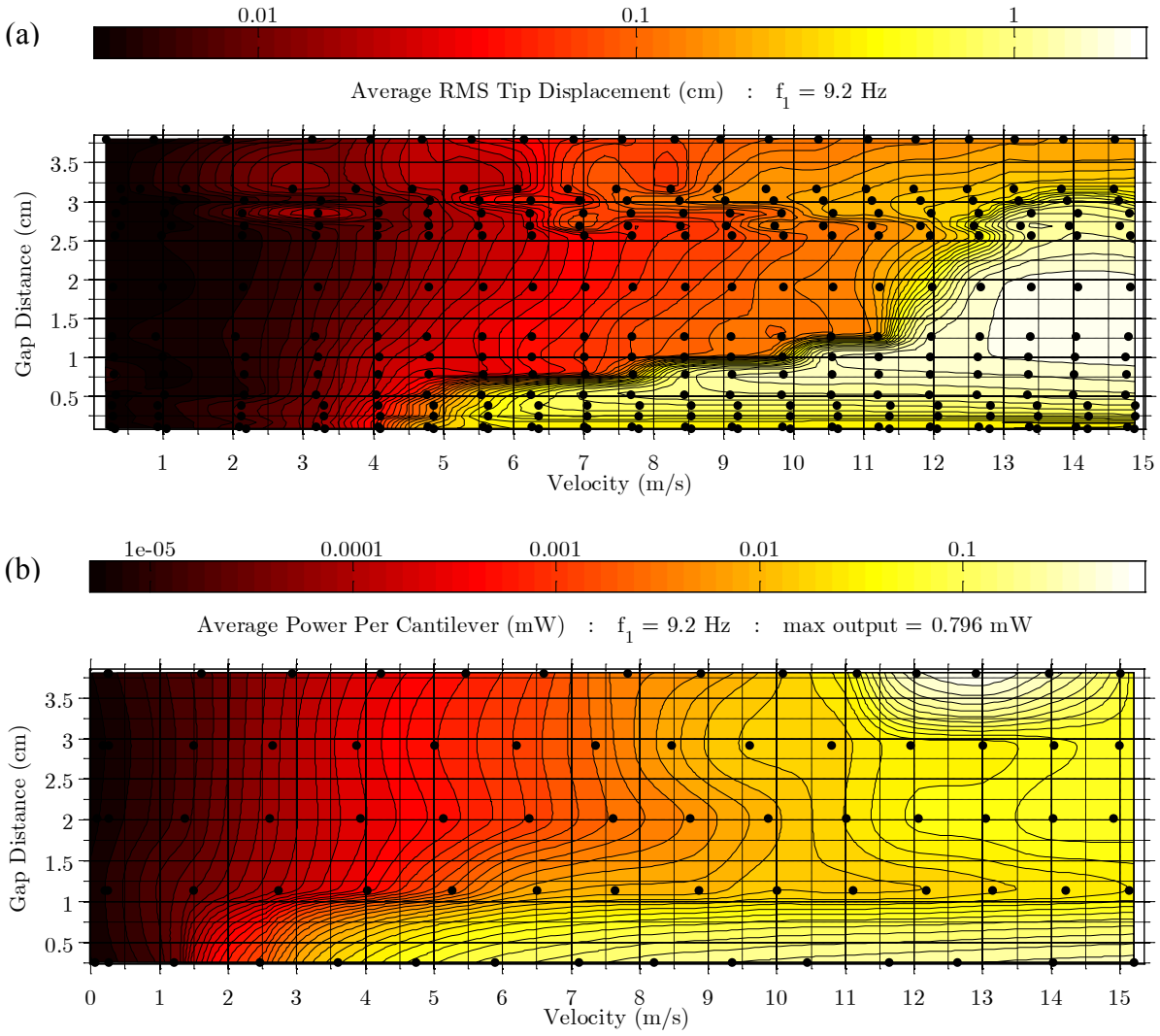

Figure 6.12: Plots summarizing the results of two dual cantilever flutter case studies showing (a) passive cantilever RMS tip displacement, and (b) active cantilever power output both as functions of air velocity and gap distance.

The results of two DCF case studies are summarized in Figure 6.12 where trends in RMS tip displacement and average power output are shown as functions of air velocity and gap distance. Note that the z-axis of both plots is represented in a logarithmic scale. Passive cantilevers were used for the tip displacement data and active cantilevers were used to generate the power data. Tip masses were used to adjust the natural frequency of both pairs to approximately 9.2 Hz. Each

black dot shown on the plots in Figure 6.12 represents the gap distance and average flow velocity for a given dataset.

Figure 6.12a shows clearly defined regions of large and small amplitude vibrations. This large amplitude region is where DCF occurs. Notice that the onset of DCF is highly sensitive to velocity where the amplitude increases suddenly to a high amplitude state with a small velocity increase of only about 0.5 m/s. Figure 6.12a also shows that DCF is highly sensitive to gap distance especially between the range of approximately 0.5 cm to 1.25 cm. Notice that after DCF occurs the flow velocity has very little effect on the vibration amplitude, and the cantilevers become *locked-in* a high amplitude resonance-type state of vibration. The average power trends shown in Figure 6.12b are similar to the tip displacement trends. These power trends show that for smaller gap distances (between 0.25 cm and 1.0 cm) the cantilevers can produce a significant amount of power over a very large range of velocity (from 3 m/s to 15 m/s).

6.5 Chapter Summary

This chapter presents the results of an investigation on a flow-induced vibration phenomenon referred to as dual cantilever flutter (DCF). A lumped parameter entrainment model was able to successfully predict the effects of fluid coupling between two adjacent vibrating beams in air. This chapter discussed how the entrainment model was developed and experimentally validated. Also presented in this chapter was an experimentally validated model for predicting vibration amplitude, and mean deflection during DCF.

A novel DCF energy harvesting device was also presented in this chapter. Results of wind tunnel experiments performed with this novel device show that significant amounts of power can be harvested over a very large range of flow velocity. This energy harvesting capability over such a large velocity range makes DCF an attractive and robust energy harvesting method in areas of highly unsteady fluid flow.

CHAPTER VII

CONCLUDING STATEMENTS

7.1 Master Summary

This dissertation discusses analytical and experimental aspects of energy harvesting for autonomous self-sustaining sensor networks with a robust, biologically-inspired device called piezoelectric grass. The following is a summary of chapters 2 through 6 which highlights the primary findings, successes, and contributions of each chapter.

7.1.1 Chapter 2

Five fluid flow energy harvester concept designs were presented. Operational details, advantages, and disadvantages of each design were discussed. A final biologically-inspired concept design called piezoelectric grass was chosen because it addressed and overcame many of the design issues considered for potential application environments.

The results of an extensive experimental study on several piezoelectric grass harvester prototypes were presented. It was shown that the PZT harvester array (Type-2) was able to achieve a power output of 1.0 mW per cantilever with a mean airspeed of 11.5m/s. The similarly sized PVDF harvester array (Type-1) was expected to produce significantly less power due to a lower electromechanical coupling constant, but was still able to achieve an output of 1.47 μW

per cantilever at 6.7 m/s. From an application standpoint, note that the PZT harvester produced nearly 1000 times the output for approximately 10 times the cost compared to the PVDF harvester. However, when considering long-term deployment in an uncontrolled environment, the soft, flexible PVDF design is much less susceptible to damage than the brittle PZT design.

Harvester array results show that an optimum turbulence condition for maximum power output exists for all array configurations. It is shown that these ideal harvesting conditions are functions of both flow velocity and harvester location downstream of a bluff body. An estimate of the optimum harvester design can be attained by matching the natural frequency of the harvester to the primary vortex shedding frequency of the bluff body. Plots given in Figures 2.9 through 2.14 show how power trends from PVDF arrays appear as large plateaus which span across a wide range of both flow velocity and bluff body distance. This broadband type of behavior from the PVDF array was very different compared to the sharp peak in power output produced by the PZT array. While the array studies presented here were strictly experimental, these results may provide valuable insight for the future development of mathematical models for large harvester arrays containing many more harvester elements.

7.1.2 Chapter 3

A fully coupled electromechanical distributed parameter model for energy harvesting from turbulence-induced vibration of a cantilever unimorph harvester was presented and experimentally validated. The model includes a combination of both statistical and analytical components. The distributed turbulence-induced force was derived using a statistical model called the *acceptance integral* technique. Natural frequencies, mode shapes, and frequency response functions of the harvester were calculated using the Rayleigh-Ritz analytical

approximation method. Lastly, the electromechanical coupling terms of the unimorph harvester were derived from constitutive relationships for the 31 bending mode of a piezoelectric material.

Two custom pressure probes were used to take measurements at several locations in the turbulent wake of a bluff body in air. These measurements were used to calculate the pressure CPSD in equation (3.1) and eventually the modal forcing function given in equation (3.34). Figures 3.8-3.10 show good agreement between experimental measurements and model predictions for tip displacement PSD, load voltage PSD, RMS load voltage, and average power output as defined in equations (3.46), (3.43), and (3.39) respectively.

A brief parameter optimization study was performed using the proposed model. It was shown that simply adding a tip mass could increase the power output by 280%. This drastic increase in power was caused when the natural frequency of the harvester approached the primary vortex shedding frequency of the turbulent flow. For each optimization case, a sweep parameter was set, then a tip mass was iteratively solved for such that the harvester's natural frequency remained constant. The four geometric sweep parameters were chosen to be the length and thickness of the substrate and PZT. For every new geometric parameter value and corresponding tip mass, the power was calculated and plotted as a function of the geometric parameter and load resistance. This parametric sweep optimization study demonstrated that minimizing the thickness of the PZT or substrate, or maximizing the substrate length can cause significant increases in power output.

7.1.3 Chapter 4

The modeling and turbulence measurement techniques presented in this chapter are shown to be quite effective at predicting turbulence-induced vibration. Pressure probes were designed and constructed such that they were able to measure turbulent air flow with a full pressure range of

± 249 Pa and a sensitivity of 0.064 mV/Pa. The probes had an uncompensated bandwidth of approximately 100 Hz until the first acoustic resonance mode caused significant attenuation. An inverse FRF compensation technique was successfully employed and was shown to extend the probe bandwidth by an order of magnitude from 100 Hz to over 1000 Hz. Successful modeling and calibration methods were applied to the pressure probes to ensure reliable measurements even in highly turbulent air flow with a mean velocity range of only (0-12 m/s). Results of three case studies showed that the turbulence-induced vibration predictions agreed well with those measured in experiments. The largest error associated with predicting RMS tip deflection was found to be 0.74% for the unimorph beam design.

7.1.4 Chapter 5

This Chapter presented results and observations from a thorough experimental investigation of large arrays of piezoelectric grass harvester prototypes. Results demonstrate that large arrays of flexible structures possess dynamic characteristics which make them unique and effective energy harvesting devices. It was shown that unlike earlier studies performed with single cantilevers, the presence of a bluff body does not significantly contribute to the power output of the array. Early large array investigations showed that when the flow velocity reaches a critical point, elements in the array are forced into a resonance condition where they experience large amplitude, persistent vibration. This waving mode resonance state is called *honami* and has been found to be an extremely robust excitation mechanism for flow-induced vibration energy harvesting. Because a harvester of this type could potentially consist of hundreds or thousands of elements, it would continue to produce power even if several of the elements should become damaged. This redundancy of the biologically inspired design makes large array harvesters ideal for applications requiring long term survivability in uncontrolled environments.

The most attractive feature of the excitation mechanism that causes waving mode vibration is that large amplitude vibrations were observed to continue even after the velocity was increased by 100%. From an energy harvesting perspective, this type of broadband performance is extremely valuable. Experiments showed that waving mode vibration of the array elements occurred at nearly the same velocity both with and without a bluff body. Therefore, another advantageous feature of the waving mode excitation is that it appears to be unaffected by the presence of large-scale turbulence upstream of the array.

The model used to predict the minimum velocity at which large amplitude waving mode vibrations are initiated was developed by Finnigan in 1979 [115]. Upon observation of wheat crops waving in the wind, Finnigan was able to relate the wheat height and natural frequency to the flow velocity required for the onset of waving mode vibration. While this relationship given in equation (5.1) estimates the frequency of the fluid force, a model describing the force magnitude or amplitude of vibration is still currently under investigation.

The piezoelectric grass arrays in this study were composed of passive and active elements. Passive elements were spring steel cantilevers with uniform cross section and active elements were made by bonding a piezoelectric material to passive elements. Eventually, a tip mass was added to the active elements in order to tune them to the same natural frequency as the passive elements.

Active elements were strategically positioned throughout the array in order to provide an average power output profile for the entire array. Initial experiments were performed on three array configurations each for 14 velocity increments. Results of this initial study showed that in-line (type-1 and type-2 arrays from Figure 5.4) rather than staggered (type-3) configurations easily achieved waving mode vibration as predicted by equation (5.1). These early experiments

also showed that the waving mode vibration amplitude increased significantly when all elements in the array had approximately the same natural frequency. Considering these observations and results from the early experiments, a more in-depth analysis was performed on in-line arrays where all elements had the same natural frequency.

Power estimates from the in-depth analysis were calculated from 50 different array configurations each for 15 velocity increments. A maximum estimated area power density of 1.89 W/m^2 was achieved. Results from all 792 tests provided trends in power output versus velocity, x-spacing, and y-spacing. It was shown that maximum power density was achieved by minimizing the streamwise gap between elements (x-spacing) and maximizing the y-spacing. These results suggest that an optimum x-y spacing exists which can be found by minimizing the x-spacing and maximizing the y-spacing. Future work should focus on determining this optimum spacing along with scalability of the array and modeling techniques.

7.1.5 Chapter 6

This chapter presents the results of an investigation on a flow-induced vibration phenomenon referred to as dual cantilever flutter (DCF). A lumped parameter entrainment model was able to successfully predict the effects of fluid coupling between two adjacent vibrating beams in air. This chapter discussed how the entrainment model was developed and experimentally validated. Also presented in this chapter was an experimentally validated model for predicting vibration amplitude, and mean deflection during DCF.

A novel DCF energy harvesting device was also presented in this chapter. Results of wind tunnel experiments performed with this novel device show that significant amounts of power can be harvested over a very large range of flow velocity. This energy harvesting capability over

such a large velocity range makes DCF an attractive and robust energy harvesting method in areas of highly unsteady fluid flow.

7.2 Key Contributions of the Dissertation

The following is a summary of primary contributions that the research proposed in this dissertation provides for the analytical and experimental scientific communities of energy harvesting, flow-induce vibration, structural dynamics, and others.

- Chapter 1 delivers an extensive literature review and history of flow-induced vibration energy harvesting devices. A summary of several performance metrics from selected harvesting methods is summarized in Table 1.1. These performance metrics were calculated in the same manner in order to provide a direct comparison between existing harvesting methods and those proposed in this dissertation. Chapter 1 also highlights the novelty of the proposed harvester design by showing how unique it is compared to the most similar harvester designs found in the literature.
- Chapter 3 presents a fully coupled electromechanical model for turbulence-induced vibration energy harvesting of a single unimorph cantilever in cross-flow. There are two primary novel aspects of this model that were proposed and experimentally validated. First, it was shown that a forcing function statistically derived from actual turbulence measurements could be applied to the electromechanical energy harvesting model. Second, it was demonstrated that results of this model can produce not only average power and displacement predictions, but also voltage and displacement PSD functions. The following section about future work discusses the potential scientific merit of predicting the aforementioned PSD functions.

- Chapter 4 proposes an experimentally validated turbulence measurement technique and how said measurements can be used to predict turbulence-induced vibration of a cantilever beam in highly turbulent cross-cross flow. The primary contribution of this work was showing how invasive turbulence measurements made with two pressure probes can be used to predict displacements of a lightweight structure exposed to high-intensity turbulence. Turbulence-induced vibration prediction techniques shown in the literature typically involve fixing arrays of pressure transducers on the structure and measuring the turbulence directly. The proposed technique provides the accuracy of direct measurement while at the same time eliminates the obvious issue of adding size, mass and possibly stiffness to the structure due to fixing pressure transducers to its surface. A secondary contribution from Chapter 4 was showing the design, fabrication, and calibration of two low-cost pressure probes used for making invasive turbulence measurements.
- Chapter 5 demonstrated how large arrays of cantilevers in cross-flow achieved a resonance condition where the entire array experienced coupled, persistent, large amplitude vibration. It was found that this vibration was due to a highly robust flow-induced excitation mechanism. This type of excitation was well known in the agricultural community; however, it had never been investigated in an energy harvesting study.
- Chapter 6 introduced a novel flow-induced excitation phenomenon based on the piezoelectric grass concept referred to as dual cantilever flutter (DCF). A lumped mass model for DCF was proposed and experimentally validated. This model was able to accurately predict fluid entrainment coupling and the flow-induced excitation between two adjacent cantilevers. The entrainment and flutter dynamics were also successfully

modeled using a commercial CFD code (See Appendix B). Another key contribution of Chapter 6 was the proposal of a novel energy harvesting device that took advantage of the DCF phenomenon.

7.3 Recommendations for Future Work

The following discussion focusses on potential future investigations inspired by the research presented in this dissertation.

- Extensive experimental analyses were performed with piezoelectric grass harvester prototypes in a laboratory setting; however, the long-term performance and durability of these prototypes was not investigated. Future work should focus on field tests in uncontrolled, remote, natural, or potentially hazardous environments where a piezoelectric grass harvester can be compared directly with existing traditional and/or non-traditional devices. (See Chapter 1 for examples of such devices.) A primary task of this study would be to simultaneously monitor the structural integrity and record power output from a piezoelectric grass harvester and an existing harvester for a period of several months, possibly a year.
- As mentioned in Section 7.2, Chapter 3 presents a model for predicting the voltage and displacement PSD functions. It was found that this model can also be used to measure turbulence with a novel, single-sensor measurement technique. Rather than making a series of tedious pressure probe measurements, a single unimorph cantilever can be inserted into the flow and the voltage output from the PZT can be measured. After the output voltage is gathered, the voltage PSD function can be calculated. Using the coupled electromechanical model proposed in Chapter 3, it is then possible to calculate the PSD

of the turbulence-induced force on the beam. This forcing function can then be used to predict the turbulence-induced vibration of another structure placed in that flow.

This concept was validated with a simple experiment where the turbulence-induced force PSD was determined with a single unimorph beam using the method previously stated. This unimorph was removed and a second beam having a different design was inserted into the flow. Using the turbulence-induced force PSD measured with the unimorph, the displacement of the second beam was then predicted. The success of this novel turbulence measurement technique was made apparent by comparing the predicted displacement of the second beam with laser displacement measurements.

- A third area of potential future work would focus on the design and implementation of an efficient energy harvesting circuit for large arrays of piezoelectric grass. Collecting the alternating voltage from several unimorph or bimorph elements in a series or parallel configuration would lead to a significant amount of cancellation thus reducing harvester efficiency. An obvious alternative would be to design an individual harvesting circuit for each element in the array; however, this may be expensive and add unnecessary mass to the harvester. The goal of this work would be to develop a circuit that could harvest the most power without adding significant cost or weight.
- Future work should also be focused on energy harvesting from DCF as proposed in Chapter 6. This work includes determining the physical significance of the coupling and excitation parameters used in the lumped parameter model. Additional CFD modeling (See Appendix B) should be performed and compared to experimental and analytical results. Future work should also be directed toward developing a coupled electromechanical model for energy harvesting from DCF.

- Other future work dedicated to the topic of DCF should include a non-dimensional analysis of the equations of motion given in equations (6.21) and (6.22). Part of this study would investigate the effects of having the mass, damping, and/or stiffness terms of one beam differ significantly from those of the adjacent beam. It may be found that an optimum combination of these parameters could maximize the energy output of a DCF-type harvester.

APPENDIX A

WIND TUNNEL DESIGN

This Appendix provides a detailed description of the wind tunnel which was designed and built primarily for experiments presented in Chapters 5 and 6. All major design aspects of the wind tunnel will be discussed including part and assembly drawings, materials, flow calculations, motor and fan selection, control circuitry, instrumentation, calibration, and LabVIEW programming.

Several wind tunnels were available to borrow for the work presented in Chapters 5 and 6. It was decided, however, that due to the extensive amount of testing required, having a dedicated wind tunnel in a more private laboratory setting would allow experiments and equipment to be left setup and secured for many days. Having a dedicated wind tunnel would also eliminate the need to schedule time in other facilities and would ultimately be the most efficient investment of time and resources.

A specific list of wind tunnel design requirements and capabilities could be made for the experiments presented in this dissertation. Rather than imposing such limitations on the wind tunnel capabilities, the focus throughout the design process was placed on making the tunnel as functional, versatile, and user-friendly as possible for current and future research projects.

A.1 Primary Wind Tunnel Components

The wind tunnel had a typical single stage, open circuit design. The tunnel was comprised of five major components: contraction (or nozzle), test section, fan vibration isolator, diffuser, and finally the fan and motor assembly. The supporting framework was also a major part of the design project which was all cut and assembled out of both slotted and solid steel 1.625 x 1.625 inch strut. The strut stock and all standard assembly hardware was supplied from McMaster-Carr.

A.1.1 Contraction Section

The contraction section was the only existing component of the wind tunnel which was salvaged from a dismantled vertical wind tunnel facility from the University of Michigan. Snapshots of the contraction section are shown in Figure A.1.

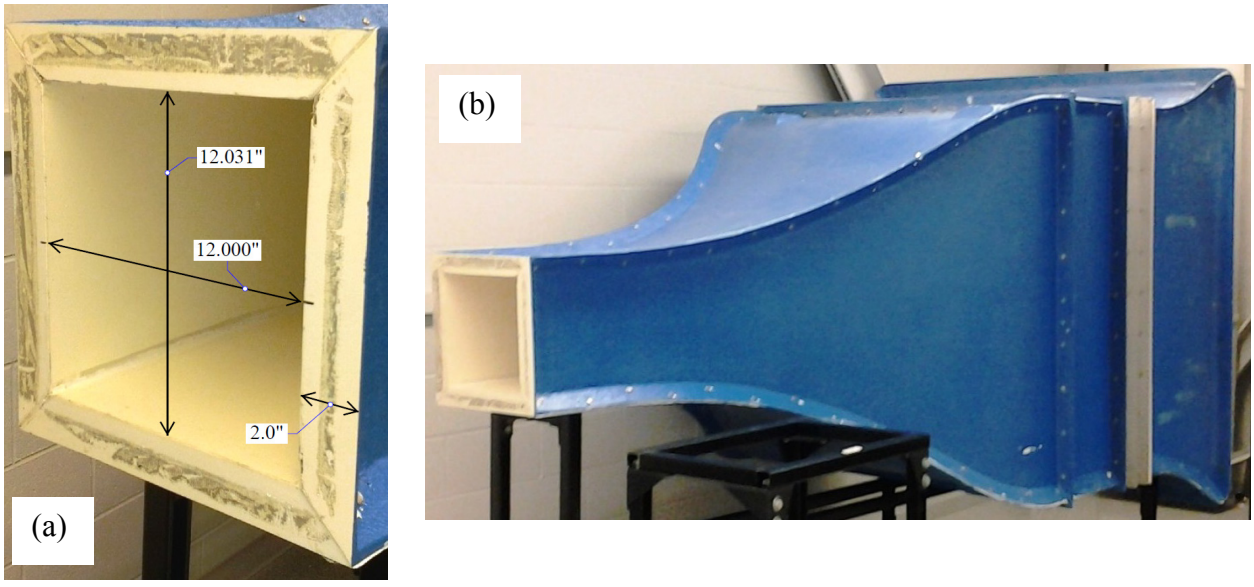

Figure A.1: Snapshots of the wind tunnel contraction section showing (a) a detailed view of the throat and mounting flange including dimensions, and (b) the entire contraction section resting on a steel strut support structure.

The contraction ratio was 16:1 and the throat or exit of the contraction had a height and width of 12.031 x 12.000 inches respectively. The test section mounting flange was 2.0 inches wide and had no existing bolt pattern as shown in Figure A.1a. A 3.25-inch thick aluminum honeycomb flow straightener was installed at the entrance of the contraction section. Immediately after the flow straightener was a steel coarse mesh screen which was then followed by a finer mesh screen. The screens and flow straightener were all spaced approximately 3.25 inches apart. The total length of the contraction section including the nozzle and flow conditioning inserts was 111 inches.

A.1.2 Test Section

Perhaps the most critical and intricate component of the wind tunnel was the test section. A majority of the design efforts including both time and expenses were dedicated to the test section. The following is a list of initial design specifications which includes specific items such as overall dimensions and tolerances.

Initial Test Section Design Considerations:

a. The test section is for an open-loop wind tunnel with a rectangular (approximately square) cross section.

b. The current wind tunnel position is such that while standing at the test section, flow is from right to left. Considering that the wind tunnel may be repositioned or moved in the future, one should be able to unbolt the section at its flanges and rotate it such that the access door can be on either side. In other words, the bolt patterns, alignment, and edge transitions should be smooth and symmetric such that the quality of air flow and overall functionality is not dependent on the test section orientation.

c. Velocity range: (subsonic) $\sim$ 0-50 mph

d. Max pressure: 2 inches of water (vacuum)

e. Test section dimensions as measured from the contraction section.

1. Inside height: 12.031 (12 + 1/32) inches
2. Inside width: 12.00 inches
3. Viewable length: 48.000 inches*

   *The *viewable length* is the length inside the test section that is viewable from outside the test section. The total test section length is not specified and will be the viewable length (48-inches) plus the total frame and flange widths at each end.

4. Tolerance on inside height and width are (+0.03, -0) inches
5. Tolerance on viewable length is ($\pm$ 0.1) inches
6. The inside corners of the test section should be square, but can be rounded or chamfered if necessary.

f. The mating flange for both ends has a 2-inch wide face on all sides that can be thru-bolted. The flange on both ends should be left 'blank' (no machined bolt pattern). A bolt pattern will be defined after receiving the vibration isolator, diffuser and test section to ensure proper alignment and symmetry between all major tunnel components.

g. The top and sides should be made of 0.375 inch thick float glass. Glass is much harder than acrylic or plexiglass and therefore less susceptible to scratching. Float glass is more brittle than tempered glass; however, it has the best optical clarity compared to tempered glass, acrylics, and plexiglass. Ultimately, float glass was chosen as the best option for allowing high-quality laser measurements and digital imaging to be made through the glass with minimal distortion.

h. The floor should be made of 1.00 or 0.75 inch thick, moderately hard, clear acrylic or plexiglass (rather than glass) so that ports for instrumentation mounts, wires, etc. could easily be machined. All glass and acrylic/plexiglass panels should be fairly easy to replace in the event that one should become damaged.

i. An entire side of the test section should hinge open to allow maximum accessibility for setting up tests. The door should hinge open with at least 90 degrees of motion - 180 degrees of motion is preferred. The door should also be held open such that it is not allowed to slam shut possibly injuring the operator or damaging the test section.

j. The access door should have a simple-to-use latching system.

k. Lastly, the test section should have its own stand with wheels, vibration isolation, and screw down leveling feet. The horizontal mid-plane of the test section should be approximately 47-inches off the ground with its feet screwed down such that there is ±1.0 inch of height adjustability.

The previous list of design considerations was sent to two companies: Engineering Laboratory Design, Inc. (ELD) and Aerolab, LLC. After more than three months of communication, neither company was able to provide an acceptable solution. It was decided to start designing the test section using Pro/Engineer (now called Creo) CAD software developed by Parametric Technology Corporation (PTC). Dimensions of the final test section design are listed in Table A.1 and renderings of the test section assembly are shown in Figures A.2 and A.3.

Table A.1: Dimensions of the final test section design.

Dimension	*Value* (inches)
Inside Height	12.031
Inside Width	12.000
Viewable Length	48.00
Total Length	55.00
Glass Thickness	0.375
Acrylic Thickness	0.750
Mounting Flange Thickness	2.00
Mid-plane Height	47.00
Height/Leveling Range	± 1.0

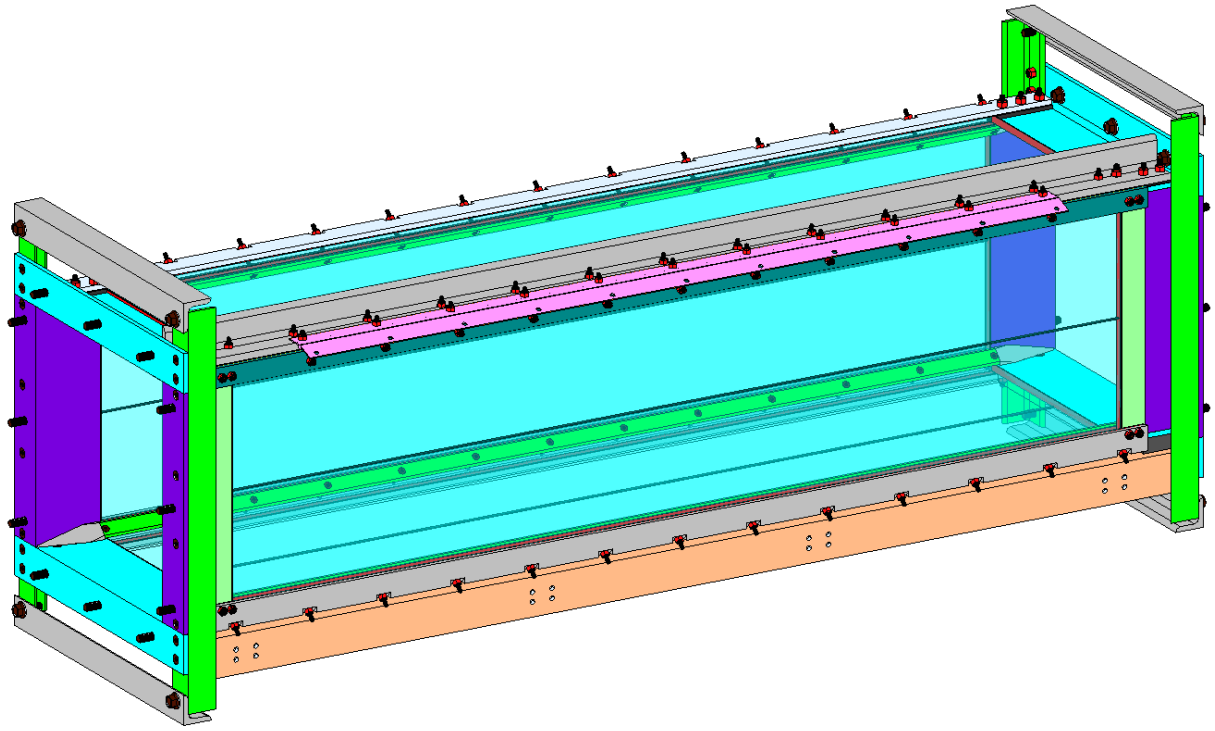

Figure A.2: A rendering of the final version of the test section design developed by the author using Pro/Engineer CAD software.

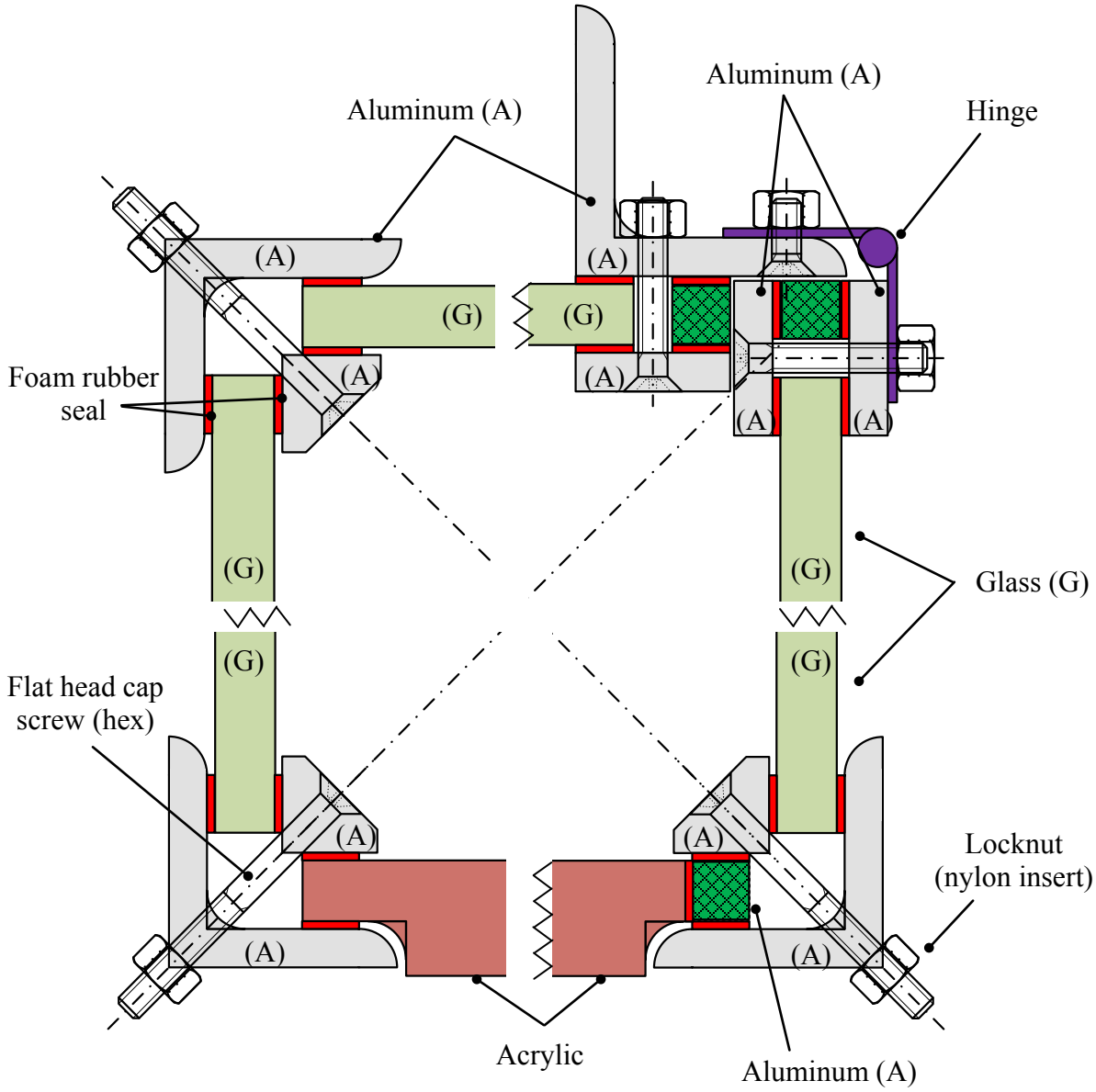

Figure A.3: A schematic (drawn to scale – not actual size) showing a cross-section view of the final design of the test section assembly. The zigzag lines represent segments of the sides, top, and bottom of the test section that were removed from the schematic in order to show greater detail in each of the four corners.

After each individual part of the test section was designed, an .stp file was created for each unique part. These .stp files were uploaded online using a service provided by QuickParts.com where material and tolerance specifications were set, and a few brief comments to the machinist were made. After the order was placed, QuickParts was able to complete all machining and fabrication and had the parts delivered within two weeks. It took the author a total of approximately two months to design the entire test section and have all of the individual pieces fabricated, delivered, and ready to assemble. A total of 52 custom parts (34 of them unique) were fabricated to form the assembly shown in Figures A.2 and A.3. Most of the custom parts were made of 6061-T6 aluminum, the door hinge was 316 stainless steel, the floor was acrylic, and 10 smaller non-structural pieces were made of PTFE – Teflon. A snapshot of all machined parts is shown in Figure A.4.

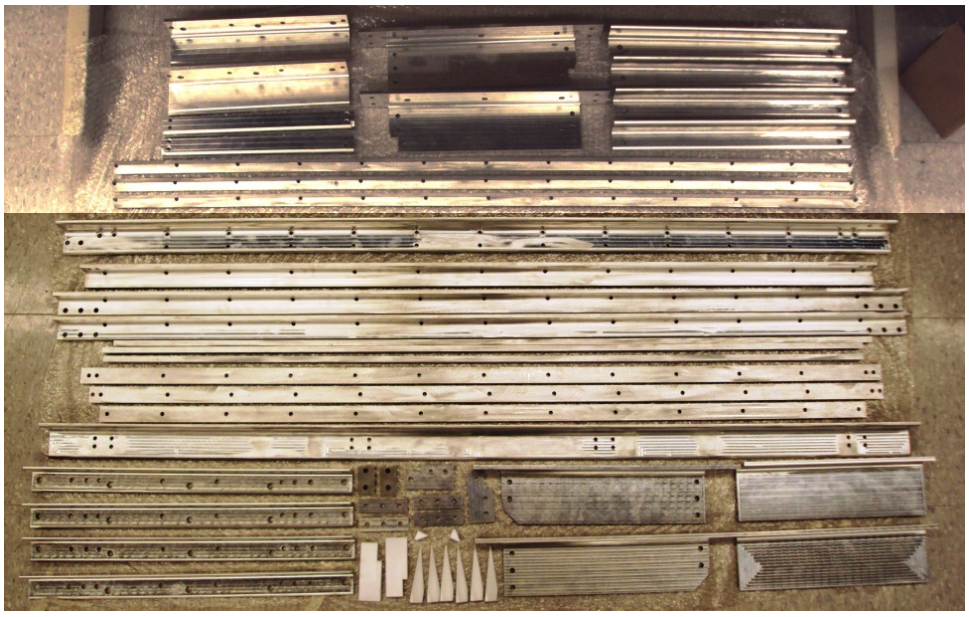

Figure A.4: A snapshot of all test section pieces machined by QuickParts prepared for assembly.

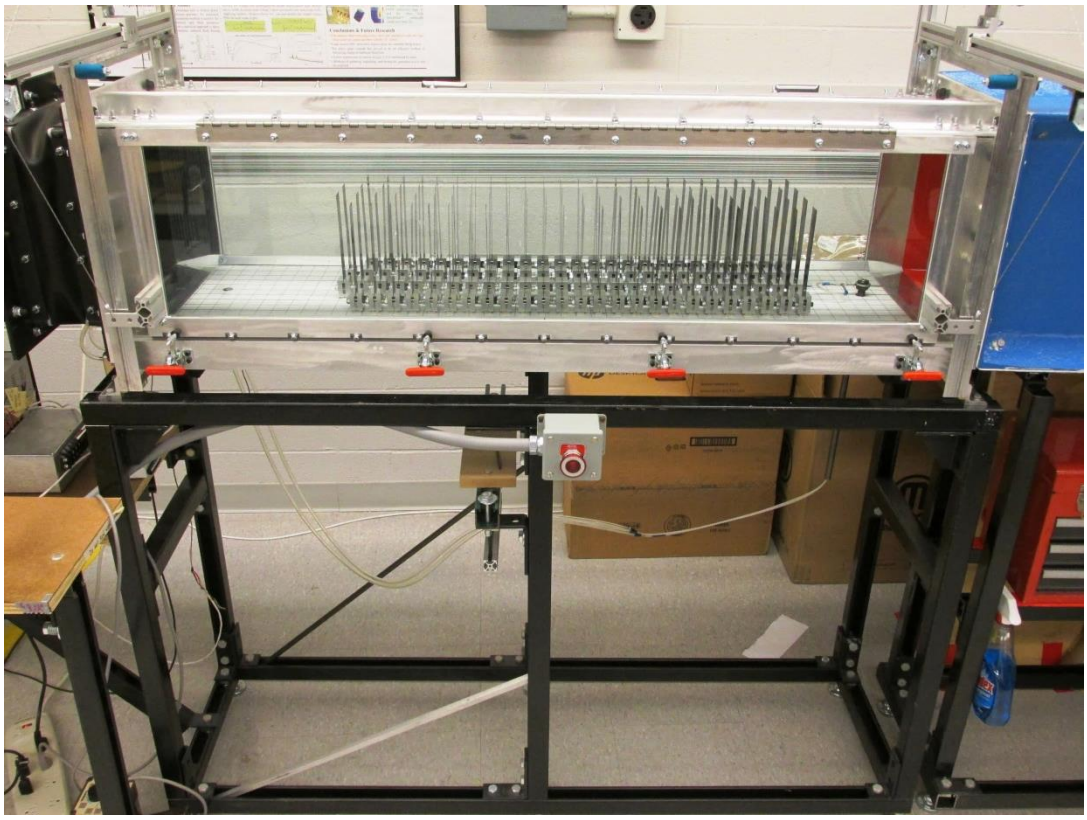

Figure A.5: A snapshot of the test section fully assembled and operational.

Immediately after assembly, the test section was mounted to a stand constructed from steel strut. Rubber-padded leveling feet were bolted into the bottom of the stand and allowed for height adjustments and leveling up to ±1.0 inch. Figure A.5 shows a snapshot of the test section mounted on its stand and bolted to the contraction (right) and vibration isolator (left).

Figure A.6 shows a series of snapshots taken at each end of the test section in order to highlight details of the latch and pulley system of the hinging door. One end of each cable is attached to the front corners of the hinging door while the other ends are attached to an adjustable counterweight (not shown). This counterweight system is used to make the heavy door very easy to open and holds the door in a stable open position.

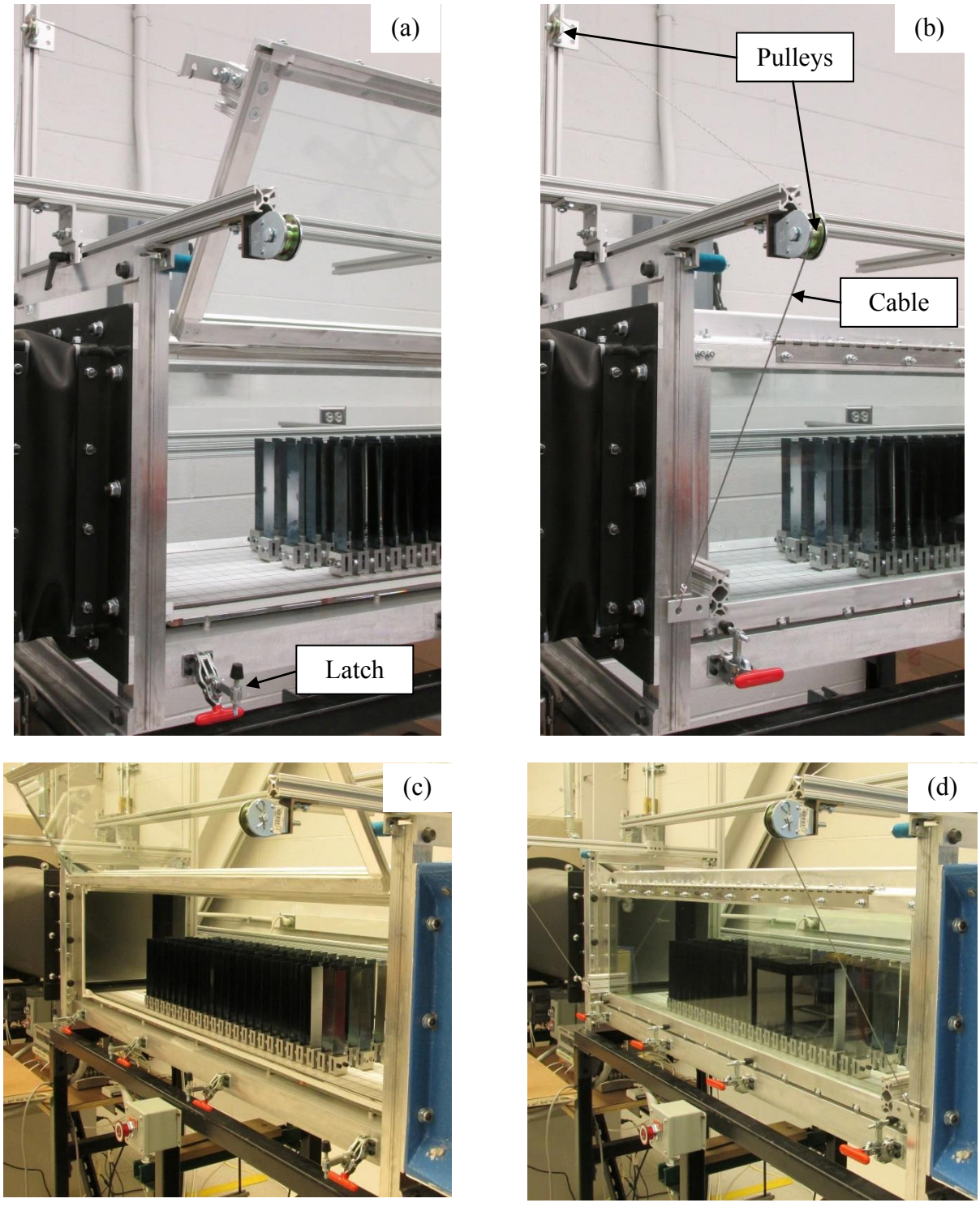

Figure A.6: Snapshots of the test section showing the latch and pulley system and the hinging door both open (a,c) and closed (b,d) at the test section exit (a,b) and entrance (c,d).

Another function of the counterweight system is to prevent the door from being slammed shut. Because there is always constant tension in the cables, the door can be dropped from any position and it will not fall shut. Restraining the door with the counterweight also protects the operator from accidentally dropping the door which could possibly cause injury or damage the test section. It was necessary to adjust the counterweight incrementally until the desired previously discussed performance was achieved.

Access ports were made in the test section by drilling a 1-inch diameter hole through the acrylic floor, and inserting the smooth end of a ¾-inch female threaded copper pipe adapter from below. The adapter was temporarily held in place with hot melt adhesive (HMA) while epoxy was poured between the acrylic floor and copper adapter. See Figure A.8c for a detailed schematic of the access port design. After the epoxy hardened, the HMA was simply peeled off. Five of these access ports were made at locations along the center line of the test section floor as shown in Figure A.7.

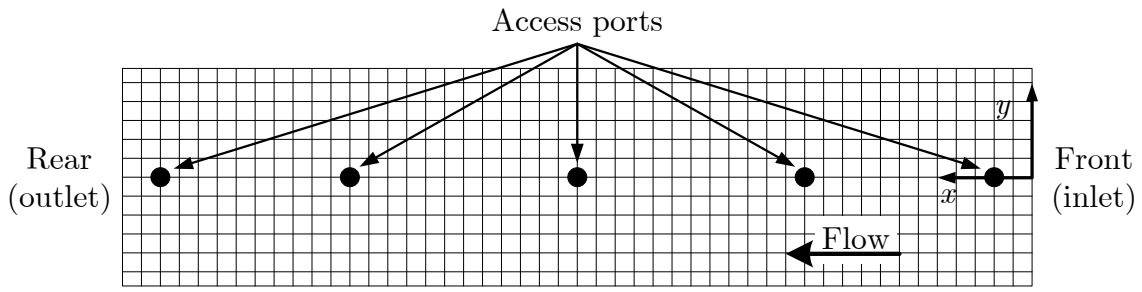

Figure A.7: A schematic of the test section floor on a square 2.54 cm grid showing access port locations and the coordinate system relative to the inlet.

A.1.3 Pitot-Static Tube Assembly

Local velocity measurements were made with a pitot-static tube system. For most experiments, the pitot tube was positioned at the front of the test-section such that the tube tip was approximately 2 to 3 cm above the floor as shown in Figure A.8a. Details of the pitot-static tube support and mounting system are shown in Figure A.8 b and c. The pitot support was a thick-walled steel pipe having an outer diameter of 1.27 cm. One end of the pitot support had a male threaded section with a hole machined perpendicularly through both walls of the pipe. The pitot-static tube was inserted through this hole then clamped in place by a pair of thin nuts, wide flange washers, and soft rubber washers as shown in Figure A.8b.

A steel shaft coupling (for 1.27 cm diameter shafts) was modified such that one end could be inserted into a ¾-inch copper pipe adapter with male threads as shown in Figure A.8c. This modified coupling was inserted into the adapter and the two parts were bonded together using epoxy. Prior to bonding, a thru hole was milled into the side of the adapter to allow a set screw to pass through the adapter to the threaded hole in the coupling. These two bonded parts could be screwed into any of the five access ports in the test section floor. The pitot support could pass freely through an access port and through the shaft coupling. Two set screws in the side of the coupling could then be tightened to fix the pitot support in place.

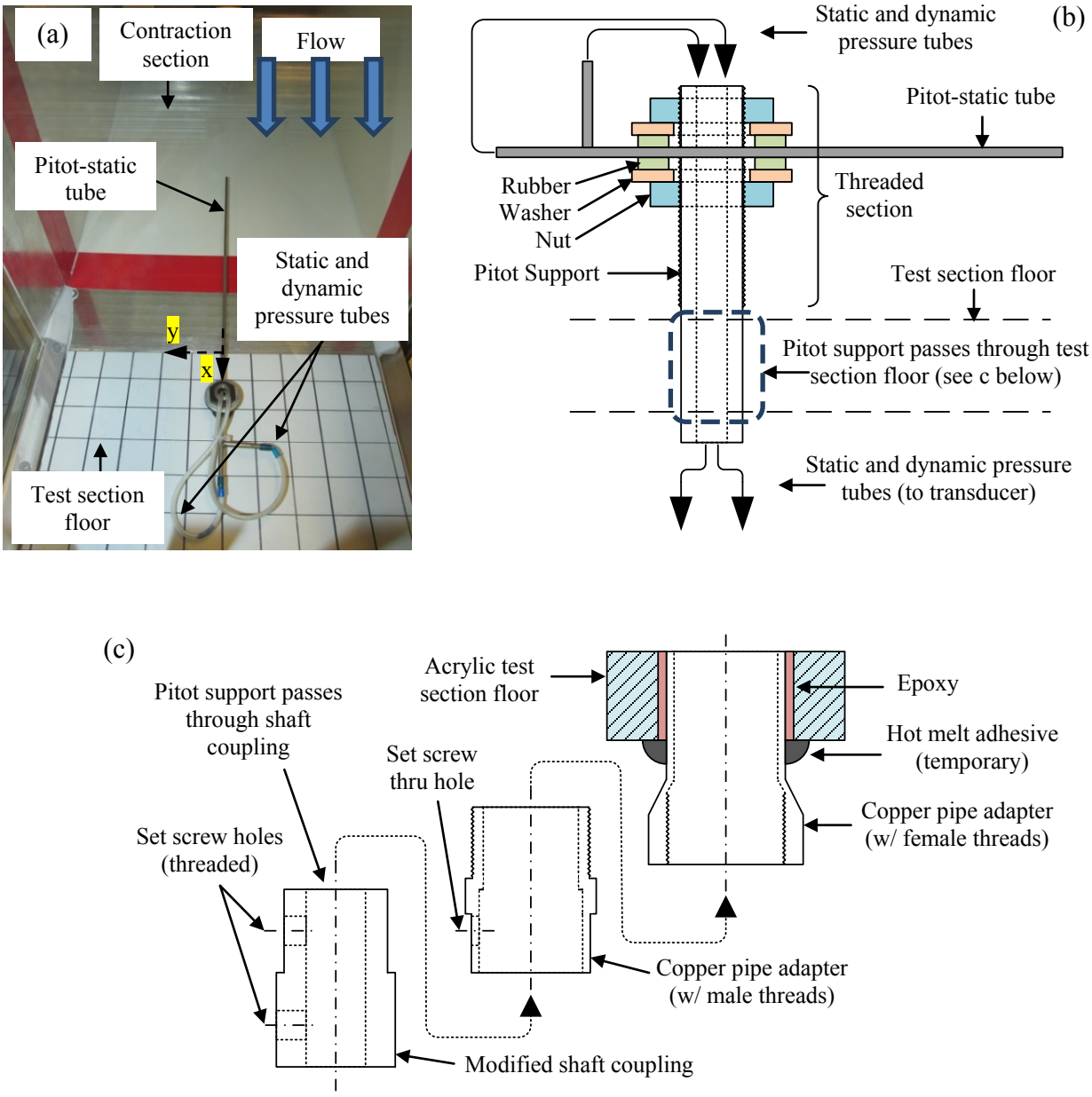

Figure A.8: Detailed views of the pitot-static tube system showing (a) a snapshot of the pitot-static tube installed in the test section, (b) a schematic of the pitot-static tube and support tube assembly, and (c) a schematic showing how the pitot support is held in place and passed through an access port in test section floor.

A.1.4 Vibration Isolation

Even though the fan assembly was dynamically balanced by the manufacturer in order to minimize vibration, significant amounts of vibration could be transmitted from the fan to the rest of the wind tunnel. Depending on the experimental setup, vibration introduced by the fan may cause measurement error, or potentially damage sensitive instrumentation. In order to reduce the transmission of this unwanted fan-induced vibration, an isolation joint was inserted between the test section and the diffuser.

The vibration isolation joint consisted of two flanges joined with a rubber jacket as shown in Figure A.9. This design allowed for robust, rigid, air-tight flange connections while allowing each flange to move independently. Figure A.9a shows an exploded view of a CAD rendering of the vibration isolation joint with one of the flanges removed for clarity. Each of the two flanges was constructed with 0.125 inch thick steel angle welded together at each corner. Figure A.9b shows another CAD rendering of the isolation joint completely assembled. A snapshot of the isolation joint assembled and installed on the wind tunnel is shown in Figure A.9c. Note that one bolt pattern was used for the contraction section, test section, isolation join and one end of the diffuser. A detailed drawing showing all dimensions of the mounting flanges and bolt pattern of the isolation joint is given in Figure A.9d.

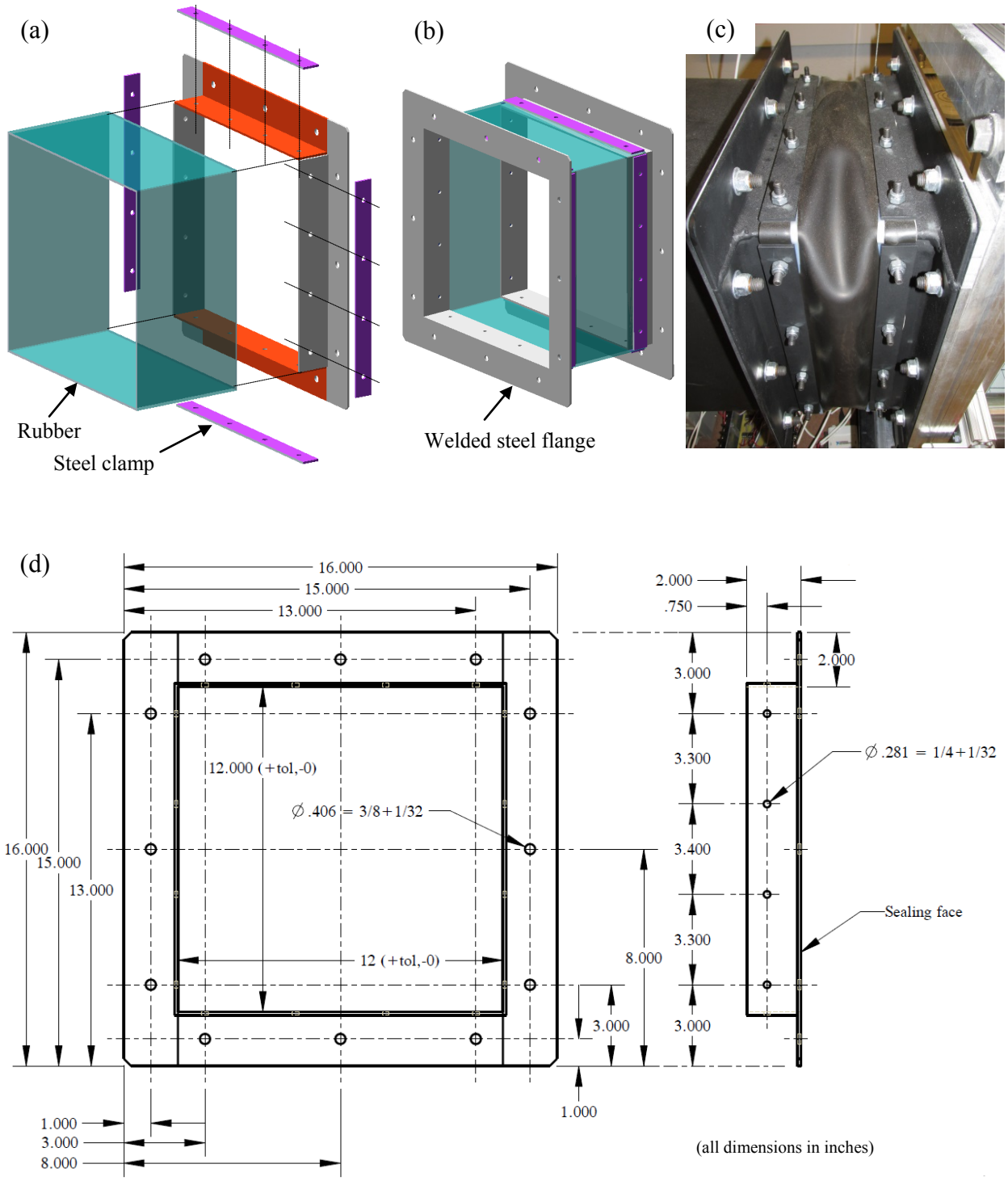

Figure A.9: Design details of the vibration isolator showing (a) an exploded view and (b) a fully assembled view of CAD renderings along with (c) a snapshot of the full assembly installed on the wind tunnel, and (d) a drawing showing the dimensions of the flange and bolt pattern.

A.1.5 Diffuser Section

The diffuser was designed simply by defining the flange width and bolt patterns at both ends to be identical to those for the fan assembly and the vibration isolation joint assembly (Figure A.9d). Because the dimensions for the flange width and bolt patterns were already known, the only dimensions needed for a complete design were the contraction section length and material thicknesses. The total diffuser length was set to 40.0 inches. The flanges were constructed from 0.125 inch thick steel while the diffuser wall was made of 0.055 inch thick steel. Seams on the sides of the diffuser were spot welded then sealed while both flanges were joined to the diffuser walls with a continuous weld joint. Complete fabrication of the diffuser was performed by the University of Michigan Sheetmetal Shop. In order to prevent unsightly and potentially damaging oxidation from forming on the steel, all surfaces of the diffuser were cleaned and painted prior to installing it on the wind tunnel assembly. A snapshot of the diffuser installed and ready for operation is shown in Figure A.10.

Figure A.10: A snapshot of the diffuser section installed on the wind tunnel assembly and ready for operation.

A.1.6 Fan Assembly

A direct drive, axial, three-blade, airfoil type fan was used to pull air through the wind tunnel. The fan assembly was purchased from Air and Liquid Systems, Inc. The fan was designed by American Fan Company, Model: 45JM/20/2/3. The motor was a NEMA, 3 HP, TEFC, Premium Efficiency, 3600 RPM, 460/230 VAC, 3-phase, 60 Hz, inverter duty motor designed by WEG, Model: 00336ET3EPM182/4Y. Drawings of the fan assembly provided by American Fan Company are shown in Figure A.11, and the corresponding labeled parameters are given in Table A.2

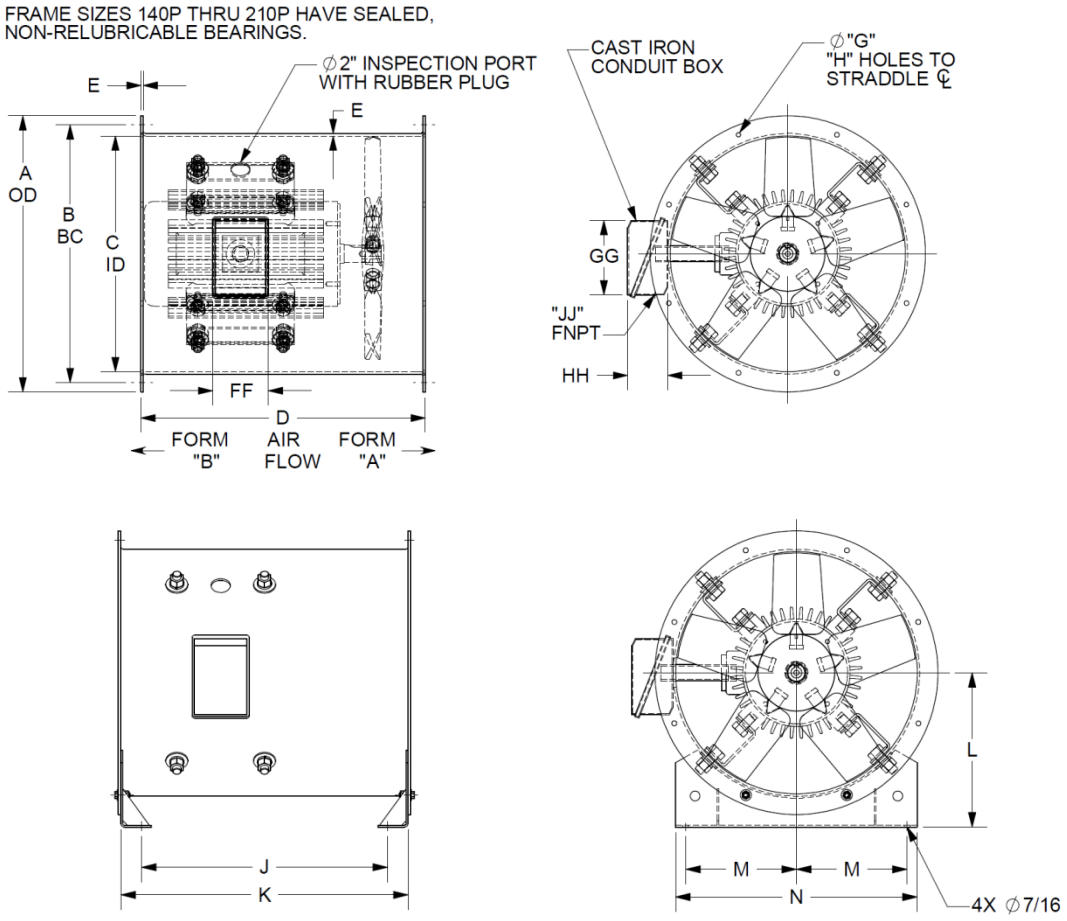

Figure A.11: Drawings of the fan assembly.

Table A.2: Parameter definitions for the drawings given in Figure A.11

Parameter	*Value*	*Units*	*Parameter*	*Value*	*Units*
A	545	mm	K	397	mm
B	500	mm	L	280	mm
C	450	mm	M	200	mm
D	406	mm	N	451	mm
E	2.5	mm	FF	122	mm
G	12.7	mm	GG	165	mm
H	8		HH	83	mm
J	321	mm	JJ	3/4	inch

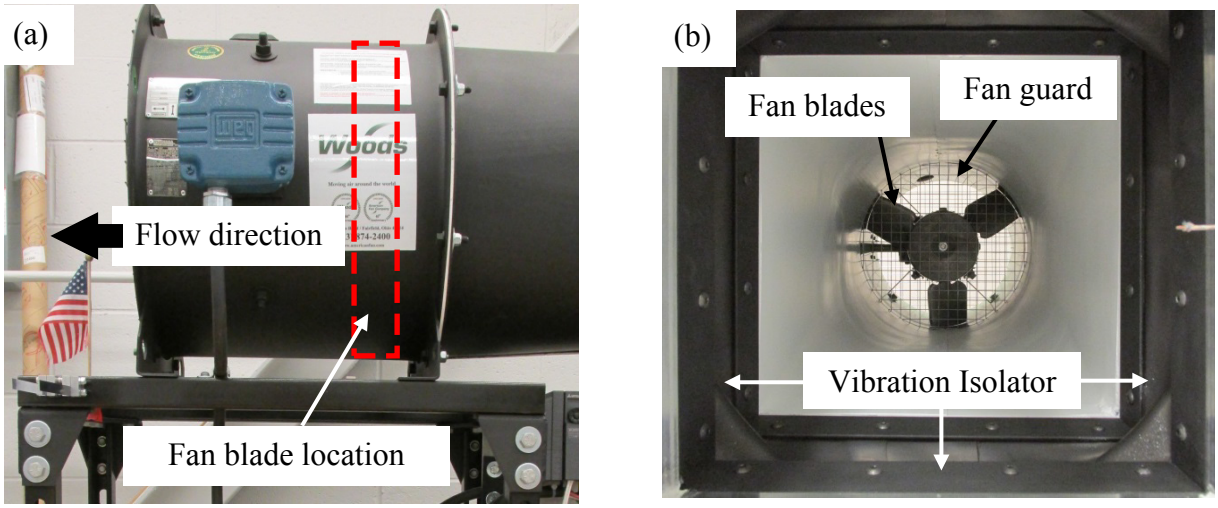

Figure A.12: Snapshots of the fan assembly installed on the wind tunnel and prepared for normal operation showing views (a) from outside the wind tunnel, and (b) from inside the test section looking downstream toward the fan.

Fan guards were constructed from 2.03 mm diameter type-304 stainless steel wire welded to form a 2.54 cm x 2.54 cm wire mesh. Two identical circular patterns were cut from the mesh and installed on the fan assembly. One guard was bolted between the diffuser and the fan housing while the other guard was bolted to the fan outlet flange. Snapshots of the fan assembly with attached fan guards are shown in Figure A.12. Notice that the fan blades are positioned closest to the diffuser side (inlet) of the fan in order to provide maximum protection against foreign objects

accidentally coming in contact with the fan blades or motor shaft from the open end (outlet) of the fan.

A.1.6.1 Fan Sizing & Flow Calculations

Motor and fan sizing and matching was performed by American Fan Company for a requested flow rate of 4500 cfm (cubic feet per minute) at a static pressure of 2.0 inH_2O (inches of water).[7] The flow rate and pressure were determined using Bernoulli equation. Treating low velocity air as an incompressible fluid, continuity was used to first estimate a volumetric flow rate based on a desired average test section velocity. The following expression was used to first calculate volumetric flow rate of air (Q) for a desired test section flow velocity (v_{ts}),

$$Q = v_{ts} A_{ts} = v_{in} A_{in} \tag{A.1}$$

where A_{ts} and A_{in} represent the cross-sectional area normal to the flow direction of the test section and contraction inlet respectively, and v_{in} is the inlet flow velocity. Given the dimensions and flow rate, Equation (A.1) was then used to calculate the inlet velocity based on the desired test section flow velocity. The pressure difference between the inlet and test section could then be estimated with Bernoulli's equation,

$$\Delta P = \frac{\rho_a}{2}\left(v_{in}^2 - v_{ts}^2\right) \tag{A.2}$$

where ΔP is the differential pressure and ρ_a is the density of air at laboratory conditions. For a desired test section flow velocity of 20 m/s the flow rate was found to be approximately 1.86 m^3/s or approximately 4000 cfm and the differential pressure was 239.1 Pa or approximately 0.96 inH_2O. These flow rate and pressure values were increased to 4500 cfm and 2 inH_2O to

[7] Standard units used in the HVAC industry for flow rate and pressure are cfm and inH_2O (respectively) rather than SI units of m^3/s and Pa.

account for losses caused by the flow straighteners, fan guards, and blockage of various future experiments and instrumentation installed in the test section.

A.2 Instrumentation & Control

This section of the Appendix will focus on all electrical aspects of the wind tunnel. Main topics of this section discuss the power supplies for both the fan motor and the instrumentation, along with the fan motor controller, pressure transducer, thermocouples, optical isolation (for electrical noise reduction), LabVIEW programming, and general wind tunnel operation. Most of the electrical components used for monitoring and control were able to be conveniently positioned under the diffuser section of the wind tunnel as shown in Figure A.13.

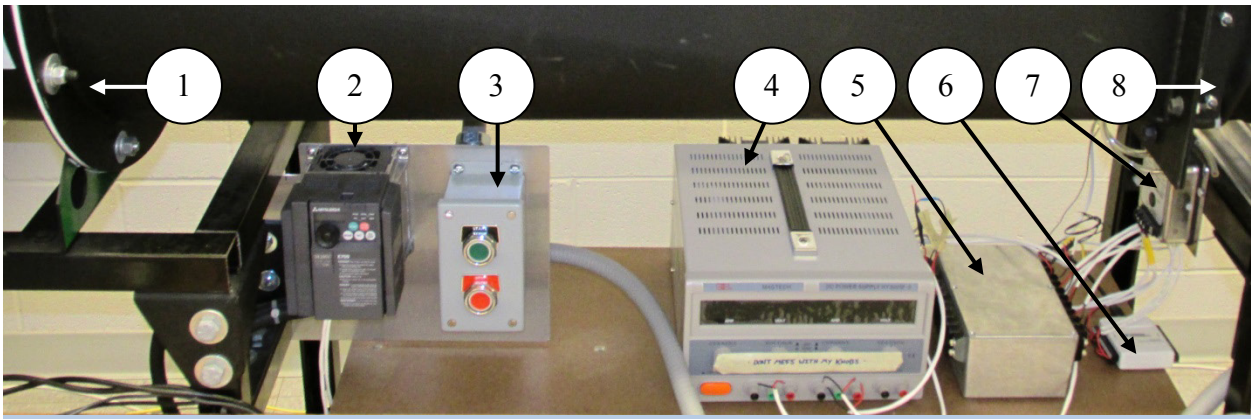

(1) Fan assembly
(2) Variable frequency motor drive controller
(3) Main ON/OFF power switch
(4) Power supply for instrumentation and low-power control circuitry
(5) Project box containing optical isolation and thermocouple amplification circuits
(6) Data acquisition hardware for wind tunnel instrumentation and control
(7) Pressure transducer
(8) Vibration isolation joint

Figure A.13: A snapshot showing a detailed view of the wind tunnel instrumentation and control circuitry. A brief description of each labeled item is provided in the numbered list.

A.2.1 Fan Motor Power Supply

Installation of the main electrical power supply was performed by licensed electricians working for the University of Michigan. An electrical disconnect box was installed in the lab near the wind tunnel. This box houses a 3-phase disconnect switch with 20 amp dual-element, time-delay, current limiting fuses on each phase. The disconnect box also contains a magnetic motor starter with 10 amp thermal overload protection elements on each phase. These disconnect fuses and thermal overloads provide two levels of protection for the motor and motor controller. The magnetic starter is a large relay or electromagnetic switch between the main disconnect switch and the motor controller. If power to the magnetic starter is interrupted, the switch will disengage and not allow power to the motor until a physical reset switch is pushed. This reset switch is located on the outside of the electrical disconnect box. An emergency stop switch was installed near the test section. If pushed, the emergency stop switch will cause the magnetic starter to fault or disengage and a red indicator light located on the disconnect box will illuminate. In order to restore power to the motor controller, the emergency stop switch must first be pulled out to the open position and the reset switch on the disconnect box must be pushed.

A.2.2 Instrumentation & Control Power Supply

A Mastech, Model: HY3005F-3 power supply was used to provide up to 30 volts and 5 amps of continuously variable regulated power from two independent outputs. A third output supplied a constant 5 VDC at 3 amps. The power supply is shown as item #4 in Figure A.13.

A.2.3 Variable Frequency Drive

After the appropriate motor size was selected by American Fan Company (See Section A.1.6), a variable frequency drive (VFD) motor controller was used to adjust and regulate motor power and speed. The VFD chosen was a Mitsubishi model: FR-E720-110-NA which is a 240

VAC, 3-phase controller for motor sizes up to 3 Hp. The most attractive features of the VFD are summarized below.

a. Motor speed could be controlled manually simply by using a turn dial located on the front of the controller.

b. Motor speed could also be controlled with an external DC voltage or current input such that motor speed is linearly proportional to the input signal.

c. Flow velocity rather than fan speed could also be controlled by enabling an on-board PID controller which uses an external voltage or current source (e.g. the output from a velocity sensor) as the feedback signal.

d. Automatic overload protection disengages motor power if the load or power demand on the motor exceeds limits set by the controller.

Only features **a**, **b,** and **d** from the previous list were successfully implemented; however, all circuitry and hardware necessary for PID velocity control (feature **c**) were designed and installed on the final wind tunnel design. Enabling feature **c** would require the operator to follow steps clearly documented in the manual provided by Mitsubishi. The VFD and ON/OFF switches were mounted on an aluminum sheet and positioned under the exit end of the diffuser (see items #2 and #3 in Figure A.13).

Feature **d** of the previous list gives added safety for the operator and electrical protection for the controller and motor. Recall that this added electrical protection is in addition to the two levels of protection already provided by the fuses and thermal overloads of the power supply

discussed in Section 0. In the case of an overload fault caused by either excessive current or voltage demanded by the controller, the controller will disconnect power to the motor and show an error code on the LCD display. The cause of the error and the procedure required to continue running the controller, are discussed in the troubleshooting section of the manual provided by Mitsubishi.

A.2.4 Pressure Transducer

A high accuracy, low pressure laboratory transducer manufactured by Omega Engineering, Inc. (Model: PX653-03D5V) was used to make differential pressure measurements from the pitot-static tube. The transducer had a differential pressure range of 0 to 748 Pa (0 to 3 inH_2O) and produced an output of 1 to 5 VDC that was linearly proportional to the pressure. The output signal was temperature compensated from 2^o C to 57^o C and was calibrated by the manufacturer. A regulated 24 VDC signal provided by the instrumentation power supply (#4 in Figure A.13) was used to power the transducer. Clear tubing having an inner diameter of 6.35 mm was pressed onto barbed pressure ports of the transducer. These tubes connected the transducer to the dynamic and static pressure ports of the pitot-static tube. For convenience, the transducer was fixed to the test section support frame and positioned under the vibration isolation joint. See item #7 in Figure A.13.

A.2.5 Thermocouples

Two T-type thermocouples were calibrated and installed inside the wind tunnel. Both thermocouples were purchased from Omega Engineering, Inc. (Model: 5TC-GG-T-20-36). One was used to measure air temperature in the test section while another was used to monitor fan motor temperature. Normal operating temperatures for the fan motor allow for an increase in temperature of 80^o C. If the fan temperature monitor detects excessive temperatures, the operator

can be warned of a potentially hazardous or damaging condition. The output of each thermocouple was amplified using a non-inverting op-amp circuit. Each amplified thermocouple voltage was then connected to the main National Instruments data acquisition box and displayed in real time using LabVIEW. All calibration measurements were performed on the amplified signals.

A.2.6 Optical Isolation

Variable frequency drives such as those used for the current wind tunnel design typically produce large amounts of electrical noise. For DC systems, most electrical noise problems can be solved with averaging and filtering. As expected, the initial wind tunnel setup had high frequency large amplitude electrical noise. Digital filtering and averaging were used to reduce most of this noise. Unfortunately, it was discovered that both AC and DC noise was generated. This electrical noise issue was compounded by the fact that the amplitudes of both the AC and DC noise were not constant and seemed to vary as unknown functions of motor speed.

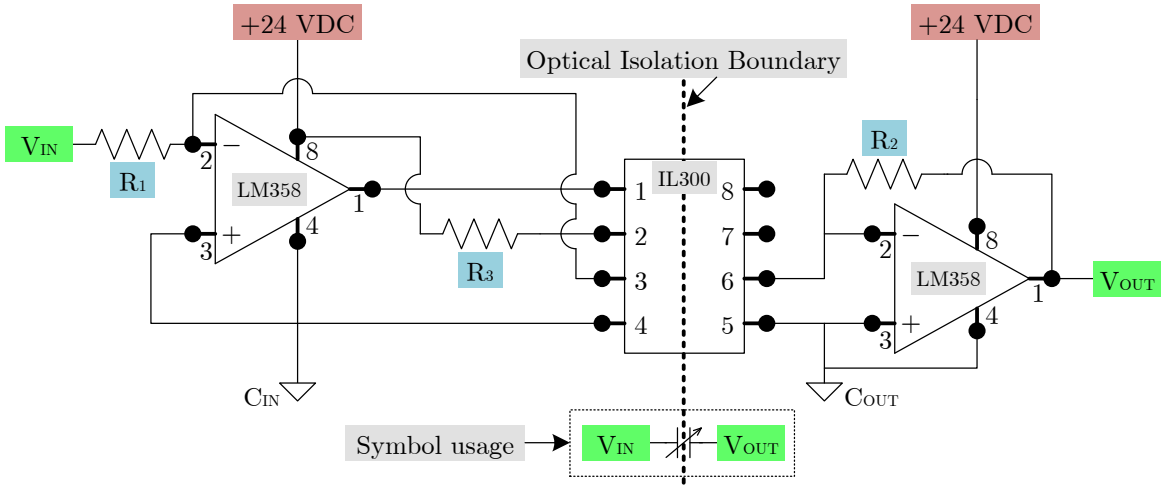

Figure A.14: A schematic of the optical isolation circuit used to isolate the VFD from the data acquisition and instrumentation circuits.

It was decided to use optical isolation in an attempt to reduce electrical noise generated by the VFD. Optical isolation uses light to transfer electrical information (typically voltage or current) across two circuits such that the two circuits act as one while being electrically independent. A linear optocoupler (Model: IL300) manufactured by Vishay Semiconductors, was used along with two operational amplifiers (Model: LM358) manufactured by National Semiconductor Corp. and three resistors (R_1, R_2, R_3) to form an isolation circuit as shown in Figure A.14. This optical isolation circuit behaves similar to a non-inverting amplifier such that the gain $K=V_{OUT}/V_{IN}$ is a function of the resistors. More details of this circuit and its components can be found in readily available technical documents provided by their manufacturers.

Table A.3: Nominal resistance values and measured gains for the optical isolation circuits.

Nominal Resistance (kΩ)			*Measured Gain* ($K_n=V_{OUT}/V_{IN}$)		
R_1	R_2	R_3	K_1	K_2	K_3
80.0	80.0	1.00	1.378	1.443	1.400

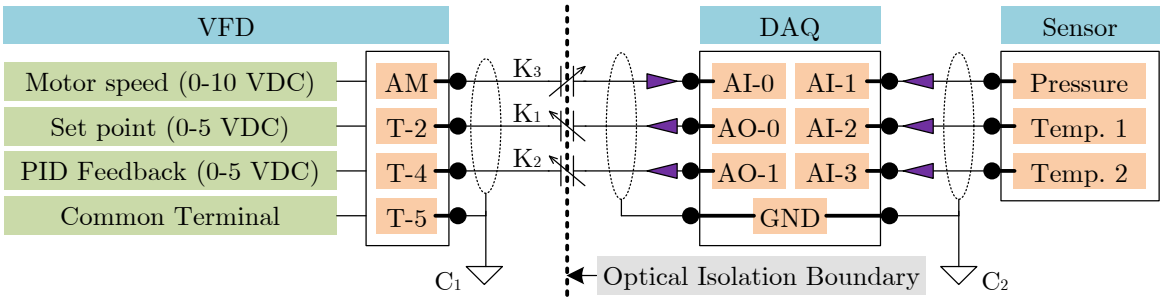

Figure A.15: A schematic illustrating where optical isolation circuits were implemented and how the VFD, thermocouples, and pressure transducer were connected to a single data acquisition device.

In order to ensure that both sides of the circuit (i.e. the input and the output) are optically isolated, the 24 VDC power supplies and their commons C_{IN} and C_{OUT} must also be electrically independent. This electrical independence was achieved by using the two independent outputs on the instrumentation power supply. Both outputs were set to 24 VDC. One output (output #1) was used for the VFD side of the optical isolation boundary while the other output (output #2) was used for the DAQ and sensor side of the boundary. For convenience, output #1 and #2 common terminals are denoted as C_1 and C_2 respectively. The VFD common terminal (terminal T-5) was connected to C_1, and the DAQ and sensor commons were all connected to C_2. Figure A.15 shows a schematic that illustrates where the optical isolation circuits were implemented. The gains for each isolation circuit (shown as K_1, K_2, and K_3 in Figure A.15) were measured after each circuit was completed. Table A.3 lists the nominal resistance values and measured gains for all three isolation circuits.

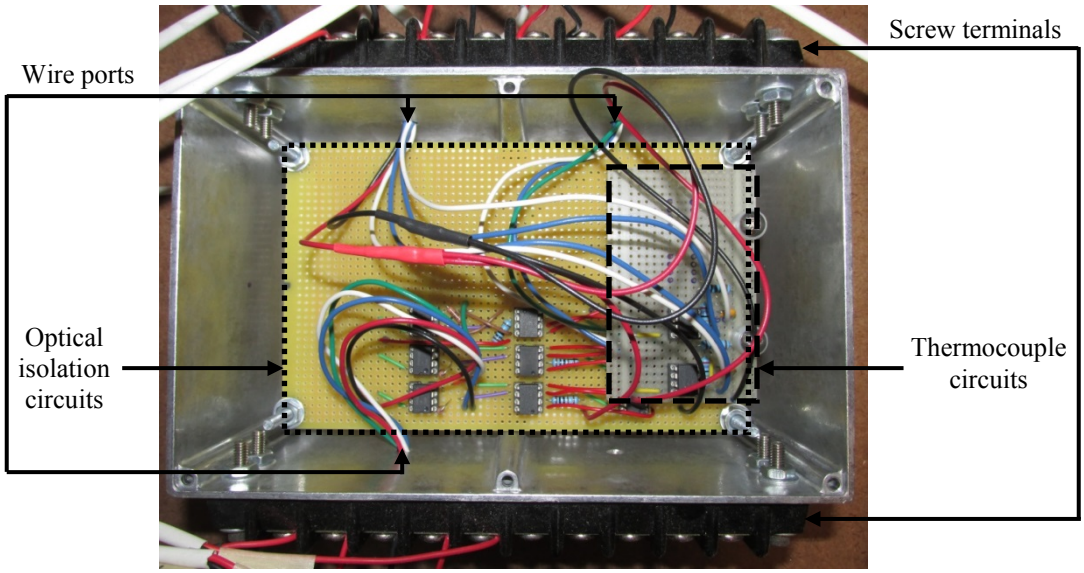

Figure A.16: A snapshot showing the inside of the project box where the optical isolation and thermocouple amplifier circuits were contained.

All three optical isolation circuits were built on a single solderable breadboard. In order to protect the circuits and help shield them from electrical noise, the breadboard was mounted inside of an aluminum project box (#5 in Figure A.13). Wires for inputs, outputs, and power supplies were extended from the breadboard and routed through ports that were milled on the side of the project box. These wires were connected to screw terminals that were fixed to the outside of the project box to provide convenient and reliable connections. A snapshot of the project box (with the lid removed) is shown in Figure A.16. Notice that the thermocouple amplifier circuits were built on a separate smaller breadboard which was also mounted inside the project box. The thermocouple circuits were mounted such that they were elevated above the optical isolation circuits with nylon spacers.

A.2.7 Data Acquisition Hardware

Fan speed was most commonly controlled by generating a DC voltage signal which could be varied from 0 to 5 volts. This voltage signal was generated by an analog output channel (AO-0) of a data acquisition (DAQ) card which was connected to the speed set point terminal (terminal T-2) of the VFD as illustrated in Figure A.15. The fan speed could then be set to a value that was linearly proportional to the voltage generated by the DAQ.

The DAQ card was an 8-channel, 14-bit, multifunctional, USB powered device produced by National Instruments (Model: USB-6009). This DAQ was connected to a PC computer dedicated to wind tunnel operation. National Instruments, LabVIEW software was used to design and develop a virtual control panel for the wind tunnel. This virtual control panel was used to vary the voltage output to the VFD based on a desired fan speed set by the operator. Voltages from the VFD AM terminal and sensors were converted within LabVIEW to display desired and actual fan speeds in RPM, air and motor temperatures in degrees Celsius, and pitot-static tube

velocity in m/s and mph. All values were displayed or controlled in real-time. LabVIEW was also used for implementing digital filtering and averaging of the measured voltage signals in order to minimize the effect of electrical noise.

A.3 Final Design & Performance Overview

Figure A.17 shows a snapshot of the completed wind tunnel fully assembled and fully operational. Immediately upon completion of the wind tunnel project, several performance tests were administered. The purpose of these tests was to define maximum and minimum limitations of the complete wind tunnel system and to ensure that the safety measures were functioning properly. All major aspects of the final design were found to exceed expected performance capabilities. Table A.4 summarizes selected performance metrics, dimensions, control options, operational functions, and safety features for the final wind tunnel design.

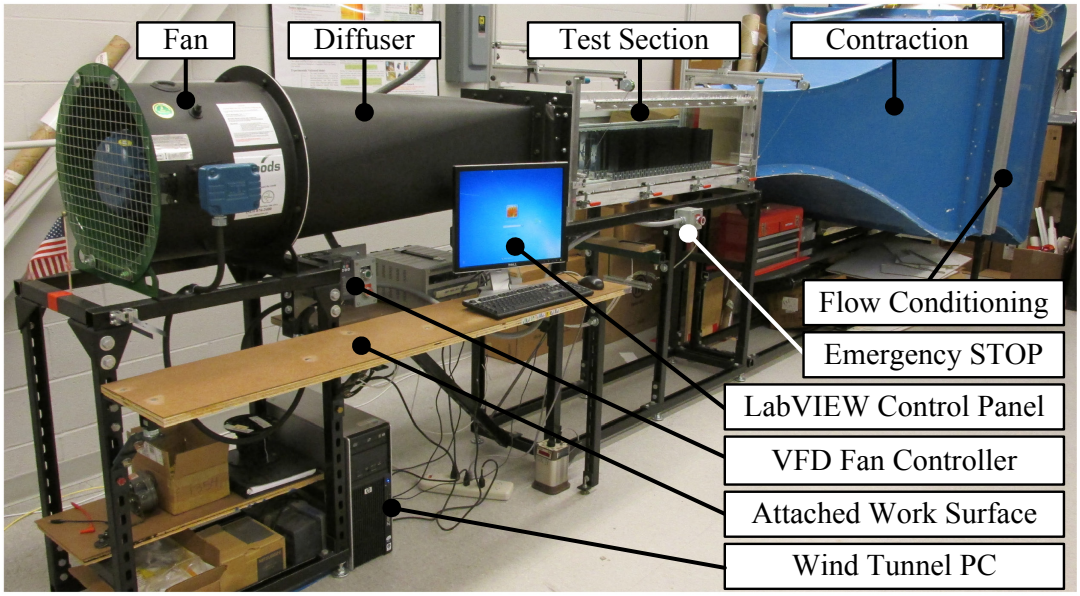

Figure A.17: A snapshot showing the completed final design of the wind tunnel testing facility fully assembled and prepared for operation.

Table A.4: Summary of performance, dimensions, and functionality of final wind tunnel design.

Parameter	*Value*	*Notes*
Maximum velocity	33 m/s (73.8 mph)	Inside empty test section
Minimum measurable velocity	0.1 m/s (0.224 mph)	
Maximum fan speed	583 rad/s (5570 RPM)	See fan specifications
Fan speed resolution	Continuously variable	
Test section height	30.48 cm (12 in)	
Test section width	30.48 cm (12 in)	
Viewable test section length	1.219 m (48 in)	Measured glass length
Total test section length	1.397 m (55 in)	Measured between flange faces
Total wind tunnel length	5.782 m (228 in)	Measured from inlet to exit
Motor controller type	VFD	Variable frequency drive
Fan type	3-blade, axial	Direct drive
Velocity measurement	Pitot-static tube	
Temperature measurement	T-type thermocouple	Air and motor temp. monitoring
Computer interface	Yes	Dedicated PC w/ LabVIEW
Electronic noise reduction	Optical isolation	
Digital filtering	Yes	LabVIEW
Manual turn dial control mode	Yes	See controller manual
Analog input control mode	Yes	See controller manual
PID velocity control mode	Yes	See controller manual
Real-time virtual control panel	Yes	Fully customizable / LabVIEW
Sacrificial element overload protection	Yes	3-phase fuses and thermal overloads
Automatic overload protection	Yes	Digitally monitored by controller
Electrical fault interruption	Yes	Electromagnetic motor starter
Emergency STOP button	Yes	Mounted on test section

APPENDIX B

DUAL CANTILEVER FLUTTER: CFD MODELING

While investigating the lumped parameter dual cantilever flutter (DCF) model from Chapter 6, a model was also developed for both entrainment and flutter using commercially available CFD code. Details of this work are presented in this Appendix.

B.1 CFD Modeling

A CFD model was developed in order to help understand what initiates the instability between two beams in a flowing fluid ultimately causing them to undergo DCF. The CFD modeling was based on a 2-D system with two rigid plates similar to the lumped parameter model discussed in Section 6.2.2. It was decided to develop this 2-D model first, rather than a computationally expensive, 3-D fluid-structure-interaction model. All properties from Table 6.2 except L and β were applied to the CFD model.

A schematic of the meshing zones designed for the CFD model is shown in Figure B.1. Two different types of CFD simulations were performed using the same basic mesh layout. The first simulations were focused on fluid coupling effects and entrainment dynamics between two plates in a quiescent fluid where one plate is released from an initial deflection causing an adjacent plate to vibrate.

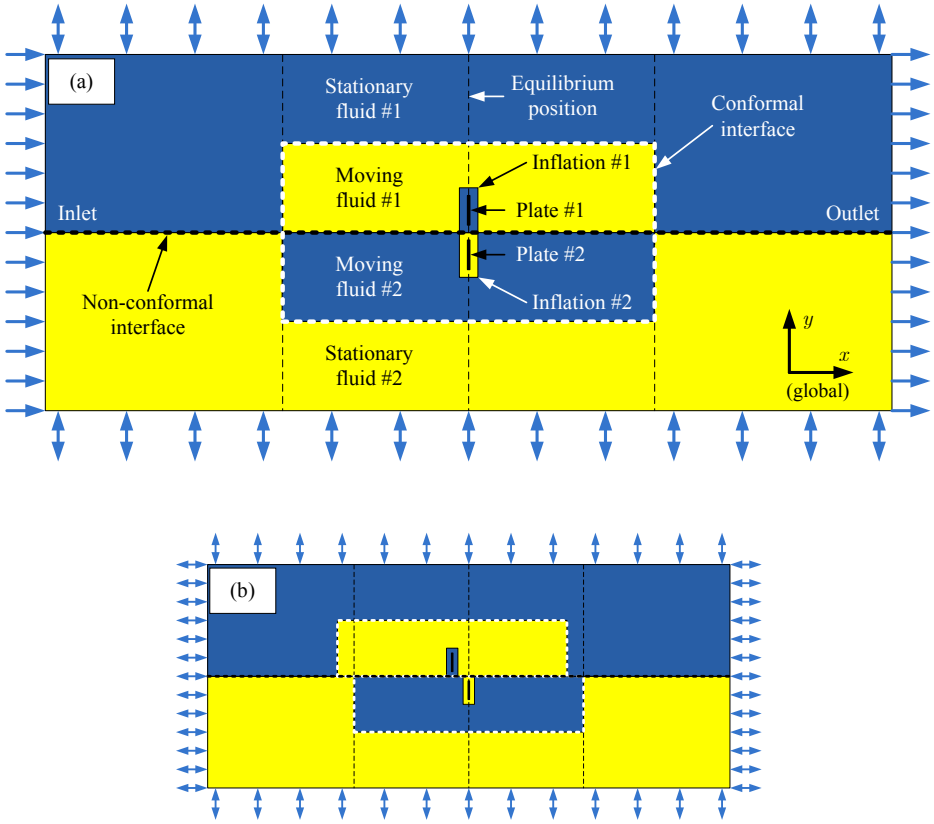

Figure B.1: A schematic showing details of the computational domain (not to scale) and various meshing zones (a) without and (b) with relative plate deflection to demonstrate the translation and deformation of the meshing zones.

The second type of CFD simulations investigated the DCF phenomenon using the same two plates and mesh as the entrainment simulations. The two primary differences between the entrainment and DCF simulations were that the DCF simulations had a non-zero velocity prescribed at the inlet, and both plates had no initial deflection or initial velocity.

B.1.1 Meshing Zones & Boundaries

Figure B.1 shows a schematic that defines the major meshing zones, interfaces, and general layout of the computational domain developed using ANSYS-CFX for the 2-D CFD simulations. Two rigid plates were placed in a surrounding fluid and assigned individual coordinate systems

which will be referred to as C1 and C2 for plate #1 and plate #2 respectively. The motion of both plates was constrained such that only translation in the x-direction was allowed. Both plates were prescribed with identical mass, stiffness, and damping parameters. Both mass and stiffness could be defined using standard rigid-body options in CFX; while the damping parameter was implemented using CFX expression language (CEL). A *no-slip wall* boundary condition was imposed on all surfaces of both plates. The top and bottom boundary conditions of the computational domain were *open* for all simulations. The left and right boundary conditions were set to *inlet* and *outlet* (respectively) for DCF simulations as shown in in Figure B.1a. For entrainment simulations however, both left and right boundary conditions were set to *open* as illustrated in Figure B.1b.

The fluid was divided into three major zones for each plate (six total zones). Immediately surrounding each plate was an *inflation* zone which contained a mapped mesh having quadrilateral elements. This mapping was designed such that the cell sizing was biased to be very small at the plate surface while increasing at a geometric rate as distance from the plate increased. Each inflation zone was surrounded by a *moving fluid* zone which was meshed with unstructured triangular elements. Cell sizing within the moving fluid zones was controlled by prescribing a maximum cell size and growth rate. The final and outermost meshing zone was called the *stationary fluid* zone which was also meshed with unstructured triangular elements. Cell sizing within the stationary fluid zones was controlled by specifying growth rate. This growth rate was defined such that the outermost cells were much larger than the cells within the moving fluid zones.

A non-conformal fluid-fluid interface was used to separate the fluid into two halves such that the mesh in each half could move completely independent of the other half. This non-conformal

interface is shown as the horizontal black dotted line that extends the entire length of the fluid between the two plates. Nodes along both sides of this interface were allowed to slide past each other and information was freely passed across the interface between adjacent nodes using an interpolation scheme. No deformation was allowed within the inflation and moving fluid meshes; however, they were able to translate with each plate as shown in Figure B.1b. This translation was made possible by linking the mesh to the local coordinates of each plate (C1 and C2) while the fluid within the mesh remained in the global coordinate system. Defining the individual coordinate systems in this way allowed the mesh to translate without affecting the fluid motion. Mesh within the stationary fluid zones was allowed to deform to serve as a buffer zone between the moving fluid zones and the fixed boundaries of the computational domain. Again, the deformation of the mesh within the stationary fluid zones did not affect the motion of the fluid. A conformal, fluid-fluid interface was used between the moving and stationary mesh zones as is shown as a white dotted line along the three outer edges of the moving fluid zones in Figure B.1. This conformal interface requires nodes on one side of the interface to be linked to those on the other such that no sliding or separation is allowed.

B.1.2 CFD Simulation Results

A significant amount of effort was devoted to developing and validating the mesh described in Section B.1.1. After many design iterations, consistent simulation results that were independent of both the mesh and the time-step were attained. A shear stress transport (SST) turbulence model was used for all final simulations because it was found to produce the most reliable results compared to laminar, k-ε, and k-ω models.

The time-series results of two CFD simulations are shown in Figure B.2. Both of these results were produced using the same parameters for the mesh, solver, and plates.

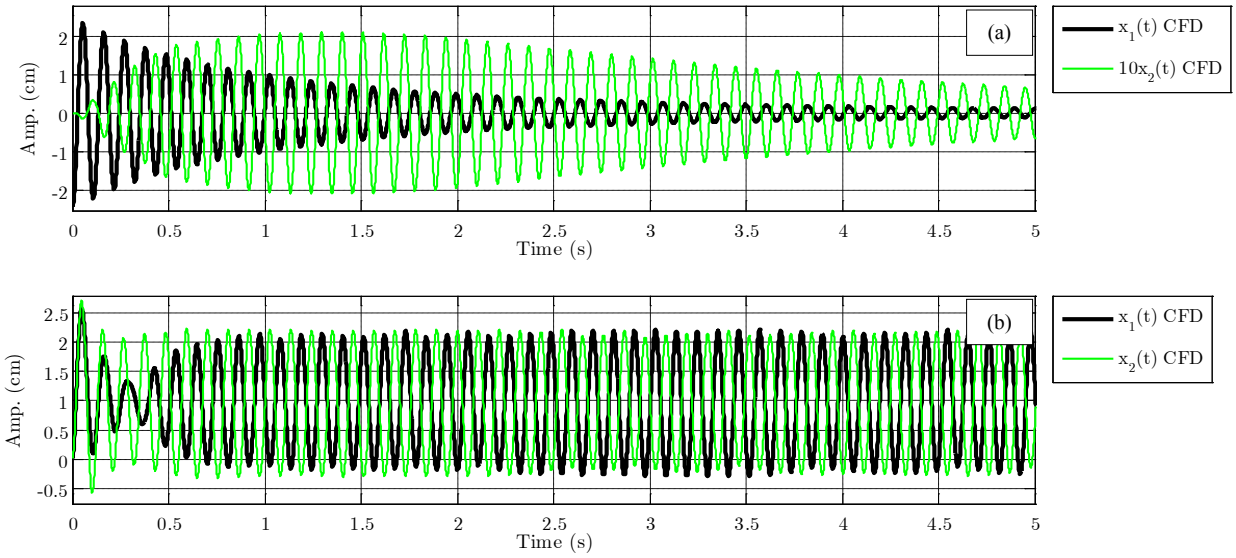

Figure B.2: Time-series displacement results of two CFD simulations demonstrating (a) the entrainment dynamics and (b) the flutter dynamics of two adjacent plates in in air.

The entrainment results shown in Figure B.2a. clearly show a similar response to the model and experimental results shown previously in Figure 6.2. The response of plate #1 gradually begins to excite plate #2 through fluid coupling only. Notice that the displacement amplitude of plate #2 in Figure B.2a is increased by a factor of ten in order to show relative motion between the plates with greater detail.

The flutter response is shown in Figure B.2b where both plates start with zero displacement and velocity, then they are quickly forced into limit cycle oscillations with a positive mean displacement. The plates have similar displacements for nearly the entire first cycle of oscillation and they maintain a similar phase for approximately 2.5 cycles before becoming *locked-in* at 180 degrees out of phase. During this phase change the amplitude of plate #1 decreases significantly below that of plate #2. After approximately 1.0 second, both plates begin oscillating at a steady and nearly identical amplitude.

BIBLIOGRAPHY

[1] Pankonien, A.M., and Ounaies, Z., "Piezoelectric Artificial Kelp for Energy Harvesting," *ASME Conference Proceedings* **2010**(44168), 223–232, ASME (2010).

[2] Hobbs, W.B., and Hu, D.L., "Tree-inspired piezoelectric energy harvesting," *Journal of Fluids and Structures* **28**, 103–114 (2012).

[3] Li, S., and Lipson, H., "Vertical-stalk flapping-leaf generator for wind energy harvesting," *Proceedings of the ASME Conference on Smart Materials, Adaptive Structures and Intelligent Systems 2009, SMASIS2009* **2**, 611–619, Oxnard, CA (2009).

[4] Wikander, Ö., *Handbook of Ancient Water Technology*, Örjan Wikander, Ed., Brill (2000).

[5] Anderson, A.F., "Sparks from steam. The story of the Armstrong hydroelectric generator," *Electronics and Power* **24**(1), 50–53 (1978).

[6] USGS, "http://ga.water.usgs.gov/edu/wuhy.html" (2013).

[7] Price, T.J., "James Blyth - Britain's first modern wind power pioneer," *Wind Engineering* **29**(3), 191–200 (2005).

[8] GWEC, "http://www.gwec.net/global-figures/wind-in-numbers/" (2013).

[9] Klakken, M., and Schmidt, V.H., "Experimental study of piezoelectric polymer blades as wind generation elements," in *Proceedings of the Montana Academy of Science* **42**, pp. 96–100 (1983).

[10] Schmidt, V.H., Klakken, M., and Darejeh, H., "PVF2 bimorphs as active elements in wind generators," *Ferroelectrics* **51**(1), 105–110, Taylor \& Francis (1983).

[11] Schmidt, V.H., "Piezoelectric wind generator," US Patent 4,536,674, Google Patents (1985).

[12] Schmidt, V.H., "Piezoelectric energy conversion in windmills," in *Ultrasonics Symposium, 1992. Proceedings., IEEE 1992*, pp. 897–904 (1992).

[13] Akaydin, H.D., Elvin, N., and Andreopoulos, Y., "Energy harvesting from highly unsteady fluid flows using piezoelectric materials," *Journal of Intelligent Material Systems and Structures* **21**(13), 1263–1278 (2010).

[14] Gao, X., Shih, W.-H., and Shih, W.Y., "Flow energy harvesting using piezoelectric cantilevers with cylindrical extension," *IEEE Transactions on Industrial Electronics* **60**(3), 1116–1118 (2013).

[15] Li, S., Yuan, J., and Lipson, H., "Ambient wind energy harvesting using cross-flow fluttering," *Journal of Applied Physics* **109**(2) (2011).

[16] Bryant, M., and Garcia, E., "Energy harvesting: A key to wireless sensor nodes," *Proceedings of SPIE - The International Society for Optical Engineering* **7493**, San Diego, CA (2009).

[17] Dunnmon, J., Stanton, S., Mann, B., and Dowell, E., "Power extraction from aeroelastic limit cycle oscillations," *Journal of Fluids and Structures*, Elsevier (2011).

[18] Karami, M.A., Farmer, J.R., and Inman, D.J., "Nonlinear dynamics of the bi-stable piezoelectric wind energy harvester," *Proceedings of SPIE - The International Society for Optical Engineering* **8341**, San Diego, CA (2012).

[19] Chen, C.-T., Islam, R.A., and Priya, S., "Electric energy generator," *IEEE Transactions on Ultrasonics, Ferroelectrics, and Frequency Control* **53**(3), 656–661 (2006).

[20] Priya, S., "Modeling of electric energy harvesting using piezoelectric windmill," *Applied Physics Letters* **87**(18), 1–3 (2005).

[21] Howey, D.A., Bansal, A., and Holmes, A.S., "Design and performance of a centimetre-scale shrouded wind turbine for energy harvesting," *Smart Materials and Structures* **20**(8) (2011).

[22] Flammini, A., Marioli, D., Sardini, E., and Serpelloni, M., "An autonomous sensor with energy harvesting capability for airflow speed measurements," *2010 IEEE International Instrumentation and Measurement Technology Conference, I2MTC 2010 - Proceedings*, 892–897, Austin, TX (2010).

[23] Rancourt, D., Tabesh, A., and Fréchette, L.G., "Evaluation of centimeter-scale micro windmills: aerodynamics and electromagnetic power generation," *Proc. PowerMEMS*, 28–29 (2007).

[24] Khan, M., Iqbal, M., and Quaicoe, J., "River current energy conversion systems: Progress, prospects and challenges," *Renewable and Sustainable Energy Reviews* **12**(8), 2177–2193, Elsevier (2008).

[25] Bansal, A., Howey, D.A., and Holmes, A.S., "CM-scale air turbine and generator for energy harvesting from low-speed flows," *Solid-State Sensors, Actuators and Microsystems Conference, 2009. TRANSDUCERS 2009. International*, 529–532 (2009).

[26] Holmes, A.S., Howey, D.A., Bansal, A., and Yates, D.C., "Self-powered wireless sensor for duct monitoring," *Proc. PowerMEMS 2010, Poster Proceedings*, 115–118 (2010).

[27] Bressers, S., Avirovik, D., Vernieri, C., Regan, J., Chappell, S., Hotze, M., Luhman, S., Lallart, M., Inman, D., et al., "Small-scale modular windmill," *American Ceramic Society Bulletin* **89**(8), 34–40, San Diego, CA (2010).

[28] Xu, F.J., Yuan, F.G., Hu, J.Z., and Qiu, Y.P., "Design of a miniature wind turbine for powering wireless sensors," *Proceedings of SPIE - The International Society for Optical Engineering* **7647**, San Diego, CA (2010).

[29] Xu, F.J., Hu, J.Z., Qiu, Y.P., and Yuan, F.G., "Physics-based model for predicting the performance of a miniature wind turbine," *Proceedings of SPIE - The International Society for Optical Engineering* **7981**, San Diego, CA (2011).

[30] Sardini, E., and Serpelloni, M., "Self-powered wireless sensor for air temperature and velocity measurements with energy harvesting capability," *IEEE Transactions on Instrumentation and Measurement* **60**(5), 1838–1844 (2011).

[31] Myers, R., Vickers, M., Kim, H., and Priya, S., "Small scale windmill," *Applied Physics Letters* **90**(5) (2007).

[32] Priya, S., "Advances in energy harvesting using low profile piezoelectric transducers," *Journal of Electroceramics* **19**(1), 167–184, Springer (2007).

[33] Tien, C.M.T., and Goo, N.S., "Use of a piezo-composite generating element for harvesting wind energy in an urban region," *Aircraft Engineering and Aerospace Technology* **82**(6), 376–381 (2010).

[34] Bressers, S., Avirovik, D., Lallart, M., Inman, D.J., and Priya, S., "Contact-less wind turbine utilizing piezoelectric bimorphs with magnetic actuation," *Conference Proceedings of the Society for Experimental Mechanics Series* **3**(PART 1), 233–243, Jacksonville, FL (2011).

[35] Alaskan, A., "http://www.absak.com/" (2013).

[36] Manufacturing, C., and Engineering, I., "http://www.custom-mfg-eng.com/contact.php" (2005).

[37] Lu, K., Rasmussen, P.O., and Ritchie, E., "An Analytical Equation for Cogging Torque Calculation in Permanent Magnet Motors," July (2006).

[38] Williamson, C.H.K., "Vortex dynamics in the cylinder wake," *Annual Review of Fluid Mechanics* **28**, 477–539 (1996).

[39] Williamson, C.H.K., and Govardhan, R., "Vortex-induced vibrations," *Annual Review of Fluid Mechanics* **36**, 413–455 (2004).

[40] Bernitsas, M.M., Raghavan, K., Ben-Simon, Y., and Garcia, E.M.H., "VIVACE (Vortex Induced Vibration Aquatic Clean Energy): A new concept in generation of clean and renewable energy from fluid flow," *Journal of Offshore Mechanics and Arctic Engineering* **130**(4) (2008).

[41] Bernitsas, M.M., and Raghavan, K., "Fluid motion energy converter," US Patent 7,493,759, Google Patents (2009).

[42] Pobering, S., Menacher, M., Ebermaier, S., and Schwesinger, N., "PIEZOELECTRIC POWER CONVERSION WITH SELF-INDUCED OSCILLATION," *PowerMEMS*, 384–387 (2009).

[43] Pobering, S., Ebermeyer, S., and Schwesinger, N., "Generation of electrical energy using short piezoelectric cantilevers in flowing media," in *Proceedings of SPIE* **7288**, p. 728807 (2009).

[44] Bischur, E., Pobering, S., Menacher, M., and Schwesinger, N., "Flow Driven Vibration Energy Harvester" (2010).

[45] Pobering, S., Ebermayer, S., and Schwesinger, N., "Energy harvesting under induced best conditions," *Conference Proceedings of the Society for Experimental Mechanics Series* **1**, 239–245, Jacksonville, FL (2011).

[46] Taylor, G.W., Burns, J.R., Kammann, S., Powers, W.B., and Welsh, T.R., "The energy harvesting eel: a small subsurface ocean/river power generator," *Oceanic Engineering, IEEE Journal of* **26**(4), 539–547, IEEE (2001).

[47] Akaydin, H.D., Elvin, N., and Andreopoulos, Y., "Experimental Study of a Self-Excited Piezoelectric Energy Harvester," *ASME Conference Proceedings* **2010**(44151), 179–185, ASME (2010).

[48] Bade, P., "Flapping-vane wind machine.," *Proceedings of the International Conference of Appropriate Technologies for Semiarid Areas: Wind and Solar Energy for Water Supply*, 83–88, West Berlin (1975).

[49] McKinney, W., and DeLaurier, J., "Wingmill: An Oscillating-wing Windmill," *Journal of energy* **5**(2), 109–115 (1981).

[50] Pobering, S., and Schwesinger, N., "A new micro hydro power device," *Nanotech* **1** (2003).

[51] De Marqui Jr., C., Erturk, A., and Inman, D.J., "Piezoaeroelastic modeling and analysis of a generator wing with continuous and segmented electrodes," *Journal of Intelligent Material Systems and Structures* **21**(10), 983–993 (2010).

[52] Robbins, W.P., Marusic, I., Morris, D., and Novak, T.O., "Wind-generated electrical energy using flexible piezoelectric materials," 9 (2006).

[53] Elvin, N.G., and Elvin, A.A., "The flutter response of a piezoelectrically damped cantilever pipe," *Journal of Intelligent Material Systems and Structures* **20**(16), 2017–2026 (2009).

[54] Tang, L., Paidoussis, M.P., and Jiang, J., "Cantilevered flexible plates in axial flow: Energy transfer and the concept of flutter-mill," *Journal of Sound and Vibration* **326**(1), 263–276, Elsevier (2009).

[55] Shimizu, E., Isogai, K., and Obayashi, S., "Multiobjective design study of a flapping wing power generator," *Journal of Fluids Engineering, Transactions of the ASME* **130**(2), 0211041–0211048 (2008).

[56] Jung, H.-J., Lee, S.-W., and Jang, D.-D., "Feasibility Study on a new energy harvesting electromagnetic device using aerodynamic instability," *IEEE Transactions on Magnetics* **45**(10), 4376–4379 (2009).

[57] Bryant, M., and Garciaa, E., "Development of an aeroelastic vibration power harvester," *Proceedings of SPIE - The International Society for Optical Engineering* **7288**, San Diego, CA (2009).

[58] Erturk, A., Vieira, W., De Marqui Jr, C., and Inman, D., "On the energy harvesting potential of piezoaeroelastic systems," *Applied physics letters* **96**, 184103 (2010).

[59] De Marqui, C., and Erturk, A., "Electroaeroelastic analysis of airfoilbased wind energy harvesting using piezoelectric transduction and electromagnetic induction," *Journal of Intelligent Material Systems and Structures* (2012).

[60] Hobeck, J.D., and Inman, D.J., "Energy harvesting from turbulence-induced vibration in air flow: Artificial piezoelectric grass concept," *ASME 2011 Conference on Smart Materials, Adaptive Structures and Intelligent Systems, SMASIS 2011* **2**, 637–646, Scottsdale, AZ (2011).

[61] Au-Yang, M.K., *Flow Induced Vibration of Power and Process Plant Components*, 1st ed., ASME Press, New York, NY (2001).

[62] Minesto, “http://www.minesto.com/deepgreentechnology/index.html” (2013).

[63] EnerKite, “http://www.enerkite.com/Home.html” (2010).

[64] Snarski, S.R., Kasper, R.G., and Bruno, A.B., “Device for electro-magnetohydrodynamic (EMHD) energy harvesting,” *Proceedings of SPIE - The International Society for Optical Engineering* **5417**, Carapezza E.M., ed., 147–161, Orlando, FL (2004).

[65] Pfenniger, A., Obrist, D., Stahel, A., Koch, V.M., and Vogel, R., “Energy harvesting through arterial wall deformation: design considerations for a magneto-hydrodynamic generator,” *Medical and Biological Engineering and Computing*, 1–15 (2013).

[66] Habermann, W., and Pommer, E.-H., “Biological fuel cells with sulphide storage capacity,” *Applied Microbiology and Biotechnology* **35**(1), 128–133 (1991).

[67] Reimers, C.E., Tender, L.M., Fertig, S., and Wang, W., “Harvesting energy from the marine sediment - Water interface,” *Environmental Science and Technology* **35**(1), 192–195, ACS, Washington, DC, United States (2001).

[68] He, Z., Shao, H., and Angenent, L.T., “Increased power production from a sediment microbial fuel cell with a rotating cathode,” *Biosensors and Bioelectronics* **22**(12), 3252 – 3255 (2007).

[69] Clair, D.S., Stabler, C., Daqaq, M.F., Luo, J., and Li, G., “A smart device for harnessing energy from aerodynamic flow fields,” *ASME International Mechanical Engineering Congress and Exposition, Proceedings* **11**, 377–381, Lake Buena Vista, FL (2009).

[70] St. Clair, D., Bibo, A., Sennakesavababu, V.R., Daqaq, M.F., and Li, G., “A scalable concept for micropower generation using flow-induced self-excited oscillations,” *Applied Physics Letters* **96**(14) (2010).

[71] Bibo, A., Li, G., and Daqaq, M.F., “Electromechanical modeling and normal form analysis of an aeroelastic micro-power generator,” *Journal of Intelligent Material Systems and Structures* **22**(6), 577–592 (2011).

[72] Zurkinden, A., Campanile, F., and Martinelli, L., “Wave energy converter through piezoelectric polymers,” in *Proceedings of the COMSOL Users Conference* (2007).

[73] Bilgen, O., “Aerodynamic and Electromechanical Design, Modeling and Implementation of Piezocomposite Airfoils” (2010).

[74] Lu, F., Lee, H., and Lim, S., “Modeling and analysis of micro piezoelectric power generators for micro-electromechanical-systems applications,” *Smart Materials and Structures* **13**, 57, IOP Publishing (2004).

[75] Erturk, A., *Electromechanical modeling of piezoelectric energy harvesters* (2009).

[76] Knisely, C.W., "Strouhal numbers of rectangular cylinders at incidence: A review and new data ," *Journal of Fluids and Structures* **4**(4), 371 – 393 (1990).

[77] Roshko, A., "Experiments on the flow past a circular cylinder at very high Reynolds number," *J. Fluid Mech* **10**(3), 345–356, Cambridge Univ Press (1961).

[78] Newland, D.E., *An introduction to random vibrations and spectral analysis*, 1st ed., Longman, London (1975).

[79] Hobeck, J.D., and Inman, D.J., "Design and Analysis of Dual Pressure Probes for Predicting Turbulence-Induced Vibration in Low Velocity Flow," *Proceedings of the 53rd AIAA/ASME/ASCE/AHS/ASC Structures, Structural Dynamics, and Materials Conference*, Honolulu, HI (2012).

[80] Hobeck, J.D., and Inman, D.J., "Artificial piezoelectric grass for energy harvesting from turbulence-induced vibration," *Smart Materials and Structures* **21**(10) (2012).

[81] Blevins, R.D., *Flow-induced vibration*, Van Nostrand Reinhold Co., New York (1977).

[82] Erturk, A., and Inman, D.J., "A distributed parameter electromechanical model for cantilevered piezoelectric energy harvesters," *Journal of Vibration and Acoustics, Transactions of the ASME* **130**(4) (2008).

[83] Priya, S., and Inman, D.J., *Energy Harvesting Technologies*, Springer London, Limited (2008).

[84] Erturk, A., Tarazaga, P.A., Farmer, J.R., and Inman, D.J., "Effect of strain nodes and electrode configuration on piezoelectric energy harvesting from cantilevered beams," *Journal of Vibration and Acoustics,* **131**(1), 0110101–01101011 (2009).

[85] Leo, D.J., *Engineering Analysis of Smart Material Systems*, Wiley (2007).

[86] Riley, W.F., Sturges, L.D., and Morris, D.H., *Mechanics of materials*, John Wiley (2006).

[87] Rao, S.S., *Vibration of Continuous Systems*, Wiley (2007).

[88] Bhat, R.B., "Natural frequencies of rectangular plates using characteristic orthogonal polynomials in rayleigh-ritz method," *Journal of Sound and Vibration* **102**(4), 493–499 (1985).

[89] Hayt, W.H., Kemmerly, J.E., and Durbin, S.M., *Engineering circuit analysis*, McGraw-Hill Higher Education (2007).

[90] Powell, A., "On the fatigue failure of structures due to vibrations excited by random pressure fields," *The Journal of the Acoustical Society of America* **30**, 1130–1135 (1958).

[91] Au-Yang, M.K., "Joint and cross acceptances for cross-flow-induced vibration - Part I: theoretical and finite element formulations," *Journal of Pressure Vessel Technology* **122**(3), 349–354 (2000).

[92] Anton, S.R., Erturk, A., and Inman, D.J., "Bending strength of piezoelectric ceramics and single crystals for multifunctional load-bearing applications," *IEEE Transactions on Ultrasonics, Ferroelectrics, and Frequency Control* **59**(6), 1085–1092 (2012).

[93] Hobeck, J.D., and Inman, D.J., "Electromechanical and statistical modeling of turbulence-induced vibration for energy harvesting," *Proceedings of SPIE - The International Society for Optical Engineering* **8688**, 86881P1–86881P14, San Diego, CA (2013).

[94] Jezdinsky, V., "Measurement of Turbulence by Pressure Probes," *AIAA Journal* **4**(11), 2072–2073 (1966).

[95] Lenherr, C., Kalfas, A.I., and Abhari, R.S., "High temperature fast response aerodynamic probe," *Journal of Engineering for Gas Turbines and Power* **133**(1) (2011).

[96] Shepherd, I.C., "Four hole pressure probe for fluid flow measurements in three dimensions," *Journal of Fluids Engineering, Transactions of the ASME* **103**(4), 590–594 (1981).

[97] Hooper, J.D., and Musgrove, A.R., "Reynolds Stress, Mean Velocity, and Dynamic Static Pressure Measurement by a Four-Hole Pressure Probe," *Experimental Thermal and Fluid Science* **15**(4), 375–383 (1997).

[98] Lee, S.W., and Jun, S.B., "Reynolds number effects on the non-nulling calibration of a cone-type five-hole probe for turbomachinery applications," *Journal of Mechanical Science and Technology* **19**(8), 1632–1648 (2005).

[99] Au-Yang, M., and Jordan, K., "Dynamic pressure inside a PWR-A study based on laboratory and field test data," *Nuclear Engineering and Design* **58**(1), 113–125, Elsevier (1980).

[100] Au-Yang, M.K., "Joint and cross acceptances for cross-flow-induced vibration - Part II: charts and applications," *Journal of Pressure Vessel Technology, Transactions of the ASME* **122**(3), 355–361 (2000).

[101] Au-Yang, M.K., "Response of reactor internals to fluctuating pressure forces," *Nuclear Engineering and Design* **35**(3), 361–375 (1975).

[102] Finnveden, S., Birgersson, F., Ross, U., and Kremer, T., "A model of wall pressure correlation for prediction of turbulence-induced vibration," *Journal of fluids and structures* **20**(8), 1127–1143, Elsevier (2005).

[103] Grover, L.K., and Weaver, D.S., "Cross-flow induced vibrations in a tube bank-Vortex shedding," *Journal of Sound and Vibration* **59**(2), 263–276 (1978).

[104] Axisa, F., Antunes, J., and Villard, B., "Random excitation of heat exchanger tubes by cross-flows," *Journal of Fluids and Structures* **4**(3), 321 – 341 (1990).

[105] Bruun, H.H., *Hot-wire anemometry: principles and signal analysis*, Oxford University Press (1995).

[106] Çengel, Y.A., and Boles, M.A., *Thermodynamics: an engineering approach*, Fifth Ed., McGraw-Hill Higher Education (2006).

[107] van Ommen, J.R., Schouten, J.C., vander Stappen, M.L.M., and van den Bleek, C.M., "Response characteristics of probe-transducer systems for pressure measurements in gas-solid fluidized beds: how to prevent pitfalls in dynamic pressure measurements," *Powder Technology* **106**(3), 199–218, Elsevier (1999).

[108] Weiss, J., Knauss, H., and Wagner, S., "Method for the determination of frequency response and signal to noise ratio for constant-temperature hot-wire anemometers," *Review of Scientific Instruments* **72**(3), 1904–1909 (2001).

[109] Bergh, H., and Tijdeman, H., *Theoretical and experimental results for the dynamic response of pressure measuring systems*, National Aero- and Astronautical Research Institute, Amsterdam, Netherlands (1965).

[110] Irwin, H., Cooper, K., and Girard, R., "Correction of distortion effects caused by tubing systems in measurements of fluctuating pressures," *Journal of Wind Engineering and Industrial Aerodynamics* **5**(1-2), 93–107, Elsevier (1979).

[111] Kupferschmied, P., Köppel, P., Gizzi, W., Roduner, C., and Gyarmathy, G., "Time-resolved flow measurements with fast-response aerodynamic probes in turbomachines," *Measurement Science and Technology* **11**, 1036, IOP Publishing (2000).

[112] Incropera, F.P., DeWitt, D.P., Bergman, T.L., and Lavine, A.S., *Introduction to Heat Transfer*, Fifth Ed., Wiley (2006).

[113] Crowe, C.C.T., Elger, D.F., and Roberson, J.A., *Engineering fluid mechanics*, Eighth Ed., John Wiley & Sons, Incorporated (2005).

[114] MISSING:hobeckIOP2012inpress, "MISSING:hobeckIOP2012inpress" (2014).

[115] Finnigan, J., "Turbulence in Waving Wheat. I. Mean Statistics and Honami," *Boundary-Layer Meteorology* **16**(2), 181–211, Springer (1979).

[116] Inoue, E., "Studies of the phenomena of waving plants (" honami") caused by wind. Part 1: Mechanism and characteristics of waving plants phenomena," *J. Agricult. Meteorol.(Japan)* **11**, 71–82 (1955).

[117] Crowe, C.T., Elger, D.F., Roberson, J.A., and Williams, B.C., *Engineering Fluid Mechanics*, John Wiley \& Sons (2008).

[118] Sarioglu, M., and Yavuz, T., "Vortex shedding from circular and rectangular cylinders placed horizontally in a turbulent flow," *Turkish Journal of Engineering \& Environmental Sciences/Turk Muhendislik ve Cevre Bilimleri Dergisi* **24**(4), 217–228 (2000).

[119] Bearman, P.W., "Vortex shedding from oscillating bluff bodies," *Annual Review of Fluid Mechanics* **16**(1), 195–222, Annual Reviews 4139 El Camino Way, PO Box 10139, Palo Alto, CA 94303-0139, USA (1984).

[120] Williamson, C., and Govardhan, R., "Dynamics and forcing of a tethered sphere in a fluid flow," *Journal of fluids and structures* **11**(3), 293–305, Elsevier (1997).

[121] Govardhan, R., and Williamson, C., "Vortex-induced vibrations of a sphere," *Journal of Fluid Mechanics* **531**(1), 11–47, Cambridge Univ Press (2005).

[122] Williamson, C., "Structure Dynamics, Vortex Dynamics and Fluid Loading on Structures in Waves and Currents" (2003).

[123] Govardhan, R., and Williamson, C., "Resonance forever: existence of a critical mass and an infinite regime of resonance in vortex-induced vibration," *Journal of Fluid Mechanics* **473**(473), 147–166, Cambridge Univ Press (2002).

[124] Sallet, D., "The lift force due to Von Karman's vortex wake," *Journal of Hydronautics* **7**(4) (1973).

[125] Weiliang, Y., and Dowell, E., "Limit cycle oscillation of a fluttering cantilever plate," *AIAA journal* **29**(11), 1929–1936 (1991).

[126] Bryant, M., Gomez, J.C., and Garcia, E., "Reduced-Order aerodynamic modeling of flapping wing energy harvesting at low reynolds number," *AIAA Journal* **51**(12), 2771–2782 (2013).

[127] Dowell, E.H., "Panel Flutter, A Review of the Aeroelastic Stability of Plates and Shells," *AIAA Journal* **8**(3), 385–399 (1970).

[128] Bisplinghoff, R.L., Ashley, H., and Halfman, R.L., *Aeroelasticity*, Dover Publications (1996).

[129] Hobeck, J.D., and Inman, D.J., "The dynamics of large arrays of flexible structures in fluid flow with applications to energy harvesting," *Proceedings of the 25th ISMA Biennial International Conference on Noise and Vibration Engineering*, Leuven, Belgium (2012).

[130] Hobeck, J.D., and Inman, D.J., "Energy Harvesting from Flow-Induced Waving Motion of a Piezoelectric Grass Array," *Proceedings of ICAST - The 24th International Conference on Adaptive Structures and Technologies*, Aruba (2013).

[131] Hagedorn, P., and Stadler, W., *Non-linear oscillations*, Clarendon Press (1981).